TAMPEREEN TEKNILLINEN YLIOPISTO
TAMPERE UNIVERSITY OF TECHNOLOGY

Ville Polojärvi

Novel III-V Heterostructures for High Efficiency Solar Cells

Studies of Electrical and Optical Properties

Julkaisu 1383 • Publication 1383

Tampere 2016

Tampereen teknillinen yliopisto. Julkaisu 1383
Tampere University of Technology. Publication 1383

Ville Polojärvi

Novel III-V Heterostructures for High Efficiency Solar Cells
Studies of Electrical and Optical Properties

Thesis for the degree of Doctor of Science in Technology to be presented with due permission for public examination and criticism in Tietotalo Building, Auditorium TB104, at Tampere University of Technology, on the 13th of May 2016, at 12 noon.

Tampereen teknillinen yliopisto - Tampere University of Technology
Tampere 2016

ISBN 978-952-15-3735-6 (printed)
ISBN 978-952-15-3750-9 (PDF)
ISSN 1459-2045

Abstract

The thesis deals with the investigation of optical, electrical and structural properties of III-V semiconductor materials and nanostructures with applications in the development of next generation solar cells. In particular, the focus is on the study of quantum well (QW) and quantum dot (QD) nanostructures, and dilute nitride materials. Nanostructures can improve solar cell performance by, e.g., extending the absorption edge, providing an intermediate band, or suppressing reflection at the solar cell surface. Dilute nitrides, on the other hand, can provide better utilization of the solar spectrum, thus increasing the conversion efficiency of multijunction solar cells. The interplay between fabrication parameters as well as post growth treatments of the investigated structures, and their optical and electrical properties, are assessed by several characterization methods, including photoluminescence and capacitance spectroscopy. The results show that small changes in these parameters can have a significant influence on the defect populations and overall properties of the heterostructure, eventually defining the solar cell performance.

Starting from the outer layer of the solar cell device, the surface structure was found to play an important role in connection with thermal annealing. Short chemical treatments modifying the GaAs surface had a huge influence on optical and structural properties of the studied QWs upon annealing. Furthermore, ammonium sulfide treatment of the solar cell AlInP window layer was found to modify the surface structure and improve the solar cell performance. Optimization of the amount of deposited InAs and use of the so-called “flushing technique” was found to remove unwanted defects in QD layers. For the GaSb QD heterostructures, the influence of material fluxes during the growth, thermal annealing, and stacking of QD layers on optical and solar cell properties was studied. Dilute nitride QWs, acting as strain compensation and mediation layers for QD layers, were found to extend the absorption edge in the solar cell structure, and provide steps for charge carriers to thermally escape from the QD layer. Stacked strain free GaAs QD nanostructures, fabricated by refilling of self-assembled nanoholes, were found to emit photoluminescence related to several quantum dot states with narrow linewidths. The investigated GaAs QDs were also extremely temperature stable upon high temperature thermal annealing, indicating low defect densities. The formation of defects in bulk dilute nitride solar cells and their relation to process parameters on the one hand, and solar cell properties on the other hand, was also studied; optimal fabrication conditions were then devised. Incorporation of Sb was found to decrease the background doping density but at the same time broaden the deep level transient spectroscopy spectra. Furthermore, the As flux used during the fabrication of the dilute nitride solar cell was found to have a remarkable influence on solar cell performance.

Acknowledgements

Research and development conducted in this thesis has been performed in the Optoelectronics Research Centre (ORC), Tampere University of Technology during the years 2007-2015. I gratefully acknowledge ORC for giving me an opportunity to work with world class facilities and highly skilled people. It has been truly a privilege and pleasure to work at ORC. I am also happy to acknowledge Finnish Funding Agency for Technology and Innovation (TEKES), European Space Agency (ESA), National Doctoral Programme in Nanoscience (NGS-NANO), Emil Aaltonen Foundation, KAUTE-Foundation, Walter Ahlström Foundation, and Tekniikan edistämissäätiö for the financial support. Furthermore, I acknowledge Doctoral training network in condensed matter and materials physics (CMMP), Doctoral training network in electronics, telecommunications, and automation (DELTA), and National Doctoral Programme in Materials Physics (NGSMP) for their support in my doctoral studies and funding conference fees.

I gratefully acknowledge Professor Mircea Guina for supervising my doctoral studies and giving me an opportunity to work in ORC's famous solar cell team. Mircea is the busiest and in many ways the most effective and successful professor I have ever worked with and it has been a truly honor to work under his supervision. I also acknowledge Professor Emeritus Markus Pessa for hiring me to ORC in 2006 as a member of essential characterization team, and for supervising my master's thesis. I want to thank also Dr. Pekka Savolainen, director of ORC, for managing ORC and making it even more successful. Furthermore, I want to thank Mrs. Anne Viherkoski and Mrs. Eija Heliniemi for handling all the administrative tasks and making lives of the ORC people (including me) much easier, thank you.

I have had a privilege to have two immediate supervisors, Andreas and Antti. I warmly thank Dr. Andreas Schramm for his guidance and priceless advices regarding science and life in general. Andreas has taught me million things about, e.g., the quantum dots and capacitance spectroscopy. Million thanks also for Dr. Antti Tukiainen, the most senior solar cell researcher of our group, for introducing me to several characterization methods, and many other things related to semiconductor science and technology. I truly appreciate the help of both of you, thank you.

Next I want to acknowledge the other members of the famous ORC solar cell team. A first thanks goes to Dr. Arto Aho, the crystal grower, who has amazing ability to fabricate state-of-the-art semiconductor materials, heterostructures, nanostructures and devices. I want to thank M.Sc. Marianna Raappana and M.Sc. Timo Aho, probably the best solar cell processors ever lived, for their huge effort. Thank you also for Mr. Lauri Hytönen for help in solar cell processing, and Mr. Riku Isoaho, and M.Sc. Pekka Malinen for their effort in material fabrication. I also want to acknowledge Ms. Wenxin

Zhang for her help on solar cell processing and characterization. The last but not least I want to thank M.Sc. Joel “Jote” Salmi for his early days effort on solar cell processing and characterization, and his help and priceless advices in every area of science and technology (and also other areas) during the last seven years.

I have got lots of support and help from many colleagues during the last ten years. I want to acknowledge Dr. Ville-Markus Korpijärvi, M.Sc. Janne Puustinen, M.Sc. Riku Koskinen, Dr. Jonna Paajaste, Dr. Soile Suomalainen, Prof. Emil-Mihai Pavelescu, Dr. Christian Heyn, and Ms. Andrea Stemmann for the sample fabrication by molecular beam epitaxy. I want to also acknowledge Dr. Eero Arola, M.Sc. Alexander Gubanov, and Dr. Charis Turtiainen for interesting scientific discussions, help in material characterization, and help in proof reading, respectively. Big thanks also for the tukevat henkilöt, the spine of the ORC, all of you have helped me with so many things!

In 2006, I started in special ORC characterization group (led by Dr. Antti) with Professor Janne Pakarinen and M.Sc., sales director, Risto Ahorinta. I want to thank characterization team for giving me good findings for my career, and showing that there are no limits for the characterization team members, thank you!

I have got big support also from Turku people. I want to especially acknowledge Professor Pekka Laukkanen, very positive and encouraging researcher from University of Turku, for his help in the field of surface science and science in general. I also want to thank M.Sc. Jaakko Mäkelä for his help in solar cell surface studies. I acknowledge Dr. Jouko Lång, Dr. Johnny Dahl, Professor Emeritus Juhani Väyrynen, M.Sc. Marjukka Tuominen, and Professor Kalevi Kokko for their assistance and fruitful collaboration.

Many thanks also to the superior members of Rahka, Olut, Fillari, Sali, Tennis, Hauiskääntö, Pikkuoravien Uimakoulu, Lounas… -zäts as well as former ORC colleagues and administrative people including: Antti, Arto, Eero, Emmi, Hanna, Heidi, Heikki, Henrik, Iiro, Ilkka, Jari, Jote, J-P, Lauri, Maija, Marcelo, Marianna, Mariia, Marko, Riku, Sanna, Soile, Suvi, Teemu, Turkka…, Pasi, Pirjo, Ozzie, Tero, Ville, Mika, Monsieur Tavast, and all the others who know they should be mentioned.

I want to thank all my friends, relatives, sisters, parents, grandparents, and Hallila people for the support you have given to me, it has been priceless. Especially I want to thank my daughter Anna (4½) for every day encouragements, and my son Toni (7) for deep but relatively short discussions, and teaching me how to build lego-things. Finally I thank my wife, Mari, for her love, support and flexibility over all these years, thank you!

Tampere, April 1st, 2016

Ville Polojärvi

Contents

List of Symbols and Abbreviations

SYMBOLS

A	Area
a_0	zero order Fourier coefficient
a_{GaAs}	GaAs lattice constant
$a_{material}$	investigated material lattice constant
a_n	n:th order Fourier cosine coefficient
b_n	n:th order Fourier sine coefficient
C	capacitance
C_{Pr}	constant indicating the ratio of the probability of nonradiative to radiative recombination
C_R	reverse bias capacitance
ΔC_0	amplitude of the capacitance transient
c	exciton concentration
c_0	exciton concentration at 0 K temperature
c_n	electron capture rate
c_p	hole capture rate
d	lattice spacing
E	energy
E_A	thermal activation energy
E_B	core electron binding energy
E_F	fermi energy

E_{FN}	Fermi level at n-side
E_{FP}	Fermi level at p-side
E_K	photoelectron kinetic energy
$E_{T(e)}$	thermal activation energy of electron lying in the trap state
$E_{T(h)}$	thermal activation energy for hole lying in the trap state
E_W	electron analyzer work function
E_X	X-ray photon energy
e	electron charge
e_{max}	emission rate corresponding to the DLTS peak maximum
e_n	electron emission rate
e_p	hole emission rate
g_1	degeneracy when trap level is occupied
g_0	degeneracy when trap level is empty
h	Planck constant
I_0	dark saturation current
I_D	diode current
I_L	light generation current
I_{SC}	short circuit current
J	current density
J_0	dark saturation current density
J_{SC}	short circuit current density
k	Boltzmann constant
m	integer

N	number of recorded transient data points
N_A	acceptor density
N_C	effective density of conduction band states
N_D	donor density
N_S	net doping density
N_T	trap density
N_V	effective density of valence band states
n	integer
$n(air)$	air refractive index
$n(AlInP)$	AlInP refractive index
n_i	diode ideality factor
P_{MAX}	solar cell maximum power
q	elementary charge
R_S	series resistance
R_{SH}	shunt resistance
T	temperature
T_{ANN}	annealing temperature
T_{GR}	growth temperature
t	time
t_{ANN}	annealing time, annealing duration
t_P	filling pulse duration in DLTS measurement
V	voltage
V_A	applied voltage

V_{BI}	built in voltage
V_{Ga}	gallium vacancy
V_{OC}	open circuit voltage
V_P	filling pulse voltage in DLTS measurement
V_R	reverse bias voltage in DLTS measurement
v_{th}	thermal velocity
$v_{th(e)}$	electron thermal velocity
$v_{th(h)}$	hole thermal velocity
$[X]$	light concentration factor
x_d	depletion region width

SYMBOLS, GREEK ALPHABET

α	constant in Varshni relation
β	constant in Varshni relation
ε_0	vacuum permittivity
ε_r	relative permittivity of the semiconductor
θ	diffraction angle
λ	wavelength
ν	frequency
τ_e	emission time constant
τ_{ex}	exciton lifetime
σ_e	defect state capture cross section for electrons
σ_h	defect state capture cross section for holes
ω	X-rays incident angle

ABBREVIATIONS

ACE	Acetone, $(CH_3)_2CO$
AFM	atomic force microscopy
BEP	beam equivalent pressure
BS	blue shift
CLPES	core-level photoelectron spectroscopy
CV	capacitance-voltage
DE	droplet etching
DLTFS	deep level transient Fourier spectroscopy
DLTS	deep level transient spectroscopy
FWHM	full width at half maximum
HMDS	hexamethyldisilazane
ICP	inductively coupled plasma (etching)
IEA	International Energy Agency
IMF	interfacial misfit
IV	current-voltage
LDE	local droplet etching
LIV	light current-voltage
MIF	metal ion free (developer)
MBE	molecular beam epitaxy
MFP	mean free path
ML	monolayer
MOCVD	metal organic chemical vapor deposition

PL	photoluminescence
UV	ultraviolet
QD	quantum dot
QW	quantum well
RHEED	reflection high-energy electron diffraction
SK	Stranski-Krastanov
WL	wetting layer
XPS	X-ray photoelectron spectroscopy
XRD	X-ray diffraction
YAG	yttrium aluminum garnet

List of Publications

The following eight publications (I - VIII) are included this thesis as appendices. In the text they are referred to as [P1] – [P8].

I. Ville Polojärvi, Joel Salmi, Andreas Schramm, Antti Tukiainen, Mircea Guina, Janne Pakarinen, Eero Arola, Jouko Lång, Juhani Väyrynen, Pekka Laukkanen, “Effects of $(NH_4)_2S$ and NH_4OH surface treatments prior to SiO_2 capping and thermal annealing of 1.3 µm GaInAsN/GaAs quantum well structures”, *Applied Physics Letters*, vol. 97, no. 11, pp. 111109:1–111109:3, 2010.

II. Ville Polojärvi, Andreas Schramm, Arto Aho, Antti Tukiainen, Markus Pessa, “Dislocation-induced electron and hole levels in InAs quantum-dot Schottky diodes”, *Physica E*, vol. 42, no. 10, pp. 2610–2613, 2010.

III. Ville Polojärvi, Andreas Schramm, Arto Aho, Antti Tukiainen, Mircea Guina, “Removal of strain relaxation induced defects by flushing of InAs quantum dots”, *Journal of Physics D: Applied Physics*, vol. 45, no. 36, pp. 365107:1–365107:5, 2012.

IV. Ville Polojärvi, Alexander Gubanov, Andreas Schramm, Riku Koskinen, Jonna Paajaste, Joel Salmi, Soile Suomalainen, Mircea Guina, “Post-growth annealing of type-II GaSb/GaAs quantum dots grown with different V/III ratios”, *Materials Science and Engineering B*, vol. 177, no. 13, pp. 1103–1107, 2012.

V. Ville Polojärvi, Emil-Mihai Pavelescu, Andreas Schramm, Antti Tukiainen, Arto Aho, Janne Puustinen, Mircea Guina, “Optical properties and thermionic emission in solar cells with InAs quantum dots embedded within GaNAs and GaInNAs”, *Scripta Materialia*, vol. 108, pp. 122–125, 2015.

VI. Ville Polojärvi, Andreas Schramm, Mircea Guina, Andrea Stemmann, Christian Heyn, “Stacked GaAs quantum dots fabricated by refilling of self-organized nanoholes: optical properties and post-growth annealing”, *Nanotechnology*, vol. 22, no. 10, pp. 105603:1–105603:4, 2011.

VII. Ville Polojärvi, Arto Aho, Antti Tukiainen, Andreas Schramm, Mircea Guina, “Comparative study of defects in GaInNAs, GaNAsSb, and GaInNAsSb solar cells”, *Applied Physics Letters*, vol. 108, no. 12, pp. 122104:1–122104:5, 2016.

VIII. Ville Polojärvi, Arto Aho, Antti Tukiainen, Marianna Raappana, Timo Aho, Andreas Schramm, Mircea Guina, “Influence of As/group-III Flux Ratio on Defects Formation and Photovoltaic Performance of GaInNAs Solar Cells”, *Solar Energy Materials & Solar cells*, vol. 149, pp. 213–220, 2016.

Author's Contribution

The results included in the thesis were obtained as part of a team effort, although major part of the work and analyses in each manuscript is done by me. I prepared the manuscripts and I am the 1st and corresponding author in [P1, P3–P8]. In [P2], I have written one third of the manuscript and I am the 1st but not corresponding author. I have been responsible for the main part of electrical, optical and X-ray diffraction measurement-related experiments, sample and device processes, results analysis, and conclusions. Growth of the semiconductor crystals, X-ray photoelectron spectroscopy measurements, external quantum efficiency measurements, and atomic force microscopy measurements have been performed by one or several co-authors. A summary of the author's contributions to the presented work in each publication is listed below.

[P1] I planned the experiments, processed the samples, recorded X-ray diffraction spectra, made the data analysis and prepared the manuscript. I did photoluminescence measurements and thermal annealing together with Joel Salmi. X-ray photoelectron spectroscopy measurements were planned with and performed by Dr. Jouko Lång and Dr. Pekka Laukkanen. The sample growth was done by Dr. Ville-Markus Korpijärvi and Janne Puustinen.

[P2] I prepared 30 % of the manuscript and performed 75 % of the measurements. The remainder of the measurements and writing were done by Dr. Andreas Schramm. The main results in this publication are based on my M.Sc. thesis. The samples were grown by Dr. Arto Aho.

[P3] I planned the experiments with Dr. Andreas Schramm. I performed the sample processing and characterization experiments, prepared the manuscript and analysed the data. The sample growth was done by Dr. Arto Aho.

[P4] I planned the annealing and characterization experiments, analysed the data, and prepared the manuscript. Thermal annealing and photoluminescence measurements were performed by me and Alexander Gubanov. Atomic force microscopy measurements were performed by Dr. Andreas Schramm. Dr. Soile Suomalainen, Dr. Jonna Paajaste, and Riku Koskinen were responsible for the sample growth.

[P5] I planned and performed the processing and characterization experiments, excluding spectral response measurements which were done by Dr. Antti Tukiainen. I also analysed the data and prepared the manuscript. The sample growth was done by Dr. Emil-Mihai Pavelescu, Dr. Andreas Schramm, and Janne Puustinen. The sample structure and fabrication was planned as team work with all the authors.

[P6] I planned the experiments together with all the co-authors, in particular Dr. Andreas Schramm. I performed annealing and characterization experiments, carried out the data analysis with Dr. Andreas Schramm, and prepared the manuscript. The sample design was done by Dr. Christian Heyn and the sample growth was assisted by Andrea Stemmann.

[P7] I planned the processing and characterization experiments, performed the characterization experiments, carried out the data analysis and prepared the manuscript. I did the sample processing with Behçet Özgür Alaydın and Marianna Raappana. The samples were grown by Dr. Arto Aho.

[P8] I planned the processing and characterization experiments, carried out the data analysis and prepared the manuscript. I processed the samples together with Marianna Raappana and Behçet Özgür Alaydın. I performed the measurements, excluding external quantum efficiency measurements, which were done by Dr. Arto Aho. Dr. Aho was also responsible for the sample growth.

Additional experiments:

The results and analysis presented in chapter 3.1 sub-section ”AlInP window layer”, were performed by me and Jaakko Mäkelä. I planned the experiments and did the measurements with Mr. Mäkelä, excluding atomic force microscopy measurements, which were done by Dr. Antti Tukiainen. Mr. Mäkelä also performed, and helped with the X-ray photoelectron spectroscopy analysis. The investigated sample was grown by Dr. Arto Aho.

The atomic force microscopy measurements, presented in chapter 3.2, were done by Dr. Andreas Schramm and analysed by me.

The experiments in chapter 3.3 section ”GaSb/GaAs quantum dots in solar cells” was performed by Wenxin Zhang, under my supervision. The analysis of the results was performed by me. Furthermore, Dr. Soile Suomalainen, Dr. Jonna Paajaste, and Riku Koskinen were responsible for the sample growth.

1 Introduction

World energy consumption is constantly increasing although fossil fuel reserves are limited. Therefore, new technologies for renewable energy production are constantly being developed. Photovoltaics is gaining momentum as a promising and rapidly growing way to produce electricity. The average power the sun radiates annually on earth surface is over 89000 TW, whereas the world average power consumption in 2014 was about 18 TW [1]. The International Energy Agency (IEA) forecasts that photovoltaics will cover 16 % of world total electricity production by 2050, and be the dominant source of electricity before year the 2100 [2]. Silicon photovoltaics is the most widely applied photovoltaic technology today, but several other technologies such as organic [3], dye sensitive [4], thin film [5], and Perovskite [6] solar cells are under development.

However, the highest conversion efficiencies are achieved by III-V semiconductor solar cells, which are the number one choice for concentrator photovoltaic (CPV) applications. CPV is very promising candidate for generating low-cost energy in areas with high direct irradiance. In CPV systems the sunlight is concentrated by optical components from a large area to one hundreds or even thousands of times smaller, where the solar cell is located [7]. Light concentration increases the conversion efficiency and reduces the relative semiconductor fabrication costs significantly. III-V semiconductor solar cells are, again, the number one choice in space PV applications because of their high power-to-mass ratio and radiation hardness. Figure 1 shows examples of PV system implementations.

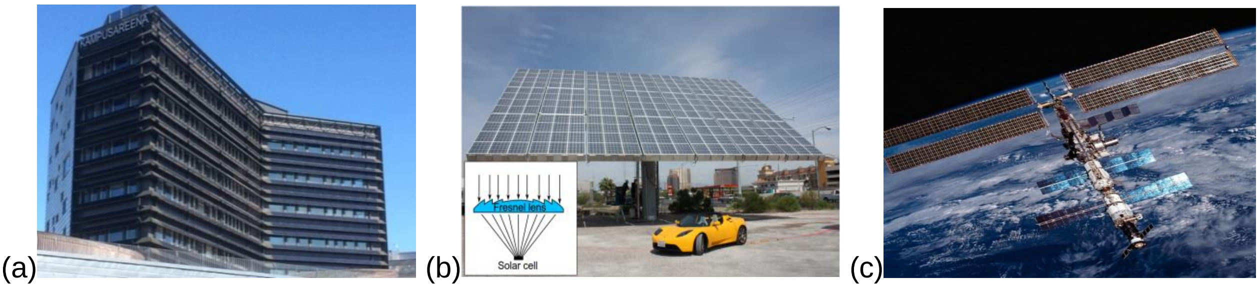

Figure 1.1 *(a) Silicon solar panels on the Tampere University of Technology Kampus Areena building, (b) CPV solar power generator by Arzon Solar [8], and (c) solar cells on the international space station [9].*

Conversion efficiency, which describes the solar cell's ability to convert light to electricity, is an extremely important parameter to be maximized, since it directly influences the price of the produced electricity. The sun emits light over a broad spectral range from ultraviolet (UV) radiation through visible wavelengths to the infrared (IR) region. The key to increasing solar cell efficiency is to utilize as big a part of the solar spectrum as efficiently as possible. A conventional solar cell consists of a single band gap energy (E_G) material, and photons that have energies smaller that E_G are not collected because they are transmitted or absorbed by free carriers. On the other hand, when photon energy is larger than E_G, the energy difference between the photon and E_G is lost as heat. As a result, the theoretical conversion efficiency limit for conventional single band gap solar cells on Earth without concentration is 33.7 %, which is known as the Shockley–Queisser limit or detailed balance limit [10]. Concentration increases that limit to over 40 %, and the ultimate thermodynamic limit for photovoltaic energy conversion in general is estimated to be 86.8 % [11]. Practical efficiencies are clearly lower compared to these theoretical maxima, and the record conversion efficiency is 46 % for a III-V multijunction solar cell under concentration [12]. However, there is still plenty of room for improvement, and a drive to increase efficiency has been present from the very first days of the solar cell research up to this point [13]. To ensure progress in the future and consequently reduce the cost of the generated electricity, new materials and approaches must be developed. This thesis deals with two types of advanced solar cell concepts based on III-V heterostructure: nanostructures and bulk dilute nitride materials. In particular, the optical and electrical properties of these structures are studied in detail, and the findings are linked, when possible, to the solar cell performance. The two main concepts are described in the following sub-sections.

Nanostructures for solar cells

When a few nanometers thick 2-dimensional layer of lower E_G semiconductor material is sandwiched between higher E_G material, a quantum well (QW) is formed, where the carriers are confined in one dimension and confined energy states are formed within the well [14]. What makes QWs particularly interesting in the field of photovoltaics is that they enable strain and band gap engineering, ultimately increasing the solar cell efficiency. QWs can be used in single junction devices or to boost the sub-junction current generation in multijunction solar cells. Figure 1.2(a) and (b) shows schematic diagrams of the absorption processes in a conventional single band gap solar cell and in a QW solar cell, respectively. The QWs are placed inside the depletion region of the p-n or p-i-n junction, where photogenerated carriers escape from the QW states *via* thermal and thermally assisted tunneling processes.

The main challenges in the development of QW solar cells are to (i) extend the absorption down to optimal energies yet maintaining high enough carrier thermal escape from the QW states, (ii) have large enough QW related absorption and photocurrent generation, and (iii) minimize the losses caused by nonradiative recombination. Advanced QW heterostructures, such as GaInAs/GaAsP or GaInNAs(Sb)/GaNAs, can be used to extend the absorption to desired energies. In those GaAs based heterostructures, the first material (GaInAs and GaInNAs) is the one creating compressively strained QWs for extended photon absorption and the latter one (GaPAs and GaNAs) is tensely stained material for strain compensation. For example, a GaAs based GaInAs/GaAsP QW solar cell with a conversion efficiency of 28.3% has been demonstrated [15]. Several QW layers, stacked on top of each other, are needed to obtain high enough photocurrent generation, and the QWs must be located in the electric field for field-aided collection right after the thermal excitation process. However, a big challenge is to minimize the formation of defects and dislocations, which often act as recombination centers and decrease the solar cell performance signficantly. Defects also cause background doping, shrinking the depletion region width. Defect formation can be influenced by fabrication parameters, such as material fluxes, and post-growth treatments, such as thermal annealing. Therefore, detailed information about the influence of structural changes, fabrication parameters and post-growth treatments on optical and electrical properties of the QW heterostructures is essential in solar cell development.

Another type of semiconductor quantum nanostructure is the quantum dot (QD). QDs are three dimensional nano sized structures, and when embedded in a higher band gap energy material, the charge carriers are confined in all three dimensions. A typical QD fabrication method is to utilize the Stranski-Krastanov (SK) growth mode [16] which occurs, for example, when InAs with ~7% higher lattice constant is deposited on GaAs. Surface energy minimizes via island formation where the strain is relaxed. Cross sectional transmission electron microscopy image of InAs/GaAs QDs grown by fabricating 2.2 monolayers (ML) of InAs on GaAs is presented in Figure 1.3. An approximately 1 ML thick InAs wetting layer (WL) is formed below the QD layer.

QD layers can be used in a similar way to QWs, to extend the absorption to lower energies. However, there is also another mechanism by which QDs can provide an improvement of the solar cell performance. When several layers of uniformly sized QDs are stacked, the discrete energy levels can form a so-called intermediate band (IB) in the band gap of the host semiconductor

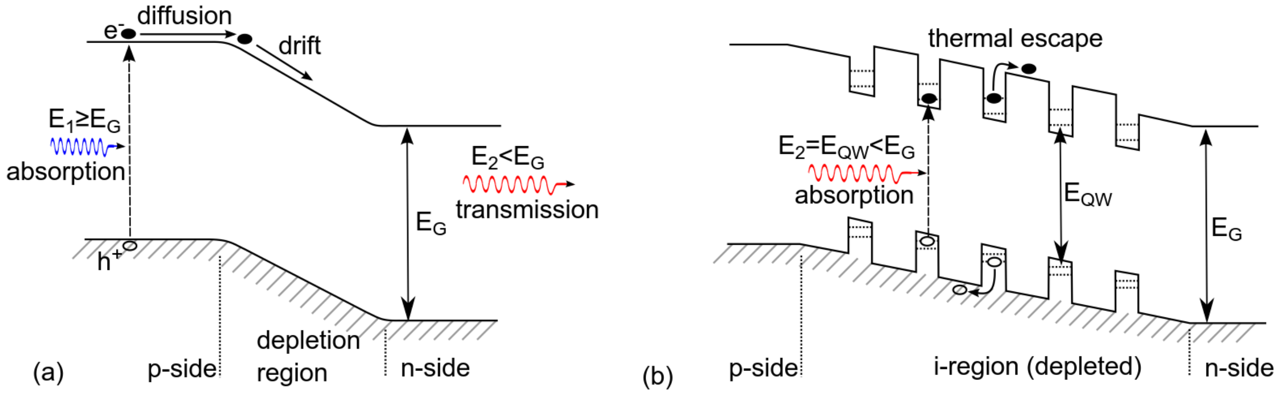

Figure 1.2 *(a) Conventional solar cell consisting of a single material, e.g. GaAs, with a single band gap. The photons with energy smaller than* E_G *are transmitted. (b) QW solar cell where several QWs are located in the i-region and electric field. The photons with energies corresponding to QW states energy differences can be absorbed, followed by thermal escape of the charge carriers to the conduction and valence band.*

material [18]. In IB solar cells, the photocurrent is generated also by low energy photon absorption (below E_G) and consequent electron excitation from the valence band to the IB, followed by (optical) excitation from the IB to the conduction band. Since the IB is isolated from the p- and n-sides of the diode, and the IB and conduction/valence bands are only optically coupled, the overall voltage is defined by the host material [19, 20]. Due to better utilization of the solar spectrum, a significant impovement in conversion efficiency could be achieved with an optimal IB solar cell, and over 60 % conversion efficiencies are predicted [20]. Figure 1.4 presents a schematic of the absorption processes in an IB solar cell.

Figure 1.3 *Cross sectional transmission electron microscope image of InAs quantum dots on GaAs [17].*

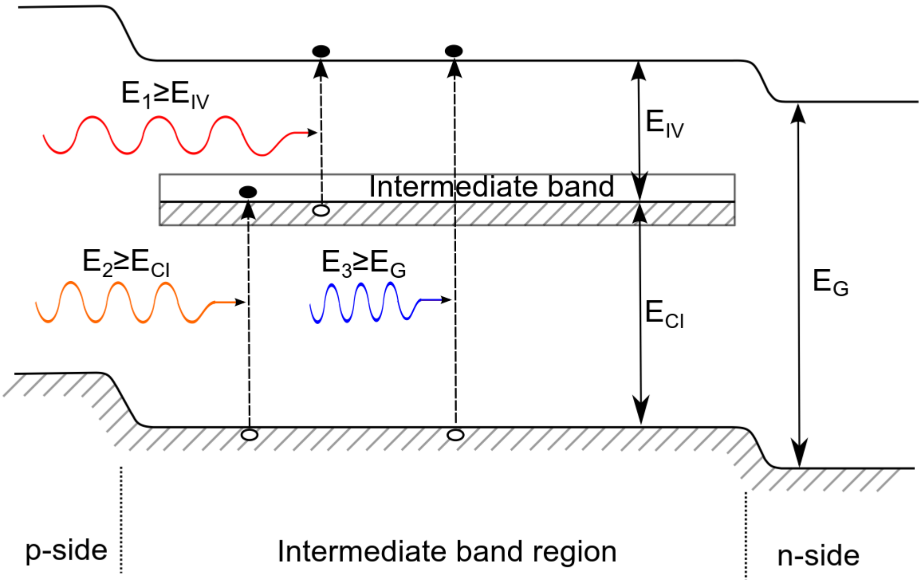

Figure 1.4 *Absorption processes in the IB solar cell. The IB enables absorption and photocurrent generation due to absorption of lower energy photons, exciting electrons from the valence band to the IB and* subsequently *from the IB to the conduction band. The IB is isolated from the n- and p-sides of the diode, and it has own independent Fermi level defining the carrier distribution within it. The* E_G *of the host material in IB solar cells can be larger compared to conventional solar cells, providing higher voltage generation.*

The main challenge in QD based IB solar cells is to produce stacks of large, uniformly sized, dense, and defect free QDs. A low QD aspect ratio (ratio between the QD base and height) is also beneficial for IB formation [21]. To maximize the QD density and optimize the aspect ratio, a maximal amount of QD material, e.g. InAs, is often deposited. However, when the amount of InAs is increased, the risk of dislocation formation increases [22]. There are also other parameters which influence the QD properties: for example, relative material fluxes have a significant influence on GaSb QD formation and their optical and electrical properties [23]. Different types of characterization methods must be applied to QD nanostructures to gain information about the influence of fabrication parameters and defect formation on QD properties, which are reflected strongly in the solar cell operation.

Furthermore, QWs and QDs are not the only nanostructures that can be utilized in solar cells. For example, semiconductor nanostructures can be used on solar cell surfaces for suppression of reflection at the semiconductor-air interface. So-called moth-eye antireflection coatings [24] provide graded refractive index from air to semiconductor material, suppressing the reflection efficiently [25, 26].

Dilute nitride materials for high efficiency multijunction solar cells

When a small fraction (typically 1-4 %) of As is replaced by N in GaAs crystal, so-called dilute nitride material is formed. When N is alloyed to GaAs it splits the conduction band into two separate bands, where the lower band defines the fundamental band gap of the material [27]. In addition to E_G reduction, N also decreases the lattice constant, making GaNAs tensile strained when grown on GaAs. Alloying In to GaAs also shrinks the E_G, but unlike GaNAs, GaInAs has a larger lattice constant than GaAs. When both In and N are alloyed, the resulting compound semiconductor is $Ga_{1-x}In_xN_yAs_{1-y}$ [28], which can be grown lattice matched on GaAs when x=2.7y [29]. Also Sb can be incorporated into GaInNAs: it increases the lattice constant, acts as a surfactant, and reduces E_G further by influencing the valence band [30-32]. The ability to tune the lattice constant and E_G makes dilute nitrides an excellent material for integration into high-efficiency multijunction solar cells for CPV and space applications [33].

Multijunction solar cells sonsist of several sub-junctions with different E_G separated by tunnel junctions. Each junction is optimized to harvest a certain part of the solar spectrum. GaInAs is in principle a very good material for absorbing photons in the energy range from 1.42 eV (GaAs E_G) to 0.354 eV (InAs E_G). However, because of the differences between the lattice constants, GaInAs can not be grown on GaAs (or Ge) at the desired E_G without strain relaxation induced dislocations, which degrade the solar cell properties. Therefore, metamorphic growth with thick buffer layers [34], inverted metamorphic growth [35], bi-facial design [36], or wafer bonding [37] must be applied. The E_G of dilute nitrides, however, can be tuned within the range of 1.42 eV to 0.8 eV [32], and whilst maintaining lattice-matching on GaAs or Ge. Figure 1.5 shows a schematic of a Ge based monolithic lattice matched 4-junction solar cell employing GaInNAs(Sb).

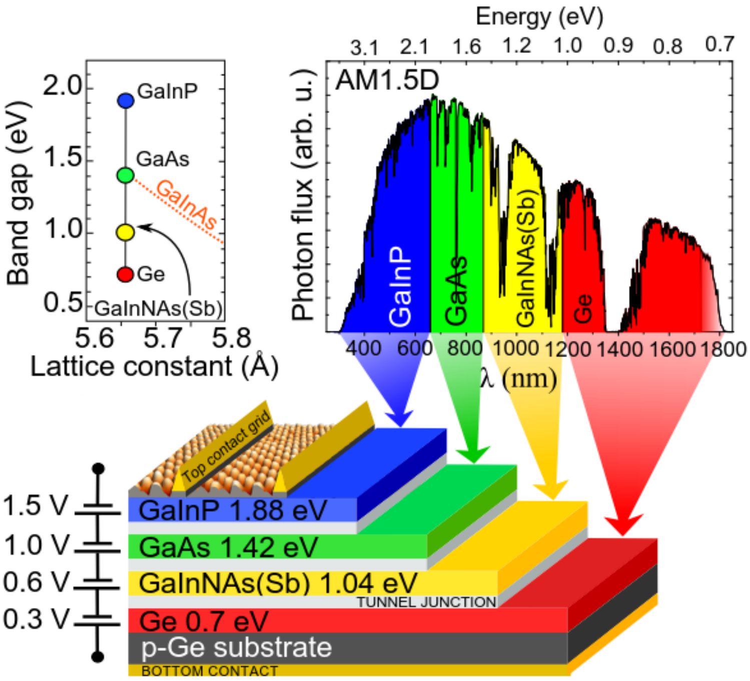

Figure 1.5 *Lattice-matched high-efficiency multijunction solar cell. Here GaInNAs(Sb) (E_G=1.04 eV) is used to harvest photons in the 1.42-1.04 eV range. All sub-junctions are separated by tunnel junctions and the solar cell voltage is the sum of the sub-junction voltages. The depicted spectrum is an AM1.5D standard solar spectrum [38].*

The least current producing sub-cell defines the whole device's maximum current, and therefore the absorption edges and thicknesses of each sub cell must be chosen in the right way to achieve the highest possible efficiency. The higher energy photons ($E \geq$1.42 eV) can be efficiently collected with (Al)GaAs- and (Al)GaInP-based compounds which can be grown lattice-matched on GaAs and Ge. Dilute nitrides have been successfully applied in 3-junction GaInP/GaAs/GaInNAsSb solar cells, reaching a conversion efficiency of 44 % under concentrated light [39, 40]. The optimal E_G for a 3 J bottom junction is 1 eV, which can be achieved by $GaIn_{0.11}N_{0.04}As$, $GaN_{0.025}AsSb_{0.06}$ and GaInNAsSb (lattice-matched on GaAs). However, over 50 % conversion efficiency is achievable if high concentration and multiple junctions are applied [41, 42].

Dilute nitrides can be also used for space solar cells. Well over 30 % conversion efficiencies are predicted for 4-junction solar cells at AM0 conditions [43]. The use of dilute nitrides is not limited to bulk lattice matched material. A large variety ranging from tensely strained to compressively strained QWs can be fabricated from this material for solar cell purposes. Because of the huge potential dilute nitride materials have in the field of high efficiency solar cells, it is essential to know their fundamental material characteristics as well as how fabrication parameters influence solar cell operation, in order to optimize current and voltage generation and maximize the conversion efficiency.

Outline

The purpose of this thesis is to investigate the optical, electrical and structural properties of several types of III-V semiconductor nanostructures, including GaInNAs and GaNAs QWs, InAs/GaAs QDs, GaSb/GaAs QDs, and strain-free GaAs QDs. Furthermore, bulk dilute nitride materials, including GaInNAs, GaNAsSb, and GaInNAsSb, for high-efficiency solar cell applications are investigated and the findings are linked to the solar cell performance. The influence of fabrication parameters and post-growth treatments on these heterostructures is characterized by several methods including optical techniques as well as capacitance spectroscopy. In particular, the influence of the amount of deposited material, material fluxes, surface treatments, and post growth annealing are investigated. One of the key areas of this thesis is defects: defect induced trap states and their influence on the optical properties of heterostructures are studied.

The structure of this thesis is as follows: The fabrication and main characterization methods are introduced briefly in chapter 2. In chapter 3, experimental results concerning surface treatments, QW and QD nanostructures, and finally bulk dilute nitride materials and solar cells are presented and discussed in succession. Conclusions are presented in chapter 4.

2 Methods

This chapter briefly describes the main methods used in this thesis, including fabrication, processing and characterization methods. Although the characterization methods listed in this chapter can be used for general purposes in material science, each method is described in the context of the work presented in this thesis.

2.1 Fabrication methods

Molecular beam epitaxy (MBE)

The fabrication method for all the semiconductor samples investigated in this thesis is solid source MBE. In this technique, the semiconductor structures are grown layer-by-layer using sublimation of atoms from heated solid sources onto a single crystalline substrate in ultra-high vacuum [44]. When the atoms hit the substrate surface, they diffuse and are eventually incorporated into the front of growing film [45]. Desorption of the material from the substrate takes also place and has to be considered in particular for incorporation of group V elements such as As. The substrate temperature is controlled by a heating element, and the substrate is typically rotated during the growth to achieve a good uniformity. An MBE system consists of a loading chamber, preparation chamber and growth chamber, which are all separated by gate valves. The system is pumped in order to obtain as high vacuum as possible. The base pressure is in the 10^{-10}–10^{-11} mbar range, which is required in order to reduce the background pressure of contaminants, and to enable a collision-free path for the source atoms to the substrate surface. A photograph and schematic structure of the MBE reactor are presented in Figure 2.1.

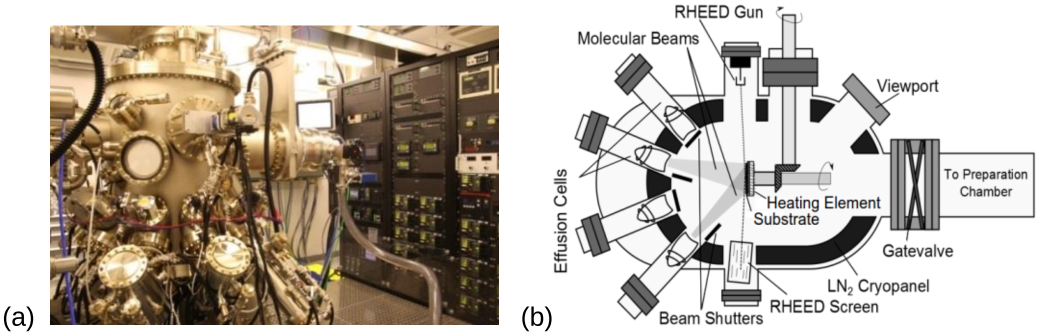

Figure 2.1 *(a) Photograph and (b) schematic picture of the MBE reactor. Reflection high energy electron diffraction (RHEED) can be used to investigate the growth and surface structure (After Nikhil P (Own work) [CC BY-SA 3.0 (http://creativecommons.org/licenses/by-sa/3.0)], via Wikimedia Commons).*

The materials used in this thesis are Al, As, Ga, In, N, P, and Sb. Be and Si are used as p- and n-type dopants, respectively. Molecular beams are generated by effusion cells for Al, In, Ga, Si, and Be. Valved crackers are used for As, Sb and P. A radio Frequency plasma source is used for N incorporation. All source materials other than N are originally in solid state at room temperature. The molecule beam can be interrupted by using mechanical shutters, and therefore the amount of deposited material can be controlled very accurately. Material quantities equivalent to fractions of monolayers can be deposited. More detailed information about the MBE can be found from the references [44, 46-49].

Sample and device processing

After the epitaxial layers are grown, the semiconductor wafer needs to be processed in order to produce devices or test structures for characterization. Common processing steps are formation of electrical contacts by metallization, and etching of semiconductor materials at selected areas. Photolithography is used to make patterns on semiconductor wafers and sample pieces to define the metallized or etched areas. Figure 2.2 shows a schematic diagram for mesa process, where a mesa structure with electric contacts is processed on a p-i-n solar cell for deep level transient spectroscopy (DLTS), capacitance voltage spectroscopy (CV), and current voltage (IV) measurements. Image reversal photoresist (*MicroChemicals GmbH*, AZ5214E) is used to define the metallized areas, because the resist profile is optimized for the lift-off technique [50] with electron beam evaporated metals. Positive photoresist (*MicroChemicals GmbH,* AZ6632) is used as an etch mask for inductively coupled plasma (ICP) reactive ion etching (RIE), because of its suitability for the dry etching technique [51]. As a result, a mesa structure with a well-defined area and Ohmic top and bottom contacts is produced. Also chemical wet etching techniques can be used in the mesa process when suitable chemicals for etching through the multilayer structure are applied. In the case of the Schottky diode process, the mesa etching step is not necessary, and a back contact can be fabricated by alloying indium (indium zinc) through the epitaxial layer to an n-type (p-type) back contact layer or substrate. This can be done by placing a piece of indium or indium zinc on top of

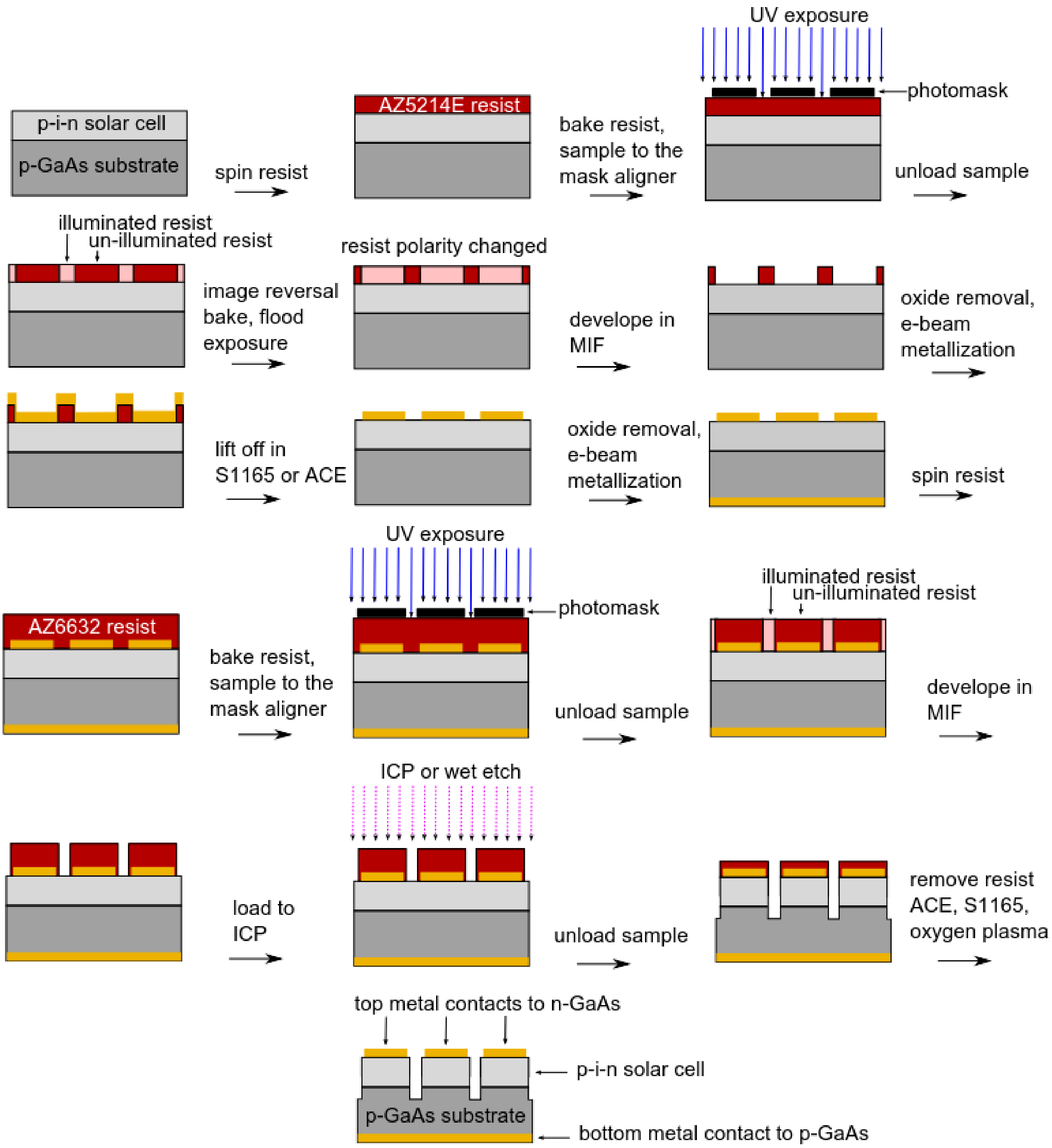

Figure 2.2 *Schematic diagram presenting processing steps of mesa sample process. Mesa etching is not necessary for Schottky diode process, and the device is ready to be measured after back contact e-beam metallization.*

the sample followed by heating in a nitrogen atmosphere at ~400 °C for approximately 2 min, and letting the metal diffuse through the epitaxial layers to a highly doped back contact. Also a simple shadow mask can also be used for making Schottky contacts on the sample surface. The benefits of a shadow mask process are that it is fast and that the surface of the material is not contamined by the photoresist and chemicals needed for resist development and removal. The disadvantage of the shadow mask process is that the area of the Schottky contact is not as well defined compared to the litography process.

The solar cell process is very much similar to the mesa sample process. Photolitography is used to produce a metal contact grid on top of the solar cell, and an etching step isolates the p- and n-sides and determines the size of the solar cell. A highly doped contact GaAs layer is selectively etched between the fingers, revealing an AlInP window layer, and an AR coating is fabricated on top of the solar cell. A photograph of a CPV multijunction solar cell is presented in Figure 2.3(a).

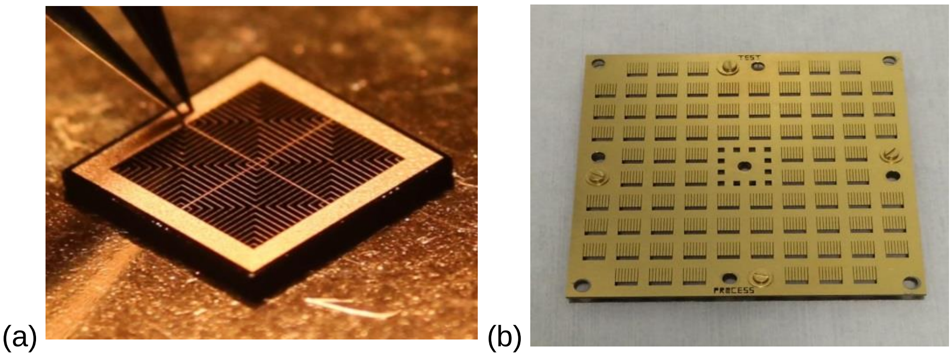

Figure 2.3 *(a) CPV multijunction solar cell (photograph by A. Tukiainen). The solar cell was designed, fabricated, and processed at ORC.(b) Photograph of the test process sample holder. Laser cut grid on metal plate acts as a shadow mask for front grid metallization.*

The solar cell lithography process requires several tens of processing steps and is time consuming. In order to obtain information about the solar cell properties as quickly as possible, a so-called test process was developed. In the test process, an optimized cleaving procedure is applied in order to isolate the p- and n-sides of the solar cell and also to define the solar cell area. A top metal grid is fabricated using a shadow mask, presented in Figure 2.3(b). The test process is found to be a reliable, reproducible and fast way to gain information about solar cell properties. However, the shadowing of the front contacts is large and the metal thickness is on the order of 100 nm, limiting the test process to material and structural development of the solar cell devices only.

2.2 Material characterization

Photoluminescence spectroscopy (PL)

PL is widely used to characterize the optical properties of direct band gap materials. Electrons are excited from the valence band to the conduction band by illumination of the investigated sample by a laser with photon energy larger than the E_G of the investigated material. Figure 2.4 presents three steps in the photoluminescence measurement in bulk material: (a) absorption of a laser emitted photon resulting in an electron-hole pair, (b) thermal relaxation of the electron and hole to the conduction band minimum and valence band maximum, respectively, (c) photon emission through spontaneous emission, and (d) nonradiative recombination through a defect state. The energy of the emitted photon correlates with the band gap of the investigated material. The amount of emitted photons at each wavelength is typically measured with a suitable detector and a monochromator array. By comparing the amount of photons emitted by different samples, one can gain information about, e.g., nonradiative recombination processes, which reduce spontaneous emission and the PL signal. PL is a surface sensitive method if the electron-hole pairs are created near the sample surface, making it a powerful tool to characterize also surface properties of photoactive materials.

PL spectra recorded from the samples with QWs or QDs typically show strongest photon emission at wavelengths related to the confined energy states of the potential well, making PL a powerful tool in characterization of optically active nanostructures. Typically, in the case of QDs, with low excitation densities the recombination occurs between the initial electron and hole states. With high excitation intensity, when the recombination rate between the ground states is not high enough to exceed the generation rate for the electron-hole pairs, the excited states become populated. As a consequence, the transitions between the excited states become more visible in the PL spectra (Figure 2.5). Saturation of the ground state transition may also be observed at high excitation powers.

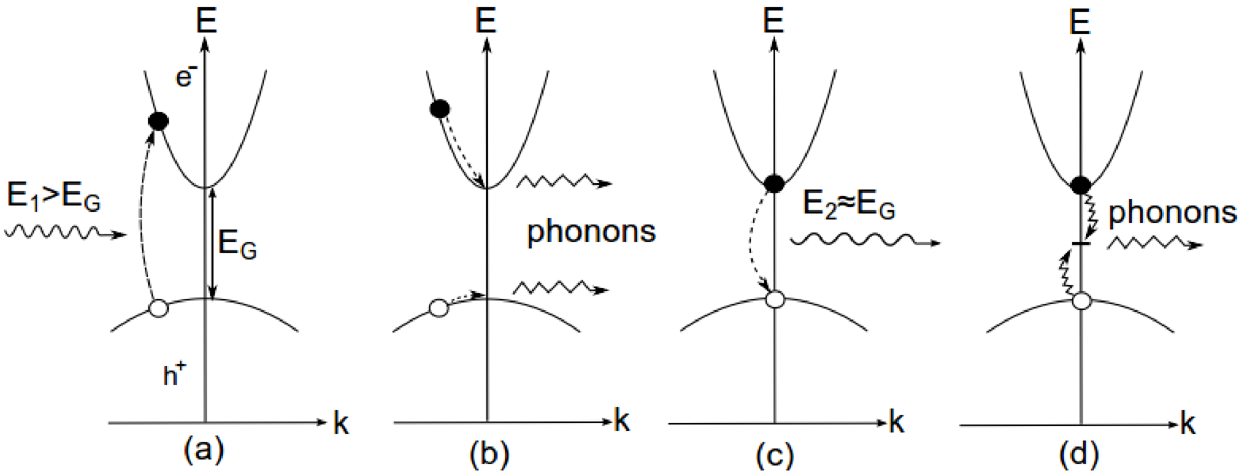

Figure 2.4 *(a) Photon absorption and creation of an electron-hole pair. (b) Nonradiative relaxation of electron and hole to the conduction band minimum and valence band maximum, respectively. (c) Electron-hole pair recombination through spontaneous emission, producing a photon with energy corresponding to the band gap of the material, and (d) nonradiative recombination of electron-hole pair through deep level state.*

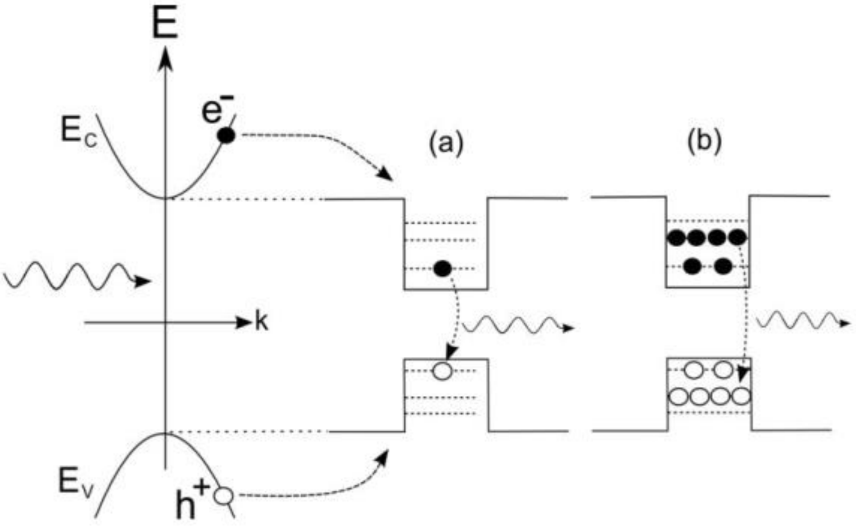

Figure 2.5 *Spontaneous emission of a photon in a QD, when the electron-hole pair recombines through (a) ground states and (b) excited states. The energy of the emitted photon corresponds to the energy difference between confined electron and hole states of the QD.*

PL measurements can also be used to determine the activation energies for charge carriers to escape from the confined states of the nanostructure, such as a QW or QD. In such samples, the temperature dependence of exciton concentration in the steady state situation can be described as

$$c(T)=\frac{c_0}{1+\left(\frac{\tau_{ex}}{\tau_0}\right)\exp\left(-\frac{E_A}{kT}\right)}, \qquad (2\text{-}1)$$

in which c is the exciton concentration, c_0 is the exciton concentration at T=0 K, τ_{ex} is the excitonic lifetime, E_A is the thermal activation energy for carrier escape, k is the Boltzmann constant, T is the temperature, and the relation $\tau_{ex}/\tau_0 \equiv C_{Pr}$ is a constant indicating the ratio of the probability of nonradiative to radiative recombination. The relative exciton concentrations can be obtained from the integrated PL peak area. By plotting the natural logarithm of the integrated peak area versus the inverse of temperature (Arrhenius evaluation), and fitting equation (2-1) to measured data, one can obtain E_A for the thermal escape of charge carriers from the QD or QW [52]. When the temperature is decreased, a blueshift (BS) of the PL-spectrum is typically observed. This can be attributed to the increase of the material band gap, due to a decrease of the lattice constant when temperature is lowered. The empirical Varshni relation [53] is widely used to describe the temperature dependence of semiconductor material band gaps. The relation is

$$E_G(T)=E_G(0)-\frac{\alpha T^2}{T+\beta}, \qquad (2\text{-}2)$$

where α and β are constants with no direct physical meaning.

Capacitance-voltage spectroscopy (C-V)

C-V spectroscopy is a powerful tool for gaining information about electrically active centres in semiconductors [54]. The method is based on measuring the capacitance of a Schottky or pn-diode when the applied voltage and consequently the depletion region width (x_d) is varied. C-V measurements are typically used to determine the doping concentration of the investigated material. The following formula can be written for the capacitance (C) of the Schottky diode:

$$\frac{1}{C^2}=\frac{2}{\pm A^2\varepsilon_0\varepsilon_r e\left(N_A-N_D\right)}\times\left[\left(\pm V_{BI}\pm V_A\right)-\frac{kT}{e}\right], \tag{2-3}$$

where A is the diode area, ε_r is the relative permittivity of the semiconductor, ε_0 is vacuum permittivity, e is electron charge, N_A is acceptor density, N_D is donor density, V_{BI} is built-in voltage, V_A is applied voltage, k is the Boltzmann constant, and T is temperature [54]. The plus sign (+) in equation (2-3) applies to p-type ($N_A>N_D$, $V_{BI}>0$, and $V_A>0$) and the minus sign (-) applies to n-type ($N_D>N_A$, $V_{BI}<0$, and $V_A<0$) material. In uniformly doped material, a plot of $1/C^2$ versus V_A gives a straight line with slope proportional to N_A-N_D. This is called a Mott-Schottky plot [55]. The intercept of the V_A axis (C=0) gives $-V_{BI}+kT/e$. Figure 2.6 presents the Schottky junction in uniformly doped n-type semiconductor material without external bias, and when V_A is applied.

On the other hand, the capacitance of the Schottky junction can also be estimated as

$$C=\frac{\varepsilon_0\varepsilon_r A}{x_d}, \tag{2-4}$$

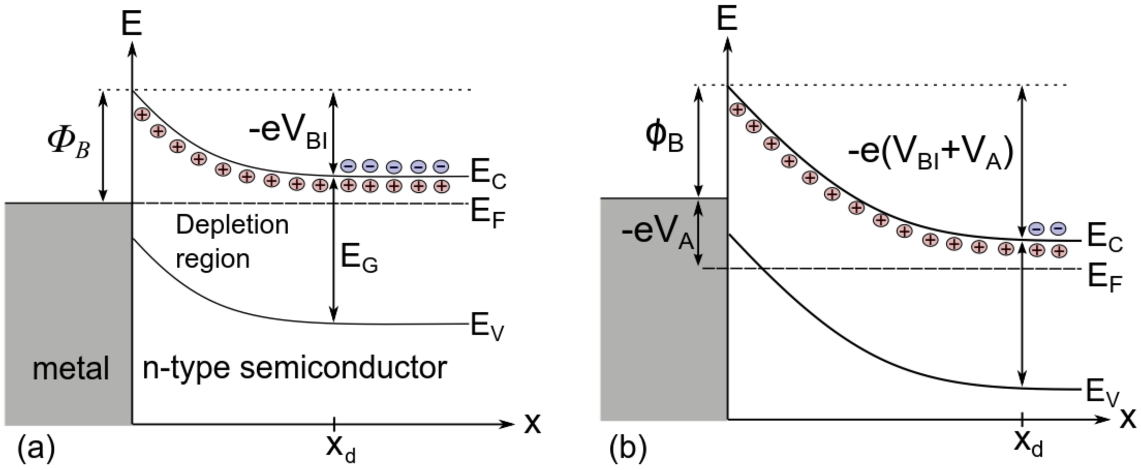

Figure 2.6 *(a) Schottky junction without applied bias, and (b) when an external bias V_A is applied. Energy is plotted on the horizontal axis, and depth from the metal-semiconductor interface is plotted on the vertical axis. The Schottky barrier height Φ_B depends on the combination of metal and semiconductor, and has a strong dependence on the atomic structure of the metal-semiconductor interface [56].*

which is identical to the expression for capacitance of a plate capacitor consisting of two plates with area A, separation x_d, and with medium relative permittivity of ε_r [54]. A valid assumption is that the charge fluctuations occur only at the depletion layer edge. This enables construction of doping profiles for non-uniformly doped materials. The local doping density can be calculated from the local slope of the C-V curve. The corresponding depth x_d can be obtained from the mean value of the capacitance.

When QD (or QW) nanostructures are embedded in the material, deviations from charge neutrality occur even with uniformly doped material. The relative positions of the Fermi level (E_F) and the QD states change when the bias voltage over the Schottky junction is varied. Figure 2.7 presents the situation where the Fermi level is (a) above and (b) below the confined QD states in an n-type Schottky diode. Charge carriers are trapped inside QD energy states, causing charge accumulation and depletion inside and near the QD layer, respectively.

Figure 2.8(a) shows a schematic picture of a C-V curve recorded from an n-type Schottky diode with an embedded QD layer. A capacitance plateau surrounded by areas with steeper slope appears in the C-V characteristics. Figure 2.7(b) shows the corresponding charge carrier depth profile. The charge accumulation peak surrounded by depleted areas is a typical C-V characteristic of a diode with an embedded QD layer.

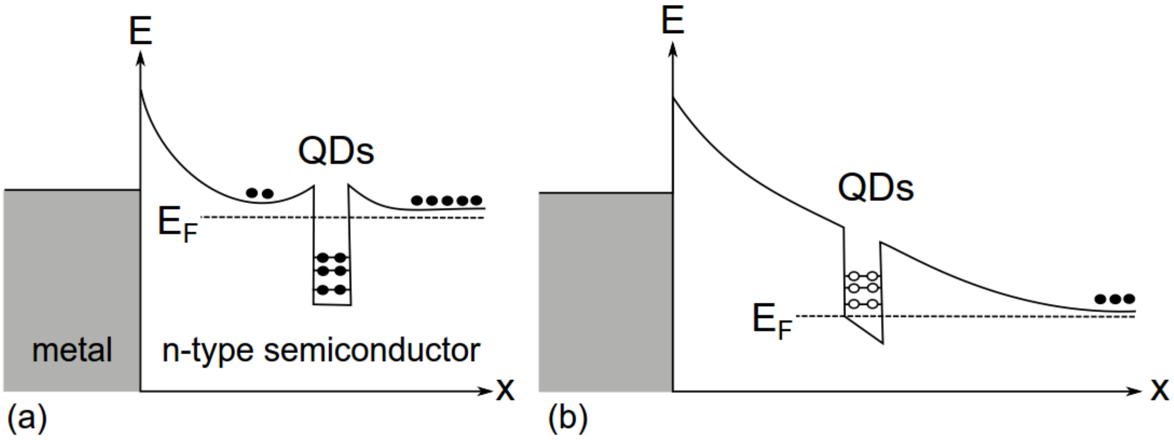

Figure 2.7 *QD layer inside Schottky diode when Fermi level is (a) above and (b) below confined QD electron states.*

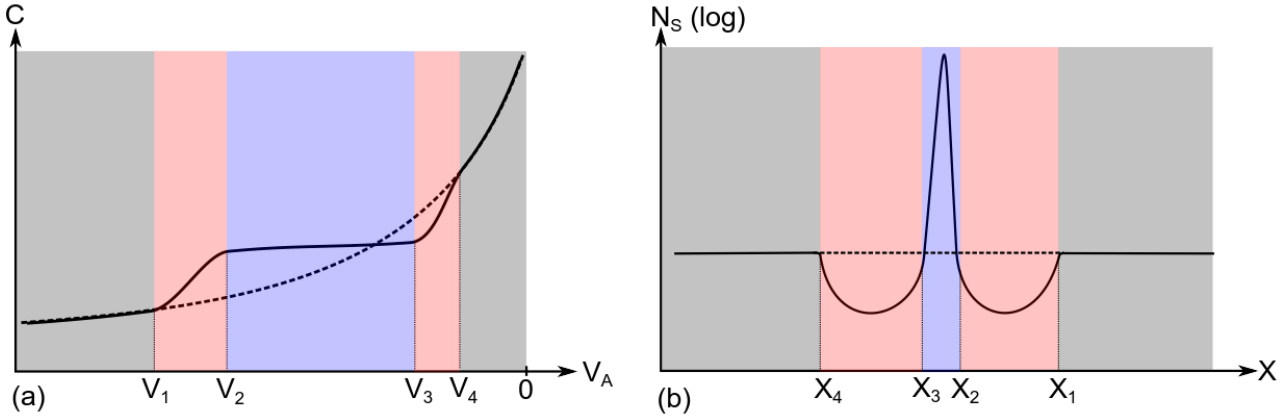

Figure 2.8 *(a) C-V curve recorded QD and bulk samples (Schottky junction on n-type material), and (b) corresponding depth profile, where x refers to the depth from Schottky junction. The dashed line refers to a uniformly doped sample without a QD layer.*

The C-V curve and corresponding depth profile, presented in Figure 2.8, can be divided into five different areas:

1. $V<V_1$, $x>x_1$ The capacitance resembles the bulk behaviour, and the Fermi level is clearly below the QD confined energy states. The depth profile shows a constant value.
2. $V_1<V<V_2$, $x_1>x>x_2$ The Fermi level reaches the depletion region caused by charge accumulation (depletion) inside (near) the QD layer, and consequent local band bending causes an increase in the capacitance. The depth profile shows charge depletion.
3. $V_2<V<V_3$, $x_2>x>x_3$ The Fermi level reaches the confined QD states, and the screening effect of a large amount of carriers located in the QD causes a plateau where the capacitance is nearly constant. The depth profile shows a charge accumulation peak.
4. $V_3<V<V_4$, $x_3>x>x_4$ The Fermi level passes the QD confined states and the depletion region underneath the QD, caused by local band bending, starts to add to the total depletion region. As a result, a sudden increase in capacitance is again observed. The depth profile again shows charge depletion.
5. $V>V_4$, $x<x_4$ Capacitance resembles the bulk behaviour, and the Fermi level is clearly above the QD confined energy states. The depth profile shows a constant value.

Similar or even more significant charge depletion, as observed near the QD layer, can be caused by deep level defects. Locally depleted areas may occur if the free carriers are trapped inside a defected layer.

Although the examples described in this chapter are for Schottky diode, the same applies for p^+n- or n^+p-junctions. In the case of a pn-junction, when reverse voltage is applied, the depletion region edges move deeper into n-type emitter and p-type collector, defining the probed area. However, if the doping level of one side (n- or p-side) is at least three orders of magnitude higher than the other (n^+p or n^+p -junction), the space charge region penetrating into the lower doped side of the junction can be neglected, and the same analysis can be done as for the Schottky junction [55].

Deep level transient spectroscopy (DLTS)

DLTS is a method to characterize electrically active defects lying inside the depletion region [57]. Whereas dopants typically form an acceptor or donor type level near the band edge, several types of point defects and dislocations form a discrete energy level deeper inside the band gap of the host semiconductor material. The position of the deep level determines whether it acts as an electron or hole trap: electron traps occur closer to the conduction band and hole traps closer to the valence band. Deep levels can capture and emit charge carriers from and to the valence or conduction bands. Figure 2.9 presents capture (c_n, c_p) and emission (e_n, e_p) processes for electrons and holes.

Every deep level has its characteristics capture and emission rates for electrons and holes. The emission rate for an electron from a deep level can be written as

$$e_n = \sigma_e v_{th(e)} N_C \frac{g_0}{g_1} \exp\left(-\frac{E_{T(e)}}{kT}\right), \tag{2-5}$$

where σ_e is the capture cross section for electrons, $v_{th(e)}$ is the electron thermal velocity, N_C is the effective density of conduction band states, g_0 and g_1 are the degeneracies when the trap level is empty and occupied, respectively, and $E_{T(e)}$ is the thermal activation energy of electrons lying in the trap state. The analogous expression for the hole emission rate is

$$e_p = \sigma_h v_{th(h)} N_V \frac{g_1}{g_0} \exp\left(-\frac{E_{T(h)}}{kT}\right), \tag{2-6}$$

where σ_h is the capture cross section for holes, $v_{th(h)}$ is the hole thermal velocity, N_V is the effective density of valence band states, and $E_{T(h)}$ is the thermal activation energy for holes inside the trap state [54, 55].

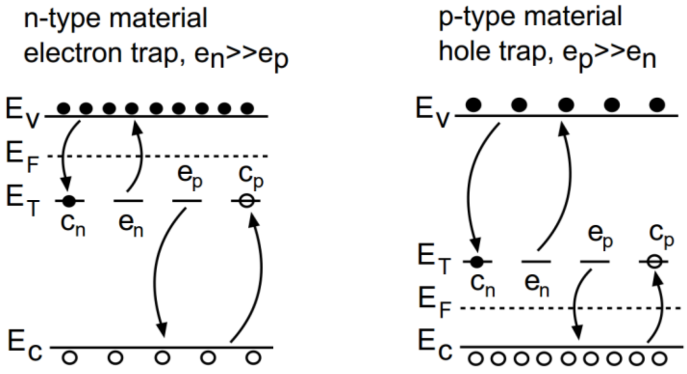

Figure 2.9 *Emission and capture of electrons and holes in n-type and p-type material, respectively.*

Emission of electrons or holes from the deep level state inside the depletion region changes the depletion region capacitance. The DLTS method is based on measuring these capacitance transients. In DLTS measurements, a certain reverse bias (V_R) is initially applied over the Schottky or pn-junction, forming a depletion region inside the material in which the trap states are empty of charge carriers. Then, as a positive filling pulse (V_P) with duration t_P is applied, the depletion region becomes narrower, and initially empty deep levels are filled with charge carriers. After the filling pulse a reverse bias is applied again, leaving trapped charge carriers inside the depletion region and under the influence of the electric field. When trapped charges are thermally emitted to the conduction or valence band, they are swept away from the depletion region by the electric field, and as a result, a capacitance transient is formed. Figure 2.10 presents the work cycle of a DLTS measurement, and the formation of a capacitance transient. The change in capacitance can be written as

$$\Delta C(t) = C(t) - C_R = \Delta C_0 \exp\left(\frac{-(t+t_0)}{\tau_e}\right), \tag{2-7}$$

where C_R is the reverse bias capacitance, ΔC_0 is the amplitude of the capacitance transient, and τ_e is the emission time constant. The emission time constant is related to the emission rates of electrons and holes as $1/\tau_e = e_n + e_p$. For electron traps $e_n \gg e_p$ leading to $1/\tau_e = e_n$. Analogously, for hole traps $e_p \gg e_n$ and $1/\tau_e = e_p$. This links the emission time constant of electrons and holes to the capacitance. After the filling pulse, by choosing two points in time and plotting the corresponding capacitance difference as a function of temperature, a peak is observed when the emission time constant falls into a chosen time window. This is called a DLTS spectrum. Figure 2.11 shows how a DLTS spectrum is formed.

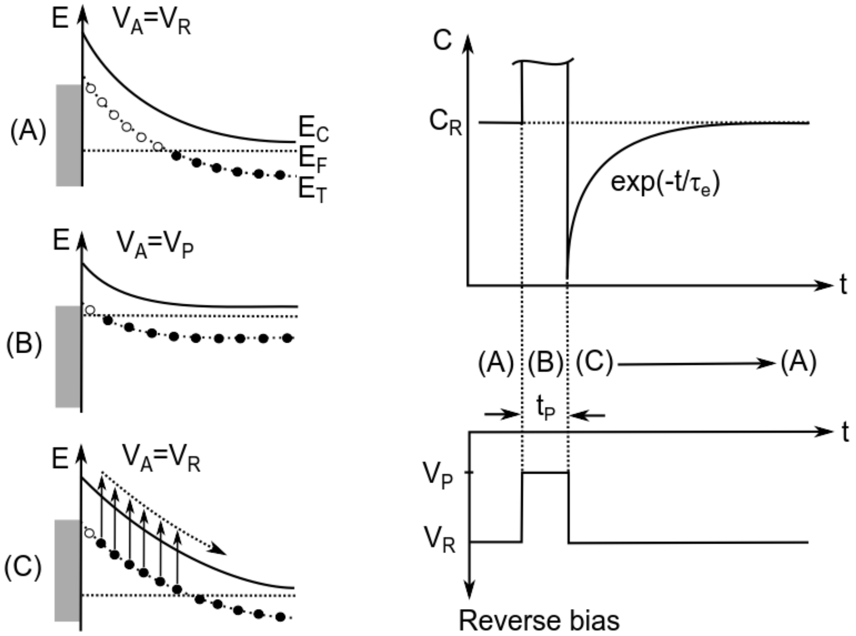

Figure 2.10 *DLTS work cycle and formation of the capacitance transient. After [58]*

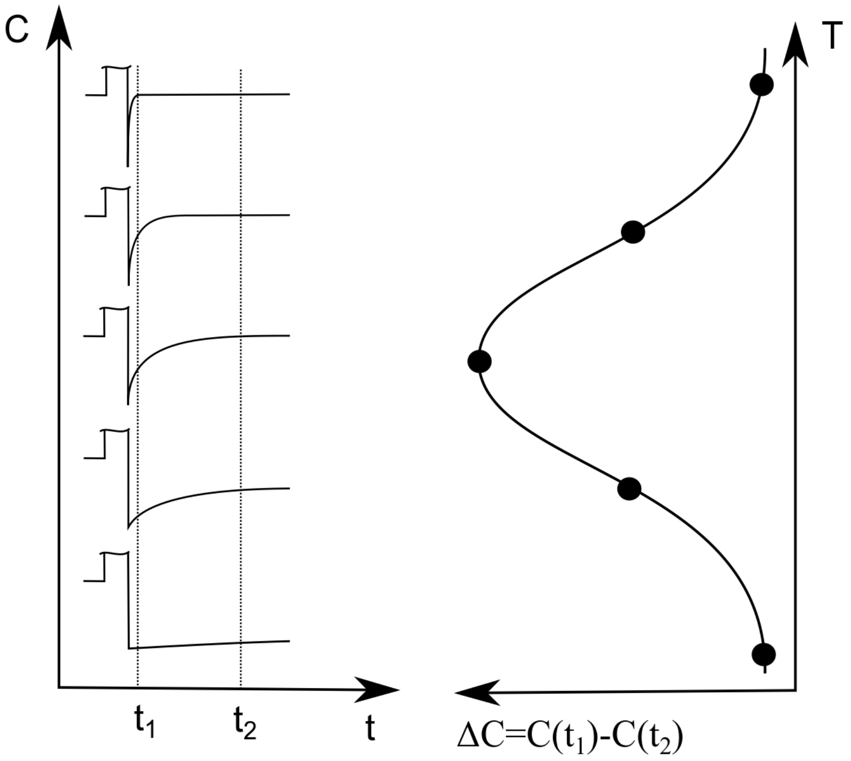

Figure 2.11 *Formation of the DLTS signal when capacitance difference is plotted against temperature.*

The emission rate corresponding to the DLTS peak maximum e_{max} can be determined using the equation

$$e_{max} = \frac{ln(t_2/t_1)}{t_2-t_1}. \tag{2-8}$$

When capacitance transients are measured as a function of temperature at various time windows, emission time constant can be extracted. With the help of emission rate equations (2-5) and (2-6), and assuming that $\sigma_{e,h}$ is independent of T, one can write

$$\ln\left(\tau v_{th(e,h)} N_{C,V}\right) = -\ln\left(\sigma_{e,h}\right) + \frac{E_{A(e,h)}}{kT}. \tag{2-9}$$

From the Arrhenius evaluation [59], E_A and σ of certain trap state can be extracted. The capacitance change related to charging and recharging N_T traps can be written as

$$\frac{\Delta C_0}{C_0} = \frac{1}{2}\frac{N_T}{N_S}, \tag{2-10}$$

where N_S is the net doping density determined from the C-V measurement. This allows the trap density to be extracted.

Fourier transform methods [60] can be used to analyze capacitance transients. This allows more accurate and faster evaluation of the DLTS data. The use of discrete Fourier series is possible in digital systems, where the whole capacitance transient with N measurement points is recorded. The DLTS method which applies the Fourier transform technique is called deep level transient Fourier spectroscopy (DLTFS) [61]. The capacitance transient can be treated as a periodic function with period width T_W, which is the period of the recorded capacitance transient. In such cases, the capacitance can be written as

$$C(t) = \frac{1}{2}a_0 + \sum_{n=1}^{N-1}\left[a_n \cos\left(\frac{2\pi nt}{T_W}\right) + b_n \sin\left(\frac{2\pi nt}{T_W}\right)\right], \tag{2-11}$$

where n is an integer, N is the number of recorded transient data points, and a_n and b_n are the Fourier coefficients. The τ_e can be calculated with the help of a_n and b_n in four different ways [61], three of which calculate a_n/a_m, b_n/b_m, and a_n/b_n when $n \neq m$:

$$\tau(a_n, a_m) = \frac{T_W}{2\pi}\sqrt{\frac{a_n - a_m}{m^2 a_m - n^2 a_n}} \tag{2-12}$$

$$\tau(b_n, b_m) = \frac{T_W}{2\pi}\sqrt{\frac{nb_n - nb_m}{m^2 nb_m - n^2 mb_n}} \tag{2-13}$$

$$\tau(a_n, b_n) = \frac{T_W b_n}{2\pi n a_n}. \tag{2-14}$$

The fourth way requires information about the capacitance offset, and is described in more detail in reference [61]. All a_n and b_n are not needed in the evaluation, because the actual transient is comprised of only low frequencies and the higher order coefficients are mainly related to the high frequency noise signal. Furthermore, the magnitude of the coefficients decreases together with n.

Another benefit of digital DLTFS measurements is the use of different correlation functions. Correlation functions are used to obtain information from the different parts of the capacitance transient, and only a single capacitance transient for each temperature point has to be recorded for the Arrhenius evaluation [62]. The discrete Fourier transform for the measured data can be computed efficiently with a fast Fourier transform algorithm [63]. Figure 2.12 presents the schematic of the DLTFS measurement setup.

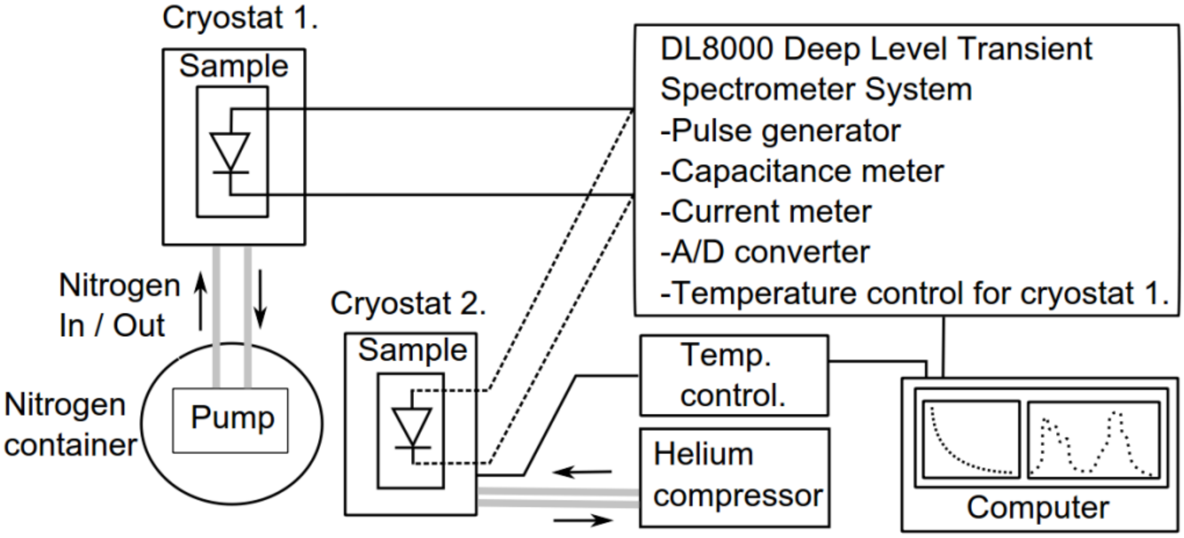

Figure 2.12 *Schematic of the DLTFS measurement system [17]. Two different cryostats are used for different temperature scales.*

Two different cryostats are used for different temperature ranges. The liquid nitrogen cryostat can operate at the 80–450 K temperature range, whereas the helium compressor cryostat can operate at the 10–320 K temperature range.

There are certain limitations for DLT(F)S measurements. One limitation is that the trap density should be at least two orders of magnitudes lower than the doping density. Other limitations can be found in reference [64].

X-ray diffraction spectroscopy (XRD)

X-ray diffraction is based on constructive interference of monochromatic X-rays when these are directed onto a crystalline sample, such as a semiconductor crystal. Bragg's law [65] relates the wavelength of the electromagnetic radiation λ to the lattice spacing d and diffraction angle θ by the following equation

$$n\lambda = 2d\sin(\theta), \tag{2-15}$$

where n is an integer. When Bragg's law is satisfied, the interaction between the incident X-rays and sample produces constructive interference. Figure 2.13(a) illustrates the conditions when X-rays, hitting the material at an incident angle of ω, are scattered from the periodic crystalline sample.

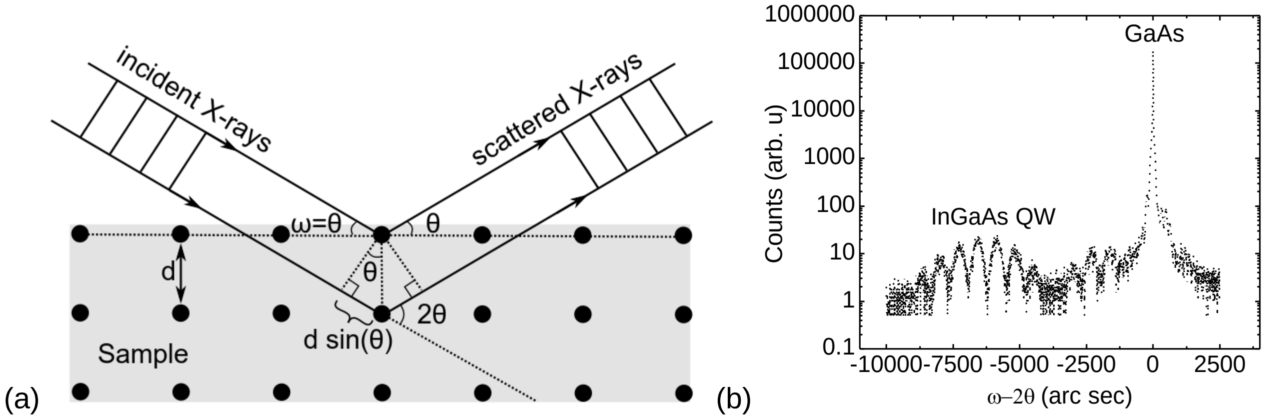

Figure 2.13 *(a) Incident X-rays scatter from the material and produce constructive interference when Bragg's law is satisfied. (b) Typical XRD rocking curve recorded from a sample with InGaAs/GaAs quantum well, where the QW related signal appears at a different angle compared to the GaAs related signal.*

XRD is often used to determine the material compositions and layer thicknesses of heterostructures grown on, e.g., GaAs substrate. Symmetric diffraction from plane 004 gives information about the lattice constants of the heterostructure at growth direction. When an investigated sample consists of layers that have different lattice constants, the diffraction peaks related to those materials appear at different angles. In a so-called ω-2θ scan, the measurement system is adjusted to show the strong diffraction from the GaAs host lattice. Then ω and 2θ angles, presented in Figure 2.13(a), are scanned to show the relative change in the diffraction angle between the GaAs host lattice and the grown layers. Figure 2.13(b) shows a typical XRD spectrum recorded from a sample with a single InGaAs QW embedded in GaAs. After measurement, the simulated XRD spectrum can be fitted to the experimental data, to get information about the layer thicknesses, lattice constants, and material compositions of the heterostructures. In symmetric diffraction $\omega=\theta$, but also asymmetric diffraction angles from various crystal planes can be measured.

Atomic force microscopy (AFM)

AFM is a powerful surface characterization method, based on a micro scale cantilever with an extremely sharp tip which scans the sample surface. An electrical stepping motor and piezoelectric crystal are used to move the tip and scan the investigated sample. The measurement mode used in this work is called *TappingMode*$^{\mathrm{TM}}$ (a trademark of Digital Instruments), where the cantilever is driven to oscillate vertically at near its resonance frequency by a piezoelectric element. The AFM tip taps the sample surface with an amplitude ranging from 20 to 100 nm, contacting the surface at the bottom of its swing. The interacting forces (Van der Waals force, dipole-dipole interaction, or other electrostatic forces) change the elastic constant of the probe, and the oscillation amplitude tends to decrease when the tip gets closer to the surface. The feedback loop maintains a constant oscillation amplitude and tip-sample interaction during the measurement by maintaining a constant RMS oscillation signal acquired by the split photodiode detector, and by moving the vertical position of the tip and cantilever. A computer stores the vertical position of the cantilever at each lateral

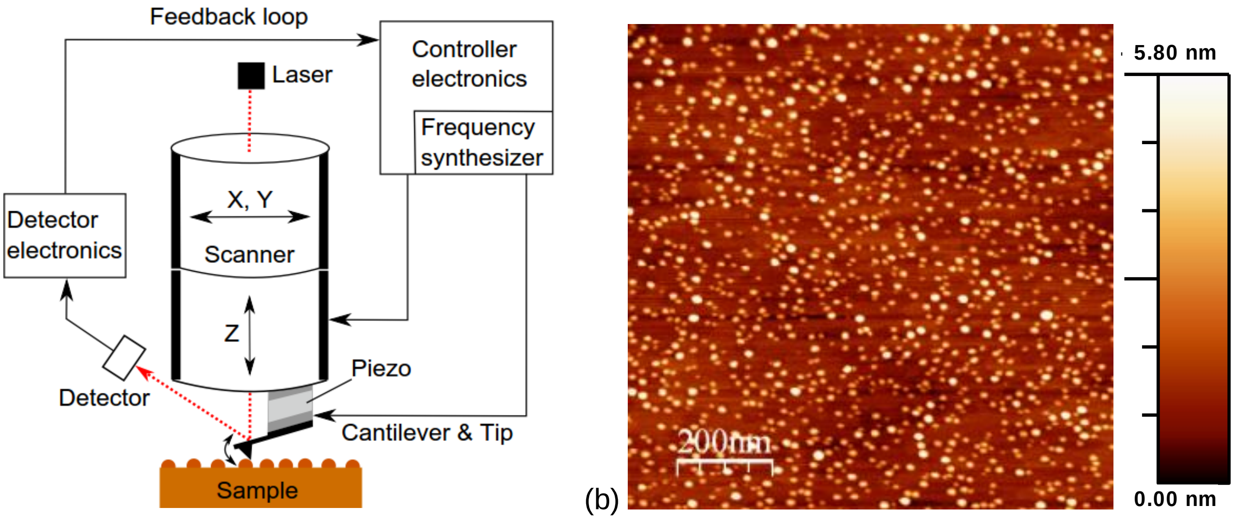

Figure 2.14 *(a) Schematic of the AFM measurement system. (b) AFM image of the InAs QDs on GaAs.*

measurement point and forms a topographic image of the sample surface. Figure 2.14(a) shows a schematic of the AFM measurement system. AFM is a good imaging technique for surface QDs. The surface QDs can effectively be used for indirect characterization of similar embedded QDs, although their properties can change when they are capped and embedded in a semiconductor matrix. Figure 2.14(b) shows an example of InAs QDs grown on GaAs. The size, shape and density of the QDs can be extracted.

X-ray photoelectron spectroscopy (XPS)

XPS is a surface sensitive characterization method which is based on the interaction between electromagnetic radiation and matter at high vacuum. The measurement utilizes X-ray photons with energy E_X produced by an X-ray source in an ultra-high vacuum environment. This energy is higher that the binding energy E_B of the core electrons in the investigated material. Therefore, an incident X-ray photon, whose energy is absorbed *via* dipole interaction by an electron of the investigated sample, produces a photoelectron with kinetic energy E_K. This energy is measured with an electron analyzer, which allows the binding energy of the electron in the investigated material to be calculated. Figure 2.15(a) presents the absorption and emission processes of the x-ray photon, respectively. A schematic image of the measurement system is presented in Figure 2.15(b).

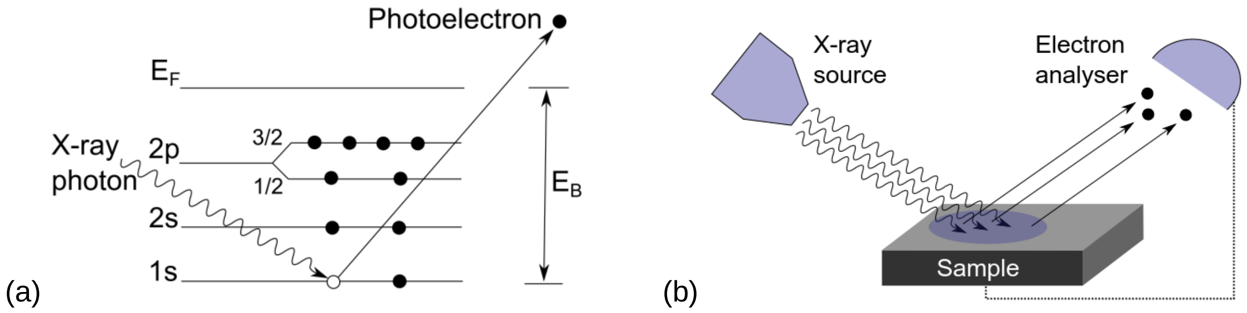

Figure 2.15 (*a) An incident X-ray photon is absorbed by an electron in the 1s orbital, and a photoelectron is produced. (b) Schematic of the measurement system, where X-ray photons produce photoelectrons in a vacuum chamber. The sample and analyzer are electrically connected.*

The binding energy E_B of the measured photoelectron can be extracted from the simple equation

$$E_B = E_X - E_W - E_K, \tag{2-16}$$

where E_W is the work function of the electron analyzer. The sample and analyzer are electrically connected, and therefore their Fermi levels are aligned. E_B is not only specific to each electron in each element, but also depends on the bonding environment of the investigated material, such as oxide components. Therefore, for example, GaAs surface oxides can be investigated by XPS: oxidized Ga atoms have fewer valence electrons around them (i.e. smaller on-site negative potential) as compared to the Ga atoms in pure GaAs, which results in a higher binding energy for the core level electrons in oxidized Ga atoms than for pure GaAs. Such an energy shift is called a core-level shift. Traditional XPS is a surface sensitive probe because of the short mean free path (MFP) of electrons in solids without inelastic collisions. The signal depth (≈3×MFP) can be up to 10 nm, depending on the kinetic energy of photoelectrons.

2.3 Device characterization

Solar cell device characterization methods used in this thesis are introduced next. Although the methods are classified under “device characterization”, they also give information about the solar cell material properties, not only device performance.

Light-biased current-voltage measurements (LIV)

LIV measurements are essential for obtaining information about the solar cell properties, such as current and voltage generation under illumination. A semiconductor solar cell is based on the photocurrent- and voltage generated by the absorption of photons and the creation of electron-hole pairs in or near the pn-junction. When a photon with energy higher that the E_G of the solar cell material enters the solar cell, it is absorbed and an electron-hole pair is created, with a probability defined by the absorption coefficient of the material at that specific wavelength. When the absorption occurs at a distance within the diffusion length of the minority carrier from the depletion region, the corresponding minority carrier drifts to the majority carrier side due to the electric field created by pn-junction. This causes a drift-induced current where photogenerated electrons and holes are separated to the n-side and p-side of the material, respectively. When n- and p-sides are in short circuit, the photogenerated electrons and holes can recombine and the net current is called the short circuit current, I_{SC}. If the n- and p-sides are isolated (open circuit condition) the separation and resulting accumulation of photogenerated electrons and holes at the n- and p-sides of the junction, respectively, causes an electric field opposite to that already created by the pn-junction. This reduces the net electric field and increases the diffusion current, which is opposite to the photogenerated current. At equilibrium these two currents are equal, and the net current is zero. The voltage at which the net current is zero is called the open circuit voltage, V_{OC}. Figure 2.16 shows a schematic band diagram and generation of photocurrent- and voltage in a GaInP solar cell. The output voltage of the solar cell is defined by the energy difference of the Fermi levels at the n- and p-sides, E_{FN}, and E_{FP}.

A solar cell can be modelled with an equivalent circuit, consisting of a current source, diode, and two resistors: a shunt resistor R_{SH}, and a series resistor R_S. A solar cell equivalent circuit is presented in Figure 2.17(a).

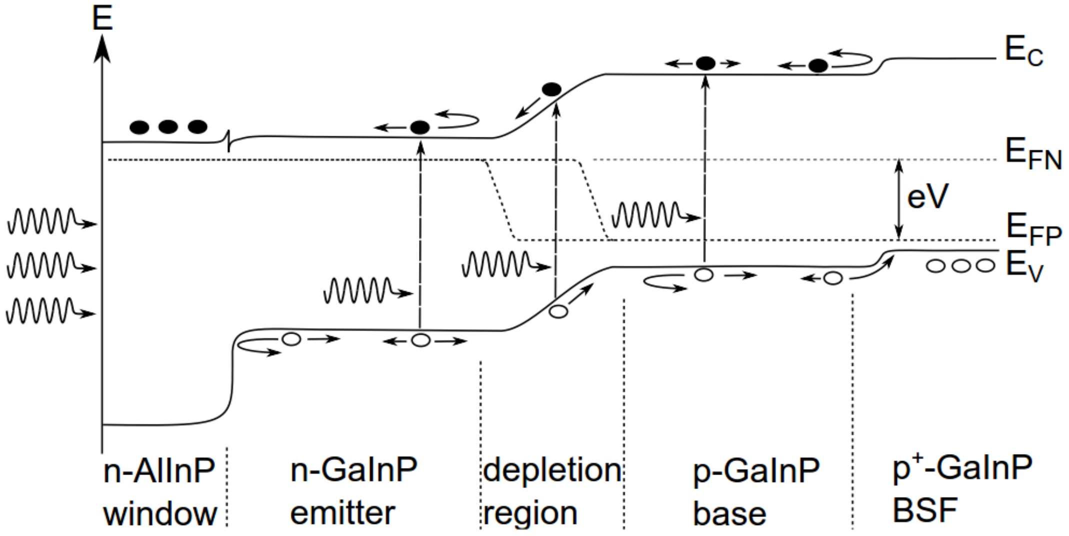

Figure 2.16 *Schematic band diagram of the GaInP solar cell under illumination producing voltage* V. *n-AlInP window and* p^+*-GaInP back surface field (BSF) layers provide energy barriers for minority carriers and significantly reduce nonradiative recombination on the surface and on the back side of the solar cell, respectively.*

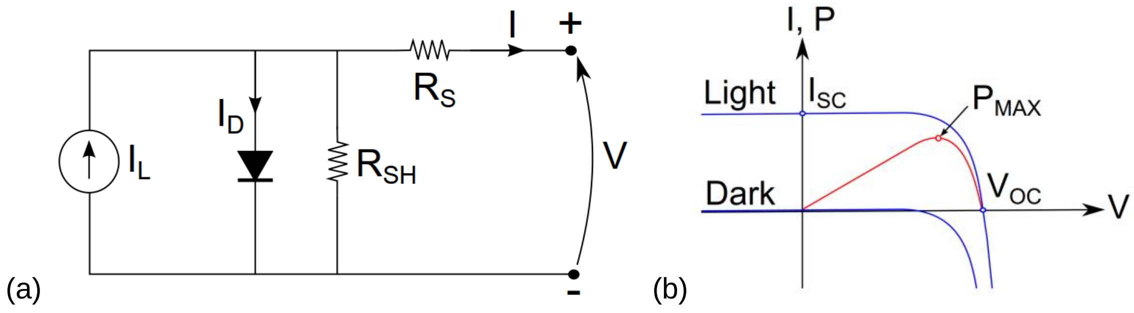

Figure 2.17 *(a) Equivalent circuit for the solar cell under illumination. (b) Schematic of solar cell LIV and IV characteristics and resulting power generation.*

The diode current I_D flowing through the diode can be written as

$$I_D = I_0\left(\exp\left[\frac{q(V+IR_S)}{n_ikT}\right]-1\right), \tag{2-17}$$

where I_0 is the dark saturation current, i.e., the sum of the current generated by minority charge carrier diffusion over the pn-junction under dark conditions and the thermal generation of electron-hole pairs within the depletion region. The term -1 can be neglected, because the exponential term is >>1 at typical operation voltage. The diode equation for the solar cell equivalent circuit becomes

$$I = I_L - I_0\exp\left[\frac{q(V+IR_S)}{n_ikT}\right]-\frac{V+IR_S}{R_{SH}}, \tag{2-18}$$

where I_L is the light generation current, q is the elementary charge, and n_i is the diode ideality factor.

Figure 2.17(b) shows IV and LIV characteristics of the solar cell. The solar cell LIV can be described as a superposition on the IV curve of the solar cell in the dark. From the LIV curve one can easily define such parameters as I_{SC}, V_{OC} and P_{MAX}, which is the maximum power point on the LIV curve. The efficiency of the solar cell can be defined by dividing P_{MAX} by the incident power of the sunlight entering the solar cell. Another often used parameter is the fill factor (FF), which is defined as the ratio of P_{MAX} to the product of V_{OC} and I_{SC}.

Light intensity has influence not only on the current but also voltage generation. If concentration factor $[X]$ is applied, and R_S is assumed to be negligible and R_{SH} very large, the V_{OC} becomes

$$V_{OC}^{[X]} = \frac{n_ikT}{q}\ln\left(\frac{[X]I_L}{I_0}\right) = \frac{n_ikT}{q}\left\{\ln\left(\frac{I_L}{I_0}\right)+\ln[X]\right\} = V_{OC}+\frac{nkT}{q}\ln[\mathrm{X}], \tag{2-19}$$

where $V_{OC}^{[X]}$ is open circuit voltage when light is concentrated with factor $[X]$.

One factor that limits solar cell performance is recombination. The three main types of recombination in solar cells are (*i*) radiative recombination (*ii*) defect assisted recombination, referred as

Shockley-Read-Hall recombination [66, 67], and (*iii*) Auger recombination [68], although the latter is not a very significant recombination process in III-V semiconductor solar cells [69]. Loss of charge carriers due to recombination directly reduces the current of the solar cell. Recombination in the pn-junction also increases the forward diffusion current, and furthermore lowers the solar cell voltage. Recombination can be reduced by optimizing the solar cell structure and material properties.

External quantum efficiency (EQE)

The EQE describes the probability that an incident photon at a certain wavelength creates an electron-hole pair which can be collected by the solar cell. The EQE takes into account all losses, such as reflection, recombination and transmission. EQE can be expressed as a percentage, as a function of wavelength or energy. Figure 2.18 presents the schematic of the EQE measurement setup.

The EQE is zero for photons which have energies smaller than the solar cell band gap energy, since they cannot induce band-to-band transitions. The absorption coefficient typically increases with photon energy in bulk material, and therefore high energy photons are more likely to be absorbed close to the front side of the solar cell. Therefore, the short wavelength side of the EQE gives information about photocurrent generation for high energy photons and corresponding electron-hole pairs created near the solar cell surface. Photons with energies closer to the band gap energy of the solar cell material are more likely to be absorbed deeper inside the solar cell, and therefore the long wavelength side of the EQE can provide information about, e.g., recombination deeper inside the solar cell. EQE alone is not enough for determination of the efficiency of the solar cell, and it can be heavily dependent on the optical and electrical bias conditions.

Spectral response measurements can be carried out with a setup similar to that for EQE measurements, but they do not require the use of a reference detector. In such measurement, a set of samples and their spectral response can be compared, but the detected signal is in arbitrary units.

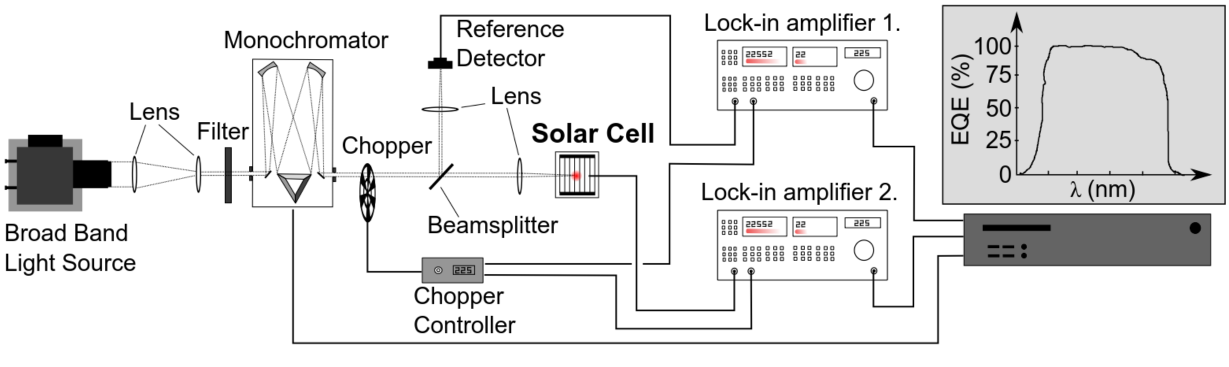

Figure 2.18 *Schematic image of the single junction solar cell EQE measurement setup. A specific wavelength from the broadband light source is chosen by the monochromator and guided to the sample and known reference detector. The necessary wavelength scale is scanned and the solar cell response is compared to the reference detector signal.*

3 Results and Discussion

Different types of semiconductor materials and nanostructures, which could potentially be incorporated into high-efficiency solar cells, have been investigated and the most important results are summarized in connection with the publications included in the thesis. Optical, electrical and structural properties of III-V heterostructures are characterized by the methods described in chapter 2.

3.1 Surface treatments

The surface is an important part of any physical structure. Many reactions happen at the material surface, which is exposed to the surrounding environment. The surface and its properties are especially important in crystalline structures: the periodic crystalline structure ends at the surface, and the surface atomic and electronic structures are therefore different compared to bulk material. Dangling bonds and oxides tend to form surface states, which typically act as effective recombination centers [70]. One way to modify the surface properties is via the application of chemical treatments. Although only the topmost monolayer is exposed to the chemical, it may have a significant effect not only on the surface structure, but also on the material's optical and electrical properties. This chapter presents studies on surface treatments and thermal annealing of GaInNAs/GaAs QW heterostructures, which can be used as absorbers in QW solar cells. Furthermore, the influence of chemical surface treatments on the AlInP window layer of a GaInP solar cell is also summarized.

GaInNAs/GaAs quantum wells [P1]

GaInNAs/GaAs QWs can be used in solar cells as well as laser applications as active layers to absorb and emit infrared radiation [P5], [71-73]. However, GaInNAs is found to be a metastable alloy and it has a large miscibility gap. Therefore, this material has to be grown under non-equilibrium conditions at relatively low temperatures to avoid phase separation and clustering effects [29]. Incorporation of relatively small and highly electronegative nitrogen atoms also introduces point defects to the material [P7, P8]. Thermal annealing is found to improve the GaInNAs material quality significantly [74-79], which is very important from the solar cell perspective. Typical annealing temperatures for GaInNAs material is in the range of 700–800 °C, and the annealing time varies from a few seconds to several minutes. Protective cappings are used to protect the surface from annealing induced degradation. For example, plasma enhanced chemical vapor deposition (PECVD) is used for growth of protective silicon dioxide (SiO_2) and silicon nitride (SiN_x) capping layers. GaAs proximity capping is also used for protection during thermal annealing [74]. Thermal annealing with SiO_2 capping is found to increase the GaInNAs QW PL emission [80]. On the other hand, also degradation in PL emission has been observed in SiO_2 coated samples upon annealing, even when compared to an uncapped reference sample [74]. The proposed reason for this is the difference between the GaAs and SiO_2 thermal expansion coefficients, which causes tension and vacancy formation at the crystal surface when the temperature is increased [81].

Since the annealing process seems to be very surface sensitive, chemical treatments prior to SiO_2 capping and thermal annealing were tested. The investigated sample consists of two 6 nm thick $Ga_{0.62}In_{0.38}N_{0.015}As_{0.985}$/GaAs quantum wells separated by a 20 nm GaAs barrier, and capped by a 100 nm thick GaAs layer. The as-grown sample emitted PL at λ=1260 nm. More detailed fabrication and measurement parameters are presented in [P1]. After the growth, the sample was cleaved into 4×4 mm^2 pieces which were treated with 20% ammonium sulfide [$(NH_4)_2S$] or 30% ammonium hydroxide (NH_4OH) solutions for 10 s, 2 min, or 30 min, resulting in six samples labelled S1, S2, S3, OH1, OH2, and OH3, respectively. The investigated samples are listed in Table I.

After the treatments, the samples were rinsed with de-ionized water, blown dry with nitrogen, and capped with 120 nm thick SiO_2 grown by PECVD. All the samples were annealed simultaneously at an annealing temperature (T_{ANN}) of 750 °C, on Si wafer, and in a nitrogen environment. T_{ANN} during multiple annealing rounds was controlled by an optical pyrometer. PL spectra were recorded after each annealing. The PL intensity as well as BS of the PL peak wavelength as a function of cumulative annealing time (t_{ANN}) is presented in Figure 3.1.

Table I. *Labelling of samples treated for different times in $(NH_4)_2S$ and NH_4OH solutions.*

Sample	Treatment	Time
S1	$(NH_4)_2S$	10 s
S2	$(NH_4)_2S$	2 min
S3	$(NH_4)_2S$	30 min
OH1	NH_4OH	10 s
OH2	NH_4OH	2 min
OH3	NH_4OH	30 min

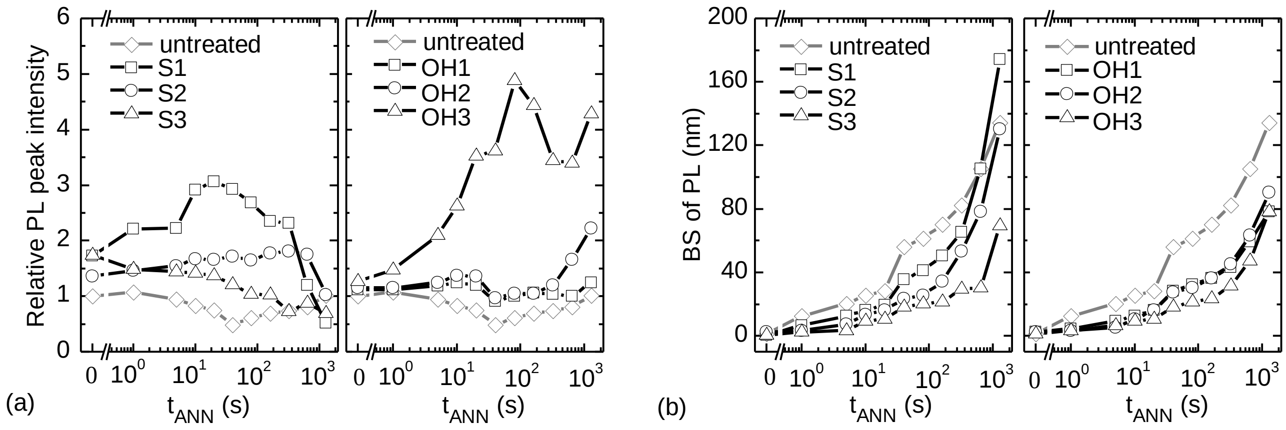

Figure 3.1 *(a) Relative PL peak intensity, and (b) BS of PL as a function of t_{ANN} (in logarithmic scale).*

Figure 3.1(a) shows that the surface treatments have a significant influence on the PL intensity behavior of the GaInNAs QW heterostructure upon annealing. The untreated sample shows no improvement in PL: the PL intensity actually decreases. Samples treated with $(NH_4)_2S$ solution show clear increase in PL already before annealing. Thermal annealing improves the PL, especially for sample S1. For samples S2 and S3, the PL intensity improves only slightly and remains constant, respectively. However, the PL intensity of all the $(NH_4)_2S$ treated samples starts to decrease at longer annealing times. A completely opposite trend is observed for samples treated in NH_4OH solution. The PL intensity clearly improves upon annealing for sample OH3 with the longest treatment time, whereas the improvement is only minor for samples OH2 and OH1. At longer annealing times, an increasing trend for PL intensity is observed. Surface treatments also significantly influence the BS of PL, as presented in Figure 3.1(b). All the treatments suppress the BS of PL with longer treatment times corresponding to smaller annealing induced BS. Especially the NH_4OH treated samples undergo a clearly smaller BS compared to the untreated reference. Only sample S1 shows a larger BS of PL compared to the untreated sample, after the longest cumulative annealing time of 1280 s.

After the annealing treatments, XRD (004) rocking curves were measured. Figure 3.2 presents the XRD data recorded from the annealed samples. After the cumulative annealing time of 1260 s the QW related Pendellosung fringes [82] at the negative angles moves closer to the GaAs peak, which is related to the relaxation of compressive lattice strain due to indium out diffusion from the QWs to the surrounding GaAs [74, 83, 84]. The shift of the QW related XRD signal goes hand in hand with the BS of PL: In out diffusion also increases the band-gap of the QW.

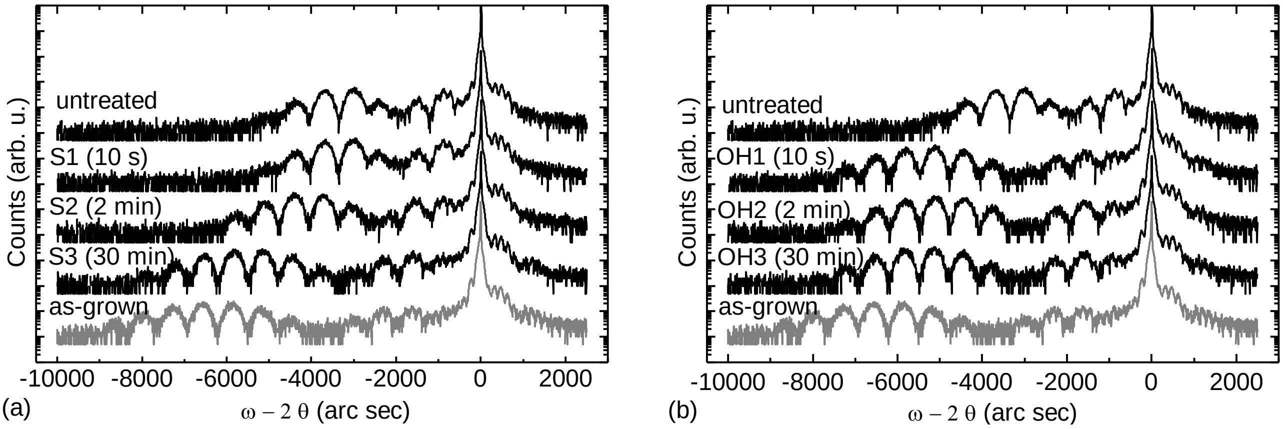

Figure 3.2 *XRD (004) rocking curves for (a) $(NH_4)_2S$ treated and (b) NH_4OH treated and cumulatively 1260 s annealed samples. The bottommost XRD spectrum (grey line) is recorded from the as-grown un-annealed sample.*

Diffusion can be expected to be induced largely by Ga vacancies and other point defects created at the GaAs/SiO_2 interface [81, 85]. This explains why surface treatments can have a drastic influence on diffusion processes. Treatment time in $(NH_4)_2S$ solution has a remarkable influence on XRD and BS behavior. Sample S1, with the shortest treatment time, has a similar XRD spectrum as the untreated annealed sample, whereas sample S3, with the longest treatment time, has a similar XRD spectrum to the as-grown sample. For NH_4OH treated samples, the treatment time does not have that significant an influence on the XRD behavior, nor on the BS of PL. There is also other mechanism which induces a shift in PL to shorter wavelengths. Short range ordering of the nearest neighbor Ga and In atoms around the N atoms, i.e., the nearly random $Ga_{4-m}In_m$-N atomic configurations with m=0,1,2,3, and 4 moves towards the In segregation configuration where m=4, which is observed in annealed GaInNAs structures as an increase in the band gap and a BS in PL wavelength [79, 86-90]. Part of the observed BS must be related to the short range ordering effect, which itself does not influence the XRD rocking curves significantly [91]. Short range ordering could explain the observed BS of PL in samples that do not show significant changes in their XRD spectra.

The annealing induced BS is often an unwanted phenomenon in QW solar cell applications, because it changes the absorption edge and therefore influences the solar cell current generation. On the other hand, thermal annealing can be a crucial step for improving the material quality. Correctly chosen surface treatment and protective capping can minimize the BS and maximize the material quality. However, these results do not provide direct information about the electrical properties of the material: for example, background doping density can vary between the samples.

In order to obtain information about the influence of surface treatments and thermal annealing on the GaAs/SiO_2 interface itself, XPS measurements were performed. Cleaved 6×12 mm^2 samples with 30 min treatments in $(NH_4)_2S$ and NH_4OH plus an untreated reference, all capped with a 2 nm thick SiO_2 grown by PECVD, were prepared. The thin SiO_2 layer was used in order to obtain an

XPS signal from the GaAs/SiO_2 interface. Mg $K\alpha$ non-monochromatic radiation was used to measure the XPS spectra before and after 20 min in situ annealing at T_{ANN}=600 °C in the XPS chamber. Although practical reasons forced the use of a thinner SiO_2 layer and lower annealing temperature compared to the PL and XRD samples, the XPS samples simulate at least partly the original annealing conditions. Figure 3.3(a) and (b) shows the Ga 3*d* XPS spectra before and after heating, respectively. Ga oxide components are divided into GaO_X, GaO_Y, and GaO_Z, using previously reported energy shifts of 0.6±0.05 eV and 1.2±0.05 eV for GaO_X and GaO_Y, respectively [92, 93]. For GaO_Z, the shift was allowed to vary between 1.6 and 2.0 eV. GaO_X, GaO_Y, and GaO_Z have been previously related to Ga_2O, Ga_2O_3, and $Ga(AsO_3)O_3$, respectively.

Based on the XPS data, GaO_Z does not seem to have an influence on the PL or XRD behavior of the sample since it is visible only for the untreated and annealed NH_4OH treated sample. However, GaOy could be linked with decreased PL intensity since its XPS intensity is higher for untreated and NH_4OH treated samples compared to the $(NH_4)_2S$ treated sample, which showed higher PL signal after the treatment and before the annealing. Furthermore, the GaO_Y XPS intensity for the untreated sample increases upon annealing, while the PL intensity decreases. GaO_X can be linked with increased PL intensity, because its XPS signal increases in the NH_4OH treated sample after annealing, when the PL intensity is also enhanced. These results are consistent with previous reports [93-95], which indicate that different forms of Ga oxides can be vital or fatal from the PL perspective. The GaO_X bonding configuration formed may also impede Ga diffusion into the SiO_2 capping layer and Ga vacancy diffusion into the GaAs, resulting in suppressed In out diffusion.

The results related to Ga oxides cannot alone explain the PL and XRD behavior of the annealed samples. However, the ratio between As and Ga oxides seems to be correlated with the In out diffusion. Based on As oxide XPS data (not shown), both chemical treatments are found to remove As oxides from the surface, leaving it Ga terminated. The untreated sample, however, shows clear

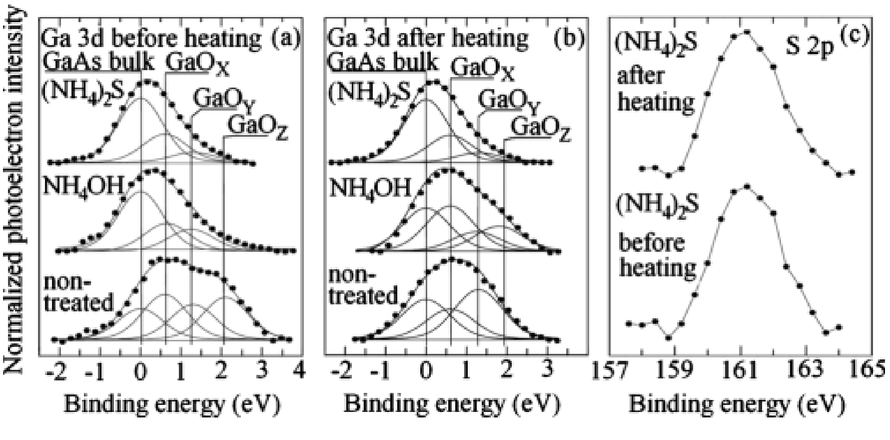

Figure 3.3 *Fittings of Ga 3d spectra measured by XPS (a) before and (b) after heating for 20 min at 600 °C for untreated, NH_4OH treated, and $(NH_4)_2S$ treated samples. Binding energy scale is relative to the GaAs bulk components. (c) S 2p photoemission spectra for $(NH_4)_2S$ treated sample before and after heating.*

photoemission from As oxides. This result indicates that the Ga terminated surface is more resistant to defect formation upon annealing: less diffusion inducing defects are created at the GaAs/SiO_2 interface, resulting in suppression of In out-diffusion.

Figure 3.3(c) shows that the $(NH_4)_2S$ treated sample contains S, which is known to passivate III-V semiconductors surfaces [96-98] and significantly increase the PL intensity [99]. Therefore, the PL increase in samples S1, S2 and S3 prior to annealing can be linked to S passivation. The reason for rapidly decreasing PL intensity and increasing BS for $(NH_4)_2S$ treated samples upon longer annealing times can be linked to S diffusion in the QW area. Figure 3.3(c) shows that S 2*p* XPS spectrum becomes broader upon annealing, which indicates that the S atoms in the vicinity of the GaAs/SiO_2 interface possess several nonequivalent bonding configurations, possibly via complex S diffusion processes [100, 101]. Diffused S may create nonradiative recombination centers, decreasing the PL intensity and possibly even enhancing the In out-diffusion.

It is evident that surface treatments have a significant influence on annealing behavior of the GaInNaAs QW sample. However, one cannot conclude that the improved PL emission is due only to decreased surface recombination, because thermal annealing also has a significant influence on the GaInNAs material's structural and optical properties, and presumably also on defects and nonradiative recombination in bulk GaAs and at GaInNAs/GaAs interfaces. The optical properties of the investigated samples are linked to the structural properties of the whole crystal, where the surface plays an important role. Furthermore, one can assume that surface properties have an influence also on the properties of other types of III-V semiconductor heterostructure upon annealing.

Chemical treatments for AlInP window layer

AlInP is a commonly used window layer material in III-V semiconductor solar cells. It provides an energy barrier for minority carriers for diffusion to the sample surface, where the surface state induced nonradiative recombination rate is high (see Figure 2.16). $Al_{0.47}In_{0.53}P$ is lattice matched to GaAs resulting in a ~2.3 eV band gap, corresponding to 540 nm wavelength. High band gap energy is essential for the window layer since it has to be transparent to solar radiation and have a low refractive index, in order to make more effective AR coating designs possible. Although AlInP is a very good window layer material, it absorbs part of the ultraviolet (UV) radiation, causing losses especially in space applications, where UV radiation is not influenced by the ozone layer or other parts of the atmosphere.

Previously, promising results have been obtained by treating the AlInP window layers of multijunction III-V solar cells with $(NH_4)_2S$ solution [102, 103]. The proposed reason for the improved solar cell characteristics in references [102] and [103] is a decrease of the harmful surface states due to S passivation. Therefore, the influence of $(NH_4)_2S$ treatment on the AlInP window layer grown on a GaInP solar cell was tested. The investigated sample was a GaInP solar cell with an AlInP window layer and a GaAs top contact layer, grown on p-type GaAs(100) substrate. The test process was utilized to make solar cell chips from the as-grown wafer. After the selective contact GaAs etch by $NO_4OH:H_2O_2$, 1:30, the solar cell's PL, LIV and EQE was measured. After these measurements, the window layer was treated in heated (T=60 °C) 20% $(NH_4)_2S$ solution for 20 minutes, rinsed with de-ionized water, blown dry with nitrogen, and the same measurements were repeated. Figure 3.4 shows PL, LIV and EQE data before and after $(NH_4)_2S$ treatment.

Surface treatment with $(NH_4)_2S$ improves PL intensity, current generation, and short wavelength EQE. The improved current generation is due to better utilization of the short wavelength photons. Interestingly, EQE is improved exactly in the wavelength range where photons are expected to be absorbed, at least partly, by the AlInP window layer. In order to investigate the treated AlInP surface and find the reasons behind the improved solar cell characteristics, AFM and reflectance measurements were performed, and the results are shown in Figure 3.5.

AFM measurement reveals a nanostructure on the $(NH_4)_2S$ treated AlInP surface, with lateral dimensions in the range from tens of nanometers to approximately 100 nm, and a maximum height of about 50 nm, although $(NH_4)_2S$ is not reported to etch AlInP. Furthermore, reflection measure-

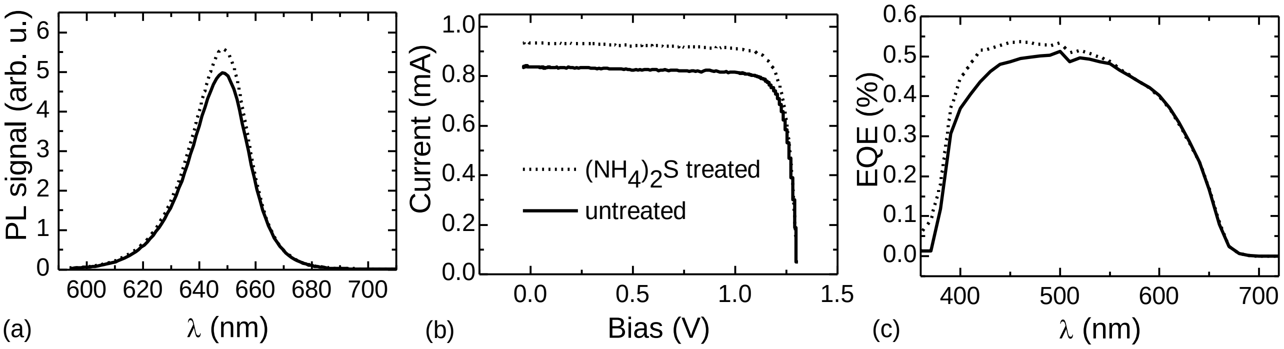

Figure 3.4 *(a) PL spectra, (b) LIV data, and (c) EQE recorded from the GaInP solar cell before and after* $(NH_4)_2S$ *treatments. The Oriel solar simulator, used for LIV, was equipped with an AM1.5G filter and calibrated with a known GaInP/GaAs tandem calibration solar cell.*

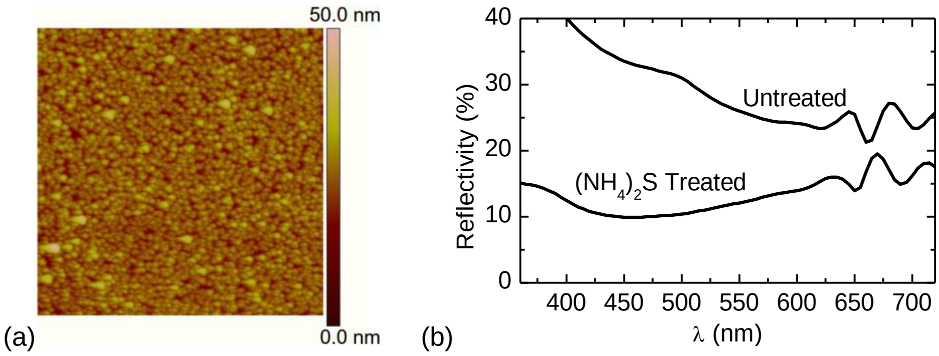

Figure 3.5 *(a) 3×3 µm AMF image revealing nanostructured surface. (b) Reflectivity measured from the* $(NH_4)_2S$ *treated and untreated samples.*

ment shows clearly suppressed reflection, especially at UV wavelengths. The observed nanostructure can suppress the reflection by providing a graded refractive index from air to AlInP, as presented in Figure 3.6(a). Reflection suppressing nanostructures are also called “moth-eye nanostructures”: certain moths have periodically nanostructured cornea in order to see better in the dark [24]. Moth eye nanostructures have been applied successfully onto different semiconductor surfaces [104-107], including an AlInP window layer [25, 26]. The same phenomenon is familiar from so-called black silicon solar cells, where reflection is suppressed and conversion efficiency is increased by etching a nanostructure on the silicon solar cell surface [108]. Suppression of reflection can explain the improved current and EQE of the investigated GaInP solar cell.

In order to gain more information about the surface, XPS was applied. Al $K\alpha$ non-monochromatic radiation was used in XPS measurements on treated and untreated AlInP surfaces. XPS data showed that the relative amount of S (compared to all elements) increased from 0.0% to 5.1 % due to $(NH_4)_2S$ treatment. At the same time, the relative amount of oxygen decreased from 20.3 % to 10.9 %. Furthermore, when In oxides decreased from 5.1% to 0.8%, In sulfides increased from 0.0% to 3.2 % due to the treatment. Also residual As and As oxides was measured from the untreated sample, but the As-related XPS signal disappeared after the $(NH_4)_2S$ treatment. The XPS results are somewhat similar to those in reference [102], where a reduction of oxides and an increase in sulfides was observed, resulting in a reduction in surface states. A similar passivation of surface states can be expected to be present also in the samples investigated here. Figure 3.6(b) shows how passivation of the AlInP surface could reduce the surface-states and surface-state-induced band bending, resulting in a lower surface recombination rate. Therefore, the minority carriers (holes in this case), generated due to absorption of the UV light at the window layer, would not recombine with the majority carriers (electrons in this case) immediately at the AlInP surface, but at least part of the minority carriers would diffuse to the depletion region and contribute to the solar cell current.

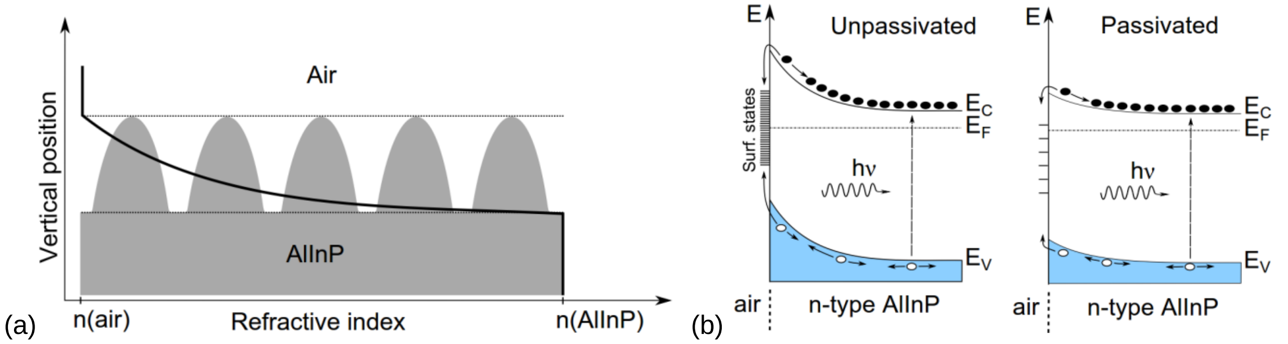

Figure 3.6 *(a) Nanostructure provides graded refractive index when moving from air to AlInP. (b) Passivation and reduction of the number of surface states decreases the nonradiative recombination. Surface state induced band bending, which drives the minority carriers to the surface, is reduced.*

Two mechanisms which can improve the solar cell properties are observed in $(NH_4)_2S$ treated samples: i) nanostructure/suppressed reflection, and ii) reduction in oxides/increase in sulfides/surface passivation. Suppressed reflection has a direct influence on the solar cell characteristics, and the PL, LIV and EQE results can be explained by the reduced reflectivity. However, the reflectivity is lower for the whole absorption band of the GaInP solar cell, but the EQE improves only for wavelengths that are absorbed by the AlInP window layer. The EQE result indicates that the increase in solar cell current could be a result of the passivation of surface states, and photons absorbed by AlInP would generate extra current when corresponding photocarriers would not recombined directly at the AlInP surface. However, since the voltage does not show an improvement in LIV curve, the surface treatment does not significantly influence the dark saturation current of the solar cell.

Because the results are not unambiguous, other surface treatment tests were carried out on the AlInP window layer of GaInP, GaAs, and GaInP/GaAs/GaInNAs solar cells. It appeared that the results were not repeatable, and large variations in the changes in LIV characteristics, surface morphology and reflectivity were observed. Some of the samples did not show improvement in solar cell current, evidence of nanostructure, or suppressed reflectivity. Apparently the outcome of the $(NH_4)_2S$ treatment is very sensitive to the growth parameters of the AlInP widow layer or its composition, or to the properties of the $(NH_4)_2S$ solution itself. More studies on this topic should be carried out in order to explain the observed phenomena. One of the interesting features is the material composition of the formed nanostructure. Furthermore, since the $(NH_4)_2S$ treatment changes the reflectivity of the solar cell surface, an additional antireflection coating should be designed for this changed condition.

3.2 Defects in InAs/GaAs quantum dot nanostructures

Defects are imperfections in the periodic crystal structure. Although in some cases the presence of defects can be advantageous, typically they degrade the semiconductor material’s optical and electrical properties [109]. Defects are particularly detrimental for solar cells, and therefore it is important to gain knowledge about defects in semiconductor materials to be used in solar cells. Defects inside crystalline material can be divided roughly into two categories, i) point defects and ii) dislocations/extended defects. Point defects can be single impurity atoms or intrinsic automatic imperfections, such as vacancies or interstitials. Dislocations are typically formed when material with a different lattice constant compared to the substrate material is grown beyond a specific critical thickness. This is the case when fabricating InAs/GaAs nanostructures: when the amount of deposited InAs exceeds ~2.5 ML, the strain of the InAs QD is relaxed via formation of dislocations [22]. In this chapter, the properties of the strain-relaxation-induced defects are investigated by DLTS and CV [P2]. Furthermore, the influence of the so-called flushing step during the MBE growth on defect formation is studied [P3].

Dislocations, extended defects and point defects in relaxed quantum dots [P2]

Self-assembled InAs QD nanostructures can be obtained by the strain-driven Stranski-Krastanov growth mode [16] on GaAs. The surface energy is minimized due to island formation, and a QD layer is formed [110]. Coherently strained defect-free InAs/GaAs QDs are formed when the amount of deposited InAs is between 1.7 and 2.5 ML [22, 111]. For smaller amounts of deposited InAs the QDs are not formed, and for higher amounts strain relaxation occurs. The influence of strain relaxation on defect formation was studied. Three different cases showing the evolution of InAs/GaAs QDs formation are illustrated in Figure 3.7, which shows AFM images after deposition of 1, 2, and 3 ML InAs on GaAs. The fabrication parameters are presented in [P2]. Figure 3.7 also shows the whole structure of the samples, with embedded and surface QD layers.

Deposition of 1 ML InAs is not enough for QD formation, resulting in a flat surface. After 2 ML InAs deposition QDs with a maximum height of 9.6 nm appear on the sample surface. When the amount of deposited InAs is increased to 3 ML, additional large clusters with a maximum height of 28 nm are observed. Figure 3.8(a) and (b) show the QD size distribution for 2 ML and 3 ML samples, respectively. Total QD densities are 4.0×10^{10} cm^{-2} and 4.5×10^{10} cm^{-2} for 2 ML and 3 ML samples, respectively. Increasing the amount of InAs results in a smaller height distribution in coherently strained QDs. However, larger 10–30 nm high clusters are appearing on the sample surface. These large clusters/coalesced islands can be linked to strain relaxation. To investigate the strain relaxation induced defects in the embedded QD layer, Schottky diodes were processed with Cr and Al gates for n- and p-type materials, respectively. Figure 3.8(c) shows the recorded DLTFS spectra.

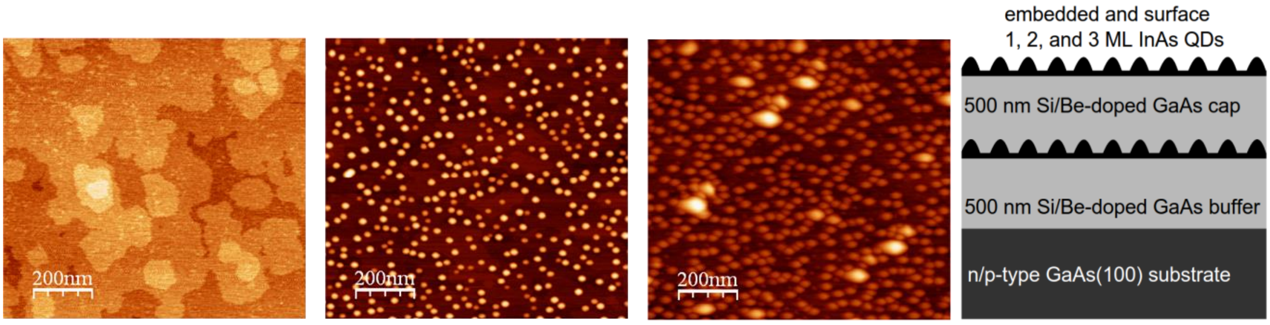

Figure 3.7 *1×1 µm AFM images taken after deposition of 1, 2, and 3 ML InAs on GaAs(100) surface (from left to right) [17]. The corresponding height scales are 1 nm, 9.6 nm and 28 nm. Schematic sample structure with embedded and surface QD layers, grown with identical growth parameters, is shown on the right.*

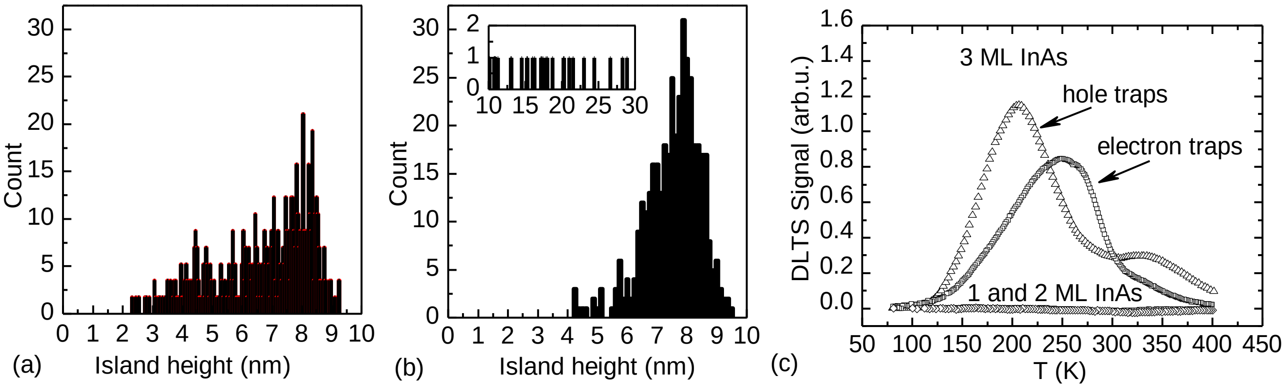

Figure 3.8 *Size distribution of QDs when (a) 2 ML, and (b) 3 ML are deposited. (c) DLTS spectra showing electron and hole traps in 3 ML samples. The measurement parameters were: V_R=-2V, V_P=0 V, T_W=100 ms, and t_P=10 ms.*

A broad DLTFS signal related to electron and hole traps is measured from Schottky diodes with 3 ML InAs QDs. Such a broad spectrum can be attributed to the mixture of dislocations, extended defects, and point defects in the InAs QD layer [22, 112-115]. Samples with 1 ML and 2 ML InAs do not show a distinct DLTFS signal in the measurement range. This confirms that the measured DLTFS signal and related defects are merely strain-relaxation induced.

Next, the deep electron levels in Si-doped Schottky diode with 3 ML InAs QDs are investigated in more detail. Figure 3.9(a) presents the CV data, recorded with 1 MHz measurement frequency and 100 mV amplitude at T=300 K. The QD induced capacitance plateau is observed at a voltage range between -3.5 V and -1.5 V. The calculated free carrier depth profile, presented in Figure 3.9(b), shows a charge accumulation peak surrounded by depleted areas with lower carrier concentration. The calculated charge accumulation peak is located deeper than the actual QD layer (~600 nm vs 500 nm), because the calculated depth corresponds to the location of the depletion region edge, and electrons in confined QD states are probed (Fermi level crosses the QD states) when the depletion region edge has already moved below the QD layer. Significant defect-related charge depletion is not observed in CV data, although defects can be at least partially responsible for the larger depleted area above the QD layer.

Figure 3.10 shows DLTFS scans where different depths of the Schottky junction are probed by varying V_R and V_P. Essentially the entire DLTFS signal is originating from the area which is probed at voltages between -5 V and -2 V. The DLTFS signal and related electron traps appear to be located somewhat deeper than the actual QD layer, when compared to the CV data.

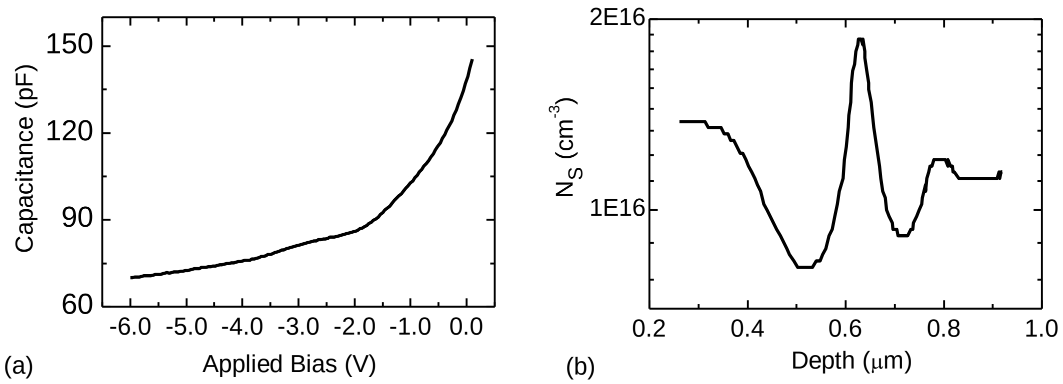

Figure 3.9 *(a) CV curve and (b) corresponding calculated free carrier depth profile. Change accumulation in the QD layer can be seen as a capacitance plateau and peak in the CV curve and depth profile, respectively.*

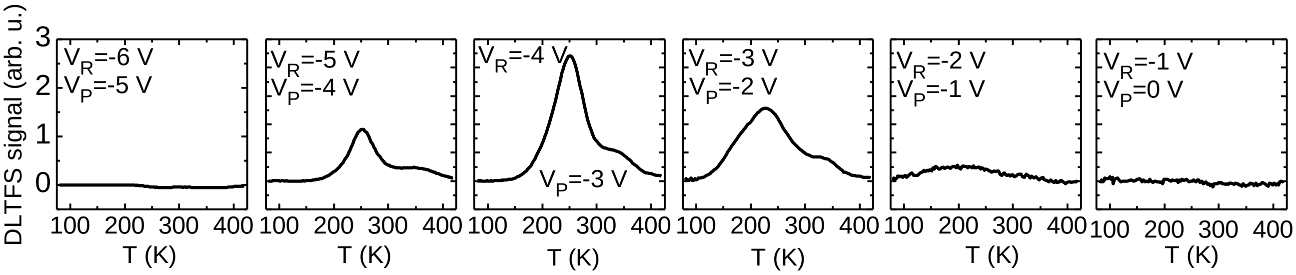

Figure 3.10 *DLTFS spectra where depth of the probed area is varied by varying V_R and V_P. Scanned area moves deeper below the Schottky contact when moving from the left to the right end of the Figure (from smaller reverse biases to higher reverse biases).*

In order to probe the deep defect levels in and near the QD layer, the depletion region edge must be below the QD layer so that the Fermi level can cross the defect levels during the measurement. This explains why the DLTFS signal appears at larger reverse bias (deeper) than would be expected when comparing the DLTFS data directly to the CV data.

Gaussian peaks were fitted to the DLTFS data, in order to resolve different components of the broad DLTFS spectrum. Figure 3.11(a) shows three Gaussian fits and the corresponding Arrhenius evaluation, for the electron traps labeled T1, T2, and T3. The data based on the Arrhenius analysis are presented in Table II. In order to resolve the nature of the observed defects, DLTFS measurements with different t_P were made. Furthermore, isothermal DLTFS measurements were carried out where t_P was varied at the temperature corresponding to each DLTFS peak. Figure 3.11(b) shows the data from these measurements.

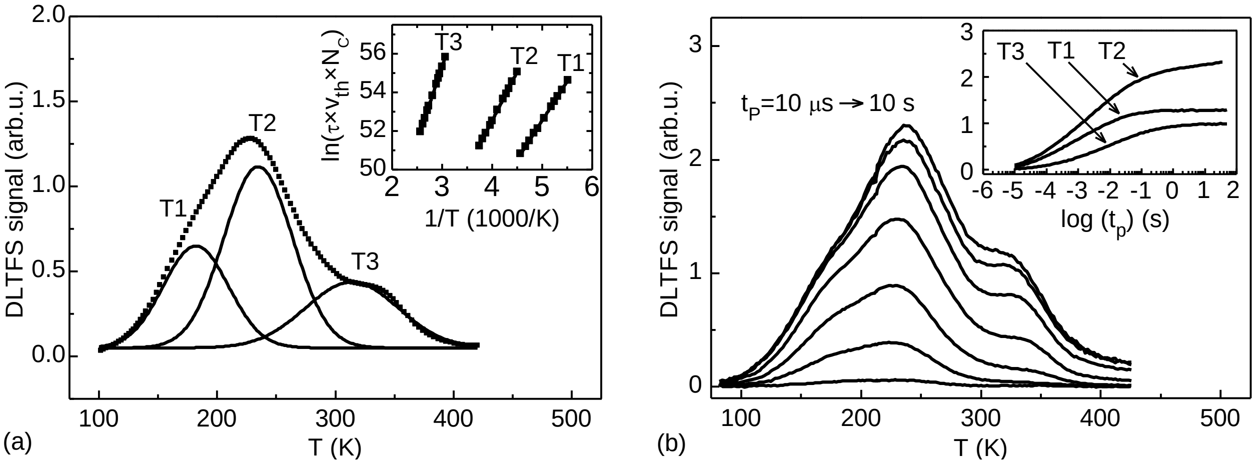

Figure 3.11 *(a) Gaussian fits showing different components of the DLTFS spectra, labelled T1, T2, and T3. The corresponding Arrhenius evaluation is shown as an inset. (b) DLTFS spectra recorded with different* t_P*. Inset shows the DLTFS signal plotted against the logarithm of* t_P *for each trap.*

Table II *Trap parameters obtained from the DLTFS measurements and corresponding Arrhenius evaluation presented in Figure 3.11.*

Trap	N_T (cm^{-3})	E_T (meV)	σ (cm^2)
T1	1.9×10^{13}	349	9.6×10^{-15}
T2	5.7×10^{13}	500	1.0×10^{-14}
T3	1.7×10^{13}	665	1.0×10^{-14}

The nature of the defect, whether it is related to dislocations/extended defects or point defects, can be evaluated from the DLTFS data when t_P is varied and other measurement parameters are kept fixed. Dislocations form defect bands due to closely spaced traps. These defect bands exhibit a time-dependent Coulomb barrier when the defect states are filled, limiting capture of the charge carriers. As a result, the DLTFS signal does not saturate even for long filling pulses (t_P>100 ms), and a linear slope is observed when the DLTFS signal is plotted against the logarithm of the t_P [116-119]. Point-defects behave differently; saturation of the DLTFS signal is typically observed already at t_P<100 ms [118]. The trap T1 DLTFS signal saturates already at t_P=100 ms, indicating that T1 is related to a point defect. Based on the evaluated trap parameters, it is possible that trap T1 is a so-called EL6 point defect, observed in GaAs with a thermal activation energy of 350 meV [120-123]. EL6 is commonly considered to be a Ga vacancy-As interstitial (V_{Ga}-As$_i$) complex [122]. Saturation of the DLTFS signal is not observed for T2, even when t_P is increased to 10 s. Therefore, T2 must be related to dislocations or extended defects. Interestingly, the slope of the T2 related DLTFS vs log(t_P) curve changes at the same t_P value for which saturation occurs for T1. Overlapping DLTFS signals originating from point defects and dislocations can explain this behavior. The same applies to T3, which shows no saturation, but a change in the DLTFS signal vs log(t_P) slope is present at around t_P=500 ms. This is also a clear indication that T3 is related to dislocations or extended defects. However, it is possible that T3 overlaps with the so-called EL2 point defect, identified as an As_{Ga} antisite. Activation energies ranging from 580 meV to 840 meV have been reported for the EL2 trap in GaAs [124-127].

Strain relaxation induces a remarkable amount of defects at various energies in and near the InAs QD layer. Although the formed defects are related to dislocation formation and InAs clustering related extended defects, there is a clear indication that also point defects are formed near the relaxed QD layer. Dislocations and point defects both increase nonradiative recombination, and should be avoided by all means in solar cell structures.

Influence of flushing on InAs quantum dots [P3]

Large QD ensembles with high QD densities and aspect ratios are essential in solar cell applications. Stacked QD layers with a high QD sheet density increase absorption and current generation, and a large aspect ratio shifts the confined states deeper into the GaAs band-gap, providing more optimal energy levels for intermediate band operation [18, 128-131]. Therefore, growth near the critical thickness for the QD plastic strain relaxation with a maximal amount of InAs deposited without defect formation is beneficial. Homogeneity of the QD layer is also important for formation of an intermediate band: a large size distribution means a large QD state energy distribution, which is not beneficial. One way to improve the homogeneity of InAs QDs and tune their shape, size and composition is the so-called flushing technique [132-137], where the QD layer is capped with a few nanometers thick GaAs layer followed by *in situ* annealing. The flushing step can also make stacked InAs QD layers more uniform, and remove unwanted InAs clusters [132]. Another method to improve InAs QD properties is cycled growth, which is reported to increase the QD density, aspect ratio, homogeneity, and also reduce the amount of InAs clusters [132, 138]. Therefore, the influence of flushing and cycled growth deposition on defect formation and optical properties was studied. The results presented in this subsection are based on [P3].

Flushing and cycled growth of InAs QDs were applied on four samples. The investigated samples consisted of a 600 nm n-GaAs buffer, a QD layer, and a 400 nm n-GaAs capping layer grown on Si doped n-GaAs(100) substrate. The QDs were grown by depositing 3 ML of InAs, which is beyond the critical thickness for strain relaxation [22]. The InAs QDs were deposited with continuous and cycled deposition, and with and without the flushing step. In cycled deposition, the shutter opening time was 1 s and the delay time 2 s. In the flushed samples, the QDs were capped with a 4 nm GaAs layer and exposed to an annealing step at T_{ANN}=605 °C for t_{ANN}=10 min under arsenic flux before growth of the GaAs cap layer. More detailed fabrication parameters can be found in [P3]. The samples, labelled A1, A2, B1, and B2, are described in Table III. Schottky diodes with 100 nm thick Cr gates were processed from each sample for DLTFS and CV measurements.

Table III *Labeling of samples where QDs were grown by continuous or cycled growth with or without flushing.*

	Continuous growth	Cycled growth
No flushing	A1	B1
Flushing	A2	B2

Figure 3.12(a) shows the DLTFS spectra recorded from each sample. A strong DLTFS signal is measured from unflushed samples over a broad temperature range, whereas the flushed samples shows no detectable signal, pointing to an absence of trap levels. Sample A1, with continuously grown unflushed QDs, shows a broader DLTFS spectrum compared to sample B1 with cycled QD growth. Figure 3.12(b) shows the DLTFS signal plotted against log(t_P) for sample B1. A nearly linear slope is observed up to t_P=10 s, indicating the presence of dislocations and extended defects due to strain relaxation and clustering effects. A similar result was obtained for sample A1. Figure 3.12(c) shows an isothermal DLTFS signal for sample B1 measured at T=230 K, corresponding to a DLTFS peak maximum. The DLTFS signal is plotted against V_R, when V_P=0.0 V and the other measurement parameters are also kept constant. The highest DLTFS signal is observed at V_R=-3.8 V. This voltage and the corresponding depletion region depth correlates with the depth of the QD layer, proving that the DLTFS signal is caused by the defects in or near the QD layer. Again, sample A1 shows similar behavior.

CV measurements were performed to probe the free carrier distributions in each sample. Figure 3.13(a) shows the free carrier depth profile calculated from the CV measurement data, recorded at T=300K with 1 MHZ and 100 mV measurement frequency and amplitude, respectively. A strong depletion is observed for unflushed samples A1 and B1 at around 300–600 nm depth. Charge depletion is caused by electron trapping inside dislocations, extended defects and point defects located in and near the QD layer. The trapped electrons cannot follow the 1 MHz measurement signal. Charge accumulation peaks at ~630–650 nm depth are also related to trapped electrons which are released and contribute to the capacitance when the Fermi energy has moved below the trap states at higher reverse bias values [139, 140]. Flushed samples A2 and B2 show charge accumu-

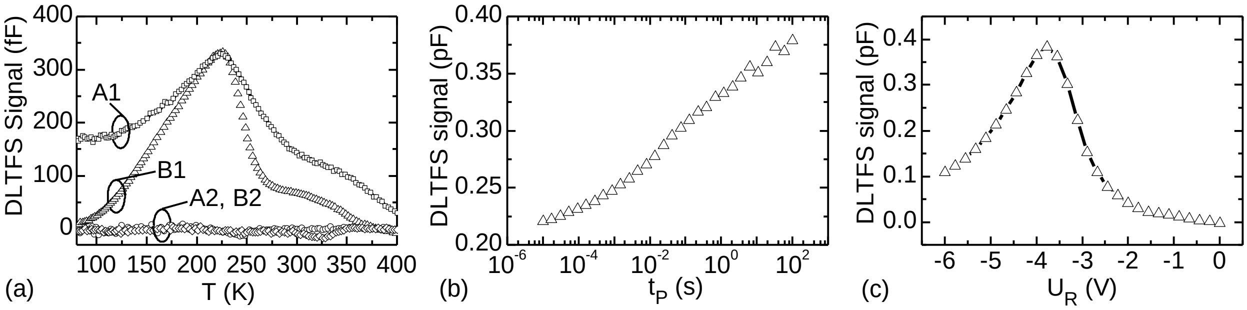

Figure 3.12 *(a) DLTFS spectra measured from samples A1, A2, B1, and B2. Measurement parameters were U_R=-4.0 V, U_P=0.0 V, T_W=200 ms and t_P=10 ms. (b) Isothermal DLTFS signal plotted against log(t_P) at T=230 K showing a linear slope up to t_P= 10 s.*

lation at a depth of 480 nm, accompanied by slightly depleted areas below and above. This is related to electrons from the surrounding areas accumulating at the confined QD states. Defect-related charge accumulation is not observed in the flushed samples. Charge accumulation peaks are shifted deeper into the calculated depth profile because the Fermi level crosses the confined QD states and deep defect states when the depletion region edge, which defines the depth in the calculated depth profile, is already at a greater depth. The deeper the probed state lies in the band gap, the greater is the shift.

Figure 3.13(b) shows PL spectra recorded from all four samples at T=300 K by a diode laser operating at λ=785 nm and an InGaAs detector array. The features in the PL spectra of all samples can be divided into four parts: emission from the QDs, emission from GaAs at ~1.4 eV, and broad emission related to substrate impurities at ~0.9 eV. Furthermore, four conclusions can be drawn from the PL data: (i) the QD PL signal is larger for samples with cycled InAs deposition, (ii) flushing increases the PL signal, (iii) flushing causes a BS of PL signal, and (iv) the BS is larger for sample A2 grown with continuous deposition. Cycled InAs deposition introduces fewer defects (lower nonradiative recombination rate), as observed by the DLTFS measurements presented in Figure 3.12(a), explaining part (i). Cluster formation in particular is suppressed due to cycled growth [138]. The same explanation is valid for part (ii): flushing removes and prevents defect formation in and near the QD layer, suppressing nonradiative recombination significantly. Furthermore, flushing influences the shape, size and composition of the QDs, causing a BS in PL emission [134], explaining part (iii). Material diffusion can be expected to be more pronounced when there are more defects which might act as diffusion promoters, which could explain the part (iv). The relative weakness of the sample A2 PL emission can be explained by the smaller energy offset between the GaAs band gap and QD states. A smaller energy offset increases the probability of thermal escape of carrier from the QD states, reducing the PL intensity.

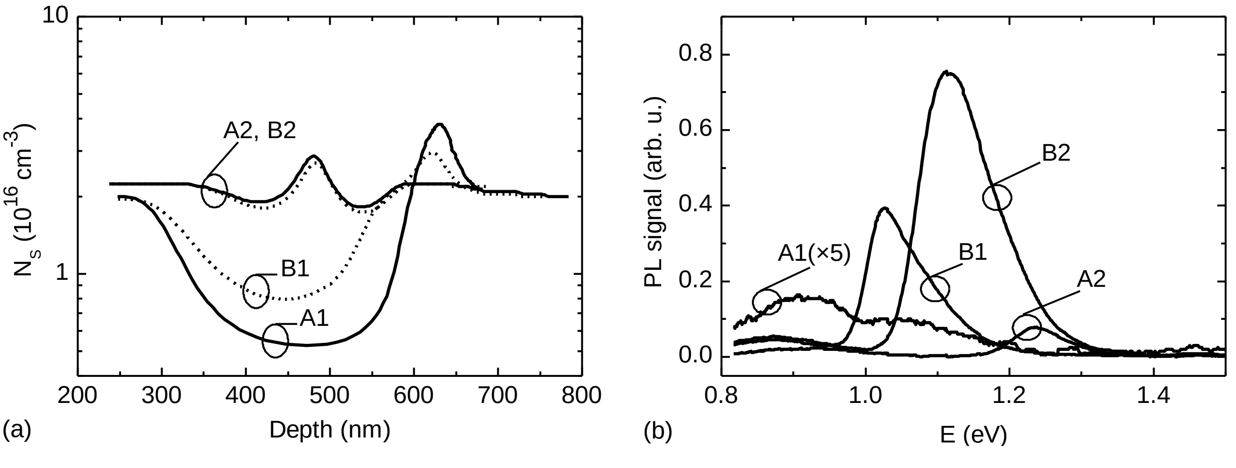

Figure 3.13 *(a) Free carrier depth profile calculated form the CV measurements (samples A1 and A2 with solid line and B1 and B2 with dotted line), and (b) PL spectra recorded from each sample.*

Flushing can be concluded to remove the majority of the strain-relaxation-induced defects. However, DLTFS measurements from n-type Schottky diodes does not probe hole traps, which could occur in any of the samples. Cycled growth is also beneficial, apparently due to reduction of InAs clustering. The flushing induced BS could be minimized by optimizing flushing time, temperature and capping layer thickness. Cycled growth combined with a flushing step could be applied for fabrication of stacked InAs/GaAs QDs, fabricated near the critical deposition limit for strain relaxation, for solar cell applications.

3.3 GaSb/GaAs quantum dot nanostructures

InAs/GaAs is not the only available material system for formation of self-assembled semiconductor QDs. Deposition of GaSb on GaAs also results in a 3D growth mode and QD formation [141]. However, GaSb QDs do not necessary follow SK growth, but also interfacial misfit (IMF) growth is possible for GaSb/GaAs structures [23, 142-144]. Furthermore, GaSb/GaAs QDs acquire a type-II band structure, where the holes are confined but the electrons are loosely bound by Coulombic interaction with holes [145]. In this chapter, the optical properties of GaSb/GaAs QDs, grown with different V/III beam equivalent pressure (BEP) ratios and exposed to thermal annealing, are reported [P4]. The properties of solar cells with stacked GaSb QDs layers are also investigated.

Optical properties of GaSb/GaAs QDs [P4]

GaSb QDs can follow either SK or IMF growth modes. The dominant growth mode in the GaSb/GaAs system can be influenced by the III/V BEP ratio [23], and the transition from SK to IMF growth is not abrupt. In IMF growth mode, the strain caused by the lattice mismatch is relieved by introducing 90° dislocations within the QD. The size of the IMF grown QDs is larger compared to SK grown QDs, changing the position of the confined energy levels inside the QDs. The size difference explains the reported differences in PL: emission at around 1.1 eV is observed for SK grown QDs [23, 141, 144, 146-151], whereas IMF grown QDs emit at ~0.95 eV [23, 144].

To investigate the optical properties of GaSb/GaAs QDs grown near the transition from SK to IMF growth mode, three samples were grown with different Sb/Ga BEP ratios. First, a 200 nm GaAs buffer layer, a 50 nm AlAs layer and a 50 nm GaAs layer were deposited on GaAs(100) substrate. Then a GaSb QD layer was fabricated by depositing 3 ML of GaSb. The structure was finalized by 50 nm GaAs, 50 nm AlGaAs, and 30 nm GaAs cap layers. More detailed fabrication parameters can be found in [P4]. Three samples were fabricated with Sb/Ga BEP ratios of 3, 5, and 7, resulting in samples labelled A, B, and C, respectively. QDs were also deposited on top of each sample using the same growth parameters as for the embedded ones.

Figure 3.14(a) and (b) shows AFM images of surface QDs on samples A and C, respectively. The higher Sb/Ga BEP ratio results in slightly larger and more rectangular QDs. The QD density was measured to be 3.3×10^{10} cm^{-3} and 2.7×10^{10} cm^{-3} for samples A and C, respectively. Larger QD size correlates with decreased QD density. The slightly rectangular shape of the QDs in sample C with the highest Sb/Ga BEP ratio can be linked to the onset of IMF growth mode, although there are also round QDs formed *via* SK growth mode in this sample. IMF growth mode is known to take place when the larger adatom (Sb) is present in larger quantities on the growth surface compared to the smaller adatom (Ga) [23]. Figure 3.14(c) shows the PL spectra recorded for each sample at T=300 K. Increasing the V/III BEP ratio reduces the PL emission and shifts it to lower energies. The red shift can be explained by the increase in average QD size. PL intensity is also expected to decrease because of the formation of misfit dislocations and the resulting increase in nonradiative recombination.

The optical properties of GaSb QDs upon thermal annealing were also studied. Cleaved 4×4 mm^2 samples were annealed for t_{ANN}=30 s on Si wafer under a GaAs proximity cap, in N_2 atmosphere at T_{ANN} ranging from 600 °C to 970 °C. Figure 3.15 shows the PL spectra recorded at T=300 K, from as-grown, 870 °C, and 970 °C annealed samples. Gaussian fits were applied to the PL data recorded from the annealed samples to obtain PL signal strength, PL energy (photon energy), and FWHM as a function of annealing temperature, presented in Figure 3.16(a), (b), and (c), respectively.

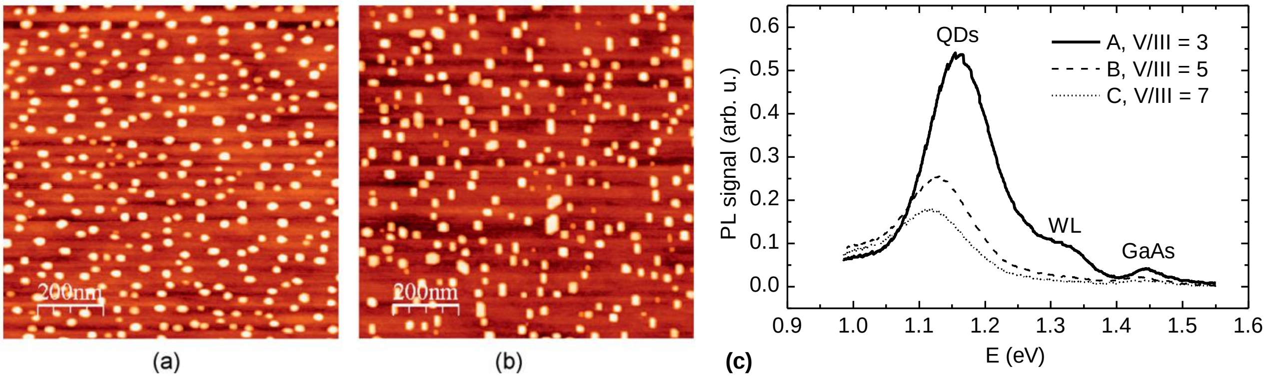

(a) (b) **(c)**

Figure 3.14 *AFM image (1μm×μ1 m) of surface QDs taken from the sample with (a) V/III = 3 (same as sample A), and (b) V/III = 7 (same as sample C). Room temperature PL spectra of as-grown QD samples A, B, and C grown with different V/III BEP ratios.*

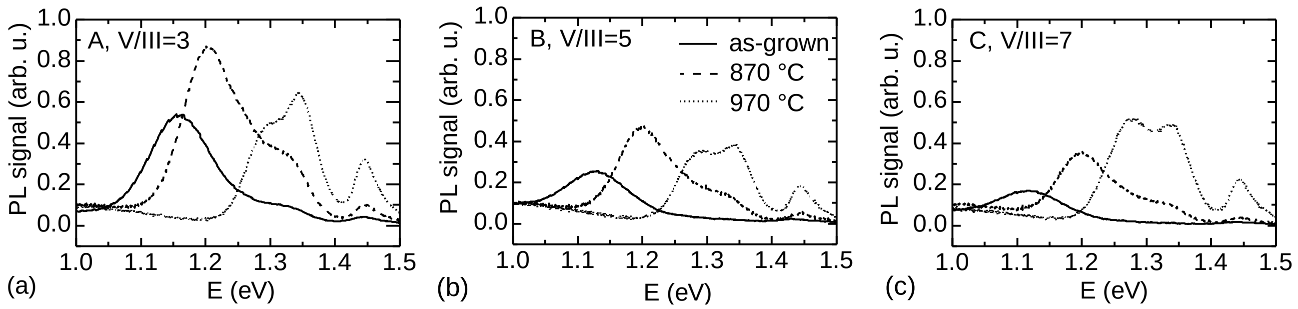

Figure 3.15 *PL spectra of as-grown and annealed samples fabricated with V/III BEP ratios of (a) 3, (b) 5, and (c) 7.*

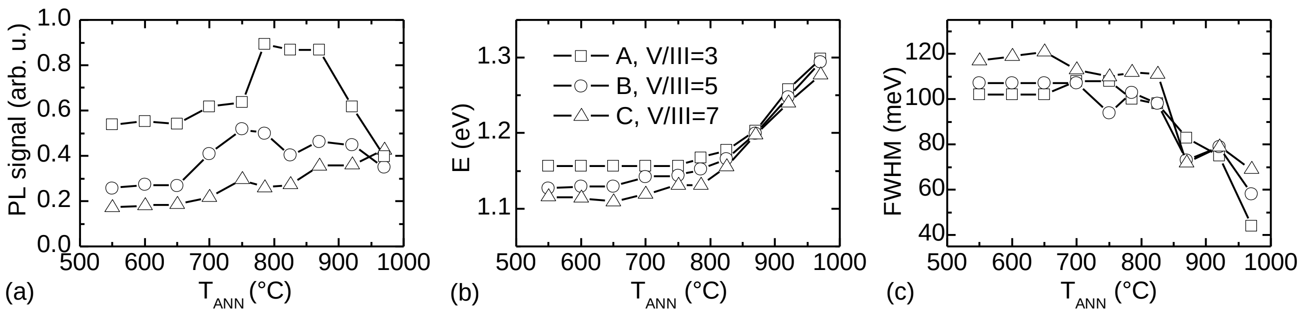

Figure 3.16 *(a) PL signal strength, (b) PL energy (energy of photons at peak maxima), and (c) FWHM as a function of T_{ANN}. Data points at T_{ANN}=550 °C correspond to as-grown sample.*

Annealing is found to increase the PL intensity, shift emission to higher energies, and decrease FWHM. Annealing of the defects in the QD and surrounding layers and interfaces improves the PL emission. The shift in PL energy is due to annealing induced material diffusion, which causes changes in the effective QD size shape and composition, and also a decrease in FWHM value [152-154]. The decrease in PL emission at high temperatures for samples A and B is accompanied by an increase of WL PL emission, as seen in Figure 3.15. The probability that electron-hole pairs recombine through spontaneous emission in the WL increases when the confined QD energy states shift closer to the WL energy states. This can explain the decreasing trend for samples A and B at high T_{ANN}. Sample C shows an increase in PL emission up to the highest annealing temperatures, because as-grown sample C emits PL at the lowest energy and the QD energy states are not shifted as close to the WL energy states as they are in samples A and B. One can also expect that sample C has the highest defect density due to the onset of IMF growth mode, and a higher annealing temperature can be needed to remove those defects. A small BS in WL emission is also observed due to annealing induced material intermixing. The BS is not found to be dependent on the Sb/Ga ratio, indicating similar diffusion mechanism in all the samples.

The influence on thermal annealing on confined QD states was further investigated by temperature-dependent PL spectroscopy. PL emission was recorded over the temperature range from T=9 K to T=300 K from as-grown, and T_{ANN}=870 °C samples. All the samples showed an increase in PL emission intensity when the temperature was decreased. The thermal activation energy was obtained for each sample by fitting equation (2-1). Fits and thermal activation energies are presented in Figure 3.17(a)-(d). Thermal activation energy is higher for sample C due to better confinement of holes located in larger sized QDs. Thermal annealing decreases the confining potential for both samples, as indicated by reduced thermal activation energies. The obtained activation energies correlate with AFM and PL findings. Power dependent PL measurements were also performed at T=9 K. Figure 3.17(e) shows PL peak position in energy scale plotted against the third root of excitation power density. A linear increase is observed for as-grown and annealed (T_{ANN}=870 C) samples A and C. This is typical for materials with type-II band alignment [141, 147, 155-158]. This result shows that thermal annealing does not change the band alignment, which is expectable since type-II band alignment appears for all Sb compositions in GaAsSb [145].

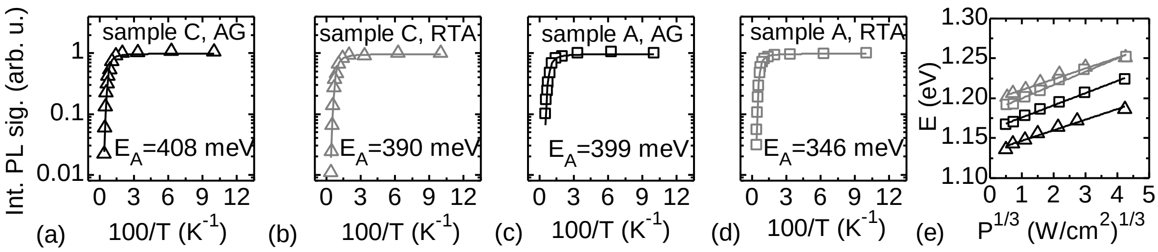

Figure 3.17 *(a)-(d) Integrated PL signal plotted against inverse of temperature. A single exponential function was fitted to the data. (e) PL emission energy plotted against the third root of excitation power showing linear increase, indicating type-II band alignment.*

Information about Sb/Ga ratio based selectivity between strained SK growth mode and IMF growth mode is important when fabricating GaSb QDs for solar cell applications. Although IMF growth results in more confined energy states and lower energy PL emission, the QD density is lower and dislocations increase nonradiative recombination. Thermal annealing can reduce the amount of defects, but it is accompanied by an unwanted BS.

GaSb/GaAs quantum dots in solar cells

The influence of stacked GaSb/GaAs QDs in p-i-n solar cells were investigated. Four GaAs p-i-n solar cells were fabricated with 0, 5, 10, and 20 layers of GaSb QDs. After the growth of 400 nm n-GaAs on n-GaAs(100) substrate, an i-region consisting of a stack of 3 ML GaASb QDs separated by 15 nm of GaAs was fabricated. A BEP Ga/Sb ratio of 3.2 was used to ensure that the growth takes place in SK mode, without formation of dislocations. The undoped i-region was capped by 300 nm of p-GaAs, forming a p-i-n diode. The fabrication of the doped GaAs layers and the i-region was performed at T_{GR}=580 °C, and T_{GR}=500 °C, respectively.

Figure 3.18(a), (b), and (c) shows PL spectra, LIV, and EQE data, respectively, recorded from GaSb QD solar cells. There are no remarkable differences in PL emission between the samples although they contain different amounts of stacked QD layers. The PL emission is most likely originating from the topmost QD layers, since a large fraction of the photons emitted by the laser are already absorbed within the 300 nm GaAs capping layer. The sample without a QD layer shows only strong bulk GaAs related PL (not shown). The LIV results show that introducing a QD layer to the structure decreases the solar cell voltage: V_{OC} is 0.87 V, 0.74 V, 0.70 V, and 0.69 V for samples with 0, 5, 10, and 20 QD layers, respectively. QD solar cells typically have lower voltages compared to a reference without QDs due to increased rate of recombination [159-163]. The positive observations are, that (i) the voltage drop seems to saturate, and (ii) the drop is smaller compared to earlier reported values [159, 162, 163]. Only minor changes in I_{SC} are observed: the lowest value is recorded from the sample with 5 QD layers, whereas 20 QD layers and the GaAs reference solar cell produce the highest I_{SC}. However, Figure 3.18(c) shows that absorption in the WL and QDs does occur, and it gets stronger when the amount of layers is increased. Apparently at least some of the QD layers induce recombination that reduces the current (and voltage), but the photocurrent generation by the QD layer compensates for the current losses when 20 layers are stacked. A quantity of QD layers at least an order of magnitude larger should be fabricated in order to achieve significant QD induced current generation.

Thermal annealing was tested, because it is known to improve the PL intensity and remove defects. Carefully cleaved 4×4 mm^2 samples were annealed on Si wafer under a GaAs proximity cap in a N_2 atmosphere. Figure 3.19 shows QD related (a) PL intensity, (b) PL energy, and (c) FWHM as a function of T_{ANN}. All the samples behave similarly, showing first an increase in PL intensity followed by a decrease after T_{ANN}≈800 °C. A shift of QD PL peak to higher energies also occurs, and the BS is clearly enhanced at the same temperature when the PL intensity starts to drop. A decrease in FWHM is also present, starting also at T_{ANN}=800 °C.

Since the WL has a larger spectral response than the QDs, the PL emission of the WL was analyzed as well. Figure 3.20 shows WL related (a) PL intensity, (b) PL energy, and (c) FWHM as a function of T_{ANN} for the sample with 5 QD layers. The other two samples' WL PL emission seemed to show similar behavior upon annealing, the only clear difference being PL intensity, which was from 1.5 to 2.5 times higher for the sample with 5 QD layers. The reason why only the 5 QD layer

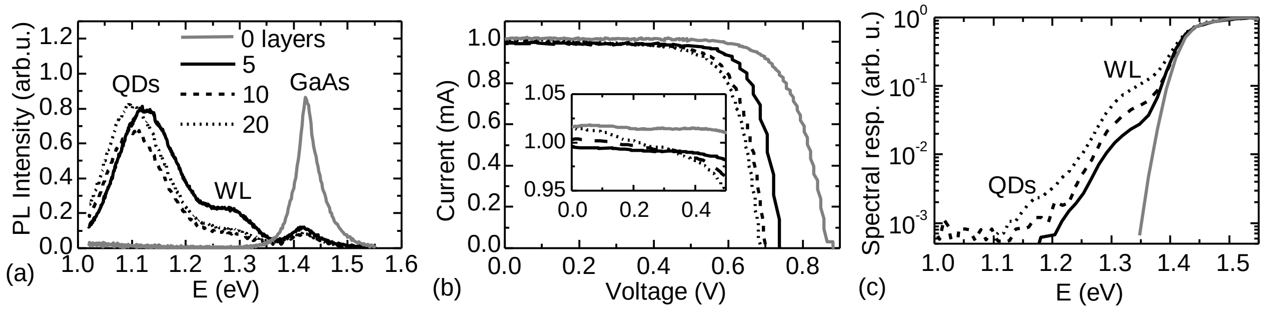

Figure 3.18 *(a) PL spectra, (b) LIV curves, and (c) EQE data recorded from GaSb/GaAs QD solar cells. Increase in amount of stacked layers manifests as increase in solar cell current generation and EQE but decrease in solar cell voltage.*

sample is plotted here is the weakness in the WL PL emission and overlapping with the stronger QD related PL peak for the other two samples, preventing reliable fitting of Gaussian peaks. The WL PL intensity is found to increase up to T_{ANN}=826 °C, after which it decreases. Emission also shifts to higher energy when T_{ANN} is increased. Furthermore, the FWHM decreases when T_{ANN} is increased. The PL behavior is, in general, similar for WL PL emission and QD PL emission. Both PL peaks shows similar changes in PL intensity, a diffusion related energy shift, and a decrease in FWHM.

After the PL measurements, cleaved 4×4 mm^2 samples were processed into solar cells using the test process described in section 2.1. The impact of thermal annealing is presented in Figure 3.21(a), (b), and (c), showing annealed solar cells I_{SC}, V_{OC} and FF, respectively. The data show that thermal annealing has no significant influence on solar cell operation. The highest current is measured from the 5 and 20 layer samples annealed at T_{ANN}=700 °C, but the increase compared to as-

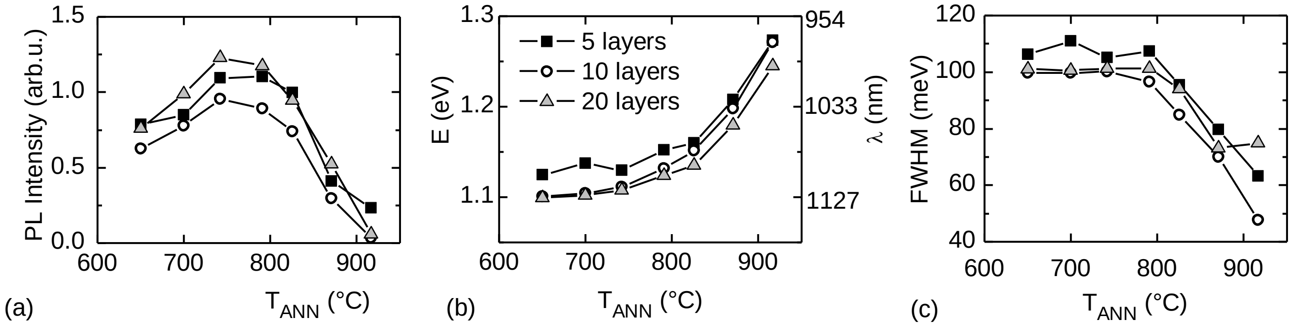

Figure 3.19 QD related *(a) PL intensity, (b) PL energy, and (c) FWHM as a function of T_{ANN}. Data points at T_{ANN}=650 °C correspond to as-grown sample. The data are obtained from the Gaussian peaks fitted to PL spectra.*

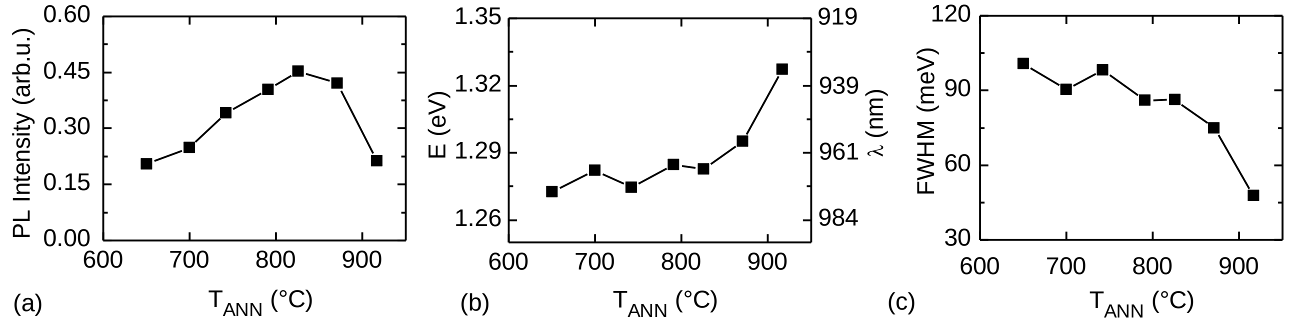

Figure 3.20 *WL related (a) PL intensity, (b) PL energy, and (c) FWHM as a function of T_{ANN}. Data points at T_{ANN}=650 °C correspond to as-grown sample. The data are obtained from the Gaussian peaks fitted to PL spectra for the sample with 5 QD layers.*

grown samples is only 2-3%. The highest V_{OC} is measured from the 5 layer sample annealed at T_{ANN}=742 °C, but the increase compared to the as-grown sample is only ~2 %. The best FF is measured from the as-grown 5 layer sample. A small decreasing trend and increasing dispersion in I_{SC}, V_{OC} and FF values takes place when T_{ANN} is increased.

Figure 3.22 shows the spectral response measured from the as-grown and annealed (T_{ANN}=791 °C) 10-layer sample. Although the PL intensity is clearly enhanced upon annealing, there are only extremely small changes in spectral response. Minor degradation and a BS is observed for WL absorption in the annealed sample, as shown in Figure 3.22(b), but the difference in spectral response is less than 10 %.

Although the insertion of QDs results in absorption and a spectral response related to WL and QD confined energy states, the efficiency is not increased due to reduction of solar cell voltage. Thermal annealing does not seem to have a significant influence on investigated GaSb QD solar cells, although it strongly influences QD and WL PL emission. A larger amount of stacked layers should be applied in order to increase the absorption in the QD layer. The problem with increasing the number of layers is strain accumulation, which limits the amount of stacked layers in SK grown structures. Strain compensation layers can be applied to QD solar cell structures, enabling larger

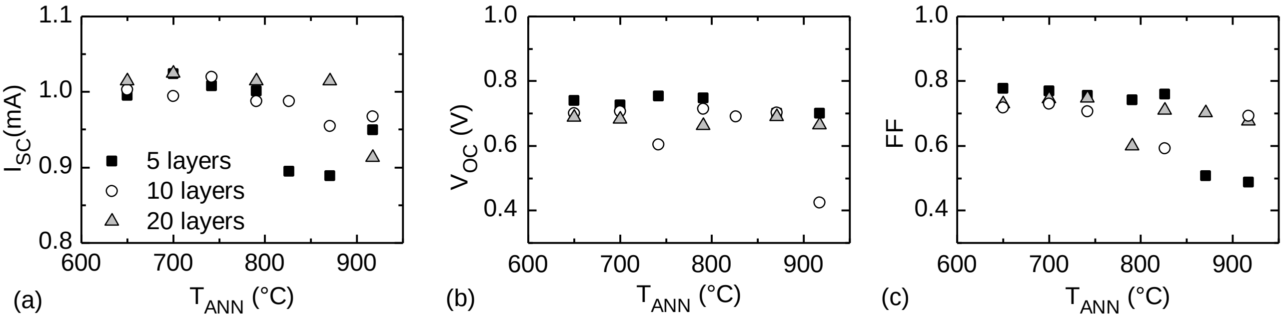

Figure 3.21 *(a) I_{SC}, (b) V_{OC}, and (c) FF as a function of T_{ANN}, measured from GaAb QD solar cells. Data points at T_{ANN}=650 °C correspond to as-grown sample.*

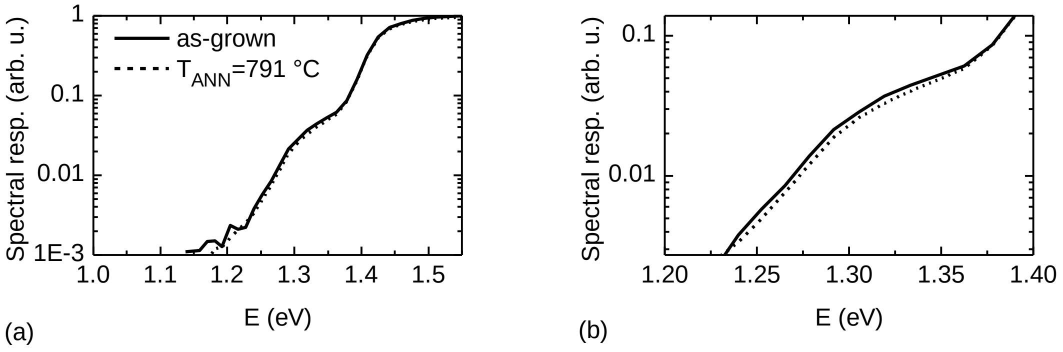

Figure 3.22 *(a) Spectral response recorded from as-grown and annealed (T_{ANN}=791 °C) sample with 10 QD layers. (b) Magnification to WL absorption showing only small changes in spectral response.*

amounts of stacked layers [160, 164-169]. Strain compensation layers would most likely influence also the annealing properties of the QD stack. Also, introducing n-doping into the inter-dot space could improve the QD photocurrent generation, due to the increased probability of transition of electrons from confined QD states to the conduction band [170]. Furthermore, in order to characterize the GaSb QD IB operation in more detail, an EQE setup described in the reference [18] should be used.

3.4 InAs quantum dots embedded in GaNAs and GaInNAs

Tensile strained layers have been successfully incorporated into stacked QD solar cell structures, preventing strain accumulation and improving the size homogeneity of the QD stack [160, 164-169]. GaNAs strain compensation layers have enabled stacking of several tens of InAs QD layers without strain accumulation or changes in QD sizes [166, 167, 169, 171, 172]. In addition, GaNAs is also used as an absorber in QW solar cells [173]. Another strain-engineering technique is strain mediation. Strain mediation layers have been used to mediate the compressively strained layers in telecommunication laser applications [174]. Thin, slightly compressively strained GaInNAs layers deposited on the InAs QD layer mediate the compressive strain caused by lattice mismatch. In solar cell structures, GaNAs and GaInNAs layers would also act as QW absorbers and provide steps for electrons and holes to thermally excite to the conduction and valence bands, respectively. In this chapter, the influence of GaNAs strain compensation and GaInNAs strain mediation layers on optical properties and charge carrier thermionic emission in InAs QD solar cells are summarized [P5].

The influence of Ga(In)NAs layers on optical properties [P5]

A set of p-i-n type solar cell samples were fabricated in which the i-regions were varied. Figure 3.23(a) shows the schematic sample structure for samples A, B, C, and D, consisting of GaAs, InAs/GaAs, InAs/GaNAs/GaAs, and GaInNAs/InAs/GaNAs/GaAs i-regions, respectively. A more detailed description of the fabrication process is given in [P5]. The amount of deposited InAs was 2 ML, resulting in coherently strained defect-free QD layers. First, the composition of the dilute nitride layers was defined by the XRD measurements presented in Figure 3.23(b). The composition of GaNAs was determined from the XRD data recorded from sample C, and using that information, the composition of GaInNAs was determined from the sample D XRD data. The compositions, band gaps, and lattice mismatch on GaAs are presented in Table IV. The XRD fringes appear to be sharper for sample D compared to sample C, indicating sharper interfaces and higher material quality.

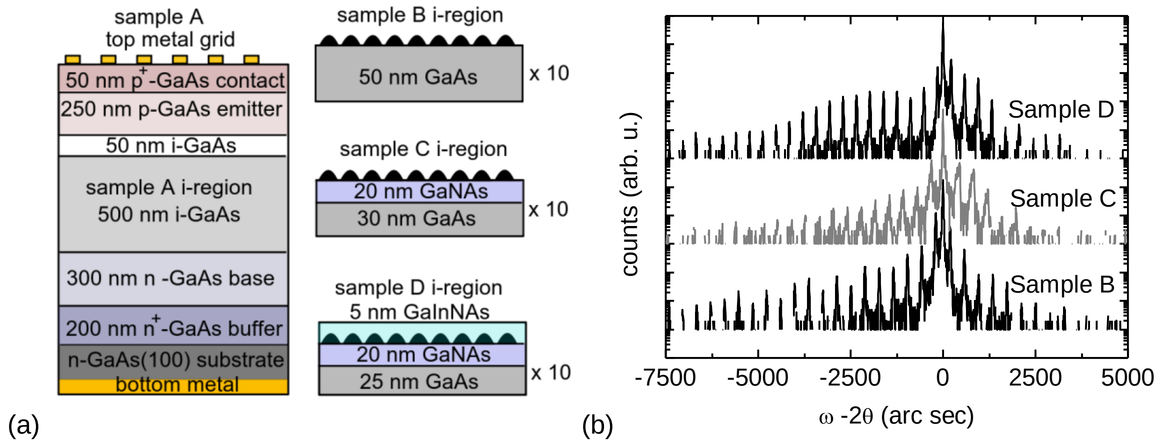

Figure 3.23 *(a) Schematic sample structure. (b) XRD rocking curves in ω-2θ geometry for samples B, C, and D.*

Table IV *Compositions, band-gaps, and lattice mismatch defined as* $(a_{GaAs}-a_{material})/a_{GaAs}$ *for investigated materials.*

Material	N-composition	In-composition	Band-gap (eV)	Lattice mismatch on GaAs (%)
GaAs	0.00	0.00	1.424	0.000
InAs	0.00	1.00	0.354	-6.686
GaNAs	0.01	0.00	1.232	0.204
GaInNAs	0.01	0.06	1.191	-0.226

Insertion of dilute nitride layers strongly influence the QD PL emission, as shown in Figure 3.24(a). Addition of GaNAs layer redshifts the QD PL emission from λ=990 nm to λ=1090 nm, and insertion of GaInNAs strain mediation layers further redshifts the PL up to λ=1250 nm. PL intensity decreases significantly when a GaNAs strain compensation layer (sample C) is added to the structure. Incorporation of N induces defects in the material [175], which can be expected to increase the nonradiative recombination rate and decrease the PL intensity. However, insertion of GaInNAs on top of the QDs (sample D), results in significantly higher PL intensity compared to sample C. Increase in PL intensity and sharper XRD fringes in sample D is evidence for improved material quality. The influence of GaNAs and GaInNAs layers on confined energy states within the QDs is illustrated schematically in Figure 3.24(b). Dilute nitride materials (which have smaller band gap than GaAs) modifies the confining potential for electrons and holes inside the QD layer, shrinking the energy difference between electron and hole states and causing a red shift in the PL spectra.

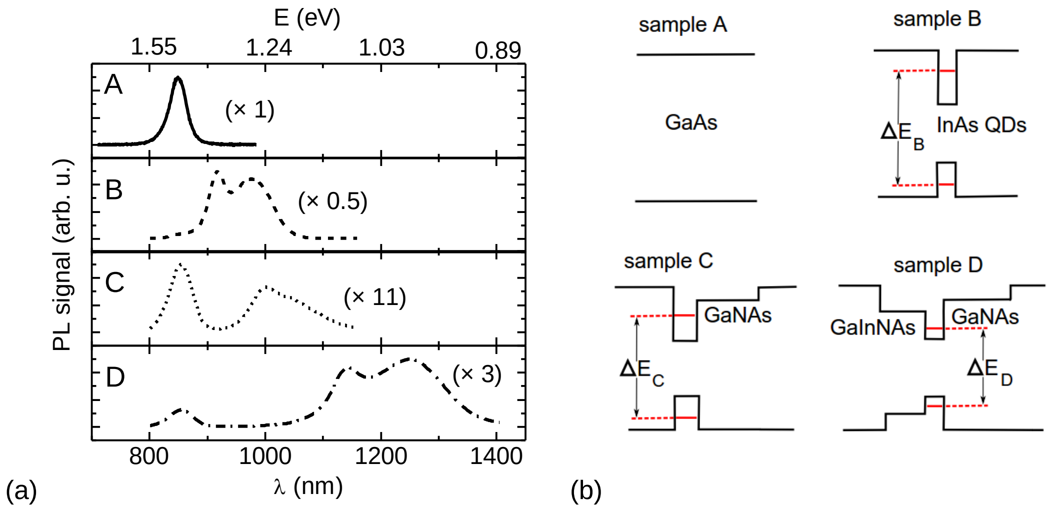

Figure 3.24 *(a) PL spectra for samples A–D, at T=293 K, showing the shift of QD PL emission to longer wavelengths. (b) Schematic image of band diagrams of samples A–D. The insertion of dilute nitride layers shifts the difference between confined electron and hole levels: $\Delta E_B > \Delta E_C > \Delta E_D$.*

The influence of dilute nitride layers on the spectral response of the p-i-n solar cells is presented in Figure 3.25. A reduction in spectral response occurs at λ<870 nm for all the samples with QD layers. The reduction becomes more pronounced when GaNAs and furthermore GaInNAs are added to the structure. This can be linked to at least three different phenomena, which are (i) N-related defects, (ii) an increase in background doping and subsequent shrinkage of the depletion region, and (iii) a reduction in the total amount of GaAs. The N incorporation not only creates deep defect levels, but it also introduces background doping to the material [P7, P8][78, 79, 176-186]. Increased background doping directly influences the width of the depletion region, and as a consequence at least part of the QD layers can be left totally outside of the depletion region. When a QD layer, embedded in GaNAs and GaInNAs, lies outside the depletion region, the charge carriers are not influenced by the electric field and the probability for nonradiative recombination at QD layer increases. When part of the i-GaAs, which can be grown at relatively high quality, is replaced with the QD and dilute nitride layers which induce potential well surrounded by N-related defects located outside the depletion region, the reduction in spectral response is inevitable. Although the spectral response decreases at short wavelengths, a clear increase in absorption and related photocurrent generation is observed at λ>900 nm. The absorption edge moves to longer wavelengths when moving from sample A to sample D. As for the PL, the addition of GaNAs and furthermore GaInNAs shifts the absorption to longer wavelengths. In sample B, the InAs QD layer related absorption occurs at λ=900–950 nm. GaNAs shifts the absorption edge up to λ=1050 nm: a broad peak in the spectral response of sample C at λ=900–1050 nm is related to the absorption to InAs and GaNAs. Addition of GaInNAs shifts the absorption edge up to λ=1200 nm. The spectral response of sample D consists of direct absorption in GaNAs, GaInNAs and the QD layer. When comparing the PL and spectral response data, one can see that the absorption related to confined QD states is very weak.

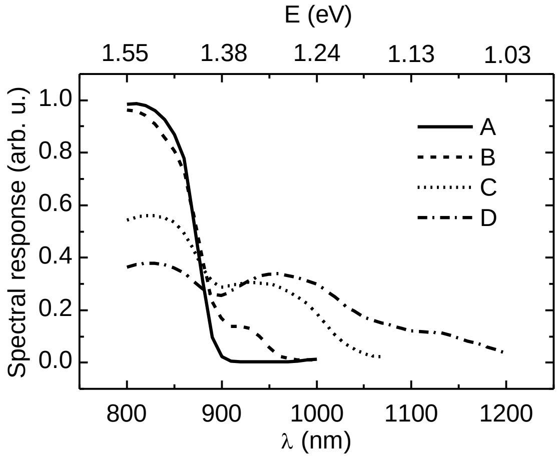

Figure 3.25 *Normalized spectral response of samples A–D showing dilute nitride and QD induced absorption at longer (>900 nm) wavelengths*.

However, the WL related absorption and consequent current generation is detectable. Absorption in GaNAs and GaInNAs QWs is much stronger. The insertion of GaNAs and GaInNAs layers seem to have positive and negative effects on the p-i-n solar cell operation. Reduction in spectral response is accompanied by increased current generation from longer wavelength photons. There is also a fundamental difference between the investigated samples: because dilute nitrides create a potential well or QW in the structure, they should be labelled “QD boosted” QW solar cells. Sample B, however, contains only InAs QD layers, and in the optimal case, such a structure could create an isolated intermediate band in the structure, generating a voltage equal to that of the GaAs reference cell, but with a higher current due to intermediate band related absorption.

The influence of Ga(In)NAs on charge carrier thermionic emission [P5]

Dilute nitride layers influence the solar cell operation also through another mechanism, which is not related, at least not directly, to extension of the absorption edge to longer wavelengths. Additionally, GaNAs and GaInNAs create steps for electrons and holes to thermally escape from the QD layer. Figure 3.26(a) illustrates schematically how electrons and holes escape from the QD layer to the GaAs conduction and valence bands, respectively. Thermionic emission of carriers can be investigated by measuring the current generation of the solar cell at different temperatures. Figure 3.26(b) shows I_{SC} as a function of T for all four samples when illuminated by a halogen lamp through a λ=900 nm long-pass filter. The current increases clearly when moving from sample A to sample D. Current generation is in agreement with the spectral response data, presented in Figure 3.25: the higher the spectral response is at λ>900 nm, the higher the current is throughout the whole temperature range. The more interesting result is that when current at T=450 K is normalized to one for all of the samples, a clear difference in relative increase in current is observed. Figure 3.26(c) shows how temperature dependence of the current, generated by the photons at λ>900 nm, de-

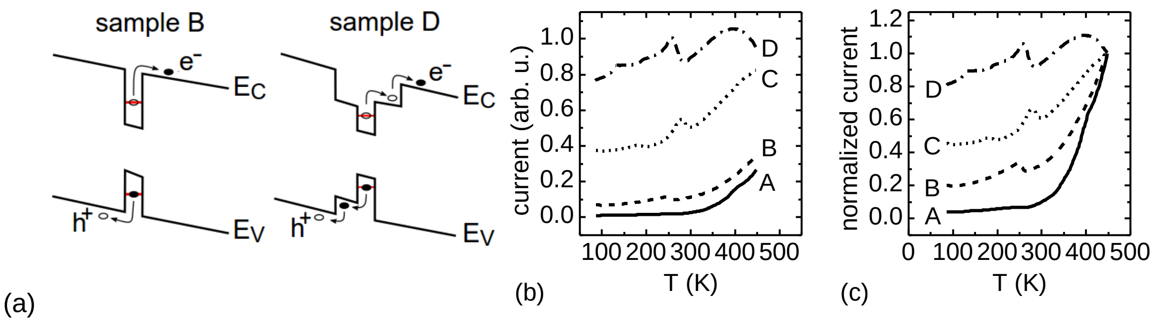

Figure 3.26 *(a) Schematic of the thermal excitation process from QD layer to GaAs conduction band in sample B and D.* I_{SC} *as a function of temperature plotted as (b) absolute value and (c) normalized at* T*=450 K. Samples are illuminated through a 900 nm long-pass filter.*

creases when moving from sample A to sample D. A small increase in I_{SC} is observed for samples C and D at T=260–280 K. This can be related to the carrier freeze out effect, where charge carriers are trapped to deep level states at a certain temperature, due to lack of thermal energy. This reduces the background doping and widens the depletion region, which can influence current generation positively.

The results show how dilute nitrides influence InAs QD solar cell operation in various ways. GaNAs and GaInNAs act as strain compensation and mediation layers for InAs QDs, shift QD layer PL emission and spectral response to longer wavelengths, provide steps for charge carriers to escape from the QD layer, and contribute to the solar cell current generation by absorbing photons for which GaAs is transparent. Such structures could be used, for example, as part of a multijunction solar cell, although the amount of stacked layers should be several times higher in order to increase the absorption. For example, a typical thickness for a GaAs solar cell is >3 µm [187], whereas the whole i-region thickness in samples A-D is only 550 nm.

3.5 Strain-free GaAs quantum dot nanostructures

Semiconductor QDs do not have to be strained like SK grown QDs or contain misfit dislocations like IMF grown QDs. Droplet epitaxy is a method where liquid droplets, consisting of a group III element such as Ga, are first deposited on the sample and then crystallized under pressure of a group V element, such as As [188-191]. This growth process does not require strain or presence of dislocations. However, droplet epitaxy requires low growth temperatures, leading to high point defect densities [192]. Another method for fabricating strain-free QDs is related to so-called local droplet etching [193-195], where group III element droplets are fabricated on the sample surface at higher temperatures compared to droplet epitaxy. Nano sized holes are formed, e.g., on AlAs surface due to As desorption underneath the deposited Ga droplets. The resulting nano holes can be filled with a lattice-matched semiconductor, such as GaAs, and strain-free QDs are created. One of the benefits of this method is that low-temperature growth is not needed, leading to lower defect densities compared to droplet epitaxy. Strain- and defect-free highly uniform QD layers which would not require strain compensation, even when multiple layers are stacked on top of each other, could be applied in high-efficiency QD solar cells or lasers. In this chapter, optical properties and the influence of thermal annealing on a strain-free GaAs/AlGaAs QD stack, fabricated by refilling of self-organized nano holes, are investigated. The results presented in the following two sections are based on [P6].

Optical properties of strain-free GaAs quantum dots [P6]

A sample with a stack of five QD layers was fabricated on semi-insulating GaAs(100) substrate. First, lattice-matched GaAs and AlGaAs layers were grown. Then, a 5 nm thick AlAs layer was grown, on which 3.2 ML of Al was deposited forming Al droplets. The sample was annealed for 180 s resulting in As desorption beneath the droplets and formation of 16 nm deep nano-holes. Cycled deposition of 0.6 nm GaAs partly filled the formed nano-holes, resulting in 8 nm high GaAs QDs with a density of about 4×10^{8} cm^{-2}. The QD layer was capped with a 20 nm thick AlGaAs layer, and a new 5 nm AlAs layer was deposited for the next QD layer. This sequence was repeated until a stack of five QD layers was grown. The whole structure was further capped with AlGaAs and GaAs layers. Additional details for the growth process can be found in [196, 197].

Figure 3.27(a) shows PL spectra of the GaAs QD sample recorded at T=8 K (closed cycle helium cryostat). The excitation power of the argon ion laser, operating at λ=488 nm, was varied from 1 to 30 W cm^{-2} and the PL signal was detected by a CCD detector. Four different QD states, labelled E_0, E_1, E_2, and E_3 become visible at higher excitation powers, whereas only the ground state related transition E_0 is visible when the lowest excitation power is used. Also GaAs WL and AlGaAs PL emission is visible at E=1.82 eV, and E=1.84 eV, respectively. A shoulder at the low energy side of the E_0 peak is related to GaAs bulk emission. The FWHM of the E_0 transition at T=8 K is only 13 meV. A similar reference sample with a single QD layer shows similar PL emission with a FWHM of 14 meV for the E_0 transition at T=8 K. This indicates that the stacking does not influence the individual QD layers, and several layers can be stacked without degradation in QD optical properties.

PL emission at various temperatures is plotted in Figure 3.27(b). The PL intensity increases with decreasing temperature and emission shifts to higher energies. Figure 3.28(a) shows the integrated PL intensity of the E_0 transition plotted against the inverse of T. A single exponential equation (equation (2-1)) was fitted to the data, giving thermal activation energy of 412 meV for nonradiative recombination. This energy describes the thermal energy required for charge carriers to escape from the QDs, and the energy is higher than the confining potential for electrons and holes. Therefore, it cannot be linked solely to the energy barrier to the energy barrier created by AlGaAs or AlAs layers, and some other effect must influence the thermal activation energy for nonradiative recombination.

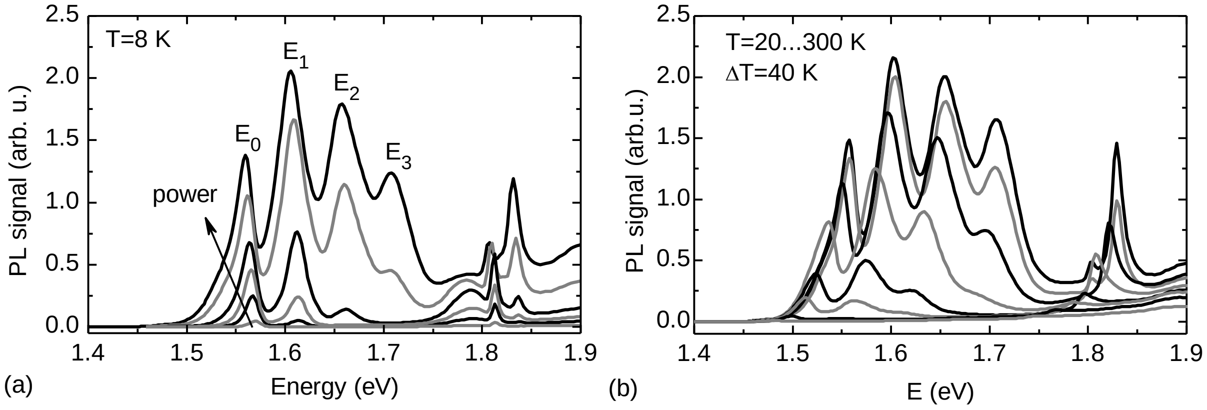

Figure 3.27 *(a) Power-dependent PL spectra of GaAs QDs at T=8 K. The excitation power is varied from 1 to 30 W cm^{-2} (b) PL spectra measured at various temperatures. Excitation power is 30 W cm^{-2}. Decreasing T increases the PL intensity.*

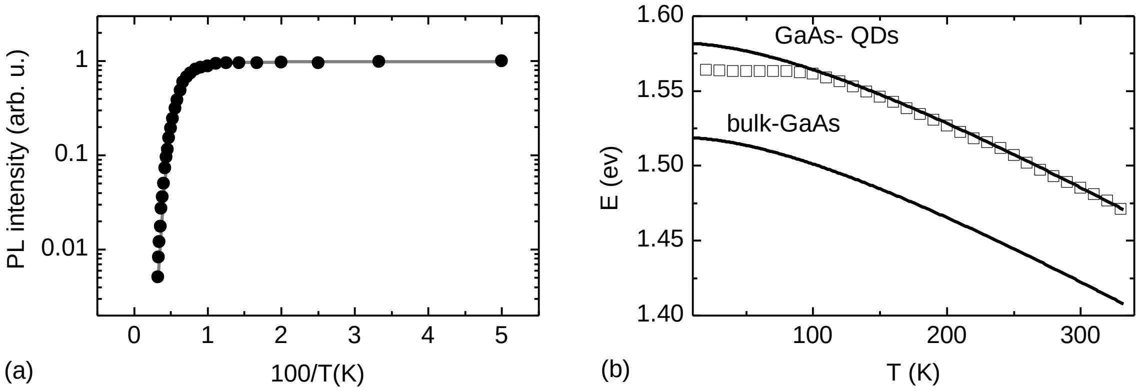

Figure 3.28 *Temperature dependence of (a) PL intensity and (b) PL peak position of the E_0 transition using an excitation power of 30 W cm^{-2}. The straight line in (a) is the single exponential fit to the experimental data. The empirical Varshni relation is fitted to the data points in (b). Additionally, the temperature dependence of the bulk GaAs band gap energy is plotted in (b).*

Figure 3.28(b) shows how the PL peak of the E_0 transition shifts as a function of T. A BS of 93 meV occurs when the temperature is decreased from 300 K to 8 K. The empirical Varshni relation (equation (2-2)) for bulk GaAs calculated with the parameters $E(0)$=1.58 eV, α=5.41×10^{-4} eV K^{-1} and β=204 K [198], is plotted in the Figure. The Varshni relation is also fitted to the empirical data with the same parameters α and β as for bulk GaAs, but with $E(0)$=1.52 eV. The measurements follows the GaAs Varshni relation when T>110 K with a constant shift in the energy. This kind of behavior can be expected if (i) carrier hopping between the QDs is absent or (ii) the variations in the QD properties are very small. For example, a significantly higher energy shift, compared to temperature dependent bandgap variations, is observed in InAs/GaAs QD PL emission, and is related to the hopping of charge carriers between the QDs [199]. It is apparent that hopping between the QDs is present also here, and the reason for the well-behaved temperature dependence of the emitted photon energy is due to is due to the uniform size of the QDs with close to equal energy levels. At lower temperatures (T<100 K) the E_0 peak position is constant, which can be explained, at least partly, by the strong exciton localization effects in the QDs lowering the emitted photon energy [200, 201]. Excitons are released at T≈110 K, corresponding to ~9.5 meV thermal energy, whereas the energy difference between the Varshni relation and the linearly extrapolated data at T=0 K is ~14 meV.

PL measurements show that high-quality GaAs/AlGaAs QDs can be fabricated by refilling LDE-grown nano holes. Stacking of the QDs up to 5 layers does not lead to degradation of optical quality, because the whole structure is lattice-matched and strain accumulation is not present. This is a promising result for fabrication of GaAs/AlGaAs QD solar cells. One parameter to be optimized is the QD density, which is low for the sample investigated here. Several LDE steps could be applied to increase the nano hole and consequently the QD density.

Influence of thermal annealing [P6]

Thermal annealing was performed on the stacked GaAs QD sample. The sample was capped by a 120 nm thick SiO_2 layer grown by PECVD, and the surface was not treated with any chemical before capping. Thermal annealing was performed in an N_2 environment on a Si wafer for 2×2 mm^2 cleaved sample pieces. Figure 3.29 shows normalized PL spectra recorded from samples annealed at different T_{ANN} for t_{ANN}=30 s. The PL peak shape remained fairly constant until T_{ANN} >1000 °C was applied. This is an implication of extremely high thermal stability. Higher annealing temperatures could not be used because the SiO_2 capping layer was destroyed.

More accurate data collected from annealed samples are presented in Figure 3.30. Two annealing tests were done where t_{ANN} was constant and T_{ANN} was varied, and vice versa. Figure 3.30(a) shows PL intensity and BS, related to the E_0 transition, as a function of T_{ANN} when t_{ANN} was fixed at 30 s. Material diffusion induced BS does not occur until extremely high annealing temperatures are applied, and even then the BS is fairly small. Totally different results have been published for GaAs QDs fabricated by droplet epitaxy, where a clear BS occurs already at low annealing temperatures [202, 203]. This confirms that the material diffusion is to a large degree defect assisted, and the defect density of the GaAs QDs investigated here is very low. Interestingly, the PL intensity stays relatively constant, until a clear increase occurs at the same temperatures where the BS starts. This can be just coincidence, and a high annealing temperature is required to remove remaining defects in the QD layer, or alternatively the increase in PL intensity is directly related to the material diffusion. Figure 3.30(b) shows PL intensity and BS, related to the E_0 transition, as a function of cumulative annealing time at T_{ANN}=970 °C. The PL peak remains at the same energy/wavelength until t_{ANN}>50 s is applied, after which BS occurs. The intensity of the PL emission, however, improves almost constantly when t_{ANN} is increased, indicating that the detectable material diffusion is not mandatory for PL improvement. Figure 3.30(b) proves also, that the temperature limit for the material diffusion and consequent BS is exceeded at T_{ANN}=970 °C, but diffusion does not occur

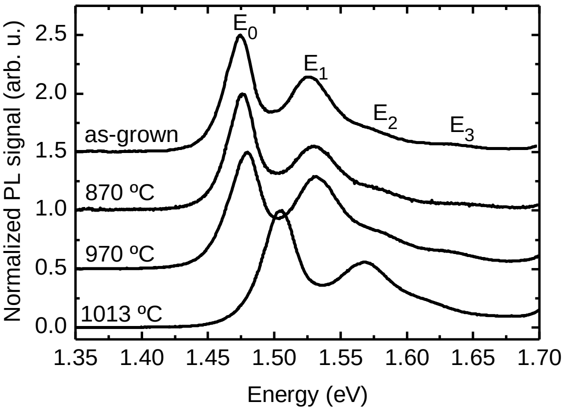

Figure 3.29 *Room temperature PL spectra of samples annealed with* t_{ANN}*=30 s at* T_{ANN}*=870 °C, 970 °C, and 1013 °C. The PL spectra are normalized to one.*

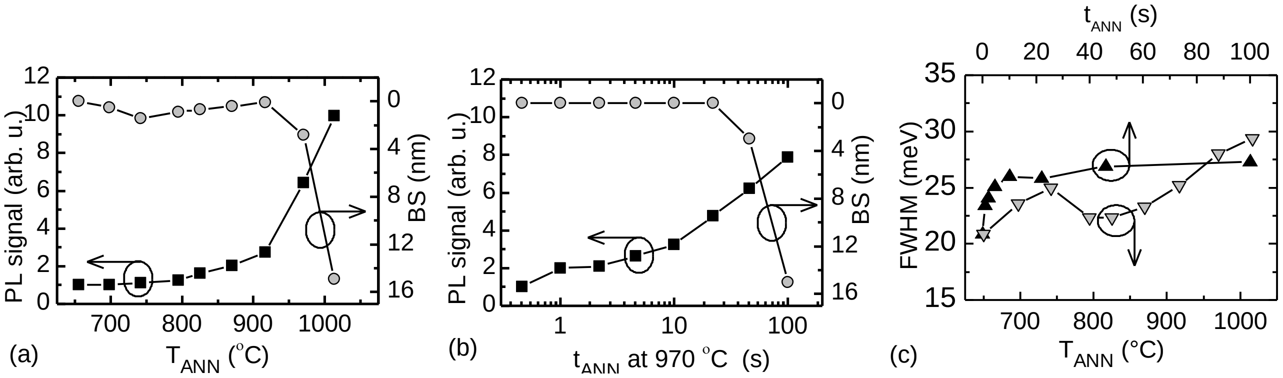

Figure 3.30 *PL intensity and BS of PL plotted versus (a)* T_{ann} *(*t_{ANN}*=30 s) and (b) versus* t_{ann} *(*T_{ANN}*=970 °C). (c) FWHM as a function of* T_{ANN} *and* t_{ANN} *when* t_{ANN}*=30 s and* T_{ANN}*=970 °C, respectively. The point at* T_{ANN}*=650 °C refers to as-grown sample.*

immediately. Most likely point defects, such as vacancies formed at the GaAs/SiO_2 interface during annealing [81], diffuse to the QD layer and catalyze material diffusion. Therefore, the BS does not start until the vacancies have diffused to the QD layer, and at T_{ANN}=970 °C the required time is ~50 s.

Figure 3.30(c) shows the FWHM of the E_0 transition related PL peak at T=300 K when T_{ANN} and t_{ANN} are varied. The changes in the FWHM are more consistent when t_{ANN} is varied, because the same sample is measured at the same spot after each annealing step, and the data do not contain any spatial variations over the wafer, to which the FWHM value is sensitive. The FWHM value is found to increase upon annealing. The increase saturates after t_{ANN}≈10 s when T_{ANN}=970 °C is applied. An annealing induced process is occurring in the QD layer within the first 10 s of annealing, which widens the E_0 transition PL peak but does not induce BS. Increasing T_{ANN} also increases the FWHM, but the behavior is not clear because a local minimum of the FWHM is present at T_{ANN}≈800–850 °C. The reason for this behavior could be changes between the samples due to spatial variations or different temperature dependent mechanisms, some of which causing an increase and some a decrease in the FWHM.

Thermal annealing tests showed that GaAs QDs, fabricated by refilling self-organized nano holes obtained by LDE, can be very temperature stable, contain a low density of defects, and do not undergo significant material diffusion even at high T_{ANN}. However, thermal annealing can improve the PL emission, and a BS occurs if extremely high annealing temperatures are applied. The annealing behavior could also be different if the sample surface were treated with, for example, NH_4OH as described in section 3.1. Also GaAs proximity capping could lead to different annealing behavior, but in general, the material was found to be extremely stable upon annealing.

3.6 Lattice matched dilute nitride materials for multijunction solar cells

Dilute nitrides, lattice matched to GaAs or Ge, are rapidly emerging as a practical approach for significantly increasing the efficiency of III-V multijunction solar cells for terrestrial concentrators as well as space applications. Dilute nitrides can be grown lattice matched on GaAs or Ge with a band gap energy ranging from 1.42 eV to 0.8 eV [32]. Therefore, using optimized material they could enable monolithic integration of 4 to 6 junctions, ultimately enabling over 50 % conversion efficiency under concentrated illumination [41, 42]. However, the fabrication of dilute nitrides is not straightforward. Nitrogen is a relatively small as well as reactive atom which has a tendency to generate defects, degrading the GaInNAs solar cell performance [175, 204]. A radio frequency plasma source is typically used to crack N_2 molecules to nitrogen atoms before incorporation into the crystal. So-called deflector plates which generate a static electric field perpendicular to the material flux can be used to deflect part of the remaining ions, and the use of deflector plates is found to improve the device performance [184, 205]. Also the relatively low optimal T_{GR} of dilute nitrides compared to InGaAs causes unwanted point defects [206], as observed also in low temperature grown GaAs [207].

Thermal annealing is found to be an effective way to improve dilute nitride material quality, which is observed as an increase in quantum well PL emission [74, 75], improved laser operation [76, 77], and higher solar cell performance [78, 79]. Because of the relatively high defect densities and low carrier diffusion lengths, p-i-n type junctions are typically applied in dilute nitride solar cells. The benefit of the p-i-n design, compared to a p-n junction, is the wider depletion region due to the i-region. However, unintentional background doping levels in the range of N_S=6×10^{15}-1×10^{17} cm^{-3} or even higher are measured from dilute nitride materials, limiting the depletion region width, especially when the band gap is on the order of 1 eV or lower [176, 184]. In order to achieve high-quality dilute nitride material with low defect densities and background doping levels, detailed information about the defects in this material is essential. In this chapter, studies on defects formed in dilute nitride p-i-n solar cells are presented. Furthermore, the influence of fabrication parameters on defect formation and solar cell performance are summarized.

Defects in dilute nitride solar cells [P7]

Defects in three types of dilute nitride p-i-n diodes were investigated [P7]. The p-i-n structures were deposited on p-GaAs substrate. After the growth of an n-type GaAs buffer layer, GaInP BSF and GaAs collector, an unintentionally dilute nitride layer was deposited at T_{GR}=420 °C. Samples S1, S2, and S3 had i-regions consisting of $GaIn_{0.11}N_{0.04}As$, $GaN_{0.025}AsSb_{0.06}$, and $GaIn_{0.05}N_{0.03}AsSb_{0.03}$, respectively. All the dilute nitride materials had a 1 eV band gap energy and were lattice matched to GaAs. The intrinsic regions were capped with an n-GaAs emitter, n-AlInP window layer, and n-GaAs contact layer, resulting in a p-i-n structure. The doping density for emitter and collector was set to 1×10^{18} cm^{-3}, and 5×10^{18} cm^{-3}, respectively. Round mesa structures with a diameter of 800 µm were processed for DLTS and CV measurements. Bottom and top Ohmic metal contacts consisting of Ti/Au and Ni/Au layers, respectively, were fabricated by e-beam metallization equipment. Figure 3.31 shows the schematic sample structure.

First, the background doping density N_S was determined from the CV measurements, performed with 1 MHz frequency and 100 mV amplitude. Figure 3.32(a) shows the recorded CV curves in the range from 0 V to -4 V. Figure 3.32(b) shows corresponding Mott-Schottky plots: a straight lines corresponding to constant N_S at the probed area. Figure 3.32(c) shows the calculated N_S profiles. Here, the depth means the width of the depletion region inside the i-region. Background doping levels of 3.7×10^{16} cm^{-3}, 5.4×10^{15} cm^{-3}, and 2.7×10^{15} cm^{-3} were determined for samples S1, S2, and S3, respectively. Background doping was confirmed to be p-type, based on results obtained from separate Hall samples and the EQE behavior. P-type background doping is beneficial when p-type

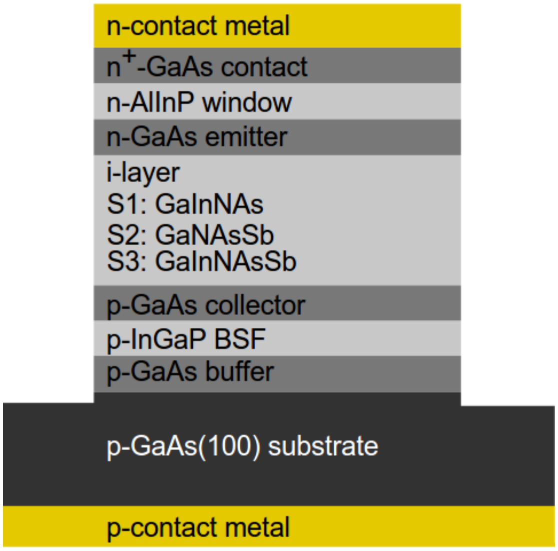

Figure 3.31 *Schematic sample structure. Only the composition of the 1 eV band gap i-region is varied between S1, S2, and S3.*

substrates are used, because then the depletion region forms at the top part of the junction where light enters the material. More photons are then absorbed at the depletion region and the probability for nonradiative recombination is lower. In addition, the diffusion length for electrons is longer than for holes, making p-type material favorable. The results show that the incorporation of Sb suppresses N_S, resulting in a wider depletion region, which is indeed a positive effect. Antimony was reported to reduce N_S also earlier by Jackrell *et al* [184]. However, in that study the background doping was n-type, whereas in the samples investigated here it is p-type. Since Sb incorporation is found to reduce N_S in n-type and p-type dilute nitride material, the possibility of a compensation effect is ruled out. It is more likely that the incorporation of Sb improves the crystal quality and prevents the formation of such defects that contribute to N_S. Sb also acts as a surfactant, helping elements to be incorporated into the right lattice sites, as suggested by several earlier reports [208-212]. It is also proposed that Sb could inhibit impurity incorporation [184].

The doping profile of sample A is not uniform: a local depletion is observed at a depth of ~200 nm. This can be related to a local defect population near the GaAs-GaInNAs interface, causing charge depletion. N_S also decreases linearly after a depth of 600 nm, which is due to increased leakage current during the measurement and does not represent real changes in the background doping. A remarkable increase in N_S is observed at a depth of ~1750 nm for samples S2, and S2. Because N_S is significantly lower for these samples, the depletion region edge reaches the highly doped collector layer at higher reverse bias values, which is seen as an increase in the free carrier depth profile. An estimated value of ε_r=12.1 was applied in calculations, based on previous results where the simulations were compared to measured solar cell parameters. Since the calculated i-region thickness is the same for both samples S2 and S3 (depletion region reaches the highle doped GaAs layer at the same depth) when the same ε_r value is used in calculations, it this proves that the actual ε_r value must be close to identical for both samples.

Next, DLTFS measurements were performed utilizing an N_2 cryostat. Figure 3.33(a) shows the DLTFS spectra in the temperature range of 80-430 K, recorded with the measurement parameters V_R=-2 V, V_P=0 V, t_P=100 ms, and T_W=200 ms. For S1, a larger reverse bias of -4 V, was used be-

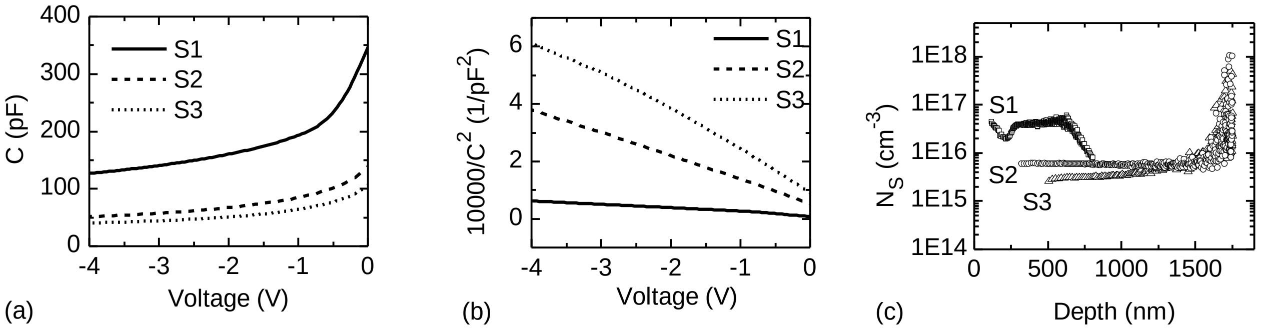

Figure 3.32 *(a) CV curves and (b) 1/C^2 vs voltage curves for samples A, B, and C.*

cause the probed volume would otherwise be significantly smaller due to higher background doping. Four different peaks, labelled T1, T2, T3, and T4 can be identified in the spectra. The DLTFS spectra are related to the emission of majority carriers (holes) from the trap states to the valence band. Since there is a large difference between the N_S values of the samples, the heights of the DLTFS spectra cannot be directly compared in order to draw conclusions about the trap densities. The inset in Figure 3.33(a) shows normalized DLTFS spectra, showing that the widths of the DLTFS spectra increase when moving from S1 to S3. When the material consists of several elements, a certain defect can appear at different energies depending on the nearest (or next nearest) neighbor environment. Therefore, it is logical that sample S3 exhibits the widest spectrum because its i-region consists of five different elements, whereas samples S1 and S2 have only four elements in their i-regions. Figure 3.33(b) shows Arrhenius plots for each DLTFS peak, and the corresponding trap parameters are collected in Table V.

An exact identification of the observed deep hole traps is not possible on the basis of these measurements. Several deep levels with different thermal activation energies have been observed in dilute nitride materials [179-182, 184, 213]. The possibilities for different material orientations are high in these quaternary and quinary compounds, and therefore one type of point defect, e.g., vacancy, antisite or Interstitial, can occur at different energies depending on the surrounding atom

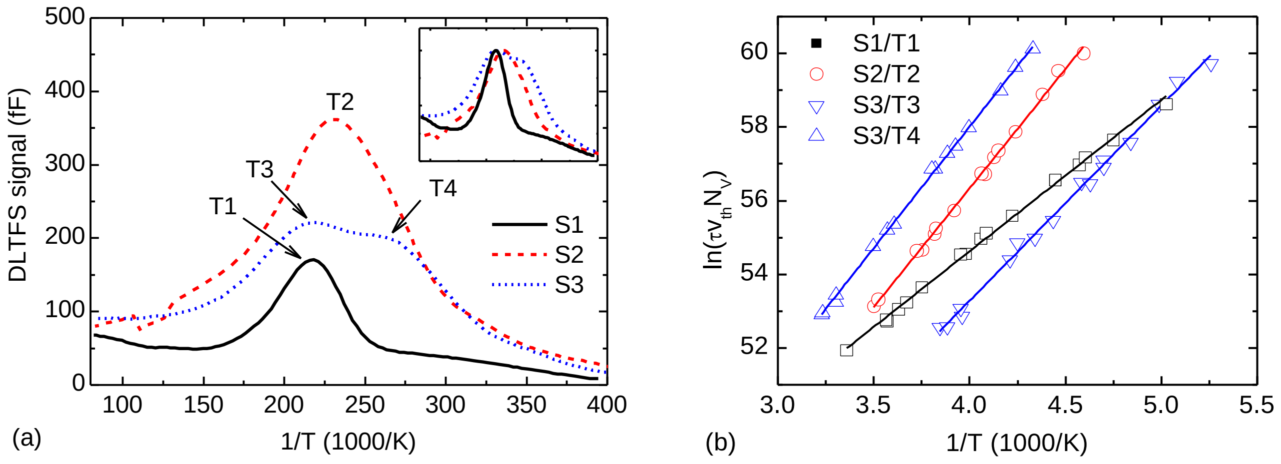

Figure 3.33 *(a) DLTS spectra recorded from samples S1, S2, and S3. Inset in upper right corner shows normalized DLTFS spectra. (b) Arrhenius evaluations for all labelled traps.*

Table V *Trap parameters obtained from Arrhenius evaluation.*

trap	N_T (cm^{-3})	E_A (meV)	σ (cm^2)
T1	2.3×10^{14}	350	2.0×10^{-17}
T2	2.3×10^{14}	560	5.6×10^{-14}
T3	9.0×10^{13}	470	2.4×10^{-14}
T4	8.3×10^{13}	570	1.9×10^{-14}

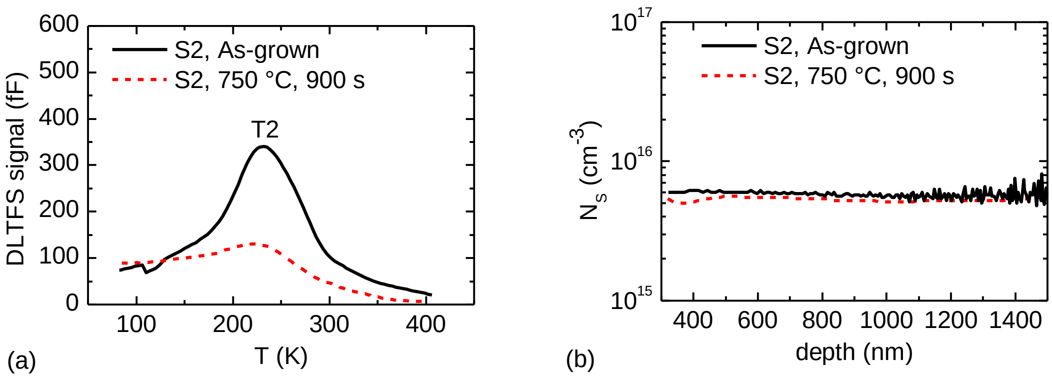

Figure 3.34 (a) *DLTFS spectra and (b) background doping profile, recorded from as-grown and annealed (T_{ANN}=750 °C, t_{ANN}=900 s) solar cell S2.*

configurations, partly explaining the broad DLTFS spectra. However, the main reason behind broad DLTFS spectra and related defects is considered to be nitrogen incorporation and low growth temperature related defects. Capture cross sections for trap states are found to be larger for samples with Sb. Also, the thermal activation energy for the main trap located at T≈230 K is smaller for S1. Incorporation of Sb clearly influences the trap energies as well as capture cross sections. A significant difference in trap densities is not observed between the samples: the lowest values are recorded from S3, but it in turn also shows the broadest DLTFS spectrum.

Since the DLTFS spectra are broad and surprisingly similar to those recorded from relaxed InAs QDs, it is reasonable to question if the DLTFS signal is originating from dislocations or extended defects. The shape of the DLTFS spectra remained the same for all traps when filling pulse duration was varied. Furthermore, when the DLTFS signal was plotted for each trap state as a function of ln(t_P), a saturation effect is observed at t_P≈100 ms, indicating that not all the observed traps are related to extended defect or dislocations [118]. Furthermore, since the DLTFS peak maximum does not move when t_P is increased, the defects can be labelled as localized rather than band-like.

Thermal annealing test was done for sample S2, which was annealed on a Si wafer, in an N_2 atmosphere, and under a GaAs proximity cap at T_{ANN}=750 °C for t_{ANN}=900 s. The DLTFS spectra recorded from as-grown and annealed S2 are presented in Figure 3.34(a). Thermal annealing clearly reduces the DLTFS signal at T>120 K. Furthermore, a minor decrease (<10 %) in the background doping was observed (Figure 3.34 (b)), but based on one experiment one cannot conclude if the change is mainly due to annealing or spatial variation. Thermal annealing is indeed expected to remove defects and improve the material properties, which is evident also in this case. Thermal annealing can also influence the crystal structure. For example, columnar chain-like nitrogen ordering is observed in as-grown dilute nitride materials, and thermal annealing is found to change the close range ordering of atoms towards an In-N bonding configuration in GaInNAs [79, 214-216]. However, since the DLTFS signal is point defect related, one can except that the decreased DLTDS signal is due to a reduction of point defects. More annealing tests with various T_{ANN} and t_{ANN} should be performed to find the optimal annealing conditions for each sample.

Although all the samples showed a broad DLTFS spectrum with a maximum at T≈230 K, clear differences in background doping densities and defect parameters were observed depending on the material composition. Positive and negative effects were observed for Sb incorporation: reduction of N_S is clearly beneficial, but increased trap capture cross section is unfavorable. The fabrication parameters, such as T_{GR} and material fluxes, should be optimized for each material separately in order to make a justified comparison regarding which of the materials would be the most suitable for solar cell applications. Also the optimal thermal annealing parameters may differ between the samples, but in general thermal annealing can significantly influence the defect densities and more importantly, directly to the solar cell power generation.

The influence of material fluxes on defect formation [P8]

Several fabrication parameters influence dilute nitride material quality considerably. Changes in T_{GR}, plasma parameters, or material fluxes are known to influence the material structural, optical and electrical properties [29, 217, 218]. One critical parameter is the ratio between the material fluxes of group V and group III elements [219]. Therefore, the influence of the BEP ratio between As and group III elements on a 1 eV band gap GaInNAs solar cell was investigated. The schematic sample structure is similar to that presented in Figure 3.31. The sample structure as well as fabrication parameters are identical to those for sample S1 in the previous section, the only difference being the varied As/III BEP ratio during the fabrication of the GaInNAs layer. Three samples labelled S4, S5, and S6 were fabricated with As/III BEP ratios of 6, 7, and 9, respectively.

Figure 3.35(a) and (b) shows the measured CV characteristics and calculated N_S profiles, respectively. A clear dependence on As/III BEP ratio and N_S is observed: by decreasing the As/III BEP ratio from 9 to 7 and furthermore to 6 results in N_S values of 8.3×10^{16} cm^{-3}, 4.6×10^{16} cm^{-3}, and 2.2×10^{16} cm^{-3}, respectively. The background doping was determined to be p-type for all of the samples. The leakage current prevented measurement of the CV curves of S4, and S5 up to -20.4 V, which is the highest reverse bias value the measurement system can provide. Again, interface defect related local depletion of the charge carriers is apparently observed, as for S1 in the previous section.

The cause of the p-type background doping must be defects. Gallium vacancies (V_{Ga}) associated with N, resulting in N-V_{Ga} complexes are reported to act as acceptors in dilute nitride materials, and furthermore N-V_{Ga} complexes have lower formation energies compared to V_{Ga} [220]. The presence of hydrogen further lowers the defect formation energy, resulting in H-N-V_{Ga} complexes, which together with C doping, has been the cause of high p-type background doping in MOCVD grown GaInNAs [220]. Interestingly, it was reported that V_{Ga} are the dominant acceptors in low temperature.

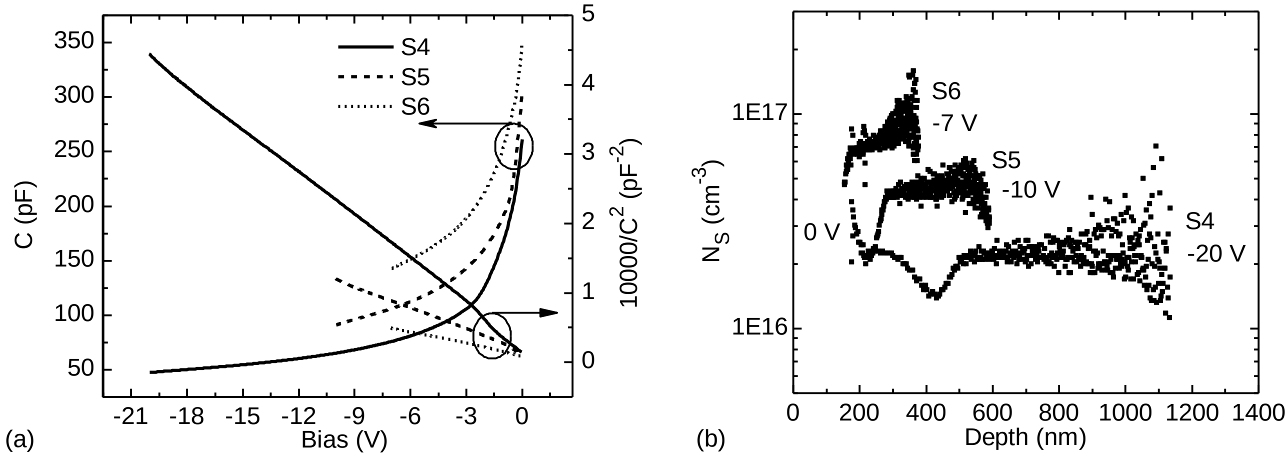

Figure 3.35 *(a) Capacitance-voltage characteristics and (b) calculated background doping profiles for investigated samples. Background doping increases together with arsenic pressure.*

MBE grown GaAs, and that the density of V_{Ga} increases with the V/III BEP ratio [221-223]. This would agree with another result showing that the formation energy of V_{Ga} in GaAs decreases when As pressure is increased, and furthermore that V_{Ga} density increases when growth temperature decreases [224]. Based on the results presented here and previous findings, the cause for the measured p-type doping in S1-S6 is suggested to be related to V_{Ga} and N-V_{Ga} complexes.

Next, DLTFS spectra were recorded utilizing a helium cryostat. Figure 3.36(a) shows the DLTFS spectra in the temperature range of 35-405 K, recorded with the measurement parameters of V_{R}=-3 V, V_{P}=-1 V, t_{P}=100 ms, and T_{W}=20 ms. Three DLTFS peaks, labelled T5, T6, and T7 are visible. Since Ns differ between the samples, the heights of the DLTFS signals cannot be directly compared. Arrhenius evaluation for each peak is presented in [P8]. Table VI shows the corresponding trap parameters. T5 parameters could not be evaluated for samples S5 and S6 due to carrier freeze-out effects at low temperatures. Furthermore, the error margins for the T6 capture cross section were large, and therefore σ could not be evaluated for that trap. Figure 3.36(b) shows measured and simulated DLTFS spectra for sample S4. Trap parameters from Table VI were used in simulations. The actual DLTFS peaks are much broader than the simulated peaks, indicating that the extracted trap values present an average value for each trap population.

Several studies have revealed deep hole levels in MOCVD or MBE grown GaInNAs materials with thermal activation energies ranging from 100 meV to 530 meV [179-182, 184, 213, 225]. For example, a similar type of DLTS spectrum has been recorded for p-type MOCVD grown GaInNAs with a 1.05 eV band gap, indicating, that the defect formation is an intrinsic feature for this material [179]. The common feature in all dilute nitride studies is that a broad DLT(F)S signal is detected over a wide temperature range, and that defect formation is concluded to be largely related to N incorporation and low growth temperature.

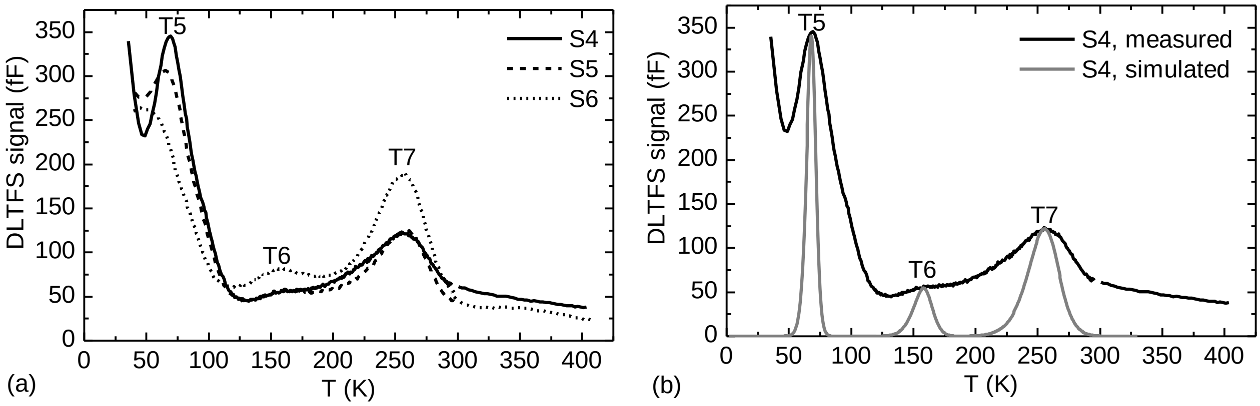

Figure 3.36 (a) DLTS spectra recorded from investigated samples. Three different peaks, labelled T5, T6, and T7 are observed. (b) Measured and simulated DLTS spectra for S4.

Table VI N_T, E_A, and σ for T5, T6, and T7 determined by Arrhenius evaluation of DLTFS data.

Trap	N_T (cm^{-3})	E_A (meV)	σ (cm^2)
T5	S4: 2.7×10^{14} S5: not eval. S6: not eval.	100-110	2.0×10^{-15}
T6	S4: 3.1×10^{13} S5: 4.9×10^{13} S6: 9.3×10^{13}	250-360	not eval.
T7	S4: 6.4×10^{13} S5: 1.1×10^{14} S6: 2.1×10^{14}	450-485	$1.1\text{-}3.2\times10^{-15}$

The position of T5 moves towards lower T when the As/III BEP ratio is increased. Since the electric field of the pn-junction increases together with background doping density, it could be possible that the position of T5 depends on the electric field strength inside the p-n junction. The electric field dependence of the hole emission rate from T5 was studied by varying V_R to adjust the electric field strength. No shift in the peak position was observed, which suggests that the activation energy of T5 is not sensitive to electric field, and apparently E_A of T5 depends on the As/III BEP ratio.

Also PL spectroscopy and dark IV measurements were used to characterize the S4, S5, and S6. PL intensity, FWHM and dark saturation current density J_0, correlating with Shockley-Read-Hall recombination, were measured. Figure 3.37 shows all measured parameters as a function of As/III BEP ratio. Interestingly PL intensity, J_0, N_S, T6 density N_{T6}, and T7 density N_{T7} show a linear dependence on the As/III BEP ratio. PL intensity decreased while all other parameters increased linearly with increasing As/III BEP ratio. Also the FWHM value increases, but not linearly. All the measured parameters indicate that the defect density increases (even linearly) together with the As/III BEP ratio over the investigated range. The data show that by changing the relative material fluxes one can directly influence several critical material parameters, which again has a direct influence on solar cell performance. Since the best results are obtained from the sample grown with the lowest As/III BEP ratio, an even lower ratio was tested. However, lowering the As/III BEP ratio to 5 resulted in appreciable degradation of crystal quality. In terms of the As/III BEP ratio, the highest quality GaInNAs is achieved under conditions where a high enough but not too high As flux is applied. This condition can be assumed to be near the stoichiometric limit for As deposition for GaInNAs fabrication under the used conditions.

The nature of the detected defects was investigated by isothermal DLTFS measurements where t_P was varied when the DLTFS signal was measured for each DLTFS peak. Figure 3.38 shows DLTFS signal plotted against ln(t_P). While the T6 and T7 related DLTFS signals saturate at t_P <100 ms, the T5 related signal shows no sign of saturation even when t_P=10 s is applied. Therefore, it can be concluded that T6 and T7 originate from point defects, whereas T5 is related to dislocations or extended defects. Since the material is lattice-matched, T5 is most likely due to extended defects. The shape of the DLTFS spectrum does not change when t_P is varied, indicating that T5 related traps are localized rather than band-like.

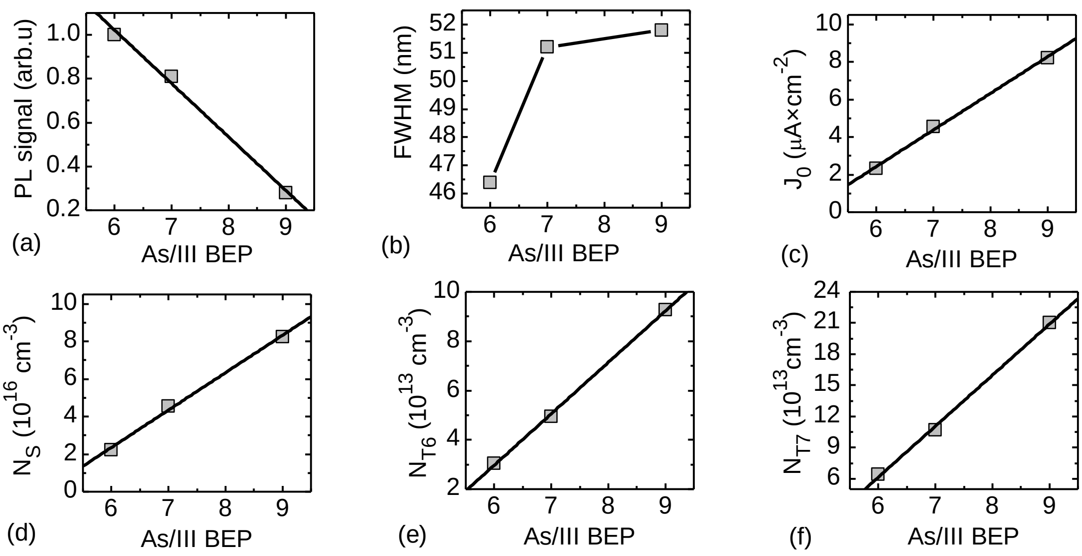

Figure 3.37 *(a) PL intensity, (b) PL FWHM, (c) J_0, (d) N_S, (e) N_{T6}, and (f) N_{T7} as a function of V/III BEP ratio.*

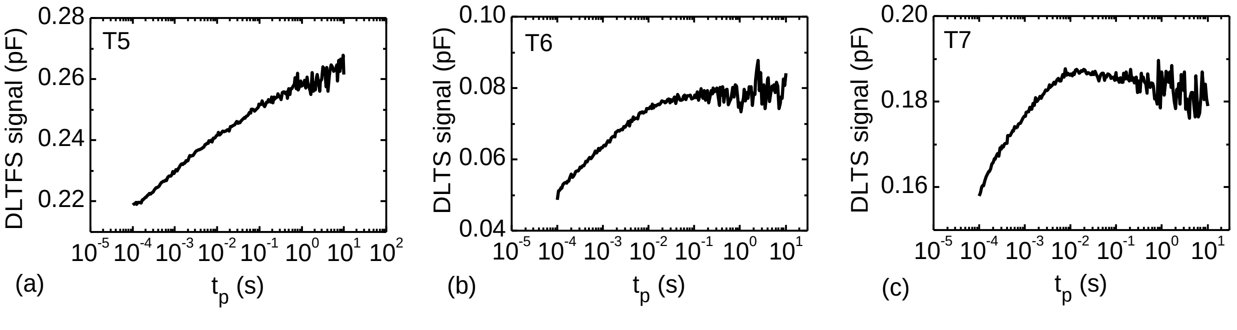

Figure 3.38 *Isothermal measurements for sample F (a) T5, (b) T6, and (c) T7, when t_P is varied. An almost linear increase is measured for T5 whereas saturation at t_P<100 ms occurs for T6 and T7.*

The presented DLTFS measurements probe only majority carriers. A positive filling pulse is required to inject also minority carriers into the depletion region. DLTFS spectra were recorded also at different positive filling pulse voltages, and the data are shown in [P8]. The negative signal is related to electron (minority carrier) emission to the conduction band. The minority carrier signal increases when higher positive voltages are applied, because more current and therefore more electrons flow through the junction and are trapped at defect states. Unfortunately, an evaluation for minority carrier traps is not possible because of the overlapping majority carrier signal. The majority carrier signal is itself also influenced by the positive filling pulse, and therefore the measured data cannot be separated into majority and minority carrier spectra. The most clear difference between the samples is seen at T<150 K, where the negative DLTFS spectra increase with As/III BEP ratio Apparently higher BEP ratios are responsible for the introduction of shallower traps in particular to the material.

A considerable influence on defect formation is observed when the As/III BEP ratio is varied. Even small changes in material fluxes cause significant changes in defect densities and background doping levels. The linear dependence between As/III BEP and various defect-related parameters shows how extra As atoms are directly responsible for defect formation. Since the measured defect population appears to be the same for all the samples and only the amount of defects changes, this opens an opportunity to investigate how the density of these defects influences solar cell operation.

The influence of defects on dilute nitride solar cell performance [P7, P8]

Since the As/III BEP ratio has a clear and even linear dependence on defect formation, it should influence also solar cell performance. Therefore, a solar cell process was devised for S4, S5, and S6. After deposition of Ni/As and Ti/Au top and bottom contacts and selective contact GaAs etching, a TiO_2/SiO_2 antireflection coating was fabricated by e-beam evaporation. The processed 4×4 mm^2 solar cells' LIV were measured under AM1.5G simulation and the data is presented in Figure 3.39(a). A clear increase in solar cell current density (J) and voltage is observed together with decreasing As/III BEP ratio. EQE measurements, presented in Figure 3.39(b), show the same effect: the highest (lowest) EQE at the wavelength scale of λ=800–1350 nm is recorded from S4 (S6) grown with the lowest (highest) As/III BEP ratio. QE data shows that the absorption edge moves slightly to shorter λ when moving from S4 to S6. This indicates that S4 has the smallest E_G, although the differences are not significant. When the As/III BEP ratio is increased, the competition between group V elements As and N limits the N incorporation which is seen as increased E_G. This phenomenon is observed also in dilute nitride QW structures [226-228].

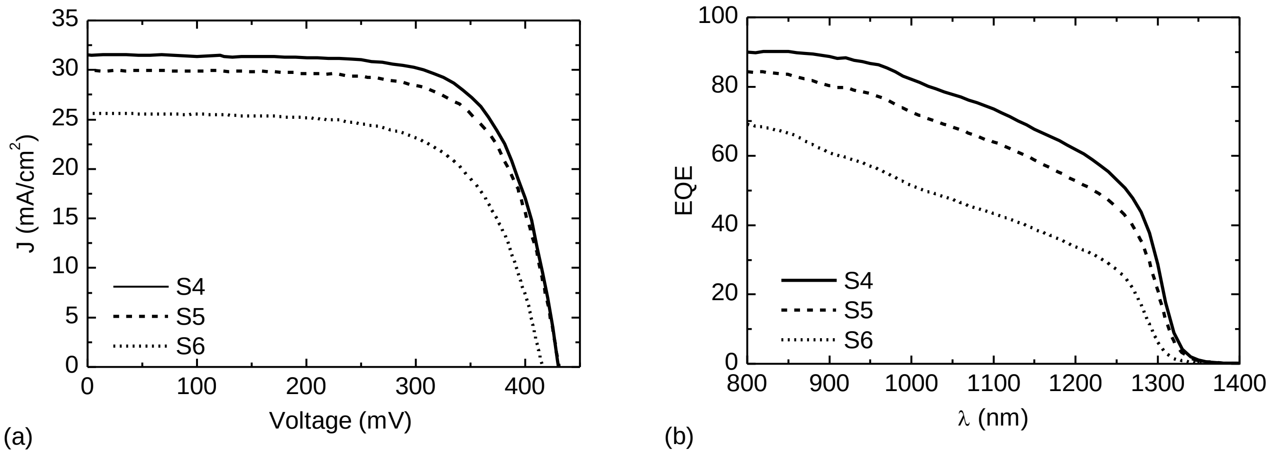

Figure 3.39 *(a) Current-voltage characteristics, and (b) EQE of the investigated samples. Short circuit current density (J_{SC}), V_{OC}, and EQE increases with decreasing As/III BEP ratio.*

Figure 3.40(a) shows J_{SC}, calculated from the EQE data using a standard AM1.5D spectrum [38], as a function of As/III BEP ratio. J_{SC} increases linearly with decreasing As/III BEP ratio, showing the highest value of 13.7 mA/cm^2 for S4. When looking at the diode equation (2-18), and Figure 3.37(c) showing linear behavior for J_0, one can conclude that the increased current generation is due to decreased defect density and a related decrease in J_0. Also V_{OC} increases together with decreased BEP ratio, as presented in Figure 3.40(b), which can be explained by improved material quality, and reduced nonradiative recombination. Table VII shows J_{SC} values calculated from the EQE data for AM0, AM1.5G, and AM1.5D conditions [38]. Also the target J_{SC}, showing the required current generation for a state-of-the-art GaInP/GaAs solar cell [42], is presented for all three spectral conditions. S4, grown with a As/III BEP ratio of 6, satisfies the current matching requirements under AM0 and AM1.5G conditions and is only ~0.1 mA/cm^2 behind under AM1.5D conditions. The results show again how relatively small changes in fabrication parameters and consequent defect densities influence solar cell performance dramatically, and define whether the material can or cannot improve the efficiency of a multijunction solar cell.

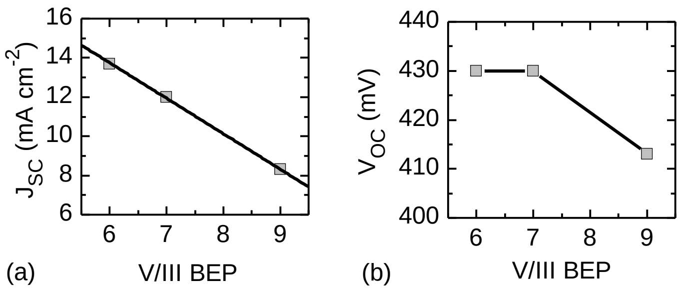

Figure 3.40 (a) J_{SC} calculated from the EQE data using standard AM1.5D spectrum, and (b) V_{OC} as a function of V/III BEP ratio.

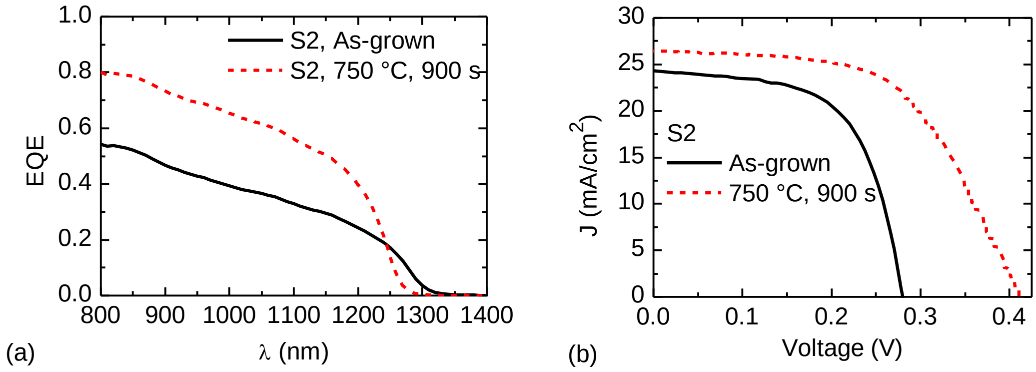

Figure 3.41 *LIV data recorded from as-grown and annealed (T_{ANN}=750 °C, t_{ANN}=900 s) solar cells based on sample B.*

Table VII J_{SC} *values calculated from the EQE data using standard AM0, AM1.5G, and AM1.5D spectra. Also the target* J_{SC} *value, referring to current matching condition of a state-of-the-art GaInP/GaAs solar cell are shown*

Sample	J_{SC} AM0 (mA/cm^2)	J_{SC} AM1.5G (mA/cm^2)	J_{SC} AM1.5D (mA/cm^2)
S4	**17.9**	**14.5**	**13.7**
S5	15.7	12.7	12.0
S6	10.9	8.8	8.3
Target	**17.8**	**14.5**	**13.8**

There are also parameters other than the As/III BEP ratio which can have a huge impact on dilute nitride solar cell performance. As shown in Figure 3.34, thermal annealing can reduce the defect density significantly. The influence of thermal annealing on solar cell performance was tested on S2. Figure 3.41 shows EQE and LIV data from as-grown and annealed (T_{ANN}=750 C, t_{ANN}=900 s) samples. The annealing procedure was identical to that for the DLTS sample, presented in Figure 3.34. Thermal annealing causes a significant increase in solar cell current and voltage: I_{SC} improves by 10 % and V_{OC} by 48 % due to annealing. This result underlines the importance of thermal annealing in dilute nitride based devices. Furthermore, annealing induced BS is visible in EQE. This is caused by the changes in nearest neighbor environment, observed in various dilute nitride material systems, improved homogeneity of the alloy as observed in various N containing compounds including GaNAs [229, 230], GaNAsSb [231, 232], GaInNAs [233, 234], and InSbN [235].

Overall, fabrication parameters such as As/III BEP ratio or thermal annealing can influence dilute nitride solar cell performance significantly. Although it is typical or even unavoidable that dilute nitride materials contain defects, by optimizing fabrication parameters it is possible to reduce the defect densities and improve the material quality to the level needed for high-efficiency multijunction solar cells.

Dilute nitrides in multijunction architecture

Dilute nitride sub-junctions were integrated in GaInP/GaAs/GaInNAs multijunction devices. By careful adjustment of the growth temperature, V/As BEP ratio, thermal annealing, N_2 plasma parameters, material compositions, and many other fabrication parameters, 3-junction solar cell with 1 eV band-gap lattice matched GaInNAs and GaInNAsSb sub-junctions were fabricated. Figure 3.42 shows exemplary EQE for the 1 eV sub-junctions. GaInNAsSb junction shows clearly higher performance, mainly due to lower background doping. Figure 3.43 shows EQE for entire GaInP/GaAs/GaInNAsSb solar cells. The average EQE is close to 90% at wide spectral range.

Figure 3.44 shows LIV for GaInP/GaAs/GaInNAs and GaInP/GaAs/GaInNAsSb solar cells, measured under AM1.5 real sun conditions. One sun efficiency increases from 22 % to 31 % when Sb-containing dilute nitride bottom junction is used. GaInNAs junction limits the current generation, resulting in lower conversion efficiency, whereas GaInNAsSb can meet the current matching requirements. For this reason, the FF increases also from 80% to 90% when Sb is used.

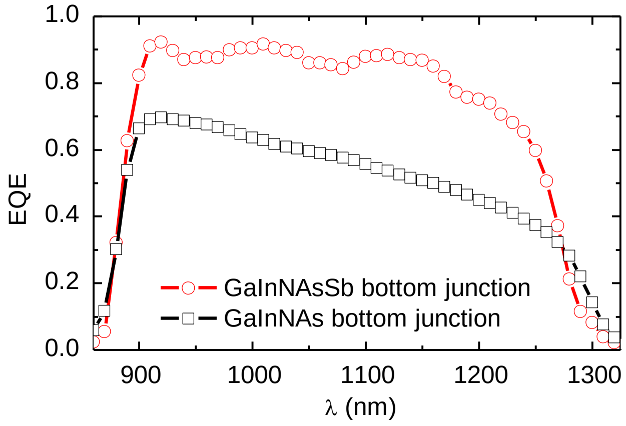

Figure 3.42 *EQE data measured from the 3-junction solar cells bottom junction consisting of dilute nitride material.*

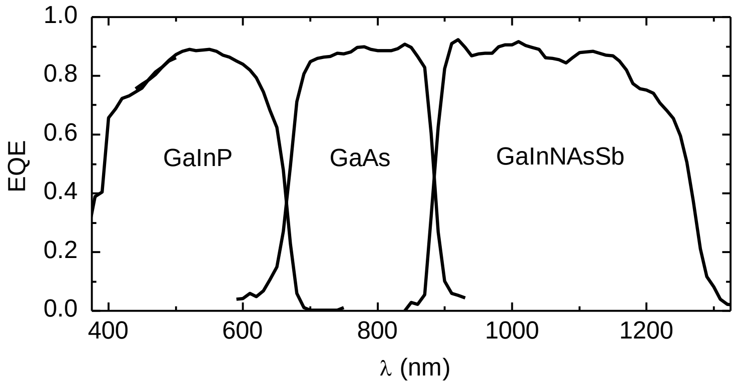

Figure 3.43 *EQE measured from GaInP/GaAs/GaInNAsSb 3-junction solar cell.*

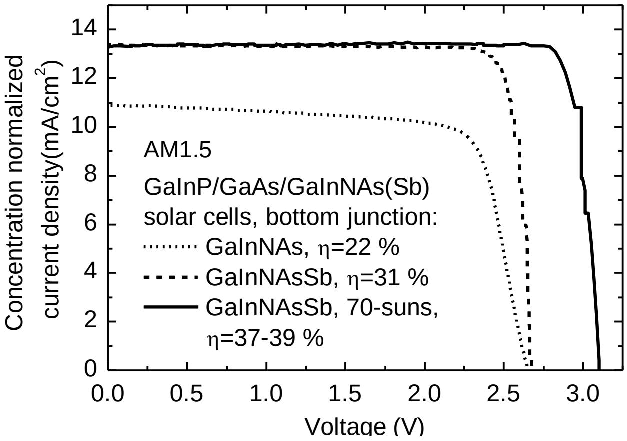

Figure 3.44 *LIV characteristics of 3-junction solar cells with dilute nitride bottom junctions.*

Efficiency increases to 37–39% when 70× light concentration is used [236-239]. The efficiency comes along with the logarithmic increase of photovoltage, as described in equation (2-19). Furthermore, higher efficiencies can be expected when higher concentrations will be used. Although the GaInNAs sub-junction did not meet the current matching requirements, very promising results and high efficiencies are obtained from GaInP/GaAs/GaInNAs space solar cells, fabricated with combined MBE-MOCVD technique, where dilute nitride is providing higher current than GaAs or GaInP junction at AM0 conditions [240].

4 Conclusions

The key findings in this thesis are related to the properties of semiconductor materials and nanostructures in the view of photovoltaic applications. The results reveal some of the most intriguing relations between the growth parameters and post growth treatments, on one hand, and material quality and the photovoltaic performance, on the other hand. The phenomena observed can be explained via modifications in lattice or surface structure. Furthermore, the optical, electrical and structural changes have an influence on photovoltaic performance in solar cell devices. The most important research questions answered by the thesis are summarized below.

NH_4OH and $(NH_4)_2S$ surface treatment of GaAs/GaInNAs/GaAs QW sample prior thermal annealing and SiO_2 capping was found to have influence on PL emission intensity as well as annealing induced BS. The XRD scans showed that the In out diffusion can be suppressed by proper surface treatment. XPS results showed that chemical treatments modified the GaAs surface oxides, which was linked with improved PL emission and reduced BS. The results shows how simple surface treatment, modifying only topmost monolayer of the crystal, can have large influence on the annealing behavior of III-V heterostructures, including solar cell devices. [P1]

AlInP window layer of GaInP solar cell was treated with $(NH_4)_2S$ solution. As a results, increase in solar cell PL emission and current generation and EQE was observed. Suppressed reflectivity of the solar cell explained the increase in current generation and EQE. The reason behind reflection suppression was revealed by AFM measurements: $(NH_4)_2S$ solution treatment modified AlInP surface creating nanostructured texture providing a graded refractive index from air to semiconductor material. Passivation of AlInP surface by S is also one possible explanation for increased solar cell current generation: XPS measurements showed a clear decrease in surface oxides and increase in S-related signal after treatment. These results are particularly interesting from the space solar cell point of view, since the treatment improved the current generation in the UV part which is more pronounced in space.

Strain relaxation induced defects were observed in InAs/GaAs quantum dot nanostructures when the amount of deposited InAs exceeded the critical thickness of plastic relaxation. Indications from dislocations, extended defect as well as point defects acting as an electron and hole traps were observed by DLTFS. The defects were locating in or near the InAs QD layer. When flushing step was introduced, the defect-related DLTFS spectra disappeared. Also the charge depletion to the defect states was not anymore present in CV measurements. Flushing also shifted the PL peak to higher energies, due to decrease in QD size. Cycled growth was found to improve the QD PL emission and decrease the amount of strain-relaxation induced defects. Flushing technique, combined with the cycled material deposition, was found to be the best alternative for formation of defect-free QDs with high PL emission. [P2, P3]

Type-II band gap GaSb/GaAs QDs structural and optical properties was influenced by changing the V/III BEP ratio. When ratio of 3 was used, all the QDs followed SK growth mode. When ratio was increased to 6, some of the QDs started to follow IMF growth mode, and PL emission energy shifted to the lower energy. Thermal annealing influenced on the PL intensity, reduced the PL peaks FWHM, and caused BS to the PL emission. Shift in PL emission, caused by the material diffusion between the QD layer and surrounding GaAs, was found to be independent of V/III BEP ratio. GaAs p-i-n solar cells with embedded GaSb QDs grown with V/III BEP ratio of 3.2 showed decrease in photovoltage generation, compared to reference solar cell without QDs. However, decrease in photovoltage was smaller compared to several earlier reports. Spectral response measurements sowed WL and QD -related photocurrent generation, and it got more pronounced when the amount of QD layers was increased. Spectral response did not show big changes after thermal annealing. Specified setup should be applied to measure intermediate band properties of the QDs. [P4]

Operation of QW solar cell incorporating also QDs was demonstrated by applying GaNAs and GaInNAs dilute nitride layers below and on top of InAs QD layers for strain compensation and mediation, respectively. Tensile strained GaNAs and compressively strained GaInNAs layers were also found to shift the InAs QD layers PL emission as well as spectral response to longer wavelength, mainly due to changes in confining potential. Also direct absorption to the dilute nitride layers, and resulting spectral response, was observed. GaNAs and GaInNAs layers were found to provide steps for electrons and holes, respectively, to thermally exit from the QD layers. Current generation became less temperature dependent due to improved thermionic emission from the QD layer and direct absorption to the dilute nitride layers. Although dilute nitride related defects increased the nonradiative recombination, the use of such structures in combination with QDs was demonstrated to improve the thermionic emission and shift the absorption edge to longer wavelengths, both of which being important features in QW solar cells to be integrated in multijunction architecture. [P5]

Strain-free stacked GaAs/AlGaAs QDs, grown by refiling of self-organized nanoholes, showed PL emission related to spontaneous emission between ground state and three excited QD states. High crystal quality and temperature stability of the material was confirmed by thermal annealing at high temperatures. Only small BS and increase in FWHM values was observed even at very high temperature annealing, which is opposite compared to droplet epitaxy grown GaAs QDs. The PL emission energy of the QDs ground state was found to follow empirical Varshni relation at temperatures higher than ~100 K. At lower temperatures, at least exciton binding effects reduces the shift to higher energy. Overall, the results imply that high-quality strain-free GaAs QDs could be used in connection with an AlGaAs solar cell, to extend the absorption edge and even provide intermediate band operation. [P6]

A broad DLTFS spectrum was recorded from three types of dilute nitride solar cells, consisting of 1 eV band gap lattice matched GaInNAs, GaNAsSb, and GaInNAsSb. Observed defects behaved as localized point defects in DLTFS measurements. CV measurements revealed that Sb reduces the unwanted p-type background doping about order of magnitude in lattice-matched bulk dilute nitride solar cells. However, at the same time, dominating deep levels capture cross section increased three orders of magnitude. Background doping was related to the formation of V_{Ga} and N-V_{Ga} complexes. Thermal annealing reduced the deep trap density in GaNAsSb, and subsequently increased the photocurrent and photovoltage generation. The observed deep trap was concluded to act as an effective recombination center in GaNAsSb. Background doping density was not found to change significantly during annealing. V/III BEP ratio, applied during fabrication of 1 eV band gap GaInNAs solar cells, was found to influence to the background doping density, defect density, dark saturation current, and PL emission of GaInNAs. Subsequently the solar cell performance increased when V/III BEP ratio was decreased from 9 to 6. Current generation requirement for integration with state-of-the-art GaInP/GaAs solar cell was achieved with the lowest V/III BEP ratio. Based on the material development on dilute nitrides, multijunction GaInP/GaAs/GaInNAsSb solar cell with conversion efficiency of 37–39% (70 sun concentration) was demonstrated, and higher efficiency is expected at higher concentrations. Successful integration of dilute nitrides into 4- or 5-junction solar cells would increase the conversion efficiency to even above 50 %, and at the same time reduce the cost of CPV systems appreciably. The same applies to space solar cells, where improved efficiency means reduced weight of the solar panels, which is a critical factor when material is launched into orbit. [P7, P8]

The connecting factor between the different materials structures investigated in this thesis is that by understanding the defect physics and relation to fabrication processes, enhanced conversion efficiency in novel solar cells can be obtained. For example, small changes in fabrication parameters or post growth treatments can change material quality considerably. Thermal annealing was applied also in many parts of this thesis. Thermal energy can, for example, induce diffusion, change the close range ordering of atoms, create or remove point defects at interfaces, and desorb atoms from the material surface.

The results and information provided by this thesis will be used as fundamental knowledge in the development of new solar cell devices. The next challenge is to investigate the use of nanostructures for increasing directly solar cell efficiency. Furthermore, the optimization of dilute nitrides as well as high band gap materials for next generation 3-, 4- and 5-junction solar cells with well over 45% conversion efficiencies is ongoing.

References

[1] *Key World Energy Statistics 2015, https://www.iea.org/publications/freepublications/publication/key-world-energy-statistics-2015.html*

[2] *Technology Roadmap: Solar Photovoltaic Energy - 2014 Edition*, https://www.iea.org/publications/freepublications/publication/technology-roadmap-solar-photovoltaic-energy---2014-edition.html

[3] D. M. DeLongchamp, "Organic photovoltaics", in *Semiconductor Materials for Solar Photovoltaic Cells*, Springer, 2016, pp. 169–196.

[4] V. Sugathan, E. John and K. Sudhakar, "Recent improvements in dye sensitized solar cells: A review", *Renewable and Sustainable Energy Reviews,* vol. 52, pp. 54-64, 2015.

[5] A. G. Aberle, "Thin-film solar cells", *Thin Solid Films,* vol. 517, pp. 4706-4710, 2009.

[6] H. J. Snaith, "Perovskites: the emergence of a new era for low-cost, high-efficiency solar cells", *The Journal of Physical Chemistry Letters,* vol. 4, pp. 3623-3630, 2013.

[7] A. L. Luque, *Concentrator Photovoltaics.* Springer, 2007.

[8] *Amonix 7700 CPV solar power generator*, https://upload.wikimedia.org/wikipedia/commons/5/5e/Amonix7700.jpg, cited 11.11.2015.

[9] *ISS on 20 August 2001, https://upload.wikimedia.org/wikipedia/commons/9/95/ISS_on_20_August_2001.jpg*, cited 11.11.2015.

[10] W. Shockley and H. J. Queisser, "Detailed balance limit of efficiency of p-n junction solar cells", *J. Appl. Phys.,* vol. 32, pp. 510-519, 1961.

[11] A. Marti and G. L. Araújo, "Limiting efficiencies for photovoltaic energy conversion in multigap systems", *Solar Energy Mater. Solar Cells,* vol. 43, pp. 203-222, 1996.

[12] M. A. Green, K. Emery, Y. Hishikawa, W. Warta and E. D. Dunlop, "Solar cell efficiency tables (Version 45)", *Prog Photovoltaics Res Appl,* vol. 23, pp. 1-9, 2015.

[13] *http://www.nrel.gov/ncpv/images/efficiency_chart.jpg*, cited 11.11.2015.

[14] R. Dingle, W. Wiegmann and C. H. Henry, "Quantum states of confined carriers in very thin Al x Ga 1− x As-GaAs-Al x Ga 1− x As heterostructures", *Phys. Rev. Lett.,* vol. 33, p. 827, 1974.

[15] J. Adams, B. Browne, I. Ballard, J. Connolly, N. Chan, A. Ioannides, W. Elder, P. Stavrinou, K. Barnham and N. Ekins-Daukes, "Recent results for single-junction and tandem quantum well solar cells", *Prog. Photovoltaics Res. Appl.,* vol. 19, pp. 865-877, 2011.

[16] I. Stranski and L. Krastanov, "Abhandlungen der mathematisch-naturwissenschaftlichen klasse IIb", *Akademie Der Wissenschaften Wien,* vol. 146, pp. 797-810, 1938.

[17] V. Polojärvi, M.Sc. thesis, "InAs/GaAs Quantum Dot Nanostructures: Deep Levels and Optical Properties", Tampere University of Technology, 2009. (TEM image by Janne Pakarinen)

[18] A. Martí, E. Antolin, C. Stanley, C. Farmer, N. López, P. Diaz, E. Cánovas, P. Linares and A. Luque, "Production of photocurrent due to intermediate-to-conduction-band transitions: a demonstration of a key operating principle of the intermediate-band solar cell", *Phys. Rev. Lett.,* vol. 97, p. 247701, 2006.

[19] A. Luque, A. Martí and C. Stanley, "Understanding intermediate-band solar cells", *Nature Photonics,* vol. 6, pp. 146-152, 2012.

[20] A. Luque and A. Martí, "Increasing the efficiency of ideal solar cells by photon induced transitions at intermediate levels", *Phys. Rev. Lett.,* vol. 78, p. 5014, 1997.

[21] A. Luque, A. Marti, E. Antolin and P. Garcia-Linares, "Intraband absorption for normal illumination in quantum dot intermediate band solar cells", *Solar Energy Mater. Solar Cells,* vol. 94, pp. 2032-2035, 2010.

[22] P. Frigeri, L. Nasi, M. Prezioso, L. Seravalli, G. Trevisi, E. Gombia, R. Mosca, F. Germini, C. Bocchi and S. Franchi, "Effects of the quantum dot ripening in high-coverage InAs/GaAs nanostructures", *J. Appl. Phys.,* vol. 102, pp. 83506-83506, 2007.

[23] G. Balakrishnan, J. Tatebayashi, A. Khoshakhlagh, S. Huang, A. Jallipalli, L. Dawson and D. Huffaker, "III/V ratio based selectivity between strained Stranski-Krastanov and strain-free GaSb quantum dots on GaAs", *Appl. Phys. Lett.,* vol. 89, p. 161104, 2006.

[24] P. Clapham and M. Hutley, "Reduction of lens reflexion by the “Moth Eye” principle", *Nature* vol. 244, pp. 281-282 1973.

[25] J. Tommila, A. Aho, A. Tukiainen, V. Polojärvi, J. Salmi, T. Niemi and M. Guina, "Moth-eye antireflection coating fabricated by nanoimprint lithography on 1 eV dilute nitride solar cell", *Prog Photovoltaics Res Appl,* vol. 21, pp. 1158-1162, 2013.

[26] J. Tommila, V. Polojärvi, A. Aho, A. Tukiainen, J. Viheriälä, J. Salmi, A. Schramm, J. Kontio, A. Turtiainen and T. Niemi, "Nanostructured broadband antireflection coatings on AlInP fabricated by nanoimprint lithography", *Solar Energy Mater. Solar Cells,* vol. 94, pp. 1845-1848, 2010.

[27] W. Shan, W. Walukiewicz, J. Ager III, E. Haller, J. Geisz, D. Friedman, J. Olson and S. R. Kurtz, "Band anticrossing in GaInNAs alloys", *Phys. Rev. Lett.,* vol. 82, p. 1221, 1999.

[28] M. Kondow, K. Uomi, A. Niwa, T. Kitatani, S. Watahiki and Y. Yazawa, "GaInNAs: a novel material for long-wavelength-range laser diodes with excellent high-temperature performance", *Japanese Journal of Applied Physics,* vol. 35, p. 1273, 1996.

[29] A. Aho, V. Polojärvi, V. Korpijärvi, J. Salmi, A. Tukiainen, P. Laukkanen and M. Guina, "Composition dependent growth dynamics in molecular beam epitaxy of GaInNAs solar cells", *Solar Energy Mater. Solar Cells,* vol. 124, pp. 150-158, 2014.

[30] J. S. Harris, "The opportunities, successes and challenges for GaInNAsSb", *J. Cryst. Growth,* vol. 278, pp. 3-17, 2005.

[31] X. Yang, M. Jurkovic, J. Heroux and W. Wang, "Molecular beam epitaxial growth of InGaAsN: Sb/GaAs quantum wells for long-wavelength semiconductor lasers", *Appl. Phys. Lett.,* vol. 75, p. 178, 1999.

[32] J. S. Harris, R. Kudrawiec, H. Yuen, S. Bank, H. Bae, M. Wistey, D. Jackrel, E. Pickett, T. Sarmiento and L. Goddard, "Development of GaInNAsSb alloys: growth, band structure, optical properties and applications", *Physica Status Solidi (B),* vol. 244, pp. 2707-2729, 2007.

[33] C. H. Henry, "Limiting efficiencies of ideal single and multiple energy gap terrestrial solar cells", *J. Appl. Phys.,* vol. 51, pp. 4494-4500, 1980.

[34] R. King, D. Law, K. Edmondson, C. Fetzer, G. Kinsey, H. Yoon, R. Sherif and N. Karam, "40% efficient metamorphic GaInP/GaInAs/Ge multijunction solar cells", *Appl. Phys. Lett.,* vol. 90, pp. 183516-183900, 2007.

[35] J. Geisz, S. Kurtz, M. Wanlass, J. Ward, A. Duda, D. Friedman, J. Olson, W. McMahon, T. Moriarty and J. Kiehl, "High-efficiency GaInP/GaAs/InGaAs triple-junction solar cells grown inverted with a metamorphic bottom junction", *Appl. Phys. Lett.,* vol. 91, p. 3502, 2007.

[36] S. Wojtczuk, P. Chiu, X. Zhang, D. Derkacs, C. Harris, D. Pulver and M. Timmons, "InGaP/GaAs/InGaAs 41% concentrator cells using bi-facial epigrowth", in *Photovoltaic Specialists Conference (PVSC), 2010 35th IEEE,* 2010, pp. 001259-001264.

[37] F. Dimroth, M. Grave, P. Beutel, U. Fiedeler, C. Karcher, T. N. Tibbits, E. Oliva, G. Siefer, M. Schachtner and A. Wekkeli, "Wafer bonded four-junction GaInP/GaAs//GaInAsP/GaInAs concentrator solar cells with 44.7% efficiency", *Prog Photovoltaics Res Appl,* vol. 22, pp. 277-282, 2014.

[38] ASTM G 173–03: *Standard tables for reference solar spectral irradiances: direct normal and hemispherical on 37° tilted surface*. West Conshohoken, PA: ASTM International; 2003. doi:10.1520/G0173-03R12

[39] J. Allen, V. Sabnis, M. Wiemer and H. Yuen, "44%-efficiency triple-junction solar cells", in *9th International Conference on Concentrator Photovoltaic Systems,* Miyazaki, Japan, 2013.

[40] D. Derkacs, R. Jones-Albertus, F. Suarez and O. Fidaner, "Lattice-matched multijunction solar cells employing a 1 eV GaInNAsSb bottom cell", *Journal of Photonics for Energy,* vol. 2, pp. 021805-1-021805-8, 2012.

[41] R. King, D. Bhusari, A. Boca, D. Larrabee, X. Liu, W. Hong, C. Fetzer, D. Law and N. Karam, "Band gap-voltage offset and energy production in next-generation multijunction solar cells", *Prog Photovoltaics Res Appl,* vol. 19, pp. 797-812, 2011.

[42] A. Aho, A. Tukiainen, V. Polojärvi and M. Guina, "Performance assessment of multijunction solar cells incorporating GaInNAsSb", *Nanoscale Research Letters,* vol. 9, pp. 1-7, 2014.

[43] R. King, C. Fetzer, K. Edmondson, D. Law, P. Colter, H. Cotal, R. Sherif, H. Yoon, T. Isshiki and D. Krut, "Metamorphic III-V materials, sublattice disorder, and multijunction solar cell approaches with over 37% efficiency". Presented at *the 19th European Photovoltaic Solar Energy Conference and Exhibition,* p. 11, 2004.

[44] M. Henini, *Molecular Beam Epitaxy: From Research to Mass Production.* Newnes, 2012.

[45] S. Franchi, G. Trevisi, L. Seravalli and P. Frigeri, "Quantum dot nanostructures and molecular beam epitaxy", *Progress in Crystal Growth and Characterization of Materials,* vol. 47, pp. 166-195, 2003.

[46] A. Cho and J. Arthur, "Molecular beam epitaxy", *Progress in Solid State Chemistry,* vol. 10, pp. 157-191, 1975.

[47] B. Joyce, "Molecular beam epitaxy", *Reports on Progress in Physics,* vol. 48, p. 1637, 1985.

[48] J. R. Arthur, "Molecular beam epitaxy", *Surf. Sci.,* vol. 500, pp. 189-217, 2002.

[49] B. R. Pamplin, *Molecular Beam Epitaxy.* Elsevier, 2013.

[50] MicroChemicals GmbH, Product Data Sheet, AZ 5214 E, Image Reversal Photoresist, http://www.microchemicals.com/micro/az_5214e.pdf, cited 24.12.2015.

[51] MicroChemicals GmbH, Product Data Sheet, AZ 6600 Series, General-Purpose Photoresist, http://www.microchemicals.com/micro/az_6600_series.pdf, cited 24.12.2015.

[52] G. Bacher, H. Schweizer, J. Kovac, A. Forchel, H. Nickel, W. Schlapp and R. Lösch, "Influence of barrier height on carrier dynamics in strained In x Ga 1− x As/GaAs quantum wells", *Physical Review B,* vol. 43, p. 9312, 1991.

[53] Y. Varshni, "Temperature dependence of the energy gap in semiconductors", *Physica,* vol. 34, pp. 149-154, 1967.

[54] P. Blood and J. W. Orton, *The Electrical Characterization of Semiconductors: Majority Carriers and Electron States.* Academic Pr, 1992.

[55] D. K. Schroder, *Semiconductor Material and Device Characterization.* John Wiley & Sons, 2006.

[56] R. T. Tung, "The physics and chemistry of the Schottky barrier height", *Applied Physics Reviews,* vol. 1, p. 011304, 2014.

[57] D. Lang, "Deep-level transient spectroscopy: A new method to characterize traps in semiconductors", *J. Appl. Phys.,* vol. 45, pp. 3023-3032, 1974.

[58] Christian Kapteyn, "*Carrier Emission and Electronic Properties of Self-Organized Semiconductor Quantum Dots*"*, Mensch-Und-Buch Verlag, Berlin, 2001*.

[59] S. A. Arrhenius, "Über die Dissociationswärme und den Einflusß der Temperatur auf den Dissociationsgrad der Elektrolyte", *Z. Physik. Chem.,* vol. 4, pp. 96–116, 1889.

[60] J. Fourier, *Theorie Analytique De La Chaleur, Par M. Fourier.* Chez Firmin Didot, père et fils, 1822.

[61] S. Weiss and R. Kassing, "Deep Level Transient Fourier Spectroscopy (DLTFS)—A technique for the analysis of deep level properties", *Solid-State Electronics,* vol. 31, pp. 1733-1742, 1988.

[62] Bio-Rad DL8000 Deep Level Transient Spectometer System Manual, February, 1996.

[63] A. Edelman, P. McCorquodale and S. Toledo, "The future fast Fourier transform?", *SIAM Journal on Scientific Computing,* vol. 20, pp. 1094-1114, 1998.

[64] Antti Tukiainen, Doctoral Thesis, "Point Defects and Luminescence Properties of Visible-Light Emitting Semiconductors", *Tampere University of Technology. Publication 515,* 2004.

[65] W. Bragg and W. Bragg, "The reflection of X-rays by crystals", *Proceedings of the Royal Society of London.Series A, Containing Papers of a Mathematical and Physical Character,* pp. 428-438, 1913.

[66] W. Shockley and W. Read Jr, "Statistics of the recombinations of holes and electrons", *Physical Review,* vol. 87, p. 835, 1952.

[67] R. N. Hall, "Electron-hole recombination in germanium", *Physical Review,* vol. 87, p. 387, 1952.

[68] P. Auger, "Sur les rayons β secondaires produits dans un gaz par des rayons X", *C.R.A.S.,* vol. 177, pp. 169-170; 171, 1925.

[69] A. Vossier, B. Hirsch and J. M. Gordon, "Is Auger recombination the ultimate performance limiter in concentrator solar cells?", *Appl. Phys. Lett.,* vol. 97, p. 193509, 2010.

[70] D. Nolte, "Surface recombination, free-carrier saturation, and dangling bonds in InP and GaAs", *Solid-State Electronics,* vol. 33, pp. 295-298, 1990.

[71] M. Courel, J. C. Rimada and L. Hernández, "GaAs/GaInNAs quantum well and superlattice solar cell", *Appl. Phys. Lett.,* vol. 100, p. 073508, 2012.

[72] V. Korpijärvi, M. Guina, J. Puustinen, P. Tuomisto, J. Rautiainen, A. Härkönen, A. Tukiainen, O. Okhotnikov and M. Pessa, "MBE grown GaInNAs-based multi-Watt disk lasers", *J. Cryst. Growth,* vol. 311, pp. 1868-1871, 2009.

[73] J. Harris Jr, "GaInNAs long-wavelength lasers: progress and challenges", *Semiconductor Science and Technology,* vol. 17, p. 880, 2002.

[74] J. Pakarinen, C. Peng, J. Puustinen, P. Laukkanen, V. Korpijarvi, A. Tukiainen and M. Pessa, "Postgrowth annealing of GaInAs/GaAs and GaInAsN/GaAs quantum well samples placed in a proximity GaAs box: A simple method to improve the crystalline quality", *Appl. Phys. Lett.,* vol. 92, p. 232105, 2008.

[75] H. Xin, K. Kavanagh, M. Kondow and C. Tu, "Effects of rapid thermal annealing on GaInNAs/GaAs multiple quantum wells", *J. Cryst. Growth,* vol. 201, pp. 419-422, 1999.

[76] G. Jaschke, R. Averbeck, L. Geelhaar and H. Riechert, "Low threshold InGaAsN/GaAs lasers beyond 1500 nm", *J. Cryst. Growth,* vol. 278, pp. 224-228, 2005.

[77] D. Bisping, D. Pucicki, M. Fischer, S. Höfling and A. Forchel, "Influence of arsenic flux on the annealing properties of GaInNAs quantum wells for long wavelength laser applications around 1.6 µm", *J. Cryst. Growth,* vol. 311, pp. 1715-1718, 2009.

[78] S. R. Kurtz, A. Allerman, E. Jones, J. Gee, J. Banas and B. Hammons, "InGaAsN solar cells with 1.0 eV band gap, lattice matched to GaAs", *Appl. Phys. Lett.,* vol. 74, pp. 729-731, 1999.

[79] K. Volz, D. Lackner, I. Nemeth, B. Kunert, W. Stolz, C. Baur, F. Dimroth and A. Bett, "Optimization of annealing conditions of (GaIn)(NAs) for solar cell applications", *J. Cryst. Growth,* vol. 310, pp. 2222-2228, 2008.

[80] C. Peng, J. Konttinen, T. Jouhti and M. Pessa, "High-gain new InGaAsN heterostructure", in *Photonics Europe,* p. 618409, 2006.

[81] B. S. Ooi, K. McIlvaney, M. W. Street, A. S. Helmy, S. G. Ayling, J. H. Marsh and J. Roberts, "Selective quantum-well intermixing in GaAs-AlGaAs structures using impurity-free vacancy diffusion", *IEEE Journal Of Quantum Electronics,* vol. 33, pp. 1784-1793, 1997.

[82] A. Lang and M. Zhen-Hong, "Pendellosung interference in the bragg reflexion of X-rays from a crystal surface". in *Proceedings of the Royal Society of London A: Mathematical, Physical and Engineering Sciences,* pp. 313-329, 1979.

[83] G. Mussler, L. Daweritz and K. H. Ploog, "Nitrogen-induced suppression of an indium-gallium interdiffusion in InxGa1-xAs1-yNy/GaAs multiple-quantum wells", *Appl. Phys. Lett.,* vol. 87, p. 81903, 2005.

[84] J. Pakarinen, C. Peng, V. Polojärvi, A. Tukiainen, V. Korpijärvi, J. Puustinen, M. Pessa, P. Laukkanen, J. Likonen and E. Arola, "Suppression of annealing-induced In diffusion in Be-doped GaInAsN/GaAs quantum well", *Appl. Phys. Lett.,* vol. 93, p. 2102, 2008.

[85] H. Liu, C. Peng, E. Pavelescu, T. Jouhti, S. Karirinne, J. Konttinen and M. Pessa, "Annealing effects on optical and structural properties of 1.3-µm GaInNAs/GaAs quantum-well samples capped with dielectric layers", *Appl. Phys. Lett.,* vol. 84, pp. 478-480, 2004.

[86] G. Ciatto, F. d'Acapito, L. Grenouillet, H. Mariette, D. De Salvador, G. Bisognin, R. Carboni, L. Floreano, R. Gotter and S. Mobilio, "Quantitative determination of short-range ordering in In x Ga 1− x As 1− y N y", *Physical Review B,* vol. 68, p. 161201, 2003.

[87] V. Gambin, V. Lordi, W. Ha, M. Wistey, T. Takizawa, K. Uno, S. Friedrich and J. Harris, "Structural changes on annealing of MBE grown (Ga, In)(N, As) as measured by X-ray absorption fine structure", *J. Cryst. Growth,* vol. 251, pp. 408-411, 2003.

[88] K. Uno, M. Yamada, I. Tanaka, O. Ohtsuki and T. Takizawa, "Thermal annealing effects and local atomic configurations in GaInNAs thin films", *J. Cryst. Growth,* vol. 278, pp. 214-218, 2005.

[89] K. Volz, T. Torunski, O. Rubel and W. Stolz, "Direct structural evidence of the change in N-III bonding in (GaIn)(NAs) before and after thermal annealing", *J. Appl. Phys.,* vol. 104, p. 053504, 2008.

[90] V. Lordi, V. Gambin, S. Friedrich, T. Funk, T. Takizawa, K. Uno and J. S. Harris, "Nearest-neighbor configuration in (GaIn)(NAs) probed by X-ray absorption spectroscopy", *Phys. Rev. Lett.,* vol. 90, p. 145505, 2003.

[91] M. Hugues, B. Damilano, J. Chauveau, J. Duboz and J. Massies, "Blue-shift mechanisms in annealed (Ga, In)(N, As)∕Ga As quantum wells", *Physical Review B,* vol. 75, p. 045313, 2007.

[92] D. C. Suh, Y. D. Cho, S. W. Kim, D. Ko, Y. Lee, M. Cho and J. Oh, "Improved thermal stability of Al2O3/HfO2/Al2O3 high-k gate dielectric stack on GaAs", *Appl. Phys. Lett.,* vol. 96, p. 2112, 2010.

[93] C. Hinkle, M. Milojevic, B. Brennan, A. Sonnet, F. Aguirre-Tostado, G. Hughes, E. Vogel and R. Wallace, "Detection of Ga suboxides and their impact on III-V passivation and Fermi-level pinning", *Appl. Phys. Lett.,* vol. 94, p. 162101, 2009.

[94] M. Hale, S. Yi, J. Sexton, A. Kummel and M. Passlack, "Scanning tunneling microscopy and spectroscopy of gallium oxide deposition and oxidation on GaAs (001)-c (2x8)/(2x4)", *J. Chem. Phys.,* vol. 119, pp. 6719-6728, 2003.

[95] M. Passlack, Z. Yu, R. Droopad, B. Bowers, C. Overgaard, J. Abrokwah and A. Kummel, "Interface charge and nonradiative carrier recombination in Ga2O3-GaAs interface structures", *Journal of Vacuum Science & Technology B,* vol. 17, pp. 49-52, 1999.

[96] B. Skromme, C. Sandroff, E. Yablonovitch and T. Gmitter, "Effects of passivating ionic films on the photoluminescence properties of GaAs", *Appl. Phys. Lett.,* vol. 51, pp. 2022-2024, 1987.

[97] C. Sandroff, R. Nottenburg, J. Bischoff and R. Bhat, "Dramatic enhancement in the gain of a GaAs/AlGaAs heterostructure bipolar transistor by surface chemical passivation", *Appl. Phys. Lett.,* vol. 51, pp. 33-35, 1987.

[98] E. Yablonovitch, C. Sandroff, R. Bhat and T. Gmitter, "Nearly ideal electronic properties of sulfide coated GaAs surfaces", *Appl. Phys. Lett.,* vol. 51, pp. 439-441, 1987.

[99] Y. Oh, S. Byun, B. Lee, T. Kang, C. Hong, S. Park, H. Lee and T. Kim, "Diminution of the surface states on GaAs by a sulfur treatment", *J. Appl. Phys.,* vol. 76, pp. 1959-1961, 1994.

[100] J. Lee, "Sulfur doping of GaAs with (NH4) 2Sx solution", *J. Appl. Phys.,* vol. 85, pp. 807-811, 1999.

[101] J. C. Ho, A. C. Ford, Y. Chueh, P. W. Leu, O. Ergen, K. Takei, G. Smith, P. Majhi, J. Bennett and A. Javey, "Nanoscale doping of InAs via sulfur monolayers", *Appl. Phys. Lett.,* vol. 95, p. 072108, 2009.

[102] L. Lai, J. Chen, L. Lou, C. Wu and C. Lee, "Performance Improvement of (NH4) 2S x-Treated III–V Compounds Multijunction Solar Cell Using Surface Treatment", *J. Electrochem. Soc.,* vol. 155, pp. B1270-B1273, 2008.

[103] C. Tseng and C. Lee, "Mechanisms of (NH4) 2Sx-treated III-V compound triple-junction solar cells incorporating with hybrid electrode", *Appl. Phys. Lett.,* vol. 101, p. 033902, 2012.

[104] Q. Chen, G. Hubbard, P. A. Shields, C. Liu, D. W. Allsopp, W. N. Wang and S. Abbott, "Broadband moth-eye antireflection coatings fabricated by low-cost nanoimprinting", *Appl. Phys. Lett.,* vol. 94, p. 263118, 2009.

[105] C. Sun, P. Jiang and B. Jiang, "Broadband moth-eye antireflection coatings on silicon", *Appl. Phys. Lett.,* vol. 92, p. 061112, 2008.

[106] C. Sun, B. J. Ho, B. Jiang and P. Jiang, "Biomimetic subwavelength antireflective gratings on GaAs", *Opt. Lett.,* vol. 33, pp. 2224-2226, 2008.

[107] W. Min, A. P. Betancourt, P. Jiang and B. Jiang, "Bioinspired broadband antireflection coatings on GaSb", *Appl. Phys. Lett.,* vol. 92, p. 141109, 2008.

[108] H. Savin, P. Repo, G. von Gastrow, P. Ortega, E. Calle, M. Garín and R. Alcubilla, "Black silicon solar cells with interdigitated back-contacts achieve 22.1% efficiency", *Nature Nanotechnology*, vol. 10, pp 624-628, 2015.

[109] H. J. Queisser and E. E. Haller, "Defects in semiconductors: some fatal, some vital", *Science,* vol. 281, pp. 945-950, Aug 14, 1998.

[110] D. Bimberg, M. Grundmann and N. N. Ledentsov, *Quantum Dot Heterostructures.* John Wiley & Sons, 1999.

[111] C. Heyn, "Critical coverage for strain-induced formation of InAs quantum dots", *Physical Review B,* vol. 64, p. 165306, 2001.

[112] J. Wang, J. Chen, J. Huang, P. Wang and X. Guo, "Carrier distribution and relaxation-induced defects of InAs/GaAs quantum dots", *Appl. Phys. Lett.,* vol. 77, pp. 3027-3029, 2000.

[113] L. Nasi, C. Bocchi, F. Germini, M. Prezioso, E. Gombia, R. Mosca, P. Frigeri, G. Trevisi, L. Seravalli and S. Franchi, "Defects in nanostructures with ripened InAs/GaAs quantum dots", *J. Mater. Sci. : Mater. Electron.,* vol. 19, pp. 96-100, 2008.

[114] M. Sobolev, A. Kovsh, V. Ustinov, A. Y. Egorov, A. Zhukov and Y. G. Musikhin, "Capacitance spectroscopy of deep states in InAs/GaAs quantum dot heterostructures", *Semiconductors,* vol. 33, pp. 157-164, 1999.

[115] M. Kaniewska, O. Engström, A. Barcz and M. Pacholak-Cybulska, "Deep levels induced by InAs/GaAs quantum dots", *Materials Science and Engineering: C,* vol. 26, pp. 871-875, 2006.

[116] W. Schröter, J. Kronewitz, U. Gnauert, F. Riedel and M. Seibt, "Bandlike and localized states at extended defects in silicon," *Physical Review B,* vol. 52, p. 13726, 1995.

[117] T. Figielski, "Electron emission from extended defects: DLTS signal in case of dislocation traps", *Physica Status Solidi (a),* vol. 121, pp. 187-193, 1990.

[118] L. Gelczuk, M. Dabrowska-Szata and G. Józwiak, "Distinguishing and identifying point and extended defects in DLTS measurements", *Materials Science-Poland,* vol. 23, pp. 625-641, 2005.

[119] M. Dąbrowska-Szata, G. Jóźwiak and D. Radziewicz, "Electronic states at misfit dislocations in partially relaxed InGaAs/GaAs heterostructures", *Physica B: Condensed Matter,* vol. 388, pp. 195-199, 2007.

[120] Z. Fang, T. Schlesinger and A. Milnes, "Evidence for EL6 (Ec− 0.35 eV) acting as a dominant recombination center in n-type horizontal Bridgman GaAs", *J. Appl. Phys.,* vol. 61, pp. 5047-5050, 1987.

[121] G. Martin, A. Mitonneau and A. Mircea, "Electron traps in bulk and epitaxial GaAs crystals", *Electron. Lett.,* vol. 13, pp. 191-193, 1977.

[122] P. Yu, G. Robinson, J. Sizelove and C. Stutz, "0.8-eV photoluminescence of GaAs grown by molecular-beam epitaxy at low temperatures", *Physical Review B,* vol. 49, p. 4689, 1994.

[123] P. Kaminski and R. Kozlowski, "High-resolution photoinduced transient spectroscopy as a new tool for quality assessment of semi-insulating GaAs", *Materials Science and Engineering: B,* vol. 91, pp. 398-402, 2002.

[124] D. Lang and C. Henry, "Nonradiative recombination at deep levels in GaAs and GaP by Lattice-Relaxation Multiphonon Emission", *Phys. Rev. Lett.,* vol. 35, p. 1525, 1975.

[125] H. Tanino and M. Tajima, "Pressure effect on the luminescence from the deep level in gallium arsenide", *Physical Review B,* vol. 33, p. 5965, 1986.

[126] A. Irvine and D. Palmer, "First observation of the EL2 lattice defect in indium gallium arsenide grown by molecular-beam epitaxy", *Phys. Rev. Lett.,* vol. 68, p. 2168, 1992.

[127] J. Bourgoin and T. Neffati, "The energy level of the EL2 defect in GaAs", *Solid-State Electronics,* vol. 43, pp. 153-158, 1999.

[128] A. Martí, N. López, E. Antolin, E. Cánovas, C. Stanley, C. Farmer, L. Cuadra and A. Luque, "Novel semiconductor solar cell structures: The quantum dot intermediate band solar cell", *Thin Solid Films,* vol. 511, pp. 638-644, 2006.

[129] A. Nozik, "Quantum dot solar cells", *Physica E: Low-Dimensional Systems and Nanostructures,* vol. 14, pp. 115-120, 2002.

[130] A. Martí, L. Cuadra and A. Luque, "Quantum dot intermediate band solar cell", in *Photovoltaic Specialists Conference, 2000. Conference Record of the Twenty-Eighth IEEE,* pp. 940-943, 2000.

[131] S. Tomić, "Intermediate-band solar cells: Influence of band formation on dynamical processes in InAs/GaAs quantum dot arrays", *Physical Review B,* vol. 82, p. 195321, 2010.

[132] J. Kim, C. Yang, U. Sim, G. Lee, J. Park, Y. Lee and E. Yoon, "Growth mechanism of highly uniform InAs/GaAs quantum dot with periodic arsine interruption by metalorganic chemical vapor deposition", *J. Appl. Phys.,* vol. 110, p. 044302, 2011.

[133] Z. Wasilewski, S. Fafard and J. McCaffrey, "Size and shape engineering of vertically stacked self-assembled quantum dots", *J. Cryst. Growth,* vol. 201, pp. 1131-1135, 1999.

[134] S. Fafard, Z. Wasilewski, C. N. Allen, D. Picard, M. Spanner, J. McCaffrey and P. Piva, "Manipulating the energy levels of semiconductor quantum dots", *Physical Review B,* vol. 59, p. 15368, 1999.

[135] J. McCaffrey, M. Robertson, S. Fafard, Z. Wasilewski, E. Griswold and L. Madsen, "Determination of the size, shape, and composition of indium-flushed self-assembled quantum dots by transmission electron microscopy", *J. Appl. Phys.,* vol. 88, pp. 2272-2277, 2000.

[136] H. Sasakura, S. Kayamori, S. Adachi and S. Muto, "Effect of indium-flush method on the control of photoluminescence energy of highly uniform self-assembled InAs quantum dots by slow molecular beam epitaxy growth", *J. Appl. Phys.,* vol. 102, p. 013515, 2007.

[137] S. Yamauchi, K. Komori, T. Sugaya and K. Goshima, "Optical characteristics of InAs/GaAs double quantum dots grown by MBE with the indium-flush method", *Japanese Journal of Applied Physics,* vol. 43, p. 2083, 2004.

[138] Y. Lee, E. Ahn, J. Kim, P. Moon, C. Yang, E. Yoon, H. Lim and H. Cheong, "Complete suppression of large InAs island formation on GaAs by metal organic chemical vapor deposition with periodic AsH_3 interruption", *Appl. Phys. Lett.,* vol. 90, p. 033105, 2007.

[139] P. Krispin, R. Hey, H. Kostial and K. Ploog, "Growth mode-related generation of electron traps at the inverted AlAs/GaAs interface", *J. Appl. Phys.,* vol. 83, pp. 1496-1498, 1998.

[140] P. Krispin, J. Lazzari and H. Kostial, "Deep and shallow electronic states at ultrathin InAs insertions in GaAs investigated by capacitance spectroscopy", *J. Appl. Phys.,* vol. 84, pp. 6135-6140, 1998.

[141] F. Hatami, N. Ledentsov, M. Grundmann, J. Böhrer, F. Heinrichsdorff, M. Beer, D. Bimberg, S. Ruvimov, P. Werner and U. Gösele, "Radiative recombination in type-II GaSb/GaAs quantum dots", *Appl. Phys. Lett.,* vol. 67, pp. 656-658, 1995.

[142] A. Rocher, "Interfacial dislocations in the GaSb/GaAs (001) heterostructure", in *Solid State Phenomena,* pp. 563-572, 1991.

[143] S. Huang, G. Balakrishnan, A. Khoshakhlagh, A. Jallipalli, L. Dawson and D. Huffaker, "Strain relief by periodic misfit arrays for low defect density GaSb on GaAs", *Appl. Phys. Lett.,* vol. 88, p. 131911, 2006.

[144] J. Tatebayashi, A. Khoshakhlagh, S. Huang, L. Dawson, G. Balakrishnan and D. Huffaker, "Formation and optical characteristics of strain-relieved and densely stacked GaSb⁄GaAs quantum dots", *Appl. Phys. Lett.,* vol. 89, p. 203116, 2006.

[145] R. Teissier, D. Sicault, J. Harmand, G. Ungaro, G. Le Roux and L. Largeau, "Temperature-dependent valence band offset and band-gap energies of pseudomorphic GaAsSb on GaAs", *J. Appl. Phys.,* vol. 89, pp. 5473-5477, 2001.

[146] E. Glaser, B. Bennett, B. Shanabrook and R. Magno, "Photoluminescence studies of self-assembled InSb, GaSb, and AlSb quantum dot heterostructures", *Appl. Phys. Lett.,* vol. 68, pp. 3614-3616, 1996.

[147] K. Suzuki, R. Hogg and Y. Arakawa, "Structural and optical properties of type II GaSb/GaAs self-assembled quantum dots grown by molecular beam epitaxy", *J. Appl. Phys.,* vol. 85, pp. 8349-8352, 1999.

[148] L. Müller-Kirsch, U. Pohl, R. Heitz, H. Kirmse, W. Neumann and D. Bimberg, "Thin GaSb insertions and quantum dot formation in GaAs by MOCVD", *J. Cryst. Growth,* vol. 221, pp. 611-615, 2000.

[149] L. Müller-Kirsch, R. Heitz, U. Pohl, D. Bimberg, I. Häusler, H. Kirmse and W. Neumann, "Temporal evolution of GaSb/GaAs quantum dot formation", *Appl. Phys. Lett.,* vol. 79, pp. 1027-1029, 2001.

[150] C. Tseng, S. Mai, W. Lin, S. Wu, B. Yu, S. Chen, S. Lin, J. Shyue and M. Wu, "Influence of As on the morphologies and optical characteristics of GaSb/GaAs quantum dots", *Quantum Electronics, IEEE Journal Of,* vol. 47, pp. 335-339, 2011.

[151] S. Lin, C. Tseng, W. Lin, S. Mai, S. Wu, S. Chen and J. Chyi, "Room-temperature operation type-II GaSb/GaAs quantum-dot infrared light-emitting diode", *Appl. Phys. Lett.,* vol. 96, p. 123503, 2010.

[152] F. Heinrichsdorff, M. Grundmann, O. Stier, A. Krost and D. Bimberg, "Influence of In/Ga intermixing on the optical properties of InGaAs/GaAs quantum dots", *J. Cryst. Growth,* vol. 195, pp. 540-545, 1998.

[153] C. Jiang and H. Sakaki, "Sb/As intermixing in self-assembled GaSb/GaAs type II quantum dot systems and control of their photoluminescence spectra", *Physica E: Low-Dimensional Systems and Nanostructures,* vol. 26, pp. 180-184, 2005.

[154] S. Fafard and C. N. Allen, "Intermixing in quantum-dot ensembles with sharp adjustable shells", *Appl. Phys. Lett.,* vol. 75, pp. 2374-2376, 1999.

[155] D. Alonso-Álvarez, B. Alén, J. M. García and J. M. Ripalda, "Optical investigation of type II GaSb/GaAs self-assembled quantum dots", *Appl. Phys. Lett.,* vol. 91, p. 263103, 2007.

[156] N. Ledentsov, J. Böhrer, M. Beer, F. Heinrichsdorff, M. Grundmann, D. Bimberg, S. Ivanov, B. Y. Meltser, S. Shaposhnikov and I. Yassievich, "Radiative states in type-II GaSb/GaAs quantum wells", *Physical Review B,* vol. 52, p. 14058, 1995.

[157] Y. Chiu, M. Ya, W. Su and Y. Chen, "Properties of photoluminescence in type-II GaAsSb/GaAs multiple quantum wells", *J. Appl. Phys.,* vol. 92, pp. 5810-5813, 2002.

[158] T. Kawazu, T. Mano, T. Noda and H. Sakaki, "Optical properties of GaSb/GaAs type-II quantum dots grown by droplet epitaxy", *Appl. Phys. Lett.,* vol. 94, p. 081911, 2009.

[159] R. Laghumavarapu, A. Moscho, A. Khoshakhlagh, M. El-Emawy, L. Lester and D. Huffaker, "GaSb⁄GaAs type II quantum dot solar cells for enhanced infrared spectral response", *Appl. Phys. Lett.,* vol. 90, p. 173125, 2007.

[160] C. G. Bailey, D. V. Forbes, R. P. Raffaelle and S. M. Hubbard, "Near 1 V open circuit voltage InAs/GaAs quantum dot solar cells", *Appl. Phys. Lett.,* vol. 98, p. 163105, 2011.

[161] D. Guimard, R. Morihara, D. Bordel, K. Tanabe, Y. Wakayama, M. Nishioka and Y. Arakawa, "Fabrication of InAs/GaAs quantum dot solar cells with enhanced photocurrent and without degradation of open circuit voltage", *Appl. Phys. Lett.,* vol. 96, p. 3507, 2010.

[162] P. J. Carrington, A. S. Mahajumi, M. C. Wagener, J. R. Botha, Q. Zhuang and A. Krier, "Type II GaSb/GaAs quantum dot/ring stacks with extended photoresponse for efficient solar cells", *Physica B: Condensed Matter,* vol. 407, pp. 1493-1496, 2012.

[163] R. B. Laghumavarapu, B. L. Liang, Z. S. Bittner, T. S. Navruz, S. M. Hubbard, A. Norman and D. L. Huffaker, "GaSb/InGaAs quantum dot–well hybrid structure active regions in solar cells", *Solar Energy Mater. Solar Cells,* vol. 114, pp. 165-171, 2013.

[164] S. Hubbard, C. Cress, C. Bailey, R. Raffaelle, S. Bailey and D. Wilt, "Effect of strain compensation on quantum dot enhanced GaAs solar cells", *Appl. Phys. Lett.,* vol. 92, p. 123512, 2008.

[165] R. Laghumavarapu, M. El-Emawy, N. Nuntawong, A. Moscho, L. Lester and D. Huffaker, "Improved device performance of InAs/GaAs quantum dot solar cells with GaP strain compensation layers", *Appl. Phys. Lett.,* vol. 91, pp. 243115-243115, 2007.

[166] R. Oshima, A. Takata and Y. Okada, "Strain-compensated InAs/GaNAs quantum dots for use in high-efficiency solar cells", *Appl. Phys. Lett.,* vol. 93, p. 3111, 2008.

[167] Y. Okada, T. Morioka, K. Yoshida, R. Oshima, Y. Shoji, T. Inoue and T. Kita, "Increase in photocurrent by optical transitions via intermediate quantum states in direct-doped InAs/GaNAs strain-compensated quantum dot solar cell", *J. Appl. Phys.,* vol. 109, p. 024301, 2011.

[168] D. Alonso-Álvarez, A. Taboada, J. M. Ripalda, B. Alén, Y. González, L. González, J. M. García, F. Briones, A. Marti and A. Luque, "Carrier recombination effects in strain compensated quantum dot stacks embedded in solar cells", *Appl. Phys. Lett.,* vol. 93, p. 123114, 2008.

[169] R. Oshima, A. Takata, Y. Shoji, K. Akahane and Y. Okada, "InAs/GaNAs strain-compensated quantum dots stacked up to 50 layers for use in high-efficiency solar cell", *Physica E: Low-Dimensional Systems and Nanostructures,* vol. 42, pp. 2757-2760, 2010.

[170] K. A. Sablon, J. W. Little, V. Mitin, A. Sergeev, N. Vagidov and K. Reinhardt, "Strong enhancement of solar cell efficiency due to quantum dots with built-in charge", *Nano Letters,* vol. 11, pp. 2311-2317, 2011.

[171] Y. Okada, R. Oshima and A. Takata, "Characteristics of InAs/GaNAs strain-compensated quantum dot solar cell", *J. Appl. Phys.,* vol. 106, p. 4306, 2009.

[172] A. Takata, R. Oshima, Y. Shoji, K. Akahane and Y. Okada, "Fabrication of 100 layer-stacked InAs/GaNAs strain-compensated quantum dots on GaAs (001) for application to intermediate band solar cell", in *Photovoltaic Specialists Conference (PVSC), 2010 35th IEEE,* 2010, pp. 001877-001880.

[173] A. Freundlich, A. Fotkatzikis, L. Bhusal, L. Williams, A. Alemu, W. Zhu, J. Coaquira, A. Feltrin and G. Radhakrishnan, "III–V dilute nitride-based multi-quantum well solar cell", *J. Cryst. Growth,* vol. 301, pp. 993-996, 2007.

[174] E. Pavelescu, C. Peng, T. Jouhti, J. Konttinen, W. Li, M. Pessa, M. Dumitrescu and S. Spanulescu, "Effects of insertion of strain-mediating layers on luminescence properties of 1.3-µm GaInNAs/GaNAs/GaAs quantum-well structures", *Appl. Phys. Lett.,* vol. 80, pp. 3054-3056, 2002.

[175] I. A. Buyanova, W. Chen and C. Tu, "Recombination processes in N-containing III–V ternary alloys", *Solid-State Electronics,* vol. 47, pp. 467-475, 2003.

[176] D. Friedman, J. Geisz, S. R. Kurtz and J. Olson, "1-eV solar cells with GaInNAs active layer", *J. Cryst. Growth,* vol. 195, pp. 409-415, 1998.

[177] A. Ptak, S. Johnston, S. Kurtz, D. Friedman and W. Metzger, "A comparison of MBE-and MOCVD-grown GaInNAs", *J. Cryst. Growth,* vol. 251, pp. 392-398, 2003.

[178] S. Kurtz, J. Geisz, D. Friedman, W. Metzger, R. King and N. Karam, "Annealing-induced-type conversion of GaInNAs", *J. Appl. Phys.,* vol. 95, pp. 2505-2508, 2004.

[179] R. Kaplar, D. Kwon, S. Ringel, A. Allerman, S. R. Kurtz, E. Jones and R. Sieg, "Deep levels in p-and n-type InGaAsN for high-efficiency multi-junction III–V solar cells", *Solar Energy Mater. Solar Cells,* vol. 69, pp. 85-91, 2001.

[180] D. Kwon, R. Kaplar, S. Ringel, A. Allerman, S. R. Kurtz and E. Jones, "Deep levels in p-type InGaAsN lattice matched to GaAs", *Appl. Phys. Lett.,* vol. 74, pp. 2830-2832, 1999.

[181] R. Kaplar, S. Ringel, S. R. Kurtz, J. Klem and A. Allerman, "Deep-level defects in InGaAsN grown by molecular-beam epitaxy", *Appl. Phys. Lett.,* vol. 80, pp. 4777-4779, 2002.

[182] S. Johnston, R. Ahrenkiel, A. Ptak, D. Friedman and S. Kurtz, "Defect Trapping in InGaAsN Measured by Deep-Level Transient Spectroscopy", *No. NREL/CP-520-33557. National Renewable Energy Laboratory (NREL), Golden, CO.,* 2003.

[183] J. S. Harris, R. Kudrawiec, H. Yuen, S. Bank, H. Bae, M. Wistey, D. Jackrel, E. Pickett, T. Sarmiento and L. Goddard, "Development of GaInNAsSb alloys: growth, band structure, optical properties and applications", *Physica Status Solidi-B-Basic Solid State Physics,* vol. 244, pp. 2707-2729, 2007.

[184] D. B. Jackrel, S. R. Bank, H. B. Yuen, M. A. Wistey, J. S. Harris Jr, A. J. Ptak, S. W. Johnston, D. J. Friedman and S. R. Kurtz, "Dilute nitride GaInNAs and GaInNAsSb solar cells by molecular beam epitaxy", *J. Appl. Phys.,* vol. 101, p. 114916, 2007.

[185] F. Abulfotuh, A. Balcioglu, D. Friedman, J. Geisz and S. Kurtz, "Investigation of deep levels in GaInNAs", in *AIP Conference Proceedings,* 1998, pp. 492-498.

[186] F. Langer, S. Perl, S. Höfling and M. Kamp, "p-to n-type conductivity transition in 1.0 eV GaInNAs solar cells controlled by the V/III ratio", *Appl. Phys. Lett.,* vol. 106, p. 063905, 2015.

[187] K. Bertness, S. R. Kurtz, D. Friedman, A. Kibbler, C. Kramer and J. Olson, "29.5%-efficient GaInP/GaAs tandem solar cells", *Appl. Phys. Lett.,* vol. 65, pp. 989-991, 1994.

[188] N. Koguchi, S. Takahashi and T. Chikyow, "New MBE growth method for InSb quantum well boxes", *J. Cryst. Growth,* vol. 111, pp. 688-692, 1991.

[189] N. Koguchi, K. Ishige and S. Takahashi, "New selective molecular-beam epitaxial growth method for direct formation of GaAs quantum dots", *Journal of Vacuum Science & Technology B,* vol. 11, pp. 787-790, 1993.

[190] T. Mano, T. Kuroda, M. Yamagiwa, G. Kido, K. Sakoda and N. Koguchi, "Lasing in GaAs⁄AlGaAs self-assembled quantum dots", *Appl. Phys. Lett.,* vol. 89, p. 183102, 2006.

[191] C. Heyn, A. Stemmann, A. Schramm, H. Welsch, W. Hansen and A. Nemcsics, "Regimes of GaAs quantum dot self-assembly by droplet epitaxy", *Physical Review B,* vol. 76, p. 075317, 2007.

[192] S. Sanguinetti, T. Mano, A. Gerosa, C. Somaschini, S. Bietti, N. Koguchi, E. Grilli, M. Guzzi, M. Gurioli and M. Abbarchi, "Rapid thermal annealing effects on self-assembled quantum dot and quantum ring structures", *J. Appl. Phys.,* vol. 104, p. 3519, 2008.

[193] Z. M. Wang, B. Liang, K. Sablon and G. Salamo, "Nanoholes fabricated by self-assembled gallium nanodrill on GaAs (100)", *Appl. Phys. Lett.,* vol. 90, p. 113120, 2007.

[194] A. Stemmann, C. Heyn, T. Köppen, T. Kipp and W. Hansen, "Local droplet etching of nanoholes and rings on GaAs and AlGaAs surfaces", *Appl. Phys. Lett.,* vol. 93, p. 123108, 2008.

[195] C. Heyn, A. Stemmann and W. Hansen, "Nanohole formation on AlGaAs surfaces by local droplet etching with gallium", *J. Cryst. Growth,* vol. 311, pp. 1839-1842, 2009.

[196] C. Heyn, A. Stemmann and W. Hansen, "Dynamics of self-assembled droplet etching", *Appl. Phys. Lett.,* vol. 95, p. 173110, 2009.

[197] C. Heyn, A. Stemmann, T. Köppen, C. Strelow, T. Kipp, M. Grave, S. Mendach and W. Hansen, "Highly uniform and strain-free GaAs quantum dots fabricated by filling of self-assembled nanoholes", *Appl. Phys. Lett.,* vol. 94, p. 183113, 2009.

[198] P. Fulay and J. Lee, *Electronic, Magnetic, and Optical Materials.* CRC Press, 2013.

[199] A. Polimeni, A. Patane, M. Henini, L. Eaves and P. Main, "Temperature dependence of the optical properties of InAs/A l$_y$Ga$_{1-y}$As self-organized quantum dots," *Physical Review B,* vol. 59, p. 5064, 1999.

[200] D. Lubyshev, P. González-Borrero, E. Marega Jr, E. Petitprez, N. La Scala Jr and P. Basmaji, "Exciton localization and temperature stability in self-organized InAs quantum dots", *Appl. Phys. Lett.,* vol. 68, pp. 205-207, 1996.

[201] Y. Dai, J. Fan, Y. Chen, R. Lin, S. Lee and H. Lin, "Temperature dependence of photoluminescence spectra in InAs/GaAs quantum dot superlattices with large thicknesses", *J. Appl. Phys.,* vol. 82, pp. 4489-4492, 1997.

[202] S. Sanguinetti, K. Watanabe, T. Kuroda, F. Minami, Y. Gotoh and N. Koguchi, "Effects of post-growth annealing on the optical properties of self-assembled GaAs/AlGaAs quantum dots", *J. Cryst. Growth,* vol. 242, pp. 321-331, 2002.

[203] V. Mantovani, S. Sanguinetti, M. Guzzi, E. Grilli, M. Gurioli, K. Watanabe and N. Koguchi, "Low density GaAs/AlGaAs quantum dots grown by modified droplet epitaxy", *J. Appl. Phys.,* vol. 96, pp. 4416-4420, 2004.

[204] A. Khan, S. R. Kurtz, S. Prasad, S. Johnston and J. Gou, "Correlation of nitrogen related traps in InGaAsN with solar cell properties", *Appl. Phys. Lett.,* vol. 90, p. 243509, 2007.

[205] M. A. Wistey, S. R. Bank, H. B. Yuen, H. Bae and J. S. Harris, "Nitrogen plasma optimization for high-quality dilute nitrides", *J. Cryst. Growth,* vol. 278, pp. 229-233, 2005.

[206] Z. Pan, L. Li, W. Zhang, Y. Lin and R. Wu, "Kinetic modeling of N incorporation in GaInNAs growth by plasma-assisted molecular-beam epitaxy", *Appl. Phys. Lett.,* vol. 77, pp. 214-216, 2000.

[207] X. Liu, A. Prasad, J. Nishio, E. Weber, Z. Liliental-Weber and W. Walukiewicz, "Native point defects in low-temperature-grown GaAs", *Appl. Phys. Lett.,* vol. 67, pp. 279-281, 1995.

[208] T. Kageyama, T. Miyamoto, M. Ohta, T. Matsuura, Y. Matsui, T. Furuhata and F. Koyama, "Sb surfactant effect on GaInAs/GaAs highly strained quantum well lasers emitting at 1200 nm range grown by molecular beam epitaxy", *J. Appl. Phys.,* vol. 96, pp. 44-48, 2004.

[209] M. Henini, *Dilute Nitride Semiconductors.* Elsevier, 2004.

[210] X. Yang, M. Jurkovic, J. Heroux and W. Wang, "Low threshold InGaAsN/GaAs single quantum well lasers grown by molecular beam epitaxy using Sb surfactant", *Electron. Lett.,* vol. 35, pp. 1081-1082, 1999.

[211] N. Miyashita, N. Ahsan and Y. Okada, "Effect of antimony on uniform incorporation of nitrogen atoms in GaInNAs films for solar cell application", *Solar Energy Mater. Solar Cells,* vol. 111, pp. 127-132, 2013.

[212] F. Dimroth, A. Howard, J. Shurtleff and G. Stringfellow, "Influence of Sb, Bi, Tl, and B on the incorporation of N in GaAs", *J. Appl. Phys.,* vol. 91, pp. 3687-3692, 2002.

[213] F. Abulfotuh, A. Balcioglu, D. Friedman, J. Geisz and S. Kurtz, "Investigation of deep levels in GaInNAs", *AIP Conference Proceedings,* pp. 492-498, 1998.

[214] K. Volz, T. Torunski and W. Stolz, "Detection of nanometer-sized strain fields in (GaIn)(NAs) alloys by specific dark field transmission electron microscopic imaging", *J. Appl. Phys.,* vol. 97, p. 014306, 2005.

[215] O. Rubel, K. Volz, T. Torunski, S. Baranovskii, F. Grosse and W. Stolz, "Columnar (001)-oriented nitrogen order in Ga (NAs) and (GaIn)(NAs) alloys", *Appl. Phys. Lett.,* vol. 85, pp. 5908-5910, 2004.

[216] K. Volz, T. Torunski, B. Kunert, O. Rubel, S. Nau, S. Reinhard and W. Stolz, "Specific structural and compositional properties of (GaIn)(NAs) and their influence on optoelectronic device performance", *J. Cryst. Growth,* vol. 272, pp. 739-747, 2004.

[217] A. Aho, V. Korpijärvi, A. Tukiainen, J. Puustinen and M. Guina, "Incorporation model of N into GaInNAs alloys grown by radio-frequency plasma-assisted molecular beam epitaxy", *J. Appl. Phys.,* vol. 116, p. 213101, 2014.

[218] A. Aho, A. Tukiainen, V. Polojärvi, J. Salmi and M. Guina, "High current generation in dilute nitride solar cells grown by molecular beam epitaxy", in *SPIE OPTO,* p. 86201, 2013.

[219] A. Aho, A. Tukiainen, V. Polojärvi, J. Salmi and M. Guina, "MBE growth of high current dilute III-VN single and triple junction solar cells", in *27th European Photovoltaic Solar Energy Conference, 24–28 September 2012; Frankfurt,* pp. 290-292, 2012.

[220] A. Janotti, S. Wei, S. Zhang, S. Kurtz and C. Van de Walle, "Interactions between nitrogen, hydrogen, and gallium vacancies in $GaAs_{1-x}N_x$ alloys", *Physical Review B,* vol. 67, p. 161201, 2003.

[221] X. Liu, A. Prasad, J. Nishio, E. Weber, Z. Liliental-Weber and W. Walukiewicz, "Native point defects in low-temperature-grown GaAs", *Appl. Phys. Lett.,* vol. 67, pp. 279-281, 1995.

[222] J. Gebauer, R. Krause-Rehberg, S. Eichler, M. Luysberg, H. Sohn and E. Weber, "Ga vacancies in low-temperature-grown GaAs identified by slow positrons", *Appl. Phys. Lett.,* vol. 71, pp. 638-640, 1997.

[223] J. Gebauer, F. Borner, R. Krause-Rehberg, P. Specht and E. Weber, "Vacancies in low-temperature-grown GaAs: Observations by positron annihilation," in *Semiconducting and Insulating Materials, 1998. (SIMC-X) Proceedings of the 10th Conference on Semiinsulating and Conducting Materials,* pp. 118-121, 1998.

[224] D. Murdick, X. Zhou and H. Wadley, "Low-temperature atomic assembly of stoichiometric gallium arsenide from equiatomic vapor", *J. Cryst. Growth,* vol. 286, pp. 197-204, 2006.

[225] B. Bouzazi, N. Kojima, Y. Ohshita and M. Yamaguchi, "Capacitance–voltage and current–voltage characteristics for the study of high background doping and conduction mechanisms in GaAsN grown by chemical beam epitaxy", *J. Alloys Compounds,* vol. 552, pp. 469-474, 2013.

[226] G. Jaschke, R. Averbeck, L. Geelhaar and H. Riechert, "Low threshold InGaAsN/GaAs lasers beyond 1500 nm", *J. Cryst. Growth,* vol. 278, pp. 224-228, 2005.

[227] V. Odnoblyudov, A. Y. Egorov, A. Kovsh, A. Zhukov, N. Maleev, E. Semenova and V. Ustinov, "Thermodynamic analysis of the MBE growth of GaInAsN", *Semiconductor Science and Technology,* vol. 16, pp. 831, 2001.

[228] A. Y. Egorov, D. Bernklau, B. Borchert, S. Illek, D. Livshits, A. Rucki, M. Schuster, A. Kaschner, A. Hoffmann and G. Dumitras, "Growth of high quality InGaAsN heterostructures and their laser application", *J. Cryst. Growth,* vol. 227, pp. 545-552, 2001.

[229] Q. Zhuang, A. Krier and C. Stanley, "Strain enhancement during annealing of GaAsN alloys", *J. Appl. Phys.,* vol. 101, p. 103536, 2007.

[230] I. Buyanova, G. Pozina, P. Hai, N. Thinh, J. Bergman, W. Chen, H. Xin and C. Tu, "Mechanism for rapid thermal annealing improvements in undoped GaNxAs1−x/GaAs structures grown by molecular beam epitaxy", *Appl. Phys. Lett.,* vol. 77, pp. 2325-2327, 2000.

[231] S. Bharatan, S. Iyer, K. Nunna, W. Collis, K. Matney, J. Reppert, A. Rao and P. Kent, "The effects of annealing on the structural, optical, and vibrational properties of lattice-matched GaAsSbN⁄GaAs grown by molecular beam epitaxy", *J. Appl. Phys.,* vol. 102, p. 023503, 2007.

[232] L. Bian, D. Jiang, P. Tan, S. Lu, B. Sun, L. Li and J. Harmand, "Photoluminescence characteristics of GaAsSbN/GaAs epilayers lattice-matched to GaAs substrates", *Solid State Commun.,* vol. 132, pp. 707-711, 2004.

[233] V. Korpijärvi, A. Aho, P. Laukkanen, A. Tukiainen, A. Laakso, M. Tuominen and M. Guina, "Study of nitrogen incorporation into GaInNAs: The role of growth temperature in molecular beam epitaxy", *J. Appl. Phys.,* vol. 112, p. 023504, 2012.

[234] K. Volz, D. Lackner, I. Nemeth, B. Kunert, W. Stolz, C. Baur, F. Dimroth and A. Bett, "Optimization of annealing conditions of (GaIn)(NAs) for solar cell applications", *J. Cryst. Growth,* vol. 310, pp. 2222-2228, 2008.

[235] N. C. Patra, S. Bharatan, J. Li and S. Iyer, "Annealing studies of heteroepitaxial InSbN on GaAs grown by molecular beam epitaxy for long-wavelength infrared detectors", *J. Appl. Phys.,* vol. 112, p. 083107, 2012.

[236] A. Aho, R. Isoaho, A. Tukiainen, V. Polojärvi, T. Aho, M. Raappana and M. Guina, "Temperature coefficients for GaInP/GaAs/GaInNAsSb solar cells," in *11TH INTERNATIONAL CONFERENCE ON CONCENTRATOR PHOTOVOLTAIC SYSTEMS: CPV-11,* p. 050001, 2015.

[237] V. Polojärvi, A. Aho, A. Tukiainen, M. Raappana, T. Aho, A. Schramm and M. Guina, "Deep levels in dilute nitride antimonide solar cell", *Proceedings of the 29th European Photovoltaic Solar Energy Conference and Exhibition, EU PVSEC 2014, September 22-26, 2014*, Amsterdam, the Netherlands 2014.

[238] A. Aho, Doctoral thesis, "Dilute Nitride Multijunction Solar Cells Grown by Molecular Beam Epitaxy," Tampere University of Technology, Publication 1343, 2015.

[239] V. Polojärvi, A. Aho, A. Tukiainen, M. Raappana, T. Aho, M. Guina, "High-efficiency dilute nitride multijunction solar cells: influence of point defects on the photovoltaic performance", *Photovoltaic technical conference - From advanced materials and processes to innovative applications, 9–11 May 2016*, Villa Méditerranée, Marseille (France), 2016.

[240] A. Tukiainen, A. Aho, G. Gori, V. Polojärvi, M. Casale, E. Greco, R. Isoaho, T. Aho, M. Raappana, R. Campesato, and M. Guina, " High-efficiency GaInP/GaAs/GaInNAs solar cells grown by combined MBE-MOCVD technique", accepted for publication in *Progress in Photovoltaics*, 2016.

ORIGINAL PAPERS

I

EFFECTS OF $(NH_4)_2S$ AND NH_4OH SURFACE TREATMENTS PRIOR TO SiO_2 CAPPING AND THERMAL ANNEALING OF 1.3 µm GaInAsN/GaAs QUANTUM WELL STRUCTURES

by

Ville Polojärvi, Joel Salmi, Andreas Schramm, Antti Tukiainen, Mircea Guina,
Janne Pakarinen, Eero Arola, Jouko Lång, Juhani Väyrynen,
and Pekka Laukkanen

Applied Physics Letters vol. 97, pp. 111109:1–111109:3, 2010.

APPLIED PHYSICS LETTERS **97**, 111109 (2010)

Effects of $(NH_4)_2S$ and NH_4OH surface treatments prior to SiO_2 capping and thermal annealing on 1.3 μm GaInAsN/GaAs quantum well structures

V. Polojärvi,[1,a)] J. Salmi,[1] A. Schramm,[1] A. Tukiainen,[1] M. Guina,[1] J. Pakarinen,[2]
E. Arola,[3] J. Lång,[4] I. J. Väyrynen,[4] and P. Laukkanen[4]
[1]*Optoelectronics Research Centre, Tampere University of Technology, FIN-33101 Tampere, Finland*
[2]*VTT Technical Research Center of Finland, P.O. Box 1000, 02044 VTT Espoo, Finland*
[3]*Department of Physics, Tampere University of Technology, FIN-33101 Tampere, Finland*
[4]*Department of Physics and Astronomy, University of Turku, FIN-20014 Turku, Finland*

(Received 1 April 2010; accepted 18 August 2010; published online 15 September 2010)

We report the influence of $(NH_4)_2S$ and NH_4OH surface treatments prior to SiO_2 capping and subsequent rapid thermal annealing, on optical properties of GaInAsN/GaAs quantum-well (QW) structures. We observed an increase in QW photoluminescence (PL) emission for the $(NH_4)_2S$ treated samples as compared to the untreated sample. After annealing, also the NH_4OH treated sample showed significant improvement in PL. The treatments were also found to decrease the In out-diffusion and reduce the blueshift upon annealing. The PL results are discussed with x-ray diffraction and x-ray photoemission data from SiO_2/GaAs, in particular, with changes found in Ga 3*d* spectra. © *2010 American Institute of Physics*. [doi:10.1063/1.3487784]

Silicon dioxide (SiO_2) layers are routinely deposited onto III-V semiconductors for device fabrication. They are used for surface protection during device processing and annealing,[1] for electrical insulation in laser applications,[1] in antireflection coatings and distributed Bragg reflectors,[2] and in metal-insulator-semiconductor (MIS) transistors.[3–5] Various surface treatments and passivations of III-V semiconductors have been studied to improve the interface quality of MIS and other transistor structures,[6–21] since the formation of the III-V oxides at the interfaces causes harmful defects in MIS devices.[12,16–21] For example, ammonium sulfide $[(NH_4)_2S]$ and ammonium hydroxide (NH_4OH) treatments remove intrinsic surface oxides of GaAs. However, there are indications that some form of Ga oxides improves the MIS interface.[21,22] Nevertheless, it has remained unclear how the surface treatments prior to SiO_2 capping affect light-emitting devices, in which quantum wells (QWs) locate well below the SiO_2/III-V semiconductor interface. Also, the effects of rapid thermal annealing (RTA) in pre-treated samples have been unclear. The RTA is often used to improve the crystal quality of device materials and is an important step in device fabrication.

In this paper we report that the $(NH_4)_2S$ and NH_4OH surface treatments, prior to the SiO_2 capping and subsequent RTA, significantly affect to photoluminescence (PL) emission from the GaInAsN/GaAs QW structures. In particular, the treated samples exhibit less blueshift (BS) of the PL spectra upon the RTA. Reduced BS can be attributed to a reduced indium out-diffusion from the QWs, as supported by our x-ray diffraction (XRD) measurements. Furthermore, x-ray photoelectron spectroscopy (XPS) measurements are used to monitor the oxides at the SiO_2/GaAs interface. The PL findings are discussed in connection with the XPS and XRD data.

The investigated sample was grown by a molecular beam epitaxy system equipped with a radio-frequency nitrogen plasma source. After deposition of a 100 nm thick GaAs buffer layer on the *n*-type GaAs (100) substrate at the substrate temperature (T_{sub}) of 580 °C, the temperature was decreased to $T_{sub}=480$ °C. The active structure was comprised of two 6 nm thick $Ga_{0.62}In_{0.38}As_{0.985}N_{0.015}$/GaAs QWs separated by a 20 nm GaAs barrier. After the QW growth, a 100 nm GaAs layer was grown on the top at $T_{sub}=580$ °C. The as-grown sample emitted PL at $\lambda=1260$ nm. The sample was cleaved into 4×4 mm^2 pieces which were treated in 20% $(NH_4)_2S$ or 30% NH_4OH solutions for 10 s, 2 min, or 30 min (samples S1, S2, S3, OH1, OH2, and OH3, respectively). One sample was left untreated. After the chemical surface treatments, the samples were rinsed in the deionized water, blown dry with nitrogen, and capped with a 120 nm thick SiO_2 layer by means of a plasma-enhanced chemical vapor deposition. The samples were simultaneously annealed at $T_{ann}=750$ °C. The PL emission was measured after each annealing at 20 °C with an Nd:YAG laser ($\lambda=532$ nm) and an InGaAs detector array. XRD rocking curves in ω-2θ geometry were recorded by using a double-crystal x-ray diffractometer (Cu K_α radiation). Three separate samples were studied by XPS: untreated, 30 min $(NH_4)_2S$ treated, and 30 min NH_4OH treated, all with 2 nm thick SiO_2 capping layers. Mg K_α radiation was used for the XPS measurements before and after 20 min *in situ* annealing at 600 °C in the XPS chamber.

Figures 1(a) and 1(b) show the PL intensities of the samples S1–S3 and OH1–OH3 during the RTA, respectively. Figure 1(a) shows that the PL intensities of the unannealed samples S1–S3 increase with respect to the reference sample. Annealing further increases the PL intensity in sample S1. The maximum is reached at $t_{ann}\approx 20$ s. However, a decreasing trend in the PL intensity is observed with the samples S1–S3 for long annealing times. Figure 1(b) shows that the PL intensities of the unannealed samples OH1–OH3 are not as much increased as in the case of the samples S1–S3. However, it is interesting to observe that annealing drastically increases the PL intensity from the sample OH3, and an increasing trend in the PL intensity is observed with all NH_4OH treated samples for long annealing times. Figures

---

[a)] Electronic mail: ville.polojarvi@tut.fi.

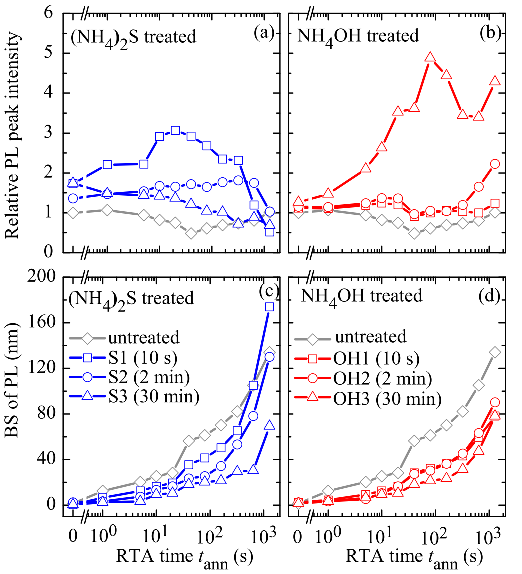

FIG. 1. (Color online) PL peak intensity and BS vs annealing time at T_{ann} =750 °C for samples treated with (NH$_4$)$_2$S (a) and (c), and NH$_4$OH (b) and (d). The behavior of an untreated sample is shown for comparison.

1(c) and 1(d) show the BS of the PL spectra versus the RTA time. The BS for the samples S1 and S2 is clearly suppressed during the RTA when compared to the BS for the untreated sample if $t_{ann} < 500$ s. In sample S3, the BS is significantly reduced for all annealing times. In samples OH1–OH3 the BS is less pronounced at all annealing times. Interestingly, out of all samples studied, the smallest BS is observed for the samples with the longest treatment times.

The PL results are discussed below in connection with XPS data. XPS survey spectra showed that no significant charging took place in our samples since the binding energies and widths of Si 2*p* reference peaks were normal and did not vary between the different samples. The Ga 3*d* spectra were fitted using the previously reported energy shifts for Ga oxides,[21,23] which are 0.6±0.05 eV and 1.2±0.05 eV for the GaO$_X$ and GaO$_Y$ respectively. For the GaO$_Z$, the shift was allowed to vary between 1.6 and 2.0 eV. GaO$_X$, GaO$_Y$, and GaO$_Z$ have been previously related to Ga$_2$O, Ga$_2$O$_3$, and Ga(AsO$_3$)O$_3$, respectively. The minimum number of components was introduced in the fittings,[24] and the doublet component was modeled by a single peak because of limited resolution of the nonmonochromatic radiation used. Figure 2 suggests that the GaO$_Z$ does not have a significant role in the PL behavior, since it is visible only in the nontreated sample and annealed NH$_4$OH treated sample. In contrast, we suggest that the presence of GaO$_Y$ decreases PL intensity since its XPS intensity is higher for the nontreated and NH$_4$OH samples than for the (NH$_4$)$_2$S sample. Furthermore, the GaO$_X$ is suggested to improve the PL since this peak clearly increases after the heating when the PL intensity of the NH$_4$OH sample also enhances. These results are in agreement with previous reports,[21,22,25] according to which one form of a Ga oxide degrades the interface with respect to the PL properties, while another form of a Ga oxide can be useful for the interface quality. In contrast, it is not easy to link the arsenic XPS results (not shown) to the PL measurements. Before heating the XPS spectra from the untreated sample show clear photoemission from As oxides, while the NH$_4$OH and (NH$_4$)$_2$S treated samples do not reveal As oxides. After heating, the amount of As oxides decreases in the nontreated sample.

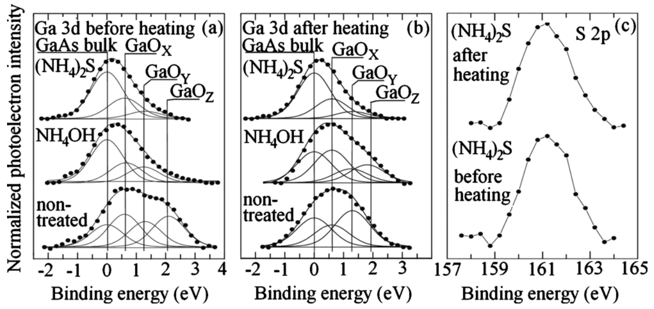

FIG. 2. Fittings of Ga 3*d* spectra measured by XPS (a) before and (b) after heating 20 min at 600 °C for untreated, NH$_4$OH treated, and (NH$_4$)$_2$S treated samples. Binding energy scale is relative to the GaAs bulk components. (c) S 2*p* photoemission spectra for (NH$_4$)$_2$S treated sample before and after heating.

XPS spectra in Fig. 2(c) show that the (NH$_4$)$_2$S treated sample contains sulfur. Analysis of the S 2*p* emission is complicated by the Ga 3*s* and Ga Auger emissions around the S 2*p* energy range. Therefore, we have subtracted the nontreated sample emission from the S 2*p* spectra of the (NH$_4$)$_2$S sample. The same subtraction procedure for the NH$_4$OH sample spectrum shows no S 2*p* like emission. Sulfur is known to passivate the III-V semiconductor surface,[6–8] which is known to increase dramatically the PL intensity.[26] This explains the increase in PL intensity in (NH$_4$)$_2$S treated samples. Furthermore, Fig. 2(c) shows that the S 2*p* XPS signal slightly broadens upon heating. This indicates that the sulfur atoms in the vicinity of the SiO$_2$/GaAs interface possess several nonequivalent bonding configurations, possibly via complex sulfur diffusion processes.[27,28] Therefore, sulfur not only modify the surface states at the SiO$_2$/GaAs interface, but also through interstitial sulfur atom diffusion to GaAs,[28] they may create nonradiative recombination center states. This could explain why the PL intensity, in the case of the (NH$_4$)$_2$S treated samples, starts to decrease toward the end of the annealing period in Fig. 1(a).

The BS of GaInAsN/GaAs QWs is commonly attributed to two distinct phenomena,[29,30] namely, (i) indium outdiffusion from the QWs and (ii) short-range ordering of the nearest-neighbor Ga and In atoms around the N atoms, i.e., the Ga$_{4-m}$In$_m$−N atomic configurations with m=0, 1, 2, 3, and 4, toward the In segregation configuration (m=4). The XRD (004) rocking curves for the (NH$_4$)$_2$S treated samples in Fig. 3(a) show that after the annealing time t_{ann}=1420 s, the QW derived Pendellosung fringes peak move closer to the GaAs peak when the treatment time is decreased. This change in the XRD pattern can be linked to a reduction in the lattice strain due to In out-diffusion from the QWs,[31–33] which is the dominating BS mechanism in our samples. The In diffusion is mainly induced by Ga vacancies and other point defects initially being created at the SiO$_2$/GaAs interface.[34,35] We suggest that the sulfur atoms passivate these vacancies, which would otherwise act as diffusion channels for In. In contrast, the XRD (004) rocking curves in Fig. 3(b) show that all the NH$_4$OH treated samples (t_{ann} =1420 s) experience only minor strain relaxation. Furthermore, the NH$_4$OH treatment suppresses In out-diffusion and the consequent BS of the PL spectra more effectively than the (NH$_4$)$_2$S treatment does. We suggest tentatively that the

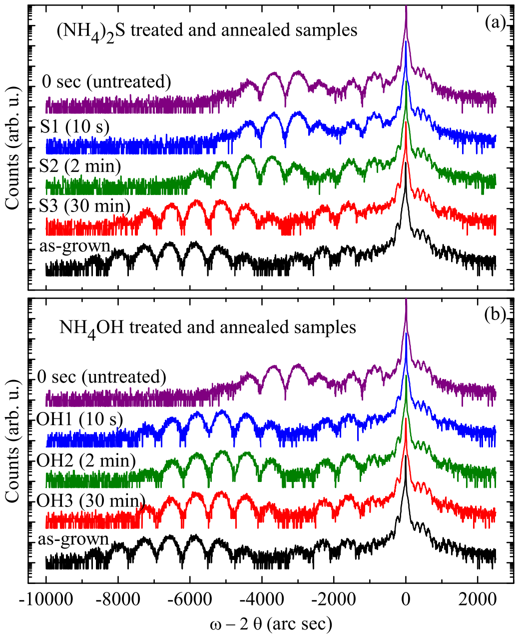

FIG. 3. (Color online) XRD spectra from (a) $(NH_4)_2S$ treated and (b) NH_4OH treated samples after $t_{ann}=1420$ s of annealing at $T_{ann}=750$ °C. For a reference purpose, as-grown XRD rocking curves are also shown (black line).

formed GaO_X bonding configurations at the $SiO_2/GaAs$ interface layer impedes Ga diffusion into SiO_2 and Ga vacancy diffusion into the GaAs, therefore, leading to suppression of In out-diffusion.

In conclusion, we have performed chemical surface treatments on GaInAsN/GaAs QW structures prior to SiO_2 capping and demonstrated that $(NH_4)_2S$ and NH_4OH treatments followed by RTA leads to improvement of the QW PL emission. The gallium vacancy-assisted indium out-diffusion from the QWs and the consequent BS of the PL spectra were also suppressed due to these surface treatments. We suggest that certain specific form of Ga oxides and the presence of sulfur atoms at the $SiO_2/GaAs$ interface play an important role in modifying the optical properties of dilute nitride materials.

The work is supported by the Finnish Funding Agency for Technology and Innovation (TEKES) project Solar III-V (Project No. 40120/09). The authors acknowledge Mr. J. Puustinen and Mr. V.-M. Korpijärvi for MBE growths, and Dr. C. S. Peng for discussions.

[1] M. Jalonen, M. Toivonen, P. Savolainen, J. Köngäs, and M. Pessa, Appl. Phys. Lett. **71**, 479 (1997).
[2] P.-H. Lei and C.-D. Yang, Solid-State Electron. **52**, 227 (2008).
[3] H. Becke, R. Hall, and J. White, Solid-State Electron. **8**, 813 (1965).
[4] H. W. Becke and J. P. White, Electronics **40**, 82 (1967).
[5] H. Altuntaş, Ş. Altındala, H. Shtrikmanb, and S. Özçelika, Microelectron. Reliab. **49**, 904 (2009).
[6] C. J. Sandroff, R. N. Nottenburg, J.-C. Bischoff, and R. Bhat, Appl. Phys. Lett. **51**, 33 (1987).
[7] B. J. Skromme, C. J. Sandroff, E. Yablonovitch, and T. Gmitter, Appl. Phys. Lett. **51**, 2022 (1987).
[8] E. Yablonovitch, C. J. Sandroff, R. Bhat, and T. Gmitter, Appl. Phys. Lett. **51**, 439 (1987).
[9] M. Hong, J. Kwo, A. R. Kortan, J. P. Mannaerts, and A. M. Sergent, Science **283**, 1897 (1999).
[10] H. Hasegawa, N. Negoro, S. Kasai, Y. Ishikawa, and H. Fujikuwa, J. Vac. Sci. Technol. B **18**, 2100 (2000).
[11] N. Negoro, S. Anantathanasarn, and H. Hasegawa, J. Vac. Sci. Technol. B **21**, 1945 (2003).
[12] Y. Liang, J. Kulik, T. C. Eschrich, R. Droopad, Z. Yu, and P. Maniar, Appl. Phys. Lett. **85**, 1217 (2004).
[13] R. F. Klie, Y. Zhu, E. I. Altman, and Y. Liang, Appl. Phys. Lett. **87**, 143106 (2005).
[14] S. Koveshnikov, W. Tsai, I. Ok, J. C. Lee, V. Torkanov, M. Yakimov, and S. Oktyabrsky, Appl. Phys. Lett. **88**, 022106 (2006).
[15] D. Shahrjerdi, E. Tutuc, and S. K. Banerjee, Appl. Phys. Lett. **91**, 063501 (2007).
[16] C. L. Hinkle, A. M. Sonnet, E. M. Vogel, S. McDonnell, G. J. Hughes, M. Milojevic, B. Lee, F. S. Aguirre-Tostado, K. J. Choi, H. C. Kim, J. Kim, and R. M. Wallace, Appl. Phys. Lett. **92**, 071901 (2008).
[17] E. O'Connor, R. D. Long, K. Cherkaoui, K. K. Thomas, F. Chalvet, I. M. Povey, B. Brennan, G. Hughes, and S. B. Newcomb, Appl. Phys. Lett. **92**, 022902 (2008).
[18] B. Shin, D. Choi, J. S. Harris, and P. C. McIntyre, Appl. Phys. Lett. **93**, 052911 (2008).
[19] P. D. Ye, J. Vac. Sci. Technol. A **26**, 697 (2008).
[20] C.-W. Cheng, J. Hennessy, D. Antoniadis, and E. A. Fitzgerald, Appl. Phys. Lett. **95**, 082106 (2009).
[21] C. L. Hinkle, M. Milojevic, B. Brennan, A. M. Sonnet, F. S. Aguirre-Tostado, G. J. Hughes, E. M. Vogel, and R. M. Wallace, Appl. Phys. Lett. **94**, 162101 (2009).
[22] M. J. Hale, S. I. Yi, J. Z. Sexton, A. C. Kummel, and M. Passlack, J. Chem. Phys. **119**, 6719 (2003).
[23] D. C. Suh, Y. D. Cho, S. W. Kim, D.-H. Ko, Y. Lee, M.-H. Cho, and J. Oh, Appl. Phys. Lett. **96**, 142112 (2010).
[24] P. Laukkanen, M. Kuzmin, R. E. Perälä, M. Ahola, S. Mattila, I. J. Väyrynen, J. Sadowski, J. Konttinen, T. Jouhti, C. Peng, M. Saarinen, and M. Pessa, Phys. Rev. B **72**, 045321 (2005).
[25] M. Passlack, Z. Yu, R. Droopad, B. Bowers, C. Overgaard, J. Abrokwah, and A. C. Kummel, J. Vac. Sci. Technol. B **17**, 49 (1999).
[26] Y. T. Oh, S. C. Byun, B. R. Lee, T. W. Kang, C. Y. Hong, S. B. Park, H. K. Lee, and T. W. Kim, J. Appl. Phys. **76**, 1959 (1994).
[27] J. C. Ho, A. C. Ford, Y.-L. Chueh, P. W. Leu, O. Ergen, K. Takei, G. Smith, P. Majhi, J. Bennett, and A. Javey, Appl. Phys. Lett. **95**, 072108 (2009).
[28] J.-L. Lee, J. Appl. Phys. **85**, 807 (1999).
[29] C. S. Peng, H. F. Liu, J. Konttinen, W. Li, and M. Pessa, J. Cryst. Growth **278**, 259 (2005).
[30] M. Hugues, B. Damilano, J.-M. Chauveau, J.-Y. Duboz, and J. Massies, Phys. Rev. B **75**, 045313 (2007).
[31] J. Pakarinen, C. S. Peng, J. Puustinen, P. Laukkanen, V.-M. Korpijärvi, A. Tukiainen, and M. Pessa, Appl. Phys. Lett. **92**, 232105 (2008).
[32] J. Pakarinen, C. S. Peng, V. Polojärvi, A. Tukiainen, V.-M. Korpijärvi, J. Puustinen, M. Pessa, P. Laukkanen, J. Likonen, and E. Arola, Appl. Phys. Lett. **93**, 052102 (2008).
[33] G. Mussler, L. Däweritz, and K. H. Bloog, Appl. Phys. Lett. **87**, 081903 (2005).
[34] B. S. Ooi, K. McIlvaney, M. W. Street, A. S. Helmy, S. G. Ayling, A. C. Bryce, J. H. Marsh, and J. S. Roberts, IEEE J. Quantum Electron. **33**, 1784 (1997).
[35] H. F. Liu, C. S. Peng, E.-M. Pavelescu, T. Jouhti, S. Karirinne, J. Konttinen, and M. Pessa, Appl. Phys. Lett. **84**, 478 (2004).

II

DISLOCATION-INDUCED ELECTRON AND HOLE LEVELS IN InAs QUANTUM-DOT SCHOTTKY DIODES

by

Ville Polojärvi, Andreas Schramm, Arto Aho, Antti Tukiainen, and Markus Pessa

Physica E vol. 42, pp. 2610–2613, 2010.

Physica E 42 (2010) 2610–2613

Contents lists available at ScienceDirect

Physica E

journal homepage: www.elsevier.com/locate/physe

Dislocation-induced electron and hole levels in InAs quantum-dot Schottky diodes

V. Polojärvi, A. Schramm [*], A. Aho, A. Tukiainen, M. Pessa

Optoelectronics Research Centre, Tampere University of Technology, Finland

ARTICLE INFO

Available online 4 November 2009

Keywords:
Nanostructures
Quantum dots
Molecular beam epitaxy
Deep level transient spectroscopy

ABSTRACT

Self-assembled InAs quantum dots (QDs) have been incorporated into GaAs Schottky diodes. We intentionally introduce defects by growing the QDs above the critical thickness for plastic relaxation. The strain-relaxed QDs introduce electrically active defects in n- as well as p-type diodes. We identify dislocation induced defects and point defects, and can show that in n-type GaAs the EL6 defect plays a major role in the relaxation of QDs. Furthermore, we compare the introduction of defects in strain relaxed QDs grown by looped and non-looped deposition and depending on an *in-situ* annealing step. We observe that looped deposited QDs exhibit a better quality compared to non-looped QDs even if they are grown beyond the critical thickness for plastic relaxation. An introduction of an annealing step after the growth of the QDs completely removes the defects in both QD system.

1. Introduction

Strained self-assembled InAs/GaAs quantum dots (QDs) are fascinating nano-objects that exhibit intriguing electronic and optical properties [1]. These can be tailored by growth parameters during the molecular beam epitaxy (MBE) process or post growth treatments. The formation of coherently strained QDs, essential for device applications, takes place only in a small window of growth parameters, e.g., the amount of InAs deposited is restricted to $1.7 < \theta < 2.5$ monolayers (ML) [2,3], with θ the nominal coverage of InAs. Growth beyond the optimal parameters yields plastically relaxed QD structures that have dislocations and may include electrically active defects which degrade device performance.

Here we study Schottky diodes that have intentionally incorporated relaxed QDs by means of deep level transient spectroscopy (DLTS) and capacitance voltage spectroscopy (CV). The relaxed QDs introduce electron as well as hole trap levels. Concentrating on the electron trap levels we identify the nature of defects and discuss a case in which the QD growth conditions are changed.

2. Experimental procedures

The samples were grown in a solid-source MBE growth system on n- and p-type GaAs(1 0 0) substrates. In all samples the InAs quantum dots were grown with a growth rate of $F = 0.06$ monolayer (ML)/s. One set of n-type samples were grown with different amount of InAs, i. e., 1, 2, and 3 ML at $T = 505\,^{\circ}$C. For comparison a p-type Schottky diode were grown with 3 ML QDs. In these aforementioned samples a second QD layer were grown for atomic force microscopy (AFM) on top of the GaAs with same growth parameters as for the embedded ones. AFM measurements reveal no QDs on the 1 ML sample, coherently strained QDs on the 2 ML sample, and coherently strained and additionally coalesced, plastically relaxed QDs on both 3 ML samples. A second set of four n-type samples were grown at $T = 485\,^{\circ}$C with 3 ML QDs deposited either via a looped growth process (1 s indium shutter open and 2 s indium shutter closed) or continuously deposited. In two samples of this set a growth interruption of 10 min at the growth temperature of GaAs of $T = 580\,^{\circ}$C were introduced after capping the samples with 4 nm of GaAs. The other samples did not have a growth interruption. Schottky diodes were fabricated by evaporating chromium and aluminum gates on the n-GaAs and p-GaAs, respectively. The back contact was provided by alloying indium and indium/zinc into the highly doped n- and p-substrates, respectively. The doping level of the Schottky diodes ranges from 2×10^{15} to $2 \times 10^{15}\,\mathrm{cm}^{-3}$. DLTS measurements were performed using nitrogen flow cryostat with variable temperature and a Phystech DLTS spectrometer setup with a Boonton capacitance meter. For the evaluation of emission rates a Fourier analysis were employed [4].

3. Results and discussions

Fig. 1 shows DLTS spectra of n-type Schottky diodes with embedded 1, 2, and 3 ML quantum-dot structures. Whereas no defects are observed in the 1 and 2 ML samples, broad DLTS signals with shoulders can be observed in the 3 ML samples in the entire temperature range of 80–400 K with a maximum at $T \approx 250$ K. Furthermore, we present DLTS spectra of a *p*-type

---

[*] Corresponding author.
E-mail address: andreas.schramm@tut.fi (A. Schramm).

1386-9477/$ - see front matter © 2009 Published by Elsevier B.V.
doi:10.1016/j.physe.2009.10.058

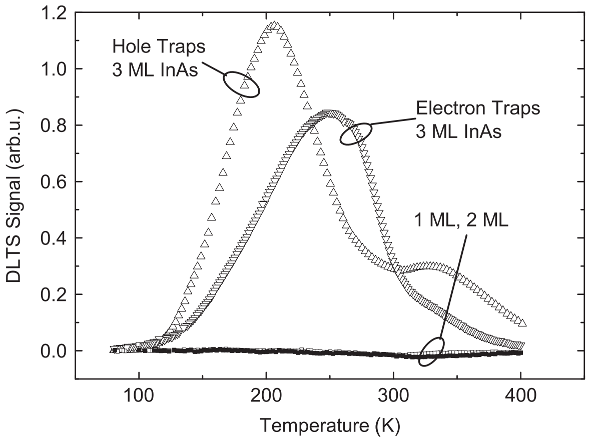

Fig. 1. DLTS spectra of n-Schottky diodes with 1, 2, and 3 ML InAs QDs and a p-type Schottky diode with 3 ML QDs. The reverse and the pulse bias are $V_r = -2.0\,\mathrm{V}$ and $V_p = 0.0\,\mathrm{V}$ for the n-type samples and $V_r = 2.5$ and $V_p = 0.0\,\mathrm{V}$ for the p sample. The pulse duration, the time window, and the emission time are $t_p = 10\,\mathrm{ms}$, $T_w = 100\,\mathrm{ms}$, and $\tau = 44\,\mathrm{ms}$, respectively.

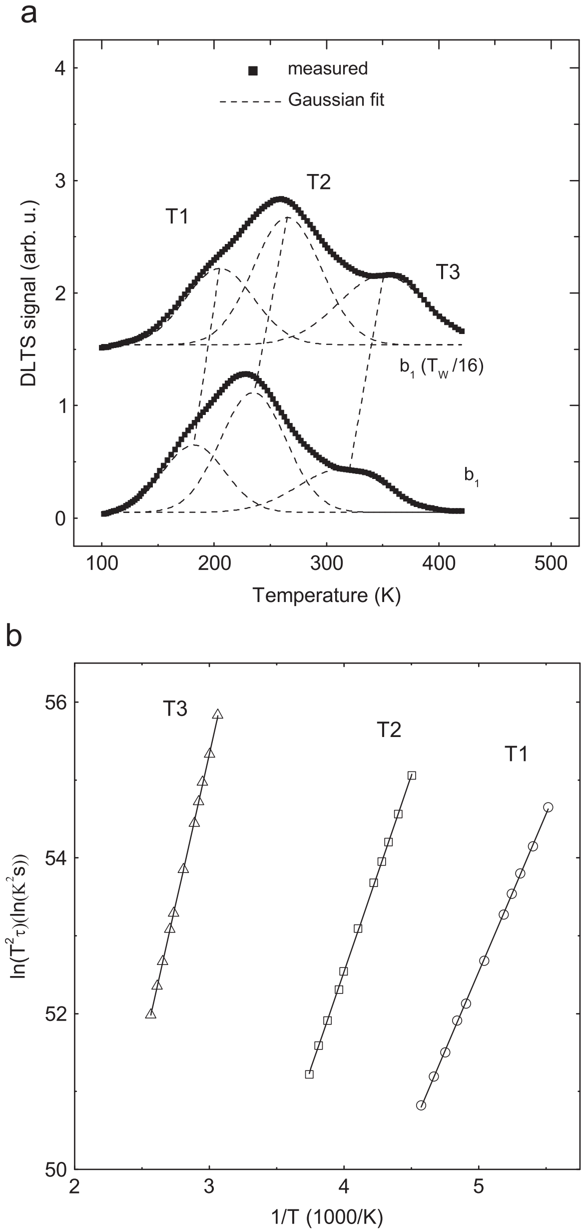

Fig. 2. (a) DLTS spectra of a Schottky diode with 3 ML QDs for different time windows T_w as indicated in the figure. Gaussians are used to fit three defect states and (b) shows the Arrhenius analysis of the defects.

Schottky diode with 3 ML QDs showing also broad DLTS signals in the entire temperature range with maximum at $T \approx 205$ and 330 K. The presence of strain-relaxed QDs grown beyond the critical thickness for coalescence introduces electrically active electron and hole trap levels. Isothermal DLTS scans (not shown here) at the maxima and shoulders in the DLTS spectra in both 3 ML samples, i.e. changing the applied reverse bias and leaving the pulse bias constantly, reveal a strong localization of the defects in close vicinity of the QD layer.

In the following we will concentrate on the n-type Schottky diodes for a more quantitative picture. We used Gaussian peaks shown in Fig. 2(a) in order to fit the broad DLTS spectra. Three Gaussians give satisfying results. Using different rate filter, i.e., in our case shorten the time window T_w shows the typical temperature-dependent shift of the spectra. The Arrhenius analysis for $T1$, $T2$, and $T3$ yield activation energies and capture cross sections of 349, 500, and 664 meV, and 9.6×10^{-15}, 1.0×10^{-14}, and $1.0 \times 10^{-14}\,\mathrm{cm}^{-2}$, respectively.

In order to resolve the nature of these defects, point-defect like or dislocation induced, isothermal DLTS measurements are performed changing the pulse duration sown in Fig. 3. This kind of measurement is the principle argument to decide whether the defect is a point defect or arising from dislocations. Dislocations form defect bands due to closely spaced traps. These bands exhibit a time-dependent Coulomb barrier when the carriers are captured, limiting the successive capture of electrons during the filling process [5,6]. For the trap $T1$ we clearly observe a saturation of the DLTS amplitude at around $t_p \approx 100\,\mathrm{ms}$ suggesting that this defect is a point defect. We assign $T1$ to the EL6 defect [7,8]. Trap $T2$ shows a linear increase in the whole range of measurements. Interestingly, the slope of the amplitude versus $\log(t_p)$ changes when the amplitude of $T1$ saturates. This fact underlines the importance of the EL6 defect in the strain relaxation process of self-assembled InAs quantum dots [9]. Due the not saturating amplitude of $T2$ with increasing t_p, the defect can be identified as dislocation-induced [6,9]. The DLTS amplitude of defect $T3$ shows a saturation at pulse lengths of about 1 s. We tentatively assign $T3$ to the EL2 defect.

In Fig. 4(a)–(i) we present DLTS measurements of Schottky diodes with embedded 3 ML QDs that are grown either via looped or continuous deposition. In each figure the reverse and the pulse bias are varied according to $V_p = V_r + 0.5\,\mathrm{V}$. These measurements are enabling us to screen the QD layer. We observe that the defects of the looped grown QDs starts to appear at lower reverse bias in comparison with the continuously deposited 3 ML QDs (Fig. 4(b)). We further observe that the defects in both samples are localized in the QD layer. Nevertheless, the looped QD sample shows broader spectra with respect to the non-looped relaxed QDs. We suggest that the looped growth enhances the defect formation in the dislocation due to additional ripening effects and thus, the defects are more spread around the quantum dots. Furthermore, two similar samples were grown that have an additional growth interruption of 10 min at $T = 580\,^{\circ}\mathrm{C}$ after capping the QDs with 4 nm GaAs. No defects are observed in the *in-situ* annealed samples. Growth interruptions can be used to eliminate the defects.

The effect of the introduced defects on the carrier confinement in the apparent doping profiles are presented in Fig. 4(j). The annealed samples with the growth interruption show a distinct carrier accumulation in the QDs at a depth of about 480 nm

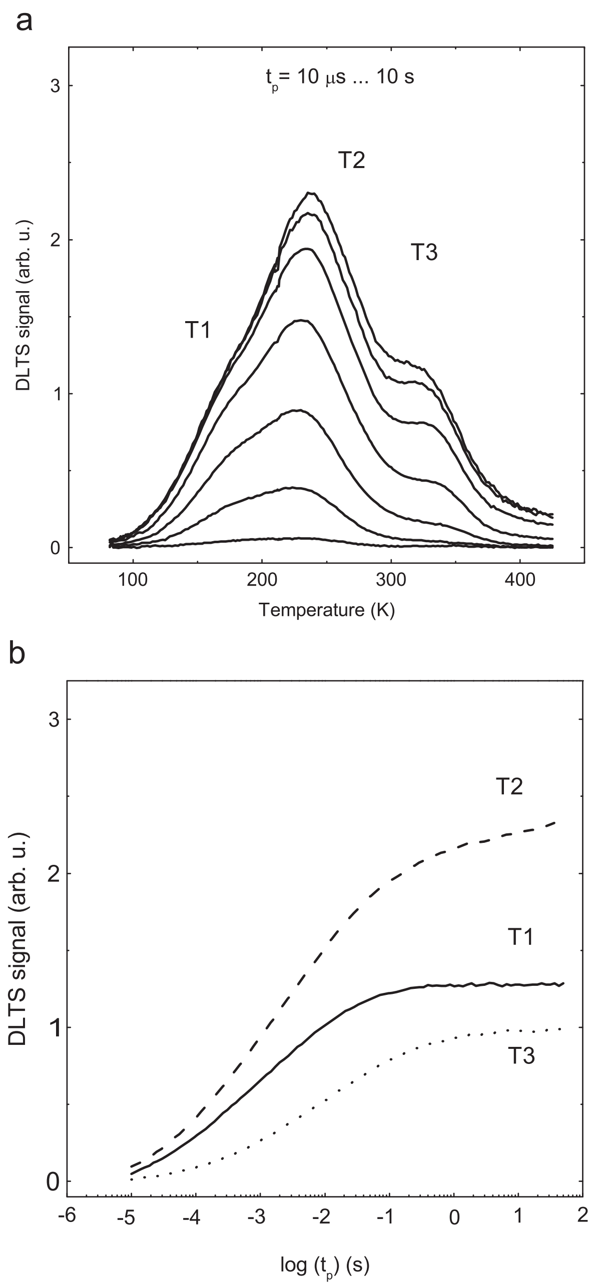

Fig. 3. (a) Pulse-duration dependent DLTS measurements of the n-type Schottky diode with 3 ML QDs. (b) shows the isothermal DLTS experiments at temperatures at the maxima of the Gaussian fits in Fig. 2.

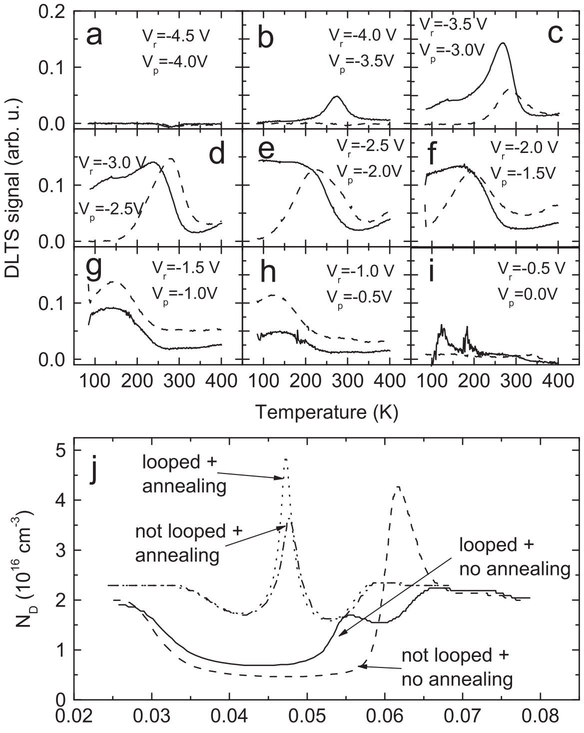

Fig. 4. (a)–(i) DLTS measurements of Schottky diodes with QDs grown via looped (full line) and continuous (dashed line) deposition with varied V_r and V_p as indicated in the figure. The pulse duration, the time window, and the emission time are $t_p = 10$ ms, $T_w = 200$ ms, and $\tau = 87$ ms, respectively and (j) shows doping profiles of the Schottky diodes with looped and continuously grown QDs and with and without annealing step. The data are obtained from 1 MHz CV measurements at 80 K.

accompanied by zones of carrier depletion above and below the QD plane. Whereas the depleted areas are very similar in both annealed samples, the carrier peak in the looped QD Schottky diode is higher compared to the one with continuously grown QDs, which is attributed to a slightly better quality of the looped QDs. This can be further corroborated by discussing the samples without growth interruption. In these samples large depletion can be observed around the QD layer at ≈400 nm. Whereas the non-looped, not-annealed sample shows no carrier confinement in QDs at all, the looped, not annealed sample shows a small carrier accumulation in the QDs at around 550 nm, also accompanied by small carrier depletion zones. Nevertheless, the defects play also the major role in the doping profile observed by the strong depletion of carriers above the QD layer. The strong carrier peak in the non-looped, non-annealed sample at 620 nm is attributed to additional capacitance contributions of the spatially localized defects [10].

4. Conclusion

InAs quantum dots were embedded into GaAs Schottky diodes. We intentionally introduce defects by growing the QDs above the critical thickness for plastic relaxation. The strain-relaxed QDs introduce electrically active defects in n- as well as p-diodes. We identify dislocation induced defects and point defects, and can show that in n-type GaAs the EL6 defect plays a major role in the relaxtion of QDs. Furthermore, we compare the introduction of defects in strain relaxed QDs grown by looped and continuous deposition and depending on an *in-situ* annealing step. We observe that looped deposited QDs exhibit a better quality compared to non-looped QDs even if the are grown beyond the critical thickness for plastic relaxation. An introduction of an annealing step after the growth of the QDs completely removes the defects in both QD system.

Acknowledgments

The authors acknowledge funding from the Academy of Finland via *Dauntless* and *Nanotomo*.

References

[1] M. Grundmann, Nano-Optoelectronics, Springer, Berlin, 2002.
[2] C. Heyn, Phys. Rev. B 64 (2001) 165306.

[3] P. Frigeri, L. Nasi, M. Prezioso, L. Seravalli, G. Trevisi, E. Gombia, R. Mosca, F. Germini, C. Bocci, S. Franchi, J. Appl. Phys. 102 (2007) 083506.
[4] S. Weiss, R. Kassing, Sol. Stat. Electr. 31 (1988) 1733.
[5] T. Figielski, Phys. Status Solidi 121 (1990) 187.
[6] L. Gelczuk, M. Dabrowska-Szata, G. Jozwiak, D. Radziewicz, Physica B 388 (2007) 195.
[7] P. Kaminski, R. Kozlowski, Mat. Sci. Eng. B 91 (2002) 398.
[8] P.W. Yu, G.D. Robinson, J.R. Sizelove, C.E. Stutz, PRB 49 (1994) 4689.
[9] J.F. Chen, C.H. Chiang, P.C. Hsieh, J.S. Wang, J. Appl. Phys. 101 (2007) 033702.
[10] P. Krispin, J.-L. Lazzari, H. Kostial, J. Appl. Phys. 84 (1998) 6135.

III

REMOVAL OF STRAIN RELAXATION INDUCED DEFECTS BY FLUSHING OF InAs QUANTUM DOTS

by

Ville Polojärvi, Andreas Schramm, Arto Aho, Antti Tukiainen, and Mircea Guina

J. Phys. D: Appl. Phys. vol. 45, pp. 365107:1–365107:3, 2012.

IOP Publishing Journal of Physics D: Applied Physics

J. Phys. D: Appl. Phys. **45** (2012) 365107 (5pp) doi:10.1088/0022-3727/45/36/365107

Removal of strain relaxation induced defects by flushing of InAs quantum dots

Ville Polojärvi, Andreas Schramm, Arto Aho, Antti Tukiainen and Mircea Guina

Optoelectronics Research Centre, Tampere University of Technology, FIN-331001, Tampere, Finland

E-mail: ville.polojarvi@tut.fi

Received 3 May 2012, in final form 26 July 2012
Published 24 August 2012
Online at stacks.iop.org/JPhysD/45/365107

Abstract

We report the effect of indium flushing on the electrical and optical properties of strain-relaxed InAs quantum dots (QDs) embedded in GaAs Schottky diodes. The InAs QDs were intentionally grown beyond the critical thickness to induce plastically relaxed QDs. The samples were fabricated by molecular beam epitaxy on GaAs(1 0 0) substrates using continuous and cycled InAs deposition. Deep level transient spectroscopy (DLTS) experiments show broad dislocation-induced defects in non-flushed samples. We show by DLTS that indium flushing after QD deposition decreases remarkably the amount of electron traps in the QD layer and suppresses the defect formation into GaAs capping layer. Using capacitance–voltage measurements we observed that the flushed samples exhibit a recovery of electron confinement in the QD states. Furthermore, we used photoluminescence experiments to analyse the effects of direct versus cycled InAs deposition and indium flushing steps.

(Some figures may appear in colour only in the online journal)

1. Introduction

Self-assembled InAs quantum dots (QDs) obtained by strain-driven Stranski–Krastanov (SK) growth processes [1] has been intensively investigated in the last two decades due to the fascinating possibilities to utilize them in optoelectronics [2, 3]. Large, homogeneous, defect-free ensembles are essential for using QDs in applications, such as lasers, solar cells, semiconductor optical amplifiers, photo detectors or novel memory devices, which exploit charge hysteresis effects [4]. To improve the homogeneity of QDs and to modify the QD properties, several approaches have been carried out, e.g. strain-compensating layers [5], low growth rates [6], and cycled InAs deposition [7, 8]. Furthermore, a major point which is strongly affecting the homogeneity of a QD ensemble is the occurrence of plastically relaxed QDs in which the strain relaxation takes place in the form of dislocations within the QDs. In turn, this leads to the formation of electrically active defect levels in or nearby the QD layer [9, 10]. Such defects can affect the properties of optoelectronic devices by increasing the threshold current densities of lasers and dark currents of photo-detectors. Defects can, in general, decrease the lifetime of semiconductor components and devices. For example, in optoelectronic and QD memory devices, large QD ensembles grown near the critical thickness for the formation of plastically relaxed QDs are required to get the highest possible dot density providing enough gain, optical response or large hysteresis effects. Stacked layers of QDs with high density and aspect ratio are also beneficial for the formation of intermediate band in QD solar cells.

One interesting way to improve the homogeneity of InAs QDs and tune their properties is the so-called *flushing* technique [7, 11, 12]. Flushing of InAs QDs means capping of the QDs by a few nanometres of GaAs followed by *in situ* annealing. Furthermore, this technique can be used to tune the shape, size, composition and optical properties of InAs QDs [12, 13]. In addition, flushing is found to make InAs QD stack more uniform [14], and to remove unwanted InAs clusters decreasing the threshold current densities in QD lasers [15].

In this paper, we investigate the influence of flushing on the electrical and optical properties of plastically relaxed InAs QDs grown with cycled and continuous QD deposition. The QDs have been grown by depositing 3 monolayers (ML) on InAs which is beyond the critical thickness of about 2.5 ML for the formation of relaxed QDs [10]. This results in dislocation-induced defect states in and near the QD layer. The effect

Table 1. Sample labelling.

	Continuous growth	Cycled growth
No flushing	A1	B1
Flushing	A2	B2

of flushing on electrical properties and on electron traps was investigated by deep level transient spectroscopy (DLTS) and capacitance–voltage (*CV*) experiments. Photoluminescence (PL) measurements were carried out to assess the optical properties of QDs, and the results are linked to the DLTS and *CV* observations.

2. Experimental procedures

The samples were grown by solid-source molecular beam epitaxy (MBE) on Si- doped n-type GaAs(1 0 0) substrate with doping concentration of $N_D = 3 \times 10^{18}\,\mathrm{cm}^{-3}$. The QD layer was embedded between two Si-doped GaAs ($N_D = 2\times10^{16}\,\mathrm{cm}^{-3}$) layers with thicknesses of 600 and 400 nm. The growth rate was $F = 1\,\mu\mathrm{m\,h}^{-1}$ and the growth temperature was $T_{gr} = 605\,^{\circ}\mathrm{C}$. InAs QDs were deposited at $T_{gr} = 485\,^{\circ}\mathrm{C}$, with a growth rate of $F = 0.05\,\mu\mathrm{m\,h}^{-1}$ and a coverage of $\theta = 3.0$ ML. The first set consisted of two samples, where InAs QDs were deposited continuously (samples A1 and A2). In the second set, QDs were grown by cycled deposition of InAs with shutter openings times of $t_{open} = 1$ s and a delay time of $t_{delay} = 2$ s (samples B1 and B2). After InAs deposition, the QDs were covered by 4 nm of GaAs and then either exposed to a high-temperature annealing step of 10 min at $T = 605\,^{\circ}\mathrm{C}$ under arsenic flux, before further growth of GaAs (samples A2 and B2), or without flushing step (samples A1 and B1). In the latter case the QD structures were overgrown directly with the GaAs host material. Table 1 summarizes how the investigated samples are labelled. Schottky contacts were formed by evaporating 100 nm thick chromium gates with a diameter of 1 mm. The ohmic back contacts were provided by alloying indium into the highly doped GaAs substrate. Schematic image of the sample structure is presented in figure 1. DLTS and *CV* measurements were performed in a nitrogen flow cryostat using a Boonton capacitance bridge, a lock-in amplifier and Fourier filtering [16]. Room-temperature PL was measured by an Accent RPM2000 PL-mapper, using a 785 nm diode laser for excitation and an InGaAs detector array.

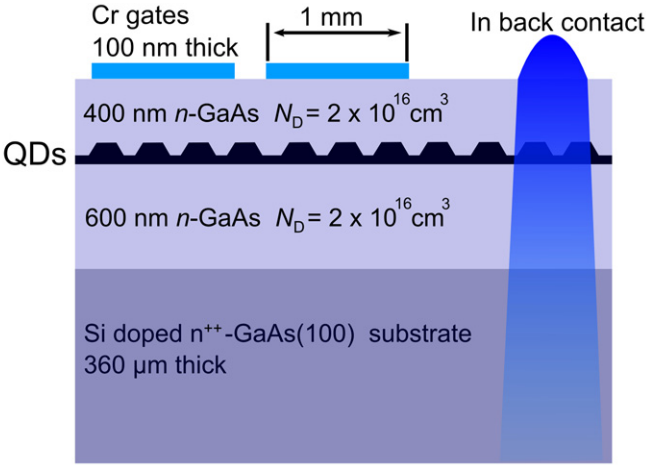

Figure 1. Schematic picture of the sample structure.

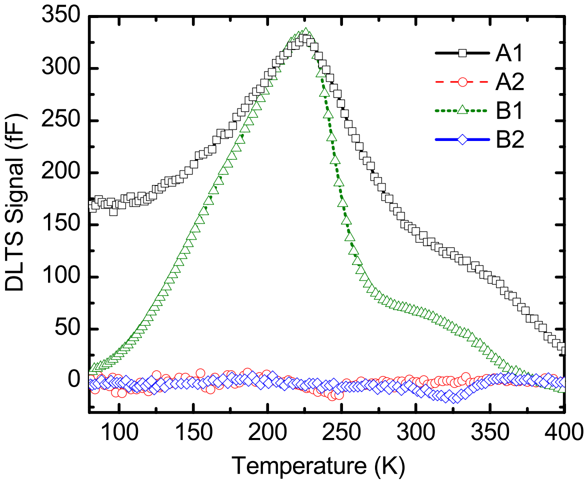

Figure 2. DLTS spectra of samples A1, A2, B2 and B2 with embedded QDs. The reverse and the pulse bias were $V_r = -4.0$ V and $V_p = 0.0$ V, respectively. The pulse duration, the period and the emission time were $t_p = 10$ ms, $t_w = 200$ ms and $\tau = 87$ ms. Samples A2 and B2 with In-flushing step have no signs of defects, whereas samples A1 and B1 grown without flushing step exhibit a broad defect band.

3. Experimental results and discussions

Figure 2 shows the DLTS spectra in a temperature range from 85 to 400 K. One can clearly observe strong DLTS signals nearly in the whole temperature range in the samples A1 and B1 that were grown without flushing step. The DLTS signals of these samples are broad and have maxima with about same height at $T \approx 225$ K. Sample A1 has higher DLTS signal for the all other temperatures investigated. Furthermore, shoulders located at around $T \approx 325$ K are observer in both samples. In contrast to that, samples A2 and B2, grown with the flushing step, show no significant DLTS signals pointing to the absence of trap levels. This result indicates that the flushing removes most of the electrically active defects in the QD region and prevents electrically active defect formation to the GaAs capping layer. The broad peaks in the DLTS spectra of samples A1 and B1 have been identified as dislocation-induced traps in close correspondence to previous publications [9, 10, 17].

The nature of the defects, whether they are point defects or dislocation-related defects, can be evaluated by measuring the amplitude of the DLTS signal versus the pulse duration applied to the Schottky diode. These measurements are exemplarily shown for sample B1 in figure 3(*a*). Sample A1 shows similar behaviour. The measured DLTS signal cannot be saturated even with very long pulses, i.e. in the range of seconds. This behaviour is generally associated with dislocation-related defects [18, 19]. Closely spaced traps in the dislocation-induced defect band are hardly charged with carriers because of a time-dependent repulsive Coulomb-like barrier caused by

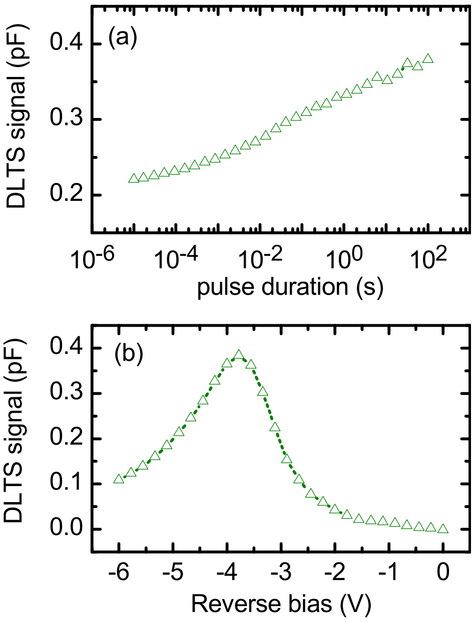

Figure 3. (*a*) Isothermal DLTS signals versus the pulse duration for sample B1 at $T = 220\,^{\circ}\mathrm{C}$ (*b*) Isothermal DLTS measurements for which the reverse bias V_r is varied.

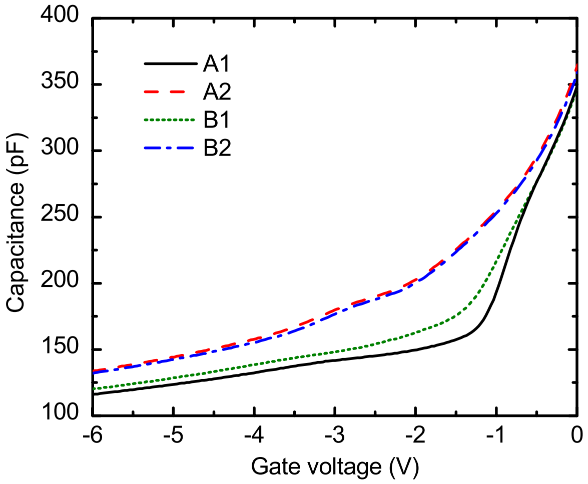

Figure 4. *CV* spectra of samples with embedded InAs QDs, measured at room temperature using $f = 1$ MHz.

a repulsive potential formed at the defect. This is limiting the successive capture of electrons during the filling process. Such an effect would not appear in the case of point defects. Figure 3(*b*) presents isothermal DLTS measurements of sample B1, in which the reverse bias is varied at $T = 220$ K. This temperature corresponds to the DLTS peak shown in figure 2. The maximum value of the isothermal DLTS signal is observed at $V_r = -3.8$ V. Again, sample A1 shows similar behaviour. The voltage and position of the depletion region edge corresponds to the depth of the depletion region in which the QD layer is positioned. This indicates that the dislocation-induced defects are in and/or close to the QD region.

Figure 4 shows *CV* measurements obtained at room temperature. In the samples A2 and B2 the capacitance increases below the gate voltage $V_g < -3.8$ V, according to the doping level of the Schottky diode. Then shallow capacitance plateaus are observed at around $V_g \approx -3.0$ V, indicating the electron confinement in the QD layer due to the intrinsic QD states. At $V_g > -2.0$ V, the capacitance of samples A2 and B2 increases in a similar fashion following the potential distribution in the Schottky diode. The capacitance traces of samples A1 and B1 (without flushing) show a significantly lower value at $V_g = -6.0$ V, when compared with the samples A2 and B2 (with flushing). The slope of the capacitance increase with higher gate voltages is less pronounced in both samples. Furthermore, capacitance plateaus are not observed in samples A1 and B1. At around $V_g \approx -1.0$ V the capacitance of samples A1 and B1 increases and reaches close to similar values at $V_g = 0$ V compared with samples A2 and B2. The *CV* experiments show that the depletion region edge can be below the QD region when the voltage is about $V_g \approx -4$ V; this is because at lower voltages the capacitance behaves as expected for $N_D = 2 \times 10^{16}\,\mathrm{cm}^{-3}$. This is in agreement with DLTS data shown in figure 3(*b*), where the maximum DLTS signal is achieved for $V_r = -3.8$ V. We can conclude that the trap levels are generated by the plastically relaxed QDs that provide deep levels in and nearby the QD layer leading to trapping of electrons and, thus, modifying the *CV* curves. To further analyse the *CV* data, we have calculated the voltage-dependent free carrier concentration [20]

$$N_D(V) = -\frac{2}{A^2 \varepsilon \varepsilon_0 e}\left(\frac{\mathrm{d}(C^{-2})}{\mathrm{d}V}\right)^{-1}, \qquad (1)$$

where A is the diode area, e is the electron charge, ε_r is the dielectric constant of GaAs and ε_0 is the permittivity of vacuum. On the other hand, the capacitance at a certain voltage is inversely proportional to the width of the depletion region edge:

$$C = \frac{\varepsilon \varepsilon_0 A}{x_d}, \qquad (2)$$

where x_d is the width (depth) of the depletion region. By combining these two equations, we calculated the depth profile of free carriers from the *C–V* data. The calculated results are shown in figure 5. It is worth noting that deep levels as well as confined QD states lie below the GaAs conduction band, which causes shifts in calculated free carrier profiles. The deep levels and confined QD states get depleted when depletion region edge is already below these layers, and charge carrier peaks are therefore shifted in calculated depth profiles. The deeper the electron states lie in the GaAs band gap the larger the shift is. A strong depletion of charge carriers is observed at a calculated depth of around 450 nm in the non-flushed samples A1 and B1. This can be explained as being caused by the high concentration of defects in or nearby the QD layer. Electrons are trapped in dislocation-induced defect levels and cannot be released with the signal with a frequency of 1 MHz. The peaks in the calculated doping profiles of the samples A1 and B1 at around 630–650 nm correspond to trapped charge at the QD region due to defect states. Trapped charges are released and are contributing to the capacitance [21, 22]. In samples A2 and B2, which show no defects in the DLTS data, carrier peaks are observed at around 480 nm accompanied by depletion regions below and above. These peaks are associated with electron

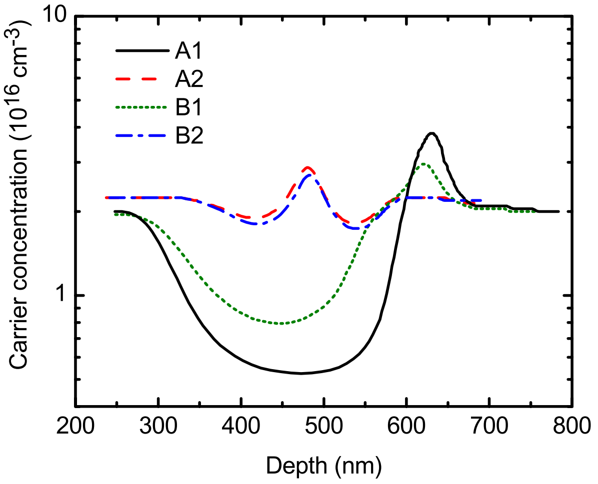

Figure 5. Free carrier profiles of the Schottky diodes calculated using the *CV* measurements at room temperature. Charge accumulation peaks related to deep levels and confined QD states, which lie inside the GaAs band gap, are shifted deeper in the calculated profile than their actual depth in the sample.

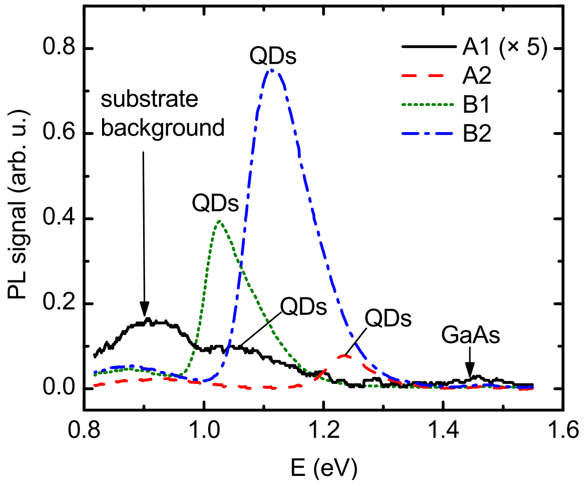

Figure 6. PL spectra of investigated samples. PL emission from GaAs, QDs and background substrate impurities (broad peak at around 1450 nm) are visible.

accumulation and depletion in the QDs and surrounding areas near QDs, respectively. No signs of defects are observed that would degrade the electron transfer between the dots and the GaAs host matrix, which is in agreement with the DLTS data. The flushing step recovers the undisturbed electron exchange in the QDs.

Figure 6 shows room-temperature PL spectra of investigated samples. Three peaks are observed for all the samples: PL emission from GaAs, QDs, and then a broad peak originating from the substrate impurities, labelled as ‘substrate background’. Four observations can be pointed from this PL data: (i) the QD PL signal is larger for samples with cycled InAs deposition, (ii) the PL signal increases with flushing, (iii) the PL signal blue shifts with flushing, and (iv) the shift is larger for sample A2 grown with continuous deposition. Cycled growth results in less as-grown defects, as confirmed by DLTS measurements in figure 1, where sample A1 has broader DLTS peak. This explains the higher PL intensity for sample B1 than for sample A1, which shows hardly detectable QD PL emission. The increase in the PL emission due to flushing is again in agreement with DLTS and *CV* data. The annealing of defects, which causes nonradiative recombination, increases the PL intensity. In-flushing induced blue shift is related to material evaporation and interdiffusion which affect to the size, shape and composition of the QDs [13]. Similar type of effects are also observed for example in post-growth annealed InAs QDs [23], InGaAs quantum wells [24] and InGaAs quantum posts [25]. Material interdiffusion can be expected to be more pronounced when there are more defects acting as a diffusion channels. This explains larger blue shift of sample A2, since sample A1 has broad DLTS spectra and larger amount of defects than sample B1. The shift of the QD PL peak closer to the energy of GaAs band gap is related to a decrease in the confining potential due to the changes in effective size, shape and composition of QDs. This leads to decrease in PL intensity, because the probability of thermal escape of carriers from the QDs is increased. This is one reason why the PL signal of sample A2 with larger blue shift is smaller compared with sample B2. Although the DLTS measurements did not show evidence of defects in flushed samples, there still might be defects which are undetectable with DLTS measurement, at least at used temperature range and measurement parameters. Furthermore, one can only observe electron traps in n-doped Schottky diode, hole traps cannot be detected. Such defects can explain the difference in PL intensity between samples A2 and B2. According to our PL results, cycled deposition of InAs reduces the defect formation.

4. Conclusion

To summarize, we have studied the influence of the In flushing on electrical and optical properties of cycled and continuously deposited InAs QD Schottky diodes. In flushing decreased the amount of QD induced defects in and nearby the QD layer and improved the electrical properties of the diodes. Due to the removal of defects, the quantum confinement effects in the QD layer are recovered. As a consequence of flushing, the PL signals increased and exhibited a blue shift emission, which was found to be more pronounced for samples grown with continuous InAs deposition. Continuous deposition was found to produce more defects compared with cycled deposition.

Acknowledgments

The authors gratefully acknowledge funding from the Finnish Academy by project #138940, and Finnish Funding Agency for Technology and Innovation (TEKES) project Solar III–V (#40120/09). Ville Polojärvi gratefully acknowledges The Emil Aaltonen Foundation for financial support.

References

[1] Bimberg D, Grundmann M and Ledentsov N 1999 *Quantum Dot Heterostructures* (New York: Wiley)
[2] Grundmann M 2002 *Nano-Optoelectronics* (Berlin: Springer)
[3] Ustinov V M, Zhukov A E, Egorov A Y and Maleev N A 2003 *Quantum Dot Lasers* (Oxford: Oxford University Press)

[4] Geller M, Marent A, Nowozin T, Bimberg D, Akcay N and Öncan N 2008 *Appl. Phys. Lett.* **92** 092108

[5] Zhang X Q, Ganapathy S, Suemune I, Kumano H, Uesugi K, Nabetani Y and Matsumoto T 2003 *Appl. Phys. Lett.* **83** 4524

[6] Alloing B, Zinoni C, Li L H, Fiore A and Patriarche G 2007 *J. Appl. Phys.* **101** 024918

[7] Kim J, Yang C, Sim U, Lee G-D, Park J, Lee Y 2011 *J. Appl. Phys.* **110** 044302

[8] Lee Y, Ahn E, Kim J, Moon P, Yang C and Yoon E 2007 *Appl. Phys. Lett.* **90** 033105

[9] Chen J F and Wang J S 2007 *J. Appl. Phys.* **102** 043705

[10] Frigeri P, Nasi L, Prezioso M, Seravalli L, Trevisi G, Gombia E, Mosca R, Germini F, Bocci C and Franchi S 2007 *J. Appl. Phys.* **102** 083506

[11] Wasilewski Z R, Fafard S and McCaffrey J P 1999 *J. Cryst. Growth* **201–202** 1131

[12] Fafard S, Wasilewski Z R, Allen C Nì, Picard D, Spanner M, McCaffrey J P and Piva P G 1999 *Phys. Rev.* B **59** 15368

[13] McCaffrey J P, Robertson M D, Fafard S, Wasilewski Z R, Griswold E M and Madsen L D 2000 *J. Appl. Phys.* **88** 2272

[14] Fafard S, Wasilewski Z R, Allen C Nì, Hinzer K, McCaffrey J P and Feng Y 1999 *Appl. Phys. Lett.* **75** 986

[15] Kaiander I N, Sellin R L, Kettler T, Ledentsov N N, Bimberg D, Zakharov N D and Werner P 2004 *Appl. Phys. Lett.* **84** 2992

[16] Weiss S and Kassing R 1988 *Solid State Electron.* **31** 1733

[17] Polojärvi V, Schramm A, Aho A, Tukiainen A and Pessa M 2010 *Physica* E **42** 2610

[18] Figielski T 1990 *Phys. Status Solidi* **121** 187

[19] Gelczuk Ł, Dąbrowska-Szata M, Jóźwiak G and Radziewicz D 2007 *Physica* B **388** 195

[20] Sze S M 1985 *Semiconductor Devices, Physics and Technology* (New York: Wiley)

[21] Krispin P, Hey R, Kostial H and Ploog K H 1998 *J. Appl. Phys.* **83** 1496

[22] Krispin P, Lazzari J-L and Kostial H 1998 *J. Appl. Phys.* **84** 6135

[23] Pakarinen J, Polojärvi V, Aho A, Laukkanen P, Peng C S, Schramm A, Tukiainen A and Pessa M 2009 *Appl. Phys. Lett.* **94** 072105

[24] Pakarinen J, Peng C S, Puustinen J, Laukkanen P, Korpijärvi V-M, Tukiainen A and Pessa M 2008 *Appl. Phys. Lett.* **92** 232105

[25] Schramm A, Polojärvi V, Hakkarainen T V, Tukiainen A and Guina M 2011 *Semicond. Sci. Technol.* **26** 055017

IV

POST-GROWTH ANNEALING OF TYPE-II GaSb/GaAs QUANTUM DOTS GROWN WITH DIFFERENT V/III RATIOS

by

Ville Polojärvi, Alexander Gubanov, Andreas Schramm, Riku Koskinen, Jonna Paajaste, Joel Salmi, Soile Suomalainen, and Mircea Guina

Mater. Sci. Eng. B vol. 177, pp. 1103–1107, 2012.

Materials Science and Engineering B 177 (2012) 1103–1107

Contents lists available at SciVerse ScienceDirect

Materials Science and Engineering B

journal homepage: www.elsevier.com/locate/mseb

Short communication

Post-growth annealing of type-II GaSb/GaAs quantum dots grown with different V/III ratios

Ville Polojärvi*, Alexander Gubanov, Andreas Schramm, Riku Koskinen, Jonna Paajaste, Joel Salmi, Soile Suomalainen, Mircea Guina

Optoelectronics Research Centre, Tampere University of Technology, FIN-33101 Tampere, Finland

ARTICLE INFO

Article history:
Received 24 January 2012
Received in revised form 24 April 2012
Accepted 28 May 2012
Available online 13 June 2012

Keywords:
Quantum dots
GaSb
Thermal annealing
Photoluminescence
Molecular beam epitaxy
III–V semiconductors

ABSTRACT

We report the influence of V/III beam-equivalent-pressure ratios and post-growth annealing on the photoluminescence of GaSb quantum dots grown on GaAs(1 0 0) by molecular beam epitaxy. Increasing the V/III beam-equivalent-pressure ratio from 3 to 5 and then to 7 results in decreased photoluminescence intensity and redshifts the photoluminescence wavelength. The post-growth annealing blueshifts the quantum dot photoluminescence emission and decreases the full-width-at-half-maximum of the photoluminescence peak when annealing temperature is increased above 800 °C. The blueshift behavior is found to be independent on the V/III ratios indicating a similar atomic interdiffusion mechanism for all investigated samples regardless of the quantum dot properties. The photoluminescence intensities of the three samples experience an increase after moderate annealing. Whereas the intensity of the sample with the highest V/III ratio further increases, the intensity of the sample with lower V/III ratios decreases again upon higher annealing steps above 900 °C. Furthermore, temperature- and power dependent photoluminescence measurements are performed on as-grown and 870 °C annealed samples with V/III ratios of 3 and 7 in order to study the reduced quantum dot confinement in more detail.

1. Introduction

Semiconductor quantum dot (QD) systems fabricated using Stranski-Krastanov (SK) growth processes have attracted great interest during the past two decades owing to unique features. QDs heterostructures render new opportunities for high impact applications including semiconductor lasers, solar cells, and photodetectors [1–8] as well as in single photon sources for quantum computing, quantum cryptography, and quantum logical elements [9–12]. The majority of QD researches and applications has focused on the InAs/GaAs QD system, which exhibit a type-I bandgap alignment. However, QDs with a type-II band structure, such as GaSb/GaAs, are drawing more and more attentions due to their peculiar properties. In GaSb/GaAs QDs the holes are confined while the non-confined electrons are loosely bound by Coulomb interactions leading to spatial charge separations. This gives access, for example, to the presence of Mott transition effects [13]. Furthermore, GaSb QD systems exhibit a wide choice of barrier materials that can be used for band-gap engineering making them to promising candidates for telecomm emitters and solar cells. More recently, GaSb QDs have been pointed out also as promising candidates for development of quantum memory elements [14–16]. Compared to the commonly exploited SK InAs/GaAs QD system, the fabrication of GaSb/GaAs QD system is affected by more growth parameters due to the exchange of the group-V element. For example, one also has to take into account the annealing times prior the QD growth after the exchange of As and Sb in order to get Sb-stabilized surfaces [17]. Furthermore, GaSb QDs do not necessary follow the SK growth mode; they can be grown using an interfacial misfit (IMF) growth mode available for the GaSb/GaAs material system [18–21]. The dominating growth mode depends on the growth conditions, such as V/III beam-equivalent-pressure (BEP) ratio, and the transition from SK to IMF is not abrupt. In the IMF growth mode, the strain of the lattice-mismatched epitaxial layers is relieved by introducing 90° dislocations within the QDs. While SK grown GaSb QDs emit photoluminescence (PL) typically above 1.1 eV [20–29], IMF grown GaSb QDs are generally larger in size and show PL around 0.95 eV [20,21].

In this paper we investigate PL properties of SK-grown GaSb/GaAs QDs using three different V/III BEP ratios, i.e. 3, 5, and 7. In particular, we study the effects of post-growth annealing treatments in the temperature range of 650–970 °C. Annealing leads changes in PL blueshifts, PL peak widths, and intensity variations due to intermixing processes. The results can be used for further studies on GaSb QDs and in development of above mentioned applications.

---

* Corresponding author. Tel.: +358 407265107; fax: +358 331153400.
E-mail address: ville.polojarvi@tut.fi (V. Polojärvi).

0921-5107/$ – see front matter © 2012 Elsevier B.V. All rights reserved.
http://dx.doi.org/10.1016/j.mseb.2012.05.017

2. Experiments

The samples were grown by solid-source molecular beam epitaxy (MBE) using valved crackers for arsenic and antimony. After growth of a 200 nm thick GaAs buffer on *n*-type GaAs(1 0 0) substrate, a 50 nm AlAs, and a 50 nm GaAs layer, we deposited 3 monolayers (ML) of GaSb QDs at a substrate temperature of 485 °C and a growth rate of 0.09 ML/s. Three QD samples were grown using V/III BEP ratios of 3, 5, and 7. For convenience, the samples are referred to as A, B, and C, respectively. The QDs were covered by 50 nm GaAs and 50 nm AlGaAs layers. The growth was finished by a 30 nm GaAs cap layer. For annealing treatments the as-grown samples were cleaved into 4 mm × 4 mm pieces. The sample pieces were annealed using a GaAs proximity cap [30], on a silicon wafer, face up, under N_2 atmosphere. The annealing temperature (T_{ann}) was controlled by an optical pyrometer. The room-temperature PL (RT-PL) spectra were recorded using excitation from a frequency doubled Nd:YAG laser, operating at $\lambda = 532$ nm, and an InGaAs detector. For the low temperature PL (LT-PL) measurements, argon-ion laser, operating at $\lambda = 488$ nm, was used.

3. Results

The recorded RT-PL spectra from samples A, B, and C are displayed in Fig. 1. Sample A shows PL peaks at 1.16 eV and 1.44 eV arising from the GaSb QDs and bulk GaAs, respectively. A shoulder is observed at around 1.31 eV that we attribute to PL from the wetting layer (WL). The PL peak in sample B is redshifted to about 1.13 eV, and the peak intensity is only half of sample A. The PL of sample C, grown with the highest V/III ratio of 7, is further redshifted to about 1.11 eV and the PL peak height accounts to only one third of the intensity of sample A. Only faint shoulder according to WL PL and small peak according to GaAs bulk-PL are observed in samples B and C.

We link the redshift of PL with increasing V/III ratio to an increased QD size, which was confirmed by atomic force microscope AFM (Fig. 2). AFM pictures were measured from reference surface QD samples grown with similar V/III ratios as samples A (V/III = 3), and C (V/III = 7). Smaller III/V ratio of 3 produces QDs with the average QD density of 3.3×10^{10} cm^{-2} whereas larger III/V ratio of 7 results in larger QDs with density of 2.7×10^{10} cm^{-2}. Because the amount of deposited GaSb is constant (3 ML), the increased QD size leads to the decreased QD density. Since the QD density (number of emitters) is closed to similar, it does not explain the differences in PL intensities between the samples: the surface QD density is 1.22 times larger for sample grown with V/III ratio of 3, but the integrated PL intensity of sample A is 2.2 times larger, when compared to sample C. There is also a clear difference in the shape of the QDs. Sample grown with V/III ratio of 3 has round QDs, indicating SK growth mode. Sample with V/III ratio of 7 has slightly rectangular QDs indicating a beginning IFM growth mode. The V/III ratio is known to affect remarkably to the growth mode of GaSb QDs. Transition to IMF growth mode takes place when larger adatom (Sb) is in larger quantity on the growth surface compared to the smaller adatom (Ga) [20]. Therefore, QDs grown with V/III ratio of 7 starts to favor not only SK, but also IMF growth mode. Transition from SK to IMF can be expected not to be abrupt. We propose that the V/III ratio of 7 is close to the border where growth mode changes from SK to IMF. The decrease of PL intensities in samples B and C might be caused by a misfit induced nonradiative recombination in the QD layer due to approaching the transition of the SK to the IMF growth mode. Deep level transient spectroscopy measurements would be needed to study defects in detail. PL emission energy shifts to smaller energy because larger QD shifts hole states closer to the conduction band. The size of the un-strained IMF grown QDs is not restricted in that sense as in the SK growth mode, where the strain is relaxing due to the three dimensional growth.

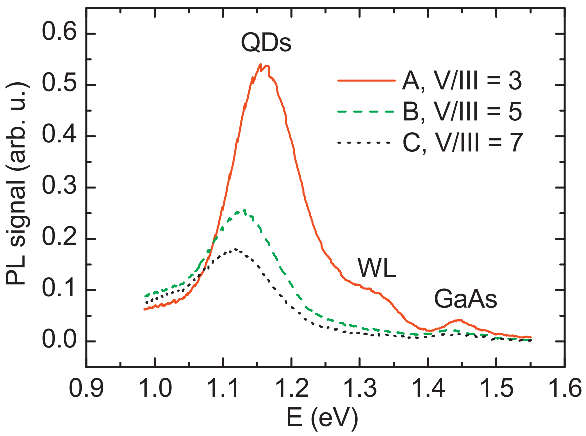

Fig. 1. Room-temperature PL spectra of as-grown QD samples A, B, and C grown with different V/III BEP ratios.

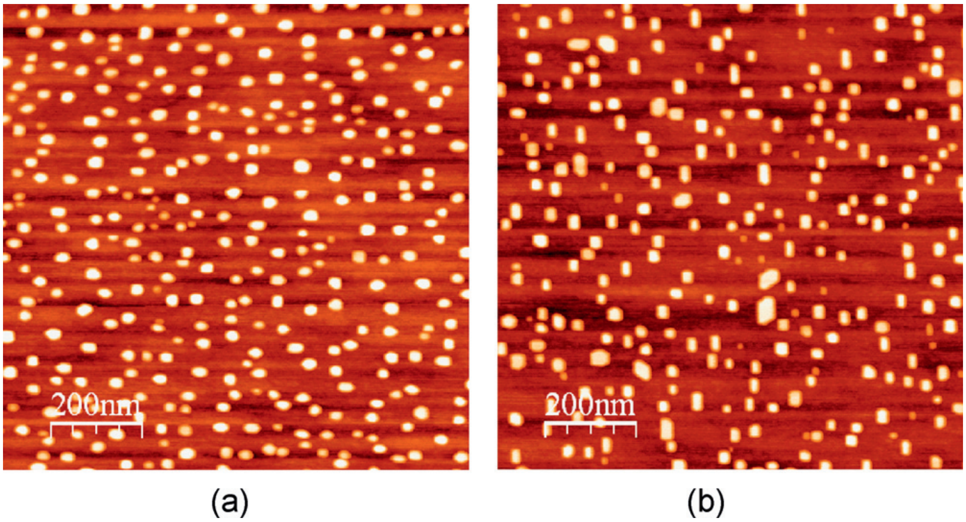

(a) (b)

Fig. 2. AFM image (1 μm × 1 μm) of surface QDs taken from the sample with (a) V/III = 3 (same as sample A), and (b) V/III = 7 (same as sample C).

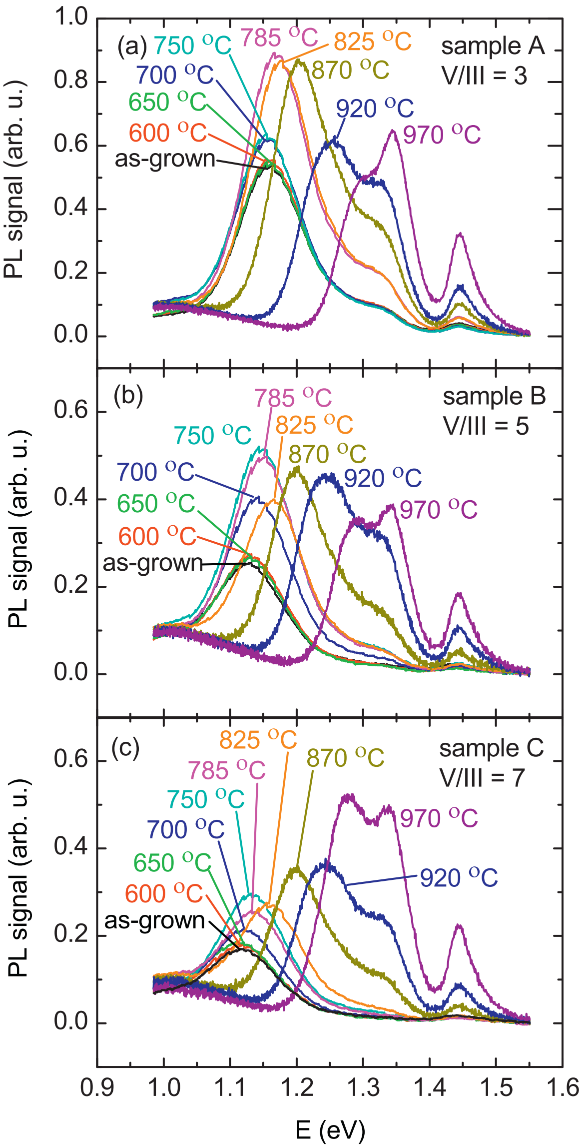

Fig. 3. RT-PL spectra of annealed and as-grown samples with (a) V/III = 3, (b) V/III = 5, and (c) V/III = 7. Annealing time was $t_{ann} = 30$ s.

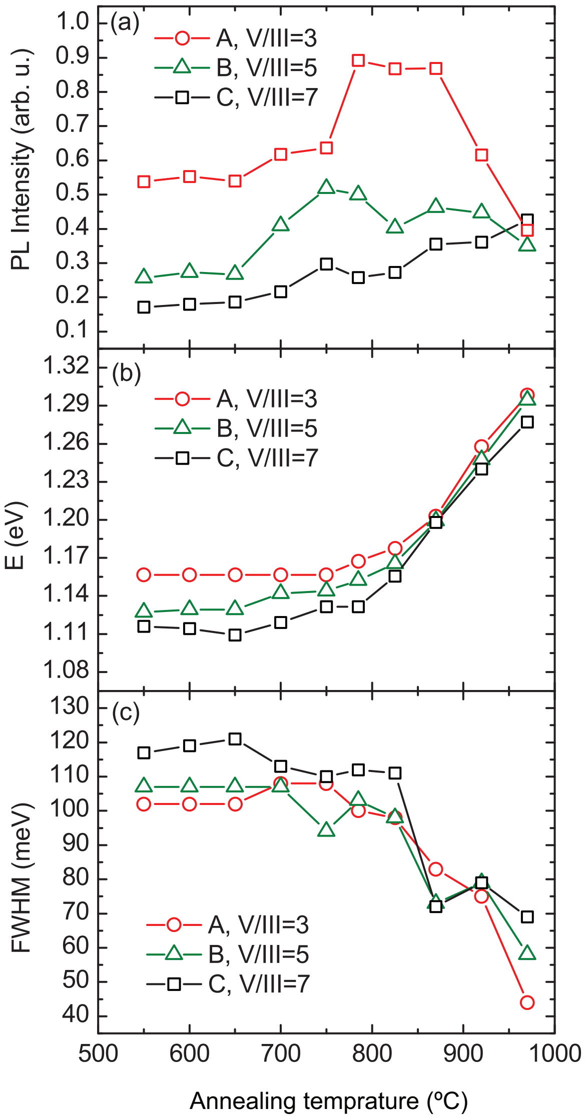

Fig. 4. (a) PL intensity, (b) PL energy, and (c) FWHM as a function of annealing temperature for samples A, B and C.

Fig. 3 shows RT-PL spectra of the samples A, B, and C upon post-growth annealing at temperatures from $T_{ann} = 650\,^\circ$C up to $T_{ann} = 970\,^\circ$C. The annealing time was $t_{ann} = 30$ s. Clear differences in QD PL peak intensity and energy are observed for all three samples when the annealing temperature is increased. The QD PL peaks increase upon moderate annealing and shifts slightly to shorter wavelengths. A blueshift of the PL peaks emerges with annealing above 800 °C for all the samples. Samples A and B show decrease in PL intensities for higher annealing temperatures, while PL peak intensity of sample C shows monotonic increase. Fig. 4 shows the QD PL intensities, emission energies and full width at half maximum (FWHM) as a function of annealing temperature. Sample A shows a slight increase in PL intensity up to 750 °C followed by a rapid increase at 785 °C. At 870 °C the intensity drops and reaches a value at 970 °C below that of the as-grown intensity. In sample B, we observe an increase of the PL intensities in the range of 650–750 °C. Further increase of annealing temperatures has nearly no influence on the intensities in sample B. The PL intensities of the QDs in sample C show a nearly monotone increase. The PL intensity (for consistence) of the sample C with $T_{ann} = 970\,^\circ$C is 2.5 times higher compared to the as-grown PL intensity of the same sample. At highest annealing temperature, the QD PL intensity is close to same for all three samples. The WL and bulkGaAs PL intensities increase during annealing, showing maximal intensity at highest annealing temperature. The blue shift starts when the annealing temperature is increased above 800 °C, and at the same time the FWHM values start to decrease. The FWHM value also depends on the V/III ratio: sample C shows broadest QD PL spectra whereas sample A shows the narrowest QD PL spectra.

The increase of PL intensities at moderate annealing temperatures can be attributed to annealing of defects in the QDs, at the interfaces, as well as in the surrounding GaAs host. The monotonically increasing PL intensity of sample C during annealing suggests that the concentration of defects in the QD layer is larger compared to samples A and B, requiring higher annealing temperature or longer annealing time. It is also possible that the nature of defects in sample C, with starting IMF growth mode, is such that annealing at very high temperatures is required to remove these defects. More detailed analysis, for example deep level transient spectroscopy measurements, would be required to show the nature and evolution of the defects with respect to the V/III ratio and annealing temperature. The decrease of PL intensity in samples A and B with high annealing temperatures comes along with an increase of PL intensities corresponding to WL and GaAs. Furthermore, the PL intensity in sample B decreases when the QD PL peak starts to shift to the higher energy (shorter wavelength), closer to the WL PL peak. The decrease in QD PL intensity at annealing above 800 °C is attributed to a decreased confinement of holes, which in turn make the recombination in the WL as the dominate radiative process. The WL PL emission does not dominate in sample C at high annealing temperatures because the PL does not shift as close to WL emission as in samples A and B. Furthermore, the hole confinement in the QDs in sample C is still large enough so that the QD PL emission dominates at room temperature. To summarize the room temperature PL intensity behavior, annealing of defects increase PL from QDs, WL and bulk GaAs, whereas decrease in QD confinement causes decrease in QD PL emission. This leads to further increase in PL emission from less confined WL states and bulk GaAs.

The origins of the QD PL peak shift to higher energy is attributed to material interdiffusion between the QDs and surrounding semiconductor host matrix, observed in numerous different QD structures upon annealing [31–35]. Notable diffusion of materials between the QDs and surrounding semiconductor occurs in our samples when the annealing temperature is increased above a "critical" value of ~800 °C. At higher annealing temperatures, the QD composition and the effective size is altered due to significant material interdiffusion. The confining energy and the energy barrier for holes and electrons, respectively, are defined by the QD size and composition. When annealing causes intermixing between the QDs and surrounding GaAs, these energies are modified. This causes shifts of the QD hole states towards the GaAs valence band edge and thus, the QD PL emission shifts to the higher energies. Additionally, the QD energy barrier for electrons in the conduction band, due to the type-II band lineup, is weakened because of the annealing induced intermixing processes. Interestingly, all three samples show a similar PL shift to higher energy. Similar blueshifts indicate similar interdiffusion mechanism which is, generally, expected in the same QD system. However, the blueshift obviously does not depend on the V/III ratio and on the structural properties of the as-grown GaSb QDs. It is worth noting that the "critical annealing temperature" depends on many parameters, such as annealing conditions, sample capping (e.g. proximity capping, dielectric capping), and sample structure itself (e.g. cladding layers). Furthermore, GaAs surface oxides and surface passivation have been reported to influence the post growth annealing as well [36,37]. Larger size distribution of QDs explains the increased FWHM value when III/V ratio is increased, because the size of the QD effects to its emission energy. Decrease of the FWHM of the QD PL emission during thermal annealing is explained by the Fickian interdiffusion model [31,33,38], where the QDs intermix with the barrier material leads to blue shift and decrease in FWHM.

In the following, we show temperature dependent PL experiments of as-grown and 870 °C annealed samples A and C in order to gain a closer look into the changed QD confinement during the annealing process depending on the V/III ratio. We choose 870 °C annealed sample because at that temperature the material interdiffusion process has started, but the QD PL emission still clearly dominates. The intensities in all four samples decrease with increasing temperatures and can be sufficiently approximated with a single exponential function. The activation energies of each sample, obtained from the fits, are displayed in Fig. 5. The as-grown sample C has slightly higher thermal activation energy than the as-grown sample A indicating larger confinement of holes for larger V/III ratio. For both V/III ratios, the activation energies decrease upon annealing which corresponds to the lowering of the confining potential. The obtained activation energies are in accordance with PL and AFM measurements: the as-grown activation energy is slightly smaller for sample A with smaller QDs and higher PL emission energy. When Sb and As atoms intermix, the effective size of the GsSb QDs gets smaller. Also, the composition of QDs is rather GaAsSb than GaSb, because of intermixing process. Therefore the confining potential for holes in the QDs gets smaller. We propose that the reduction of thermal activation energies is due to the interdiffusion of group V elements between the QD and surrounding GaAs host matrix, which also causes blue shift (shift to the higher energy, corresponding to the lowered confinement of holes in the QDs) in PL emission. Furthermore, we performed power-dependent PL experiments at 9 K (not shown), which revealed a similar behavior of the PL energies versus excitation power for all samples. The PL energy shifts linearly with the third root of the excitation power according to a type-II bandgap [6,22,24,39–42].

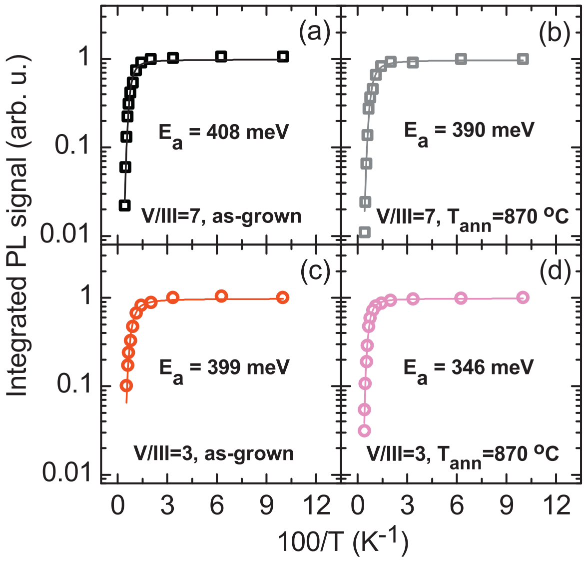

Fig. 5. QD thermal activation energies for (a), (c) as-grown and (b), (d) 870 °C annealed samples. Activation energies are obtained from single exponential fits.

4. Conclusions

We have studied the influence of V/III beam-equivalent-pressure ratios and post-growth annealing on the PL of GaSb QDs grown on GaAs(1 0 0). Increasing the V/III ratios for QD growth from 3 to 7 decreased the PL intensities and redshifted the PL wavelengths. Also, the FWHM of the PL emission gets slightly larger when V/III ratio is increased indicating larger size distribution of QDs. Annealing blueshifted the QD PL emission and decreased FWHM for annealing temperature above 800 °C, which is in accordance with Fickian interdiffusion model. The blueshift behavior is found to be independent on the V/III ratios. The differences in PL behavior between the samples grown with different V–III ratio was explained by annealing of defects and decrease in hole confinement during annealing. Temperature dependent PL experiments revealed reduced thermal activation energies for holes when QDs were grown with smaller V/III. Thermal activation energy was further reduced in the annealed samples.

Acknowledgements

The authors acknowledge funding from the Academy of Finland by the *Droplet* (decision # 138940) and from Finnish Funding Agency for Technology and Innovation (TEKES) by *SOLAR III-V* (#40120/09).

References

[1] D. Bimberg, M. Grundmann, N.N. Ledentsov, Quantum Dot Heterostructures, Wiley, Chichester, 1999.
[2] M. Grundmann (Ed.), Nano-Optoelectronics, Springer, Heidelberg, Berlin, New York, 2002.
[3] H. Lim, W. Zhang, S. Tsao, T. Silis, J. Tzafraniec, K. Mi, B. Movaghar, M. Razeghi, Physical Review B 72 (2005) 085332.
[4] A. Marti, E. Antolin, C.R. Stanley, C.D. Farmer, N. Lopez, P. Diaz, E. Canovas, P.G. Linares, A. Luque, Physical Review Letters 97 (2006) 247701.
[5] R.B. Laghumavarapu, A. Moscho, A. Khoshakhlagh, M. El-Emawy, L.F. Lester, D.L. Huffaker, Applied Physics Letters 90 (2007) 173125.
[6] D. Alonso-Álvarez, B. Alén, J.M. García, J.M. Ripalda, Applied Physics Letters 91 (2007) 263103.
[7] D. Guimard, R. Morihara, D. Bordel, K. Tanabe, Y. Wakyama, M. Nishioka, Y. Arakawa, Applied Physics Letters 96 (2010) 203507.
[8] D. Zhou, G. Sharma, S.F. Thomassen, T.W. Reenaas, B.O. Fimland, Applied Physics Letters 96 (2010) 061913.
[9] P. Michler, A. Kiraz, C. Becher, W.V. Schoenfeld, P.M. Petroff, L. Zhang, E. Hu, A. Imamoglu, Science 290 (2000) 2282.
[10] E. Knill, R. Laflamme, G.J. Milburn, Nature 409 (2001) 46.
[11] X. Li, Y. Wu, D. Steel, D. Gammon, T.H. Stievater, D.S. Katzer, D. Park, C. Piermarocchi, L.J. Sham, Science 301 (2003) 809.
[12] T.V. Hakkarainen, J. Tommila, A. Schramm, A. Tukiainen, R. Ahorinta, M. Dumitrescu, M. Guina, Applied Physics Letters 97 (2010) 173107.
[13] B. Bansal, M. Hayne, M. Geller, D. Bimberg, V.V. Moshchalkov, Physical Review B 77 (2008) 241304.
[14] M. Geller, C. Kapteyn, L. Müller-Kirsch, R. Heitz, D. Bimberg, Applied Physics Letters 82 (2003) 2406.
[15] A. Marent, M. Geller, A. Schliwa, D. Feide, K. Pötschke, D. Bimberg, N. Akcay, N. Öncan, Applied Physics Letters 91 (2007) 242109.
[16] A. Marent, T. Nowozin, M. Geller, D. Bimberg, Semiconductor Science and Technology 26 (2011) 014026.
[17] M.A. Kamarudin, M. Hayne, Q.D. Zhunag, O. Kolosov, T. Nuytten, V.V. Moshchalkov, F. Dinelli, Journal of Physics D: Applied Physics 43 (2010) 065402.
[18] A.M. Rocher, Solid State Phenomenom 19/20 (1991) 563.
[19] S.H. Huang, G. Balakrishnan, A. Khoshakhlagh, A. Jallipalli, L.R. Dawson, D.L. Huffaker, Applied Physics Letters 88 (2006) 131911.
[20] G. Balakrishnan, J. Tatebayashi, A. Khoshakhlagh, S.H. Huang, A. Jallipalli, L.R. Dawson, D.L. Huffaker, Applied Physics Letters 89 (2006) 161104.
[21] J. Tatebayashi, A. Khoshakhlagh, S.H. Huang, L.R. Dawson, G. Balakrishnan, D.L. Huffaker, Applied Physics Letters 89 (2006) 203116.
[22] A. Hatami, N.N. Ledentsov, M. Grundmann, J. Böhrer, F. Heinrichsdorff, M. Beer, D. Bimberg, S.S. Ruvimov, P. Werner, U. Gösele, J. Heydenreich, U. Richter, S.V. Ivanov, B. Ya Meltser, P. S Kop'ev, Zh. I. Alferov, Applied Physics Letters 656 (67) (1995).
[23] E.R. Glaser, B.R. Bennett, B.V. Shanabrook, R. Magno, Applied Physics Letters 68 (1996) 3614.
[24] K. Suzuki, R.A. Hogg, Y. Arakawa, Journal of Applied Physics 85 (1999) 8349.
[25] L. Müller-Kirsch, U.W. Pohl, R. Heitz, H. Kirmse, W. Neumann, D. Bimberg, Journal of Crystal Growth 221 (2000) 611.
[26] L. Müller-Kirsch, R. Heitz, U.W. Pohl, D. Bimberg, I. Häusler, H. Kirmse, W. Neumann, Applied Physics Letters 79 (2001) 1027.
[27] L. Müller-Kirsch, R. Heitz, A. Schliwa, O. Stier, D. Bimberg, H. Kirmse, W. Neumann, Applied Physics Letters 78 (2001) 1418.
[28] C.-C. Tseng, S.-C. Mai, W.-H. Lin, S.-Y. Wu, B.-Y. Yu, S.-H. Chen, S.-Y. Lin, J.-J. Shyue, M.-C. Wu, IEEE Journal of Quantum Electronics 335 (47) (2011).
[29] S.-Y. Lin, C.-C. Tseng, W.-H. Lin, S.-C. Mai, S.-Y. Wu, S.-H. Chen, J.-I. Chyi, Applied Physics Letters 96 (2010) 123503.
[30] J. Pakarinen, C.S. Peng, J. Puustinen, P. Laukkanen, V.-M. Korpijärvi, A. Tukiainen, M. Pessa, Applied Physics Letters 92 (2008) 232105.
[31] F. Heinrichsdorff, M. Grundmann, O. Stier, A. Krost, D. Bimberg, Journal of Crystal Growth 195 (1998) 540.
[32] R. Leon, S. Fafard, P.G. Piva, S. Ruvimov, Z. Liliental-Weber, Physical Review B 58 (1998) R4262.
[33] C. Jiang, H. Sakaki, Physica E 26 (2005) 180.
[34] J. Pakarinen, V. Polojärvi, A. Aho, P. Laukkanen, C.S. Peng, A. Schramm, A. Tukiainen, M. Pessa, Applied Physics Letters 94 (2009) 072105.
[35] V. Polojärvi, A. Schramm, M. Guina, A. Stemmann, C. Heyn, Nanotechnology 22 (2011) 105603.
[36] V. Polojärvi, J. Salmi, A. Schramm, A. Tukiainen, M. Guina, J. Pakarinen, E. Arola, J. Lång, I.J. Väyrynen, P. Laukkanen, Applied Physics Letters 97 (2010) 111109.
[37] J. Dahl, V. Polojärvi, J. Salmi, P. Laukkanen, M. Guina, Applied Physics Letters 99 (2011) 102105.
[38] S. Fafard, C.N. Allen, Applied Physics Letters 75 (1999) 2374.
[39] N.N. Ledentsov, J. Böhrer, M. Beer, F. Heinrichsdorff, M. Grundmann, D. Bimberg, S.V. Ivanov, B. Ya Meltser, S.V. Shaposhnikov, I.N. Yassievich, N.N. Faleev, P.S. Kop'ev, Z.I. Alferov, Physical Review B 52 (1995) 14058.
[40] F. Hatami, M. Grundmann, N.N. Ledentsov, F. Heinrichdorff, R. Heitz, J. Böhrer, D. Bimberg, S.S. Ruvimov, P. Werner, V.M. Ustinov, P.S. Kop'ev, Z.I. Alferov, Physical Review B 57 (1998) 2635.
[41] Y.S. Chiu, M.H. Ya, W.S. Su, Y.F. Chen, Journal of Applied Physics 92 (2002) 5810.
[42] T. Kawazu, T. Mano, T. Noda, H. Sakaki, Applied Physics Letters 94 (2009) 081911.

V

OPTICAL PROPERTIES AND THERMIONIC EMISSION IN SOLAR CELLS WITH InAs QUANTUM DOTS EMBEDDED IN GaNAs AND GaInNAs

by

Ville Polojärvi, Emil-Mihai Pavelescu, Andreas Schramm, Antti Tukiainen, Arto Aho, Janne Puustinen, and Mircea Guina

Scripta Materialia vol. 108, pp. 122–125, 2015.

Scripta Materialia 108 (2015) 122–125

Contents lists available at ScienceDirect

Scripta Materialia

journal homepage: www.elsevier.com/locate/scriptamat

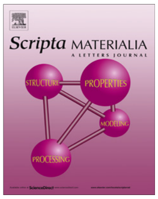

Optical properties and thermionic emission in solar cells with InAs quantum dots embedded within GaNAs and GaInNAs

Ville Polojärvi [a],*, Emil-Mihai Pavelescu [b,c], Andreas Schramm [a], Antti Tukiainen [a], Arto Aho [a], Janne Puustinen [a], Mircea Guina [a]

[a] Optoelectronics Research Centre, Tampere University of Technology, P.O. Box 692, FIN-33101 Tampere, Finland
[b] National Institute for Research and Development in Microtechnologies, Erou Iancu Nicolae 126A, 077190 Bucharest, Romania
[c] Faculty of Exact Sciences and Engineering, Hyperion University, Calea Călăraşilor 169, 030615 Bucharest, Romania

ARTICLE INFO

Article history:
Received 5 June 2015
Accepted 27 June 2015
Available online 29 June 2015

Keywords:
Quantum dot
Quantum well
Solar cell
Strain engineering
Thermal escape

ABSTRACT

The optical properties of p-i-n solar cells comprised of InAs quantum dots embedded within GaNAs and GaInNAs quantum wells are reported. Strain compensating and mediating GaNAs and GaInNAs layers shift the photoluminescence emission as well as absorption edge of the quantum dots to longer wavelengths. GaNAs and GaInNAs quantum wells contribute also to extending the absorption edge. In addition, the use of GaNAs and GaInNAs layers enhances the thermal escape of electrons from QDs by introducing steps for electrons to the GaAs conduction band.

Quantum nanostructures such as quantum wells (QW) and quantum dots (QD) have drawn interest during last years also for solar cell applications. By changing the QW materials, compositions, and thicknesses, one can optimize the band gap of the solar cell absorber for specific application, whether it is a single junction solar cell or sub-junction in multi-junction device. Different types of QW solar cells have been investigated, including InGaN/GaN, [1] AlGaAs/GaAs, [2] GaNAs/GaAs, [3] and GaAs based GaAsP/GaInAs [4] QWs. A typical problem that needs to be tackle for such multilayers structure is the compromise between the composition required to ensure a long-wavelength absorption edge and the thickness of the absorber that could be limited by the strain. To this end strain compensation techniques are used for increase the thickness of the absorber to useful level, but at the same time this makes the fabrication more cumbersome. For example, the compressive strain build-up in GaInAs/GaAs QW solar cells is balanced with tensile GaAsP layers resulting in rather complicated structures with even hundreds of interfaces. On the other hand the semiconductor QDs provide alternatives for extending the absorption band in multijunction solar cells, while being more resilient to adverse effect of the strain. Most common examples of such solar cells are based on In(Ga)As [5–7] and Ga(As)Sb [8] QDs, which are fabricated by Stranski–Krastanov (SK) epitaxy, where surface energy is minimized through formation of three-dimensional (3D) islands. However, the SK growth leads to degradation of QD properties and generation of misfit dislocations when the amount of stacked layers is increased [9]. A high level of stacking as well as a high QD sheet density is important because of limited absorption cross section of a single QD layer. Moving towards advanced QD cell concepts, achieving a dense matrix of homogenous QDs is mandatory for intermediate band solar cells. Moreover, the risk of misfit and defect formation increases when the QD density and aspect ratio are pushed to their maximal limits by depositing QDs approaching the threshold of plastic strain relaxation.

Tensile strained layers have been successfully incorporated within stacked InAs QD layers to compensate compressive strain, improving the dot size homogeneity and reducing the strain induced defects [10–15]. Promising results for GaNAs strain compensated InAs QD solar cells, with several QD layers stacked successfully, have been reported [13–15]. Furthermore, one can use strain mediation layers in combination with strain compensation layers, when fabricating stacked QD layers. To this end, a few nanometers thick GaInNAs layers can be inserted in the close proximity of the QDs in order to mediate the highly compressive strain arising from the surrounding semiconductor barriers. Strain mediation layer also forms a QW to the structure. A similar type of strain compensation/mediation has been previously used for the development of dilute nitride GaInNAs/GaNAs/GaAs QWs used in telecommunication laser applications [16]. Besides the strain aspects, when using quantum confined structures one need to pay attention to higher degree of carrier localization that hinders

---

* Corresponding author.
E-mail address: ville.polojarvi@tut.fi (V. Polojärvi).

http://dx.doi.org/10.1016/j.scriptamat.2015.06.033
1359-6462/

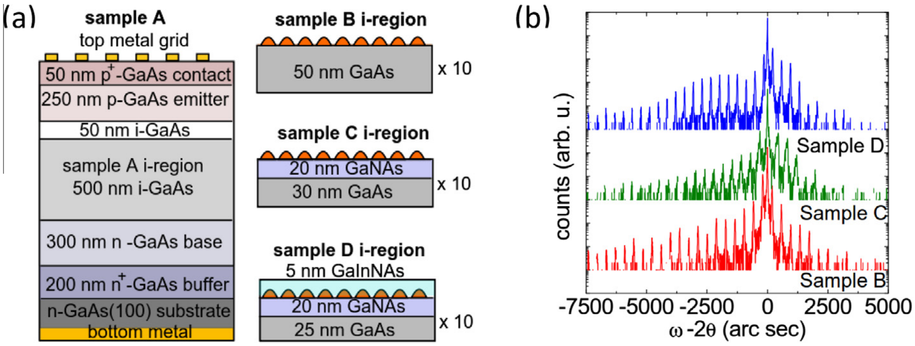

Fig. 1. (a) Schematic sample structure. (b) 2 XRD rocking curves in ω–2θ geometry for samples B–D.

transport and enhances carrier recombination. Facilitating the thermionic escape of carriers should also be considered for increasing the efficiency of the solar energy conversion.

In this paper, we investigate the properties of stacked InAs QD layers with GaNAs and GaInNAs strain compensation and mediation layers. In particular, we report the influence of dilute nitride layers on QDs luminescence properties, spectral response, and thermionic emission of carriers in p-i-n diodes.

Four p-i-n diodes with different intrinsic regions were fabricated on *n*-GaAs(100) substrate by molecular beam epitaxy (MBE). Sample structures are schematically presented in Fig. 1(a). The intrinsic region of sample A consisted of GaAs. Sample B had ten layers of InAs QDs, formed by deposition of 2 monolayers of InAs, and separated by 50 nm of GaAs. Sample C had 20 nm $GaN_{0.01}As$ strain compensation layers below each layer of QDs to compensate the strain of 2 monolayer of InAs QDs [13–15]. Sample D had an additional 5 nm $GaIn_{0.06}N_{0.01}As$ layer on top of each QD layer. The growth temperature of the intrinsic layers was kept fixed at $T_{gr} = 470\,°C$. After MBE growth, the samples were processed into 4 mm × 4 mm solar cells. We used a Ni/Au back metal contact and a Ti/Au top-grid metal contact evaporated by e-beam through a shadow mask. The composition was analyzed by measuring the X-ray diffraction (XRD) rocking curves in ω–2θ geometry using Philips diffractometer. Room temperature photoluminescence (PL) was measured from each sample using a frequency doubled Nd:YAG laser emitting at 532 nm and an InGaAs detector array (Accent RPM 2000 PL-mapper). The spectral response was measured using a standard lock-in technique while the sample was illuminated with a broadband light source through a DK240 1/4 meter monochromator. The spectral response measurement was calibrated using a NIST-traceable germanium detector.

We should point out that there is a fundamental difference between samples A–D. Although they are here compared to each other, the operation principle as a solar cell is different. Sample A is a normal GaAs solar cell, absorbing photons at higher energy than its band gap. Sample B is a QD solar cell without QW structures. Sample C is strain compensated QD solar cell, with GaNAs strain compensation layer. Sample D, with additional GaInNAs strain mediation layer, is a QW solar cell with embedded QD layers. In such cells, the QW affects strongly to the position of the quasi Fermi level and hence the output voltage of the device.

The compositions of GaNAs and GaInNAs strain compensation and strain mediation layers were estimated by XRD measurements and fit to simulations. First, we defined the N composition from sample C, and used this to define the composition of indium in sample D. The XRD rocking curves are presented in Fig. 1(b). The band anti-crossing model was used for determining the fundamental band-gaps of dilute nitride layers [17]. The composition, band-gaps and lattice mismatch of GaAs, InAs, GaNAs and GaInNAs are summarized in Table 1. Lattice mismatch is determined as a difference in the lattice constant $\Delta a = a_{substrate} - a_{material}$ divided by the lattice constant of the substrate. One thing to point out from the XRD data is, that sample C does not have as clear fringes as sample D. Although the fabrication parameters for GaAs/GaNAs and GaNAs/InAs interfaces are the same, sample D appears to have higher interface and/or material quality that could be linked to the use of additional strain mediating layers.

Table 1
Compositions, band-gaps, and lattice mismatch for investigated materials.

Material	N-composition	In-composition	Band-gap (eV)	Lattice mismatch on GaAs (%)
GaAs	0.00	0.00	1.424	0.000
InAs	0.00	1.00	0.354	−6.686
GaNAs	0.01	0.00	1.232	0.204
GaInNAs	0.01	0.06	1.191	−0.226

The effect of GaNAs and GaInNAs layers is revealed by the room temperature PL measurements, presented in the left part of the Fig. 2. The QD PL emission shifts to the longer wavelengths when moving from sample A to sample D. Sample A exhibits the GaAs PL peak, while sample B shows PL emission also from InAs wetting layer (WL) at 920 nm and QDs at 990 nm. Strain compensating GaNAs layer in sample C shifts the PL emission of the WL and QD to longer wavelengths by amount of 100 nm, when compared to sample B. Further shift of the QD PL emission, up to 1250 nm, is achieved in sample D where QD layers are capped with GaInNAs. The room temperature PL emission from GaNAs or GaInNAs is not visible in sample D, while in sample C the GaNAs PL emission might overlap with the PL peak of the WL. The drop of the PL intensity for sample C compared to sample B can be related to N-induced defects caused by unoptimized growth condition of GaNAs strain compensation layer, and related nonradiative recombination [18]. However, adding the GaInNAs strain mediation layer (sample D) increases the PL intensity, compared to sample C. When taking into account also the XRD data, it is evident that adding GaInNAs strain mediation layer improves the material quality. Surrounding GaNAs and GaInNAs layers also modifies the confining potential in the QD layer. Energy difference between confined electron and hole states decreases when QDs are surrounded by smaller band gap materials. The interpretation of the PL emission can be compared to a schematic band diagram of the structures revealing the position of the confined QD energy states, which is shown in the right part of the Fig. 2.

The spectral response of the p-i-n diodes, measured within the range of 800–1200 nm, is shown in Fig. 3. The spectral response is reduced at shorter (<900 nm) wavelengths when dilute nitride layers are added to the structure, which is explained by increased N-related defects and decreased amount of GaAs in i-region. When taking into account emitter, intrinsic region, and base, the

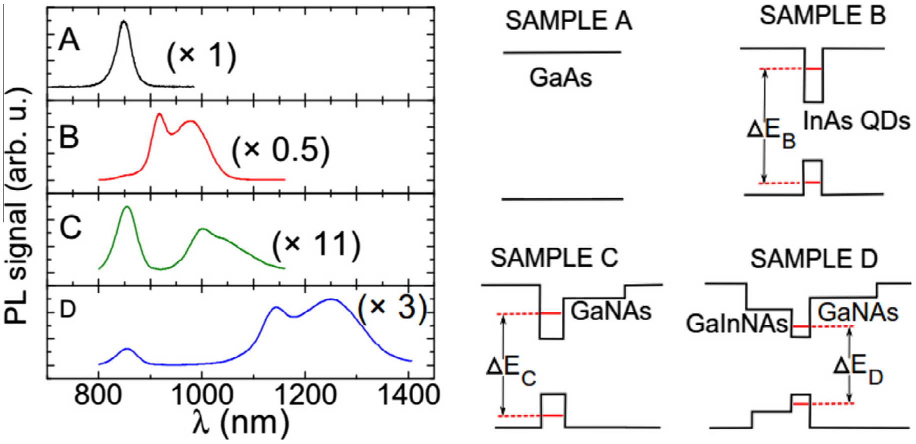

Fig. 2. (Left) PL spectra for samples A–D, at $T = 293$ K, showing the shift of QD PL emission to longer wavelengths. (Right) Schematic image of band diagrams of samples A–D. Energy difference of confined electron and hole states gets smaller when GaNAs and GaInNAs layers are added to the structure: $\Delta E_B > \Delta E_C > \Delta E_D$.

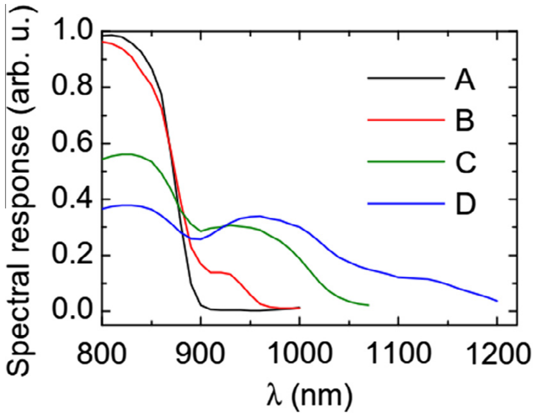

Fig. 3. Normalized spectral response of samples A–D showing dilute nitride and QD induced absorption at longer (>900 nm) wavelengths.

total thickness of GaAs is 1100 nm, 1100 nm, 900 nm, and 850 nm for samples A, B, C, and D, respectively. For comparison, thickness of GaAs junction in high efficiency solar cells can be >3 μm [19]. Shoji et al., [20] have studied InAs QDs with GaAsN strain compensation layers grown on GaAs(113) substrate. Their study did not reveal a similar decrease in spectral response at shorter wavelengths. It is possible that the depletion region does not extend over the whole QD region because of increased background doping due to nitrogen related defects. In such case where QD layer is not placed inside the electric field, it can act as a trap causing recombination and decrease in spectral response and solar cell performance. However, the absorption edge shifts to the longer wavelengths when moving from sample A to sample D. The contribution of the QD layer is visible in sample B at around 950 nm. The GaNAs layer shifts the QD layers absorption to longer wavelengths in the range of 870–1000 nm. The absorption of the QD layer is further shifted when GaInNAs layers are added to the structure, showing spectral response at around 1150 nm. A spectral signature related to the direct absorption of GaInNAs layer is also present. When taking into account both, spectral responses and the PL results, one can see that the direct absorption to the QD energy states and corresponding current generation is not visible. Spectral response related to the QD layer shown in Fig. 3 is due to absorption to the wetting layer. Thermal excitation from the QD states to the conduction band cannot be resolved in Fig. 3. It is possible that absorption by the stack of ten QD layers is not high enough to show clear spectral response for our measurement resolution, or carriers cannot escape efficiently from the lowest QD states to the conduction/valence band. Thermal escape of the carriers from the QD states could be enhanced by using wider bandgap InGaAs/GaAs QDs, for example. However, dilute nitride layers and related shift in the spectral response makes the device capable to utilize photons at longer wavelengths. Furthermore, it is possible to tune the emission and absorption wavelength of QDs [21] as well as of the dilute nitride layers [22] with thermal annealing.

The thermionic emission of the carriers from QD and dilute nitride layers to the GaAs conduction band was studied using temperature dependent short circuit current (I_{SC}) measurements. Fig. 4(a) presents the I_{SC} when the samples were illuminated with a halogen lamp through a 900 nm long-pass filter. Average I_{SC} increases when moving from sample A to sample D. Fig. 4(b) shows the same I_{SC} measurements when the current at $T = 450$ K is normalized to one. The temperature dependency of the I_{SC} clearly decreases when moving from sample A to sample D. Samples A and B, exhibit a clear temperature induced variation in current while the sample D, with GaNAs and GaInNAs layers, has a corresponding current variation of only ~25% when temperature is varied between 85 K and 450 K.

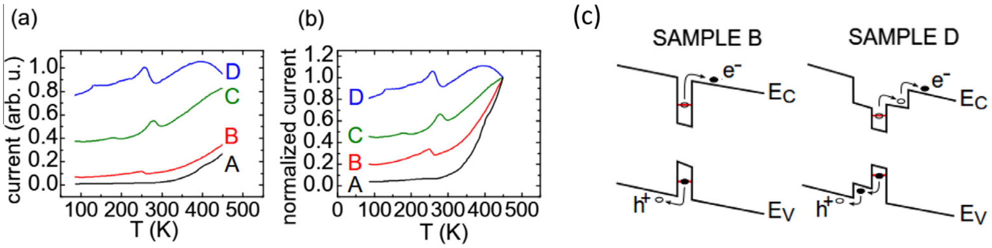

Fig. 4. Short circuit current versus temperature. Samples are illuminated through a 900 nm long-pass filter. Current is plotted in (a) absolute value and (b) normalized at $T = 450$ K. (c) Schematic of the thermal excitation process from QD layer to GaAs conduction band in sample B and D.

The absolute value of the measured current is determined mainly by the absorption of the photons at $\lambda > 900$ nm, thermal excitation of carriers, and tunneling [23]. The current levels are in agreement with the spectral response measurements at $\lambda > 900$ nm. Sample A, in principle having no absorbtion at $\lambda > 900$ nm, shows very low currents, and sample D with highest spectral response at $\lambda > 900$ nm shows the highest current. The temperature variation of the I_{SC} is also relative to the energy barriers that carriers have to overcome to get to the conduction band. Fig. 4(c) presents the thermal excitation process from QD layer (wetting layer) to GaAs conduction band in samples B and D. Dilute nitride GaNAs and GaInNAs layers provide steps for electrons and holes to thermally escape to the conduction band. Enhanced thermionic emission of electrons makes I_{SC} to be more temperature stable when cooling down to 85 K. We should point out that not only QD layers are responsible for absorbing photons with energy below GaAs band gap, but also dilute nitride layers themselves absorb low energy photons, and the generated electrons/holes are thermally excited to the conduction band/valence band.

As a conclusion, we have analyzed p-i-n diodes with InAs QDs embedded within GaNAs and GaInNAs strain compensation and mediation layers. These layers modify the emission and absorption properties of the QD layers. A redshift in the PL emission and spectral response was observed, when GaNAs and GaInNAs layers were added to the structure, enabling harvesting photons at longer wavelength. By using a GaInNAs strain mediation layer, the XRD fringes became more sharp and PL intensity was increased when compared to sample with only GaNAs strain mediation layers, indicating improved material quality. Thermal escape of electrons was found to be enhanced by GaNAs and GaInNAs. This is attributed to the fact that dilute nitride layers absorb photons and furthermore provide steps for electrons to thermally escape from QD layer to the GaAs conduction band, and contribute to the current of p-i-n diode.

This work is supported by the Finnish Funding Agency for Technology and Innovation (TEKES) projects “Solar III-V” (#40120/09) and “NextSolar” (#40239/12), by the Academy of Finland, project “Droplet” #138940, and COST Action MP0805. Ville Polojärvi gratefully acknowledges National Doctoral Programme in Nanoscience (NGS-NANO), Emil Aaltonen Foundation, KAUTE-Foundation, and Walter Ahlström Foundation for the financial support. E.-M. Pavelescu acknowledges the financial support received from the 2009–2014 EEA Grants/Contract 23SEE/30.06.2014.

References

[1] R. Dahal, B. Pantha, J. Li, J.Y. Lin, H.X. Jiang, InGaN/GaN multiple quantum well solar cells with long operating wavelengths, Appl. Phys. Lett. 94 (2009) 063505.

[2] Maykel Courel, Julio C. Rimada, Luis Hernández, AlGaAs/GaAs superlattice solar cells, Prog. Photovoltaics Res. Appl. 21 (2013) 276.

[3] A. Freundlich, A. Fotkatzikis, L. Bhusal, L. Williams, A. Alemu, W. Zhu, J.A.H. Coaquira, A. Feltrin, G. Radhakrishnan, III–V dilute nitride-based multi-quantum well solar cell, J. Cryst. Growth 301 (2007) 993.

[4] N.J. Ekins-Daukes, K.W.J. Barnham, J.P. Connolly, J.S. Roberts, J.C. Clark, G. Hill, M. Mazzer, Strain-balanced GaAsP/InGaAs quantum well solar cells, Appl. Phys. Lett. 75 (1999) 4195.

[5] A. Martí, E. Antolín, C.R. Stanley, C.D. Farmer, N. López, P. Díaz, E. Cánovas, P.G. Linares, A. Luque, Production of photocurrent due to intermediate-to-conduction-band transitions: a demonstration of a key operating principle of the intermediate-band solar cell, Phys. Rev. Lett. 97 (2006) 247701.

[6] S. Suraprapapich, S. Thainoi, S. Kanjanachuchai, S. Panyakeow, Quantum dot integration in heterostructure solar cells, Sol. Energy Mater. Sol. Cells 90 (2007) 2968.

[7] K. Laouthaiwattana, O. Tangmattajittakul, S. Suraprapapich, S. Thainoi, P. Changmuang, S. Kanjanachuchai, S. Ratanathamaphan, S. Panyakeow, Optimization of stacking high-density quantum dot molecules for photovoltaic effect, Sol. Energy Mater. Sol. Cells 93 (2009) 746.

[8] R.B. Laghumavarapu, A. Moscho, A. Khoshakhlagh, M. El-Emawy, L.F. Lester, D.L. Huffaker, GaSb/GaAs type II quantum dot solar cells for enhanced infrared spectral response, Appl. Phys. Lett. 90 (2007) 173125.

[9] A. Martí, N. López, E. Antolín, E. Cánovas, A. Luque, C.R. Stanley, C.D. Farmer, P. Díaz, Emitter degradation in quantum dot intermediate band solar cells, Appl. Phys. Lett. 90 (2007) 233510.

[10] S.M. Hubbard, C.D. Cress, C.G. Bailey, R.P. Raffaelle, S.G. Bailey, D.M. Wilt, Effect of strain compensation on quantum dot enhanced GaAs solar cells, Appl. Phys. Lett. 92 (2008) 123512.

[11] R.B. Laghumavarapu, M. El-Emawy, N. Nuntawong, A. Moscho, L.F. Lester, D.L. Huffaker, Improved device performance of InAs/GaAs quantum dot solar cells with GaP strain compensation layers, Appl. Phys. Lett. 91 (2007) 243115.

[12] C.G. Bailey, D.V. Forbes, R.P. Raffaelle, S.M. Hubbard, Near 1 V open circuit voltage InAs/GaAs quantum dot solar cells, Appl. Phys. Lett. 98 (2011) 163105.

[13] Y. Okada, R. Oshima, A. Takata, Characteristics of InAs/GaNAs strain-compensated quantum dot solar cell, J. Appl. Phys. 106 (2009) 024306.

[14] R. Oshima, A. Takata, Y. Okada, Strain-compensated InAs/GaNAs quantum dots for use in high-efficiency solar cells, Appl. Phys. Lett. 93 (2008) 083111.

[15] R. Oshima, A. Takata, Y. Shojia, K. Akahanea, Y. Okada, InAs/GaNAs strain-compensated quantum dots stacked up to 50 layers for use in high-efficiency solar cell, Physica E 42 (2010) 2757.

[16] E.-M. Pavelescu, C.S. Peng, T. Jouhti, J. Konttinen, W. Li, M. Pessa, M. Dumitrescu, S. Spânulescu, Effects of insertion of strain-mediating layers on luminescence properties of 1.3-μm GaInNAs/GaNAs/GaAs quantum-well structures, Appl. Phys. Lett. 80 (2002) 3054.

[17] I. Vurgaftman, J.R. Meyer, Band parameters for nitrogen-containing semiconductors, J. Appl. Phys. 94 (2003) 3675.

[18] I.A. Buyanova, W.M. Chen, C.W. Tu, Recombination processes in N-containing III–V ternary alloys, Solid-State Electron. 47 (2003) 467.

[19] K.A. Bertness, S.R. Kurtz, D.J. Friedman, A.E. Kibbler, C. Kramer, J.M. Olson, 29.5%-efficient GaInP/GaAs tandem solar cells, Appl. Phys. Lett. 65 (1994) 989.

[20] Y. Shoji, K. Akimoto, Y. Okada, Optical properties of multi-stacked InGaAs/GaNAs quantum dot solar cell fabricated on GaAs (311)B substrate, J. Appl. Phys. 112 (2012) 064314.

[21] J. Pakarinen, V. Polojärvi, A. Aho, P. Laukkanen, C.S. Peng, A. Schramm, A. Tukiainen, M. Pessa, Annealing of self-assembled InAs/GaAs quantum dots: a stabilizing effect of beryllium doping, Appl. Phys. Lett. 94 (2009) 072105.

[22] J. Pakarinen, C.S. Peng, J. Puustinen, P. Laukkanen, V.-M. Korpijärvi, A. Tukiainen, M. Pessa, Postgrowth annealing of GaInAs/GaAs and GaInAsN/GaAs quantum well samples placed in a proximity GaAs box: a simple method to improve the crystalline quality, Appl. Phys. Lett. 92 (2008) 232105.

[23] E. Antolín, A. Martí, C.D. Farmer, P.G. Linares, E. Hernández, A.M. Sánchez, T. Ben, S.I. Molina, C.R. Stanley, A. Luque, Reducing carrier escape in the InAs/GaAs quantum dot intermediate band solar cell, J. Appl. Phys. 108 (2010) 064513.

VI

STACKED GaAs QUANTUM DOTS FABRICATED BY REFILLING OF SELF-ORGANIZED NANOHOLES: OPTICAL PROPERTIES AND POST-GROWTH ANNEALING

by

Ville Polojärvi, Andreas Schramm, Mircea Guina, Andrea Stemmann, and Christian Heyn

Nanotechnology vol. 22, pp. 105603:1–105603:4, 2011.

IOP Publishing Nanotechnology
Nanotechnology **22** (2011) 105603 (4pp) doi:10.1088/0957-4484/22/10/105603

Stacked GaAs quantum dots fabricated by refilling of self-organized nanoholes: optical properties and post-growth annealing

Ville Polojärvi[1], Andreas Schramm[1], Mircea Guina[1], Andrea Stemmann[2] and Christian Heyn[2]

[1] Optoelectronics Research Centre, Tampere University of Technology, FIN-33101 Tampere, Finland
[2] Institute of Applied Physics, University of Hamburg, D-20355 Hamburg, Germany

E-mail: Andreas.Schramm@tut.fi

Received 3 December 2010, in final form 10 January 2011
Published 2 February 2011
Online at stacks.iop.org/Nano/22/105603

Abstract
We study the photoluminescence and impact of post-growth annealing of stacked, strain-free GaAs quantum dots fabricated by refilling of self-organized nanoholes using molecular beam epitaxy. Temperature- and power-dependent photoluminescence studies reveal an excellent optical quality of the quantum-dot stack. After high-temperature post-growth annealing only slight blueshifts and an increase in full width at half-maximum of the photoluminescence peak are observed, indicating very high-temperature stability and crystalline quality of the stacked GaAs quantum-dot structure.

(Some figures in this article are in colour only in the electronic version)

1. Introduction

Self-assembled quantum dots (QD) grown by molecular beam epitaxy (MBE) are fascinating objects that exhibit a three-dimensional confinement for charge carriers leading to narrow, intrinsic energy levels [1, 2]. Semiconductor QDs have been found to be very attractive for novel optoelectronic and electronic devices and applications, such as lasers and amplifiers [1], solar cells [3, 4] or single-photon sources for quantum computing [5], quantum cryptography [6] and quantum logical elements [7]. The vast majority of MBE-grown QDs, e.g. self-assembled InAs QDs, follows the Stranski–Krastanov (SK) growth mode in which strain is involved arising from the lattice mismatch between the substrate and the epilayer [1, 2]. Alternative QD growth procedures, such as droplet epitaxy (DE) [8–10], have been developed which allow us to generate strain-free QDs. However, DE requires low growth temperatures during the growth of QDs, which lead to a large number of defects in the QDs as well as in the surrounding barrier [11]. Recently, a promising DE-related method to create strain-free QDs has been established by exploiting self-assembled nanoholes grown by local droplet etching (LDE) [12–14]. These nanoholes can be subsequently refilled with a semiconductor either possessing a similar lattice constant as the host semiconductor or a different lattice constant. The main advantages of the LDE and refilling method with respect to DE is the use of common GaAs growth temperatures around 600 °C and the absence of the group V crystallization step during the MBE process, both processes reducing the amount of defects. Highly uniform strain-free GaAs/Al(Ga)As QDs have been recently demonstrated by using this growth method [15–17]. Stacking of these strain-free QD would be beneficial for applications requiring many QD layers, such as in QD lasers or solar cells. In order to grow high-uniform, stacked SK QD layers with narrow photoluminescence (PL) peak widths, modified layer structures have been exploited, e.g. using strain compensation layers [18, 19].

In this paper, we study the optical properties of a fivefold stack of strain-free GaAs QDs, grown by the LDE and refilling method. Our LDE GaAs QDs are found to be highly temperature stable as observed in post-growth annealing experiments. The QD PL emission does not experience a blueshift (BS) unless ultrahigh temperatures and long annealing times are used, indicating high crystal and optical quality of the QDs.

2. Experimental details

The GaAs QDs were grown on semi-insulating GaAs(001) in a solid-source MBE system equipped with an arsenic valved cracker. After the growth of GaAs and AlGaAs buffers we have grown a 5 nm AlAs layer in which nanoholes were generated using the following procedure. After growth of the AlAs layer the arsenic valve was closed and 3.2 monolayers (ML) Al were deposited at $T = 650\,^{\circ}\mathrm{C}$ to form Al droplets on the AlAs surface. Subsequently, an annealing step of 180 s was introduced during which the self-assembled nanoholes with a depth of 16 nm were formed [20]. In this case, Al was used for the LDE processes in order to create confining barriers for the following GaAs QDs. Afterwards, the nanoholes were filled by 0.6 nm GaAs in a growth-interrupted fashion [21] to enhance the filling process of the holes and then covered by 20 nm AlGaAs. The height of the resulting GaAs QDs was around 8 nm. For additional details see [20, 21]. A typical QD density of about 4×10^8 cm^{-2} per layer is obtained. The whole growth sequence was repeated five times, leading to a stack of five GaAs QD layers. The growth was finished with an AlGaAs buffer layer and GaAs cap layer. The as-grown sample was capped by a 120 nm SiO_2 layer by means of plasma-enhanced chemical vapour deposition, and cleaved in 2×2 mm^2 pieces for different annealing treatments. The sample pieces were annealed on a silicon wafer, face up in N_2 atmosphere. The annealing temperature (T_{ann}) was controlled by an optical pyrometer. Low-temperature PL was measured with an argon ion laser and a photomultiplier tube using a closed-cycle helium cryostat. The room-temperature PL spectra after annealing were measured using excitation from an Nd:YAG laser, operating at $\lambda = 532$ nm, and a CCD detector array.

3. Experimental results and discussions

Figure 1 shows low-temperature PL spectra of GaAs QDs at varied excitation powers. An increase of the excitation power clearly reveals the shell structure of the GaAs QDs. We observe distinct, very narrow PL peaks ($E_0 - E_3$) between 1.55 and 1.71 eV arising from QD transitions. A GaAs quantum-well PL peak is observed at 1.82 eV; this is related to the filling of nanoholes with GaAs. Furthermore, the graph reveals also the GaAs (shoulder at ~1.52 eV) and AlGaAs (>1.84 eV) bulk-related PL. The full width at half-maximum (FWHM) of the ground-state transition E_0 is only 13 meV at 8 K. The FWHM of a reference single GaAs QD layer is 14 meV, suggesting that the PL peak widths do not significantly change during stacking.

The temperature dependence of the ground-state PL intensity is shown in figure 2(a). The intensity remains nearly constant until 100 K and decreases exponentially with increasing temperatures. An activation energy of $E_{\mathrm{A}} = 412 \pm 6$ meV was obtained from a fit of the PL intensities using $I = I_0/[1 + C\exp(-E_{\mathrm{A}}/k_{\mathrm{B}}T)]$ associated with a single path

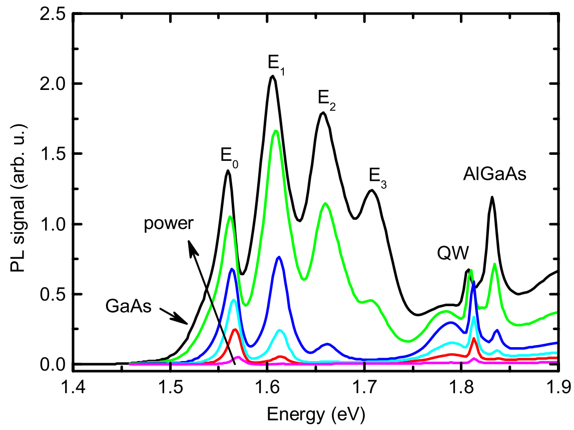

Figure 1. Power-dependent PL spectra of GaAs QDs at $T = 8$ K. The excitation power is varied from 1 to 30 W cm^{-2}.

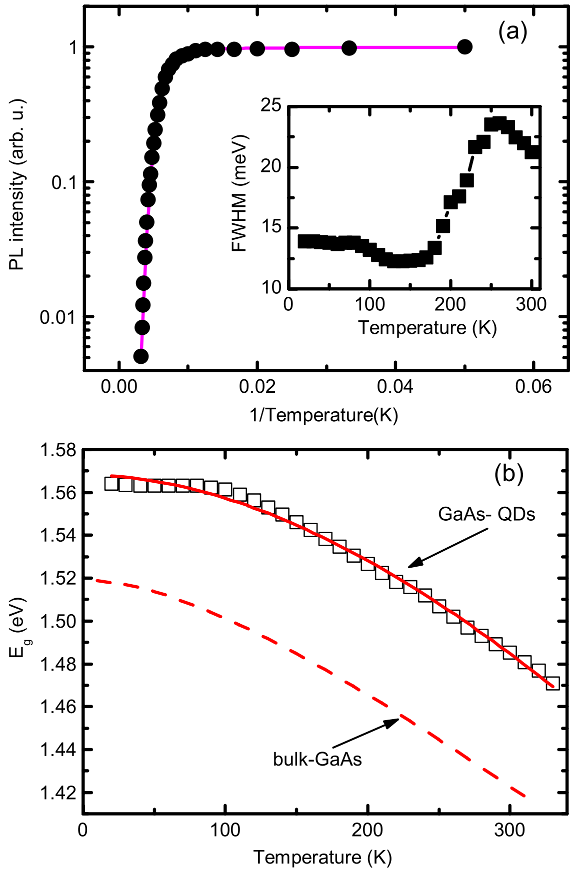

Figure 2. Temperature dependence of (a) PL intensity and (b) PL peak position of the E_0 transition using an excitation power of 30 W cm^{-2}. The inset in (a) shows the temperature dependence of the FWHM. The straight (magenta) line in (a) is the fit of the temperature dependence of the intensity. In (b) the data points are fitted (straight red line) by the empirical Varshni relation $E_g = E_0 - AT^2/(T + B)$ with $E_0 = 1.568$ eV, $A = 12.9 \times 10^{-4}$ eV K^{-1} and $B = 1091$ K. Additionally, the temperature dependence of the GaAs bulk bandgap is depicted in (b).

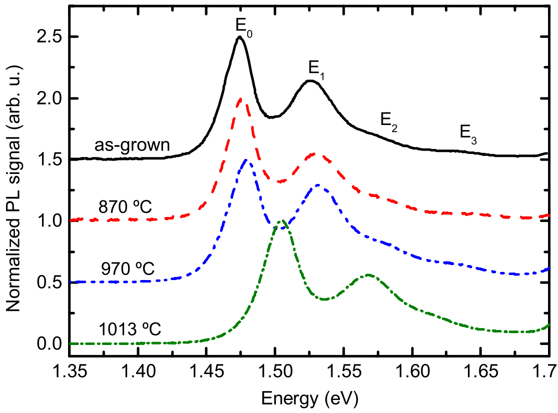

Figure 3. Room-temperature PL spectra of samples annealed with $t_{\mathrm{ann}} = 30$ s at different T_{ann}. The PL intensities are normalized.

for non-radiative losses, where I is the PL intensity, I_0 is the PL intensity at 10 K, C is a fitting parameter describing the transition rate and E_{A} is the activation energy. The resulting activation energy is similar to the AlGaAs barrier height that electrons and holes have to overcome thermally. The inset in figure 2(a) shows the temperature dependence of the FWHM of the GaAs QD ground-state transition. Up to 100 K the FWHM is nearly constant at 14 meV followed by a slight reduction of the FWHM to 12 meV between 100 and 200 K. Afterwards, the FWHM increases with rising temperatures and amounts to only 22 meV at room temperature. Figure 2(b) depicts the temperature variation of the peak position energy of the ground-state transition. We observe a redshift of about 93 meV of the E_0 peak when the temperature is increased from 10 to 300 K. Above 100 K, the PL energy nicely follows the empirical Varshni relation with rising temperatures originating in the thermal reduction of the GaAs bandgap. Deviations from the Varshni fit are observed below 100 K, where almost no shift of the PL energy is observed and which can be explained by strong exciton localization effects [22].

In order to prove the good optical properties of our GaAs QD stack fabricated by the novel LDE method, we performed high-temperature annealings. Figure 3 shows a selection of four normalized room-temperature PL spectra from samples annealed at different temperatures T_{ann} for a time of $t_{\mathrm{ann}} = 30$ s. The shape and position of the PL spectra remain nearly unchanged. Only at very high temperatures ($T_{\mathrm{ann}} = 1013\,°\mathrm{C}$) is a clear blueshift (BS) in the PL spectrum observed. Four different QD transitions ($E_0 - E_3$) are visible in room-temperature PL spectra even after annealing, and the FWHM of the E_0 transition increases only slightly up to 29 meV upon thermal annealing. In figure 4(a), the PL intensity and PL BS are depicted versus T_{ann}. We observe an increasing PL intensity with higher annealing temperatures. Especially at very high T_{ann}, the PL increase is more pronounced. The PL intensity is ten times larger upon the highest annealing step with respect to the as-grown sample. Interestingly, figure 4(a) shows that only a very small PL BS of about 15 nm is observed at the highest T_{ann}. Annealing steps at higher T_{ann} could not be performed because the quality of the protective SiO_2 was degraded. Figure 4(b) shows the PL intensities and BS for varied annealing times from 1 to 220 s at $T_{\mathrm{ann}} = 970\,°\mathrm{C}$. We observe a similar trend of an increasing PL intensity, as in figure 4(a). The PL intensity maximum is reached at $t_{\mathrm{ann}} = 100$ s. At the same time, the PL shows a BS of about 15 nm and the FWHM slightly increases up to 27 meV.

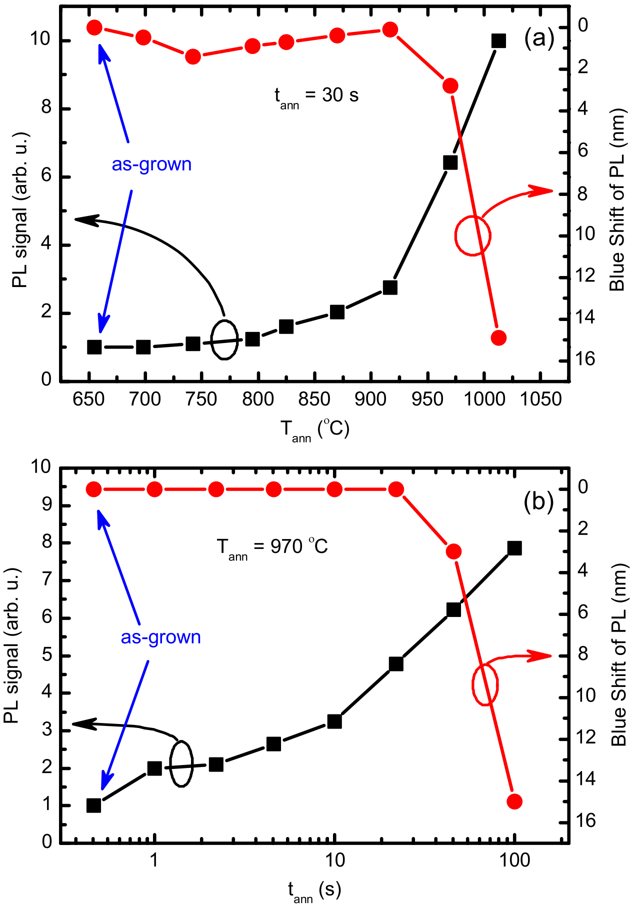

Figure 4. PL intensity and BS of PL plotted versus (a) T_{ann} ($t_{\mathrm{ann}} = 30$ s) and (b) versus t_{ann} ($T_{\mathrm{ann}} = 970\,°\mathrm{C}$).

Our annealing experiments demonstrate the very high optical quality of the present LDE GaAs QDs. Post-growth annealing is commonly exploited in order to improve material and interface quality. Previous studies have shown that the structural quality and PL intensities of GaAs/Al(Ga)As DE QDs, as well as GaAs/Al(Ga)As quantum wells (QWs), can be dramatically improved by a post-growth annealing step [11, 15, 23, 24]. However, large shifts of the DE QD PL emission to shorter wavelengths, as well as peak broadening, has been reported [15, 23]. Wavelength blueshifts are caused by annealing-induced material intermixing due to atomic interdiffusion observed in both QD and QW structures upon annealing [11, 15, 23–30]. Material temperature stability is important not only during annealing but also for devices undergoing large temperature gradients during their operation. The present QDs grown by refilling of self-assembled nanoholes are found to be highly temperature stable: only minor broadening and BS of PL exhibit an excellent thermal stability of the LDE GaAs QDs. The small BS can be explained by minor Ga and Al interdiffusion at the QD interfaces. The diffusion coefficients depend on the crystal quality, i.e. the atomic interdiffusion is driven by point defects, such as vacancies generated at low growth temperature, as in DE. The small BS in our samples, even at relatively high T_{ann}, is a consequence of optimal growth temperatures applied during LDE leading to a low density of defects and very good crystal quality in the QD surroundings. The relative increase of the PL intensity in our LDE QDs is not as large as for QDs grown via DE [11], because the amount of defects in the QDs and in the host material is considerably smaller. It is worth noticing that SiO_2 capping itself generates a large number of Ga vacancies upon annealing, which can act as diffusion channels for material interdiffusion, when they migrate to the QD region [25, 26]. Apparently, in our QD samples, the vacancies generated at the interface play no role in the annealing process and became significant only at very high temperatures, seen as a beginning BS.

4. Conclusions

In conclusion, we report on optical properties of strain-free, stacked and highly uniform GaAs/AlGaAs QDs grown by refilling of self-organized nanoholes. Excellent optical quality of the QD stack is revealed by temperature- and power-dependent PL studies. Ultrahigh post-growth annealing of the LDE GaAs QDs demonstrate their high-temperature stability and, thus, the high crystalline quality of the QDs and the barriers. The PL intensity is slightly improved while only small blueshifts and increase of the FWHM are observed upon very high-temperature annealings.

Acknowledgments

The authors acknowledge the Academy of Finland via Dauntless (123951) and Droplet (138940) and the Deutsche Forschungsgemeinschaft (DFG) for financial support via HA 2042/6-1.

References

[1] Grundmann M (ed) 2002 *Nano-Optoelectronics* (Berlin: Springer)
[2] Bimberg D, Grundmann M and Ledentsov N N 1999 *Quantum Dot Heterostructures* (Chichester: Wiley)
[3] Martí A, Antolín E, Stanley C R, Farmer C D, López N, Díaz P, Cánovas E, Linares P G and Luque A 2006 *Phys. Rev. Lett.* **97** 247701
[4] Zhou D, Sharma G, Thomassen S F, Reenaas T W and Fimland B O 2010 *Appl. Phys. Lett.* **96** 061913
[5] Knill E, Laflamme R and Milburn G J 2001 *Nature* **409** 46
[6] Michler P, Kiraz A, Becher C, Schoenfeld W V, Petroff P M, Zhang L, Hu E and Imamoglu A 2000 *Science* **290** 2282
[7] Li X, Wu Y, Steel D, Gammon D, Stievater T H, Katzer D S, Park D, Piermarocchi C and Sham L J 2003 *Science* **301** 809
[8] Koguchi N, Takahashi S and Chikyow T 1991 *J. Cryst. Growth* **111** 688
[9] Mano T, Kuroda T, Yamagiwa M, Kido G, Sakoda K and Koguchi N 2006 *Appl. Phys. Lett.* **89** 183102
[10] Heyn Ch, Stemmann A, Schramm A, Welsch H, Hansen W and Nemcsics Á 2007 *Phys. Rev.* B **76** 075317
[11] Sanguinetti S, Mano T, Gerosa A, Somaschini C, Bietti S, Koguchi N, Grilli E, Guzzi M, Gurioli M and Abbarchi M 2008 *J. Appl. Phys.* **104** 113519
[12] Wang Zh M, Liang B L, Sablon K A and Salamo G J 2007 *Appl. Phys. Lett.* **90** 113120
[13] Stemmann, Heyn Ch, Köppen T, Kipp T and Hansen W 2008 *Appl. Phys. Lett.* **93** 123108
[14] Heyn Ch, Stemmann A and Hansen W 2009 *J. Cryst. Growth* **311** 1839
[15] Sanguinetti S, Watanabe K, Kuroda T, Minami F, Gotoh Y and Koguchi N 2002 *J. Cryst. Growth* **242** 321
[16] Heyn Ch, Stemmann A, Köppen T, Strelow Ch, Kipp T, Grave M, Mendach S and Hansen W 2010 *Nanoscale Res. Lett.* **5** 576
[17] Heyn Ch, Klingbeil M, Strelow Ch, Stemmann A, Mendach S and Hansen W 2010 *Nanoscale Res. Lett.* **5** 1633
[18] Popescu V, Bester G, Hanna M C, Norman A G and Zunger A 2008 *Phys. Rev.* B **78** 205321
[19] Amano T, Sugaya T and Komori K 2006 *Appl. Phys. Lett.* **89** 171122
[20] Heyn Ch, Stemmann A and Hansen W 2009 *Appl. Phys. Lett.* **95** 173110
[21] Heyn Ch, Stemmann A, Köppen T, Strelow Ch, Kipp T, Grave M, Mendach S and Hansen W 2009 *Appl. Phys. Lett.* **94** 183113
[22] Lubyshev D I, GonzaÂlez-Borrero P P, Marega E Jr, Petitprez E, La Scala N Jr and Basmaji P 1996 *Appl. Phys. Lett.* **68** 205
[23] Mantovani V, Sanguinetti S, Guzzi M, Grilli E, Gurioli M, Watanabe K and Koguchi N 2004 *J. Appl. Phys* **96** 4416
[24] Ying M, Xia Y, Liu P, Liu X, Zhao M and Wang Z 2002 *Mater. Lett.* **57** 2932
[25] Pakarinen J, Peng C S, Puustinen J, Laukkanen P, Korpijärvi V-M, Tukiainen A and Pessa M 2008 *Appl. Phys. Lett.* **92** 232105
[26] Ooi B S, McIlvaney K, Street M W, Helmy A S, Ayling S G, Bryce A C, Marsh J H and Roberts J S 1997 *IEEE J. Quantum Electron.* **33** 1784
[27] Pakarinen J, Peng C S, Polojärvi V, Tukiainen A, Korpijärvi V-M, Puustinen J, Pessa M, Laukkanen P, Likonen J and Arola E 2008 *Appl. Phys. Lett.* **93** 052102
[28] Pakarinen J, Polojärvi V, Aho A, Laukkanen P, Peng C S, Schramm A, Tukiainen A and Pessa M 2009 *Appl. Phys. Lett.* **94** 072105
[29] Polojärvi V, Salmi J, Schramm A, Tukiainen A, Guina M, Pakarinen J, Arola E, Lång J, Väyrynen I J and Laukkanen P 2010 *Appl. Phys. Lett.* **97** 111109
[30] Schlesinger T E and Kuech T 1986 *Appl. Phys. Lett.* **49** 519

VII

COMPARATIVE STUDY OF DEFECTS LEVELS IN GaInNAs, GaNAsSb, AND GaInNAsSb FOR HIGH EFFICIENCY SOLAR CELLS

by

Ville Polojärvi, Arto Aho, Antti Tukiainen, Andreas Schramm, and Mircea Guina

Appl. Phys. Lett. vol 108, pp. 122104:1–122104:5, 2016.

APPLIED PHYSICS LETTERS **108**, 122104 (2016)

Comparative study of defect levels in GaInNAs, GaNAsSb, and GaInNAsSb for high-efficiency solar cells

Ville Polojärvi, Arto Aho, Antti Tukiainen, Andreas Schramm, and Mircea Guina
Optoelectronics Research Centre, Tampere University of Technology, FIN-33101 Tampere, Finland

(Received 27 January 2016; accepted 14 March 2016; published online 22 March 2016)

Background doping and defect levels in GaInNAs, GaNAsSb, and GaInNAsSb solar cells with 1 eV band-gap are reported. Localized point defect induced traps were observed showing broadest defect distribution in GaInNAsSb. Incorporation of Sb reduced the unintentional p-type background doping by an order of magnitude, but increased the capture cross sections of deep levels by three orders of magnitude. The thermal activation energy of the dominating hole trap was increased from 350 meV for GaInNAs to 560 meV for GaNAsSb. Annealing of GaNAsSb solar cells improved the open circuit voltage from 280 mV to 415 mV, owing to the reduction in trap density. © *2016 AIP Publishing LLC*. [http://dx.doi.org/10.1063/1.4944844]

During the recent years, the efficiency of III-V solar cells has reached record levels well beyond 40%.[1] When looking retrospectively on the evolution of conversion efficiency, a level of 50% could be expected to be reached during the next few years for III-V semiconductor solar cell under concentrated illumination. To meet this target, development of new materials providing better spectral matching is instrumental.[2] One of the most promising material groups, which has already proved its potential for increasing the efficiency of multijunction solar cells are so called dilute nitrides, which comprises GaInNAs, GaInNAsSb, and GaNAsSb compounds. These materials can be grown lattice matched on GaAs and Ge substrates with band-gaps ranging from GaAs (1.42 eV) down to 0.8 eV or even lower.[3,4]

For efficient solar cell operation, besides the optimal band gap and lattice matching, one should also ensure high material quality resulting in effective photocarrier generation. To date, only molecular beam epitaxy (MBE) has succeeded to demonstrate high photocurrent and photovoltage generation for dilute nitride materials suitable for the development of multijunction solar cells. The best triple-junction solar cells incorporating 1 eV GaInNAsSb as a bottom junction exhibit efficiencies in the range of 44% under concentrated AM1.5D illumination.[5–7] However, solar cells incorporating 1 eV GaInNAs and GaNAsSb have not yet shown similar level of performance.[8,9] In general, because of relatively low carrier diffusion length, dilute nitride solar cells usually incorporate p-i-n designs to increase the field-aided photocarrier collection. However, achieving a low enough background doping ($<10^{16}\,\mathrm{cm}^{-3}$) for a wide enough depletion region inside dilute nitrides is in general challenging. N is a small and electronegative atom which easily generates defects that ultimately cause a reduction in the diffusion length and increased background doping, reducing the solar cell performance.[10,11] These detrimental features can be minimized by adjusting the growth process parameters[9,12–14] and performing rapid thermal annealing.[15–20] At the same time, incorporation of other impurities, such as H and C, has to be minimized.[21] To this end, identifying and quantifying the defects in dilute nitride solar cell heterostructures in relation to material compositions, process parameters, and photovoltaic performance is an instrumental step towards improving the conversion efficiency.

From this standpoint, we report a comparative study of defects associated with the major classes of dilute nitride heterostructures relevant for multijunction solar cells. Namely, we study defects in p-i-n diodes incorporating GaInNAsSb, GaInNAs, and GaNAsSb bulk crystals lattice matched to GaAs(100) and having a band-gap of 1 eV. Using capacitance-voltage (CV) and deep level transient Fourier spectroscopy (DLTFS),[22,23] we report the background doping densities, deep level thermal activation energies, deep level densities, and deep level capture cross sections for majority carrier traps. Furthermore, the importance of thermal annealing for removing of mid-gap states, and improving the solar cells performance, is revealed.

The p-i-n samples were grown by molecular beam epitaxy on 2″ p-type GaAs(100) substrates. The samples were grown under similar growth conditions using an optimization process reported in Refs. 12 and 24. The generic structure of the samples is presented in Figure 1. Sample 1 (S1) comprised $\mathrm{GaIn_{0.11}N_{0.04}As}$, sample 2 (S2) $\mathrm{GaN_{0.025}AsSb_{0.06}}$, and sample 3 (S3) $\mathrm{GaIn_{0.05}N_{0.03}AsSb_{0.03}}$ intrinsic layers. X-ray diffraction measurements (not shown here) revealed that all the samples were well lattice matched, and therefore, the influence of strain is negligible. The p- and n-type GaAs layers surrounding the i-region were doped with Be and Si, and had a doping density of $5\times10^{18}\,\mathrm{cm}^{-3}$ and $1\times10^{18}\,\mathrm{cm}^{-3}$, respectively. Mesa structures with top and bottom Ohmic contacts were defined by inductively coupled plasma reactive ion etching using standard photolithography and lift-off techniques. CV and DLTFS measurements were performed with a Bio-Rad DL8000 DLTFS tool. The frequency for the capacitance measurements was 1 MHz, and the AC voltage amplitude was 100 mV. Thermal annealing tests were also conducted on S2 to prove the influence of annealing on the defect density and solar cell performance. Annealing was done in N atmosphere on a Si wafer at 750 °C for 900 s. The samples were protected by a GaAs proximity capping.[17] The as-grown and annealed GaNAsSb solar cells

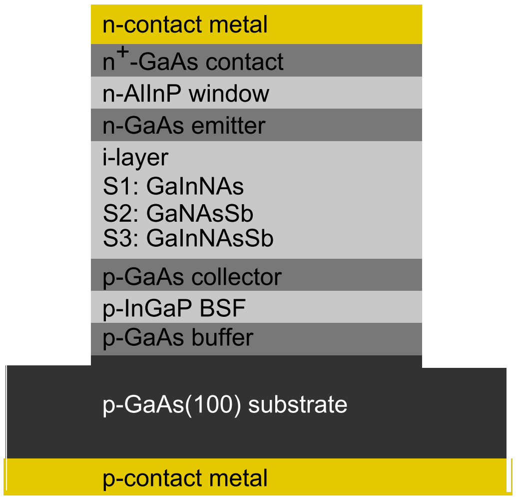

FIG. 1. Sample structure. Mesas with diameter of 0.8 mm were etched through epitaxial layers for CV and DLTFS measurements. The sizes of the fabricated solar cells were $4 \times 4\,\mathrm{mm}^2$. Ni/Au top contact metals and Ti/Au bottom contact metals were evaporated with an e-beam metallization equipment.

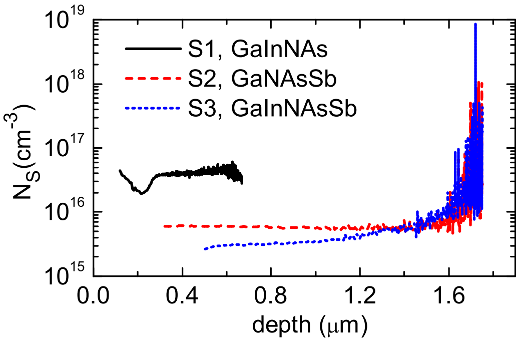

FIG. 2. Background doping depth profiles for S1-S3, derived from the CV data.

with total area of $4 \times 4\,\mathrm{mm}^2$ and TiO_2/SiO_2 antireflection coating was processed for light-current-voltage (LIV) and external quantum efficiency (EQE) measurements.

Based on the Hall measurements (not shown here) and EQE analyses, the background doping was determined to be p-type. Unintentionally doped dilute nitrides often show p-type conductivity, which has been attributed to presence of V_{Ga}-related defects[25] and contamination due C and H.[21,26] However, in MBE-grown dilute nitrides the background doping levels are reduced when compared to metalorganic chemical vapor deposition (MOCVD)-grown material mainly due to reduced C and H contamination. It has been suggested that the remaining background p-type conductivity in MBE-grown dilute nitrides arises from N-V_{Ga}-derived defects.[25,27,28]

P-type background doping is beneficial when the solar cell is grown on a p-type substrate. This is because: (i) the depletion region locates on the top part of the p-i-n junction, increasing the probability for photogeneration within the built-in electric field, and (ii) the diffusion length for electrons as minority carriers is longer compared to the diffusion length for holes. The background doping density of each sample was determined by CV measurements. When reverse voltage is applied, the edges of the depletion region move deeper into the i-region and into the n-GaAs layer, defining the probed volume. When the abrupt one-sided junction approximation is used, the background doping density of the lightly doped side of the junction can be evaluated from the slope of the $1/C^2$ vs. V graph.[29] Figure 2 shows the CV data and doping profiles, calculated by solving the Poisson equation.[29,30] Calculated depth refers to a distance from the interface between the n-GaAs emitter and the i-region. The measured doping densities for samples S1, S2, and S3 are $3.7 \times 10^{16}\,\mathrm{cm}^{-3}$, $5.4 \times 10^{15}\,\mathrm{cm}^{-3}$, and $2.7 \times 10^{15}\,\mathrm{cm}^{-3}$, respectively. Dielectric constant of $\varepsilon_r = 12$ was assumed for all dilute nitride material compositions[31] because the samples have the same bandgap of 1 eV and because In, N, and Sb compositions were relatively small.

There are clear differences in the background doping levels between the samples: S2 and S3 with Sb have clearly lower background doping compared to S1. Lower background doping results in a wider depletion region width, which is favorable for p-i-n solar cells. The doping profiles in Fig. 2 show that the background doping is fairly constant for S2 and S3 and an increase is observed when the depletion region's edge reaches the highly doped p-GaAs. A slight charge depletion is also observed at the calculated depth of ∼200 nm for S1. This can be caused by a local defect population near the dilute nitride-GaAs interface, where the trapped charge cannot follow the 1 MHz measurements signal.

Positive effect of antimony on the reduction of the background doping was reported earlier by Jackrel *et al.*[9] However, in their study, the background doping was n-type whereas in our case it is p-type. Since Sb is observed to decrease the background doping in both, intrinsically p- and n-type dilute nitride materials, this suggests that lowered background doping could be related to improved crystal quality. We assign the reduced background doping, at least partly, to the fact that Sb acts as a surfactant, reduces the surface energy and improves the incorporation of atoms to their correct lattice sites. The role of Sb as a surfactant is already reported in several studies.[9,21,32–36] It was also proposed that Sb would inhibit the incorporation of impurities from the growth environment.[9]

Figure 3 shows the DLTFS spectra for all three samples. Samples S2 and S3 were measured with a reverse bias $U_r = -2$ V, a filling pulse voltage $U_p = 0$ V, a filling pulse duration $t_p = 100$ ms, and a period width $T_w = 200$ ms. For S1, a larger reverse bias of -4 V was used because the probed volume would otherwise be significantly smaller due to higher background doping. Four different traps labelled as T1–T4 were identified and evaluated. The inset of Fig. 3 shows normalized DLTFS spectra. We should point out that the heights of the DLTFS spectra are not directly comparable due to differences in background doping. Table I shows trap densities (N_T), thermal activation energies (E_A), and capture cross sections (σ) for T1–T4, obtained from the Arrhenius evaluation.

From Fig. 3, one can see that (i) all spectra are broad, (ii) GaInNAs shows the narrowest and GaInNAsSb shows

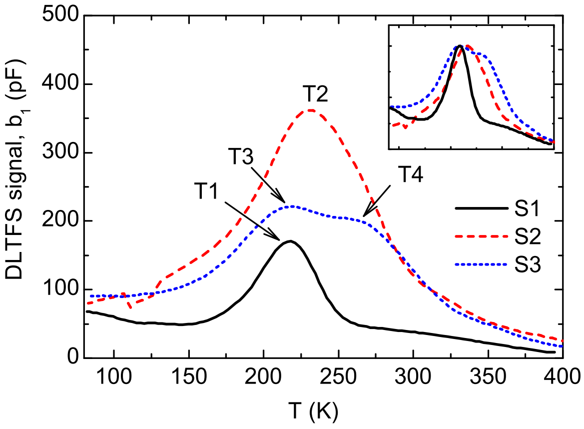

FIG. 3. DLTFS spectra for S1-S3. The inset in the upper right corner shows normalized spectra.

the broadest DLTFS spectrum, and (iii) the GaInNAsSb has two peaks (T3 and T4). Possibilities for different atomic arrangements are high in quaternary and quinary compounds, such as GaInNAs and GaInNAsSb, and therefore, one type of point defect can occur at different energies depending on the surrounding atom configurations. Furthermore, the fact that normalized DLTFS spectra are the narrowest for S1 and broadest for S3 indicates broader energy distribution of defects in materials with more constituents. Therefore, we can expect that the evaluated trap parameters describe only estimated values for activation energies for each type of traps. The evaluated trap density extracted from the dominating peak does not vary much between the samples: it is largely the same for S1 and S2, and bit smaller for traps in S3 with double peak. The width of the DLTFS peaks is not taken into account in the defect density evaluation, and one can expect that the evaluated defect density is lower compared to real trap density, and the difference increases when DLTFS peak gets broader.

Tan *et al.*[8] pointed out that a deep hole level with $E_A = 580$ meV observed in Si-doped GaNAsSb with bandgap of 1 eV is linked to As antisites (As_{Ga}); this was done by comparing this thermal activation energy of As_{Ga} in the low temperature grown GaAs.[37] The trap signatures of T2 and T4 are somewhat similar and could well be related to the As_{Ga}. However, T1 in sample S1 with GaInNAs clearly has a lower E_A. Apparently, incorporation of Sb increases the activation energy of this hole trap, or a different trap is dominating in Ga(In)NAsSb than in GaInNAs. Also, the evaluated capture cross section increases three orders of magnitude when Sb is added to the structure. Although Sb decreases the background doping, the shift of thermal activation energy and increase in capture cross section make T2, T3, and T4 more effective recombination centers. Several studies showed similar type of defects in dilute nitride materials at various thermal activation energies, but no specific identification of the origin of defect levels have been made so far.[9,38–46] What is common between all the studies is the fact that the major part of the defects is formed due to N incorporation or use of low growth temperature.

TABLE I. Trap parameters obtained from Arrhenius evaluation.

Sample/trap	N_T (cm^{-3})	E_A (meV)	σ (cm^2)
S1/T1	2.3×10^{14}	350	2.0×10^{-17}
S2/T2	2.3×10^{14}	560	5.6×10^{-14}
S3/T3	9.0×10^{13}	470	2.4×10^{-14}
S3/T4	8.3×10^{13}	570	1.9×10^{-14}

Broad DLTS peaks are caused by non-exponential capacitance transients. It is also known that dislocations cause such behavior;[47] such broad spectra were previously assigned to dislocations and extended defects in relaxed quantum dots[48,49] and quantum wells,[50,51] for example. The nature of electron and hole traps can be investigated by measuring the DLTFS by varying the filling pulse duration.[52] Thus, when the duration of the filling pulse was increased exponentially from $t_p = 10\,\mu$s to $t_p = 1$ s and DLTFS signal was plotted against $\log(t_p)$, we observed a linear increase followed by signal saturation at $t_p \approx 100$ ms for T1–T5. Such behavior is typical for point defects. Furthermore, the shape of the DLTFS spectra did not show significant changes when t_p was varied, which indicates that the observed deep levels are caused by a localized trap states rather than band-like trap population.[53]

In order to link the defect-related observations to solar cell performance, we measured the EQE and LIV characteristics of the as-grown and annealed GaNAsSb solar cells. Thermal annealing at 750 °C for 900 s under GaAs proximity cap was applied because it was found to be a very good compromise for our dilute nitride materials in common. Thermal annealing did not change the lattice-matching condition. The measurements are summarized in Fig. 4. Annealing increases the EQE, short circuit current (I_{SC}), open circuit voltage (Voc), and efficiency of the devices. There is also a minor shift of the edge of the EQE towards shorter wavelengths after annealing, which is due to short range ordering and improved homogeneity of the alloy as observed in various N containing compounds, including GaNAs,[54,55] GaNAsSb,[56,57] GaInNAs,[15,58] and InSbN.[59] The improvement of the electrical characteristics of the GaNAsSb solar cells due to thermal annealing can be understood by analyzing DLTFS measurements taken from the as-grown and annealed samples shown in Figure 4(c) as well as the CV measurements shown in Figure 4(d). The concentration of T2 is drastically reduced due to annealing while the carrier concentration remains almost the same. Less than 10% decrease in carrier concentration could be attributed to the reduction in T2, but the observed change in the carrier concentration cannot explain such large increase in V_{OC} and Isc. A feasible way to explain the improved photovoltaic characteristics of S2 is that T2 is acting as an effective recombination center, and its density can be drastically reduced by thermal annealing.

Table II shows short circuit current density (J_{SC}) targets under the state-of-the-art GaInP/GaAs solar cell[60] as well as calculated current densities under an 870 nm long pass filter, based on the standard solar spectrum[61] and EQE data presented in Fig. 4(a).

The calculated current densities show positive trends: the J_{SC} for annealed samples is already 82%–83% from target values although the material fabrication parameters and absorbing layer thickness are not optimized. The band

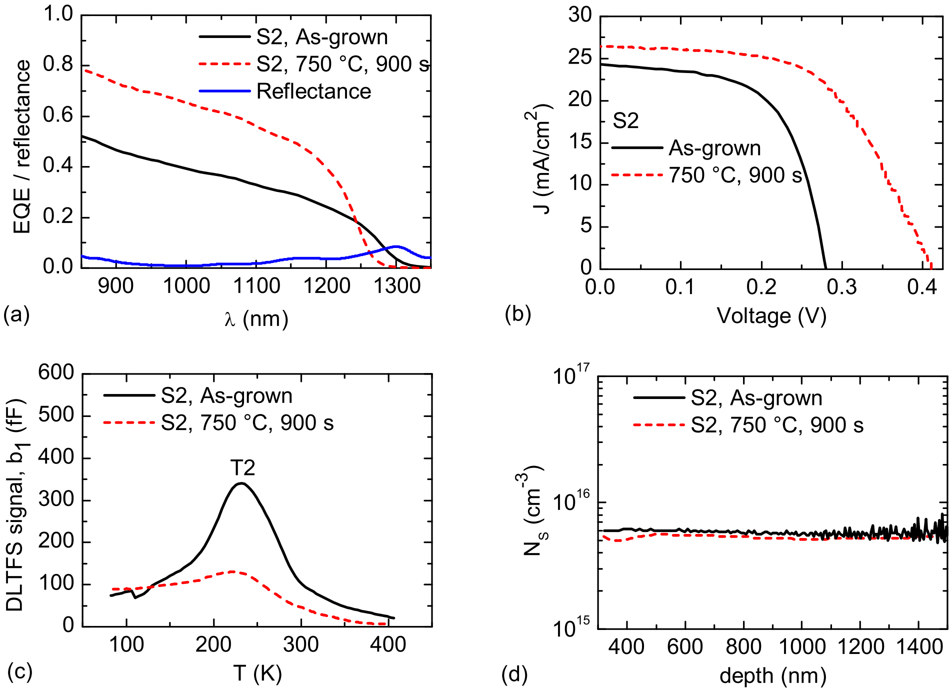

FIG. 4. (a) EQE and reflectance, (b) LIV, (c) DLTFS spectra, and (d) free carrier depth profile characteristics of as-grown and annealed solar cell S2 consisting of GaNAsSb.

gap of GaNAsSb decreases faster compared to GaInNAs, when N composition is increased. Therefore, less N is needed to get the desired band gap, which can be beneficial since N-related defects are known to degrade the material quality. A significant improvement on solar cells' performance is also seen in GaInNAs and GaInNAsSb solar cells upon thermal annealing. In addition, there are also other ways to improve the performance of dilute nitride junctions. For example, back surface reflector can effectively double the active layer thickness, which allows fabrication of thinner junction resulting potentially in higher voltage generation.[62]

In conclusion, the background doping and deep level defects in 1 eV band gap GaInNAs, GaNAsSb, and GaInNAsSb lattice matched to GaAs(100) were investigated in a comparative set of samples grown under similar epitaxial conditions (excluding material compositions). Sb was found to reduce the p-type background doping concentration. The reduction was by more than an order of magnitude higher for GaInNAsSb compared to GaInNAs. Broad majority carrier related DLTFS spectra were revealed and attributed to localized point defects appearing at different thermal activation energies. No signs of dislocations or extended defects were observed. Incorporation of Sb to GaInNAs was found to increase thermal activation energy of the dominant deep level by ∼200 meV. The incorporation of Sb was also found to increase the trap capture cross section about three orders of magnitude. The increase in the trap capture cross section together with increased thermal activation energy suggests a transformation of the trap to more effective recombination center. Thermal annealing increased the voltage and current generation of the GaNAsSb solar cell, which is explained by the reduction in density of the effective recombination center T2. Furthermore, thermal annealing did not influence remarkably the background doping level. A detailed study in which fabrication parameters and post-growth treatments are varied as a function of materials compositions would be needed in order to define whether there is certain optimal material composition for 1 eV band gap bulk dilute nitride for solar cell applications.

TABLE II. Calculated current densities for S2 (GaNAsSb) using EQE data and standard solar spectrum.[61] Target current density refers to current matching condition in GaInP/GaAs solar cell.[60]

Sample	J_{SC}, AM0 (mA/cm^2)	J_{SC}, AM1.5G (mA/cm^2)	J_{SC}, AM1.5D (mA/cm^2)
As-grown	9.3	7.7	7.3
Annealed	14.7	12.1	11.5
Target	17.8	14.5	13.8

This work was supported by the Finnish Funding Agency for Technology and Innovation (TEKES) projects "Solar III-V" (#40120/09) and "NextSolar" (#40239/12), and Academy of Finland project #138940. Ville Polojärvi gratefully acknowledges National Doctoral Programme in Nanoscience (NGS-NANO), Emil Aaltonen Foundation, KAUTE-Foundation, and Walter Ahlström Foundation for the financial support. Ms. Wenxin Zhang and Mr. Behçet Özgür Alaydin are acknowledged for their assistance in sample processing. Mr. Pekka Malinen is acknowledged for his assistance in sample fabrication.

[1] M. A. Green, K. Emery, Y. Hishikawa, W. Warta, and E. D. Dunlop, Prog. Photovoltaics **23**, 1 (2015).
[2] A. Luque, J. Appl. Phys. **110**, 031301 (2011).
[3] J. S. Harris, R. Kudrawiec, H. Yuen, S. Bank, H. Bae, M. Wistey, D. Jackrel, E. Pickett, T. Sarmiento, and L. Goddard, Phys. Status Solidi B **244**, 2707 (2007).
[4] A. Aho, V. Korpijärvi, R. Isoaho, P. Malinen, A. Tukiainen, M. Honkanen, and M. Guina, J. Cryst. Growth **438**, 49 (2016).
[5] J. Allen, V. Sabnis, M. Wiemer, and H. Yuen, in 9th International Conference on Concentrator Photovoltaic Systems: CPV-9, Miyazaki, Japan, 2013.

[6]D. Derkacs, R. Jones-Albertus, F. Suarez, and O. Fidaner, J. Photonics Energy **2**, 021805 (2012).
[7]A. Aho, R. Isoaho, A. Tukiainen, V. Polojärvi, T. Aho, M. Raappana, and M. Guina, AIP Conf. Proc. **1679**, 050001 (2015).
[8]K. Tan, S. Wicaksono, W. Loke, D. Li, S. Yoon, E. Fitzgerald, S. Ringel, and J. Harris, Jr., J. Cryst. Growth **335**, 66 (2011).
[9]D. B. Jackrel, S. R. Bank, H. B. Yuen, M. A. Wistey, J. S. Harris, Jr., A. J. Ptak, S. W. Johnston, D. J. Friedman, and S. R. Kurtz, J. Appl. Phys. **101**, 114916 (2007).
[10]A. Khan, S. R. Kurtz, S. Prasad, S. Johnston, and J. Gou, Appl. Phys. Lett. **90**, 243509 (2007).
[11]I. A. Buyanova, W. Chen, and C. Tu, Solid-State Electron. **47**, 467 (2003).
[12]A. Aho, V. Polojärvi, V. Korpijärvi, J. Salmi, A. Tukiainen, P. Laukkanen, and M. Guina, Sol. Energy Mater. Sol. Cells **124**, 150 (2014).
[13]M. A. Wistey, S. R. Bank, H. B. Yuen, H. Bae, and J. S. Harris, J. Cryst. Growth **278**, 229 (2005).
[14]Z. Pan, L. Li, W. Zhang, Y. Lin, and R. Wu, Appl. Phys. Lett. **77**, 214 (2000).
[15]K. Volz, D. Lackner, I. Nemeth, B. Kunert, W. Stolz, C. Baur, F. Dimroth, and A. Bett, J. Cryst. Growth **310**, 2222 (2008).
[16]S. R. Kurtz, A. Allerman, E. Jones, J. Gee, J. Banas, and B. Hammons, Appl. Phys. Lett. **74**, 729 (1999).
[17]J. Pakarinen, C. Peng, J. Puustinen, P. Laukkanen, V. Korpijarvi, A. Tukiainen, and M. Pessa, Appl. Phys. Lett. **92**, 232105 (2008).
[18]D. Bisping, D. Pucicki, M. Fischer, S. Höfling, and A. Forchel, J. Cryst. Growth **311**, 1715 (2009).
[19]H. Xin, K. Kavanagh, M. Kondow, and C. Tu, J. Cryst. Growth **201**, 419 (1999).
[20]G. Jaschke, R. Averbeck, L. Geelhaar, and H. Riechert, J. Cryst. Growth **278**, 224 (2005).
[21]A. Ptak, S. Johnston, S. Kurtz, D. Friedman, and W. Metzger, J. Cryst. Growth **251**, 392 (2003).
[22]D. Lang, J. Appl. Phys. **45**, 3023 (1974).
[23]S. Weiss and R. Kassing, Solid-State Electron. **31**, 1733 (1988).
[24]A. Aho, A. Tukiainen, V. Korpijärvi, V. Polojärvi, J. Salmi, and M. Guina, AIP Conf. Proc. **1477**, 49 (2012).
[25]A. Janotti, S. Wei, S. Zhang, S. Kurtz, and C. Van de Walle, Phys. Rev. B **67**, 161201 (2003).
[26]D. Friedman, A. Ptak, S. Kurtz, J. Geisz, and J. Kiehl, in International Conference on Solar Concentrators for the Generation of Electricity or Hydrogen, Scottsdale, Arizona, 2005.
[27]X. Liu, A. Prasad, J. Nishio, E. R. Weber, Z. Liliental-Weber, and W. Walukiewicz, Appl. Phys. Lett. **67**, 279 (1995).
[28]J. Gebauer, R. Krause-Rehberg, S. Eichler, M. Luysberg, H. Sohn, and E. R. Weber, Appl. Phys. Lett. **71**, 638 (1997).
[29]D. K. Schroder, *Semiconductor Material and Device Characterization* (John Wiley & Sons, 2006).
[30]P. Blood and J. W. Orton, *The Electrical Characterization of Semiconductors: Majority Carriers and Electron States* (Academic Press, 1992).
[31]A. Tukiainen, A. Aho, V. Polojärvi, and M. Guina, in *10th European Space Power Conference* (2014), Vol. 719, p. 1.
[32]T. Kageyama, T. Miyamoto, M. Ohta, T. Matsuura, Y. Matsui, T. Furuhata, and F. Koyama, J. Appl. Phys. **96**, 44 (2004).
[33]M. Henini, *Dilute Nitride Semiconductors* (Elsevier, 2004).
[34]X. Yang, M. Jurkovic, J. Heroux, and W. Wang, Electron. Lett. **35**, 1081 (1999).
[35]N. Miyashita, N. Ahsan, and Y. Okada, Sol. Energy Mater. Sol. Cells **111**, 127 (2013).
[36]F. Dimroth, A. Howard, J. Shurtleff, and G. Stringfellow, J. Appl. Phys. **91**, 3687 (2002).
[37]D. C. Look, Z. Fang, J. Sizelove, and C. Stutz, Phys. Rev. Lett. **70**, 465 (1993).
[38]R. Kaplar, D. Kwon, S. Ringel, A. Allerman, S. R. Kurtz, E. Jones, and R. Sieg, Sol. Energy Mater. Sol. Cells **69**, 85 (2001).
[39]D. Kwon, R. Kaplar, S. Ringel, A. Allerman, S. R. Kurtz, and E. Jones, Appl. Phys. Lett. **74**, 2830 (1999).
[40]R. Kaplar, S. Ringel, S. R. Kurtz, J. Klem, and A. Allerman, Appl. Phys. Lett. **80**, 4777 (2002).
[41]F. Abulfotuh, A. Balcioglu, D. Friedman, J. Geisz, and S. Kurtz, AIP Conf. Proc. **462**, 492 (1999).
[42]B. Bouzazi, N. Kojima, Y. Ohshita, and M. Yamaguchi, J. Alloys Compd. **552**, 469 (2013).
[43]S. Johnston, R. Ahrenkiel, A. Ptak, D. Friedman, and S. Kurtz, paper presented at the National Center for Photovoltaics and Solar Program Review Meeting, No. NREL/CP-520-33557, National Renewable Energy Laboratory (NREL), Golden, CO, 2003.
[44]V. Polojärvi, A. Aho, A. Tukiainen, M. Raappana, T. Aho, A. Schramm, and M. Guina, Sol. Energy Mater. Sol. Cells **149**, 213 (2016).
[45]L. L. Goddard, S. R. Bank, M. A. Wistey, H. B. Yuen, Z. Rao, and J. S. Harris, Jr., J. Appl. Phys. **97**, 083101 (2005).
[46]M. M. Islam, N. Miyashita, N. Ahsan, T. Sakurai, K. Akimoto, and Y. Okada, J. Appl. Phys. **112**, 114910 (2012).
[47]T. Figielski, Phys. Status Solidi A **121**, 187 (1990).
[48]V. Polojärvi, A. Schramm, A. Aho, A. Tukiainen, and M. Pessa, Phys. E **42**, 2610 (2010).
[49]V. Polojärvi, A. Schramm, A. Aho, A. Tukiainen, and M. Guina, J. Phys. D **45**, 365107 (2012).
[50]L. Panepinto, U. Zeimer, W. Seifert, M. Seibt, F. Bugge, M. Weyers, and W. Schröter, Mater. Sci. Eng., B **42**, 77 (1996).
[51]G. P. Watson, D. G. Ast, T. J. Anderson, B. Pathangey, and Y. Hayakawa, J. Appl. Phys. **71**, 3399 (1992).
[52]L. Gelczuk, M. Dabrowska-Szata, and G. Józwiak, Mater. Sci.-Poland **23**, 625 (2005).
[53]W. Schröter, J. Kronewitz, U. Gnauert, F. Riedel, and M. Seibt, Phys. Rev. B **52**, 13726 (1995).
[54]Q. Zhuang, A. Krier, and C. Stanley, J. Appl. Phys. **101**, 103536 (2007).
[55]I. Buyanova, G. Pozina, P. Hai, N. Thinh, J. Bergman, W. Chen, H. Xin, and C. Tu, Appl. Phys. Lett. **77**, 2325 (2000).
[56]S. Bharatan, S. Iyer, K. Nunna, W. Collis, K. Matney, J. Reppert, A. Rao, and P. Kent, J. Appl. Phys. **102**, 023503 (2007).
[57]L. Bian, D. Jiang, P. Tan, S. Lu, B. Sun, L. Li, and J. Harmand, Solid State Commun. **132**, 707 (2004).
[58]V. Korpijärvi, A. Aho, P. Laukkanen, A. Tukiainen, A. Laakso, M. Tuominen, and M. Guina, J. Appl. Phys. **112**, 023504 (2012).
[59]N. C. Patra, S. Bharatan, J. Li, and S. Iyer, J. Appl. Phys. **112**, 083107 (2012).
[60]A. Aho, A. Tukiainen, V. Polojärvi, and M. Guina, Nanoscale Res. Lett. **9**, 61 (2014).
[61]ASTM International, *173–03: Standard Tables for Reference Solar Spectral Irradiances: Direct Normal and Hemispherical on 37° Tilted Surface, West Conshohocken* (ASTM International, PA, 2003).
[62]T. Aho, A. Aho, A. Tukiainen, V. Polojärvi, J.-P. Penttinen, M. Raappana, and M. Guina, *2015 IEEE 42nd Photovoltaic Specialist Conference (PVSC), New Orleans, LA, 2015*, pp. 1–4.

VIII

INFLUENCE OF As/GROUP-III FLUX RATIO ON DEFECTS FORMATION AND PHOTOVOLTAIC PERFORMANCE OF GaInNAs SOLAR CELLS

by

Ville Polojärvi, Arto Aho, Antti Tukiainen, Marianna Raappana, Timo Aho,
Andreas Schramm, and Mircea Guina

Solar Energy Mater. Solar Cells vol. 149, pp. 213–220, 2016.

Solar Energy Materials & Solar Cells 149 (2016) 213–220

Contents lists available at ScienceDirect

Solar Energy Materials & Solar Cells

journal homepage: www.elsevier.com/locate/solmat

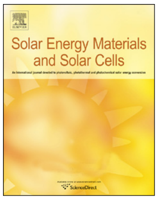

Influence of As/group-III flux ratio on defects formation and photovoltaic performance of GaInNAs solar cells

Ville Polojärvi*, Arto Aho, Antti Tukiainen, Marianna Raappana, Timo Aho, Andreas Schramm, Mircea Guina

Optoelectronics Research Centre, Tampere University of Technology, P.O. Box 692, FIN-33101 Tampere, Finland

ARTICLE INFO

Article history:
Received 13 November 2015
Received in revised form
20 January 2016
Accepted 22 January 2016

Keywords:
III–V semiconductors
Multijunction solar cells
Dilute nitrides
Material characterization
Defects
Molecular beam epitaxy

ABSTRACT

The correlation between the As to group III flux ratio and photovoltaic performance of $GaIn_{0.1}N_{0.03}As$ solar cells fabricated by molecular beam epitaxy is systematically investigated. The results show that flux ratio has a remarkable influence on the formation of defect traps. Furthermore, the formation of defects at different flux ratios is correlating with the variation of the background doping level and the photovoltaic performance. In particular, this study reveals a linear dependency between current generation, dark saturation current, defect densities, photoluminescence peak intensity and the flux ratio. A significant increase in solar cell performance, exhibiting maximum external quantum efficiency of 90%, is obtained when As/group-III ratio is decreased close to the stoichiometric limit. For optimized growth condition, the 1 eV $GaIn_{0.1}N_{0.03}As$ solar cell exhibits a short circuit current density as high as 17.9 mA/cm^2 calculated from the external quantum efficiency data (AM0 conditions) with 870 nm high-pass filter. This value reflects the potential of the GaInNAs cell for current matching and power generation in high efficiency solar cells incorporating three- or four- junctions.

1. Introduction

Multijunction solar cells based on III–V semiconductors have the highest conversion efficiency of all photovoltaic devices, with the record efficiency of 46% [1]. A high power-to-mass ratio and suitability for high concentrations make such solar cells ideal for space and terrestrial concentrator applications. Despite these remarkable attributes, the potential offered by current solar cells lies far behind theoretical predictions pointing to efficiencies beyond 50% [2]. This is largely due to the lack of high quality material with a band-gap between GaAs and Ge and lattice-matched to GaAs/Ge. To this end, dilute nitride materials have emerged as a viable solution providing a band gap that can be changed from at least 0.8 eV to 1.42 eV by incorporation of only a few percentages of N [3,4]. An optimal band-gap for bottom junction of GaInP/GaAs/GaInNAs solar cells is close to 1 eV. On the other hand, the epitaxy of these compounds has been recognized as a very challenging task because they are metastable and have a large miscibility gap [5,6]. Therefore, dilute nitrides have to be grown at non-equilibrium conditions at relatively low temperatures in order to avoid phase separation and clustering effects [7]. Furthermore, owing to its high electronegativity, N induces point defects that have a detrimental influence on material and device properties. For semiconductor solar cells the defects typically increase the non-radiative recombination reducing the minority carrier diffusion lengths and modify the doping levels, ultimately decreasing the conversion efficiencies.

In general, the formation process and the type of defects in dilute nitrides depend significantly on the epitaxy technique used. For example, when employing metal–organic chemical vapor deposition (MOCVD) for epitaxy of dilute nitride materials, the material quality is also affected by carbon contamination and subsequent increase of background-doping, presence of hydrogen that is detrimental to N incorporation, and gallium vacancies (V_{Ga}) [8]. In fact the combination of these issues has resulted in lower performance of MOCVD-grown dilute nitride solar cells compared to standard approaches without N. However, molecular beam epitaxy (MBE) has recently emerged as being suitable for alleviating some of the limitations exhibited by MOCVD, ultimately leading to demonstration of high quality GaInNAs heterostructures and very high efficiency 3-junction solar cells [7,9]. First of all, in MBE the incorporation of N can be accurately controlled using plasma sources while the detrimental presence of C and H is avoided [10]. Moreover, MBE renders several other ways to improve the quality of dilute nitrides for example, by alloying

---

* Corresponding author.
E-mail address: ville.polojarvi@tut.fi (V. Polojärvi).

http://dx.doi.org/10.1016/j.solmat.2016.01.024
0927-0248/© 2016 Elsevier B.V. All rights reserved.

small amounts of Sb to GaInNAs. Besides its known surfactant effect, the use of Sb leads to a drastic reduction of background doping level increasing the photocurrent generation, [9] ultimately leading to conversion efficiencies reaching 44%, recorded from 3-junction device [11,12]. Thermal annealing [8,13] and the use of deflector plates [9,14] are also important tools for reducing the number of N-induced defects in dilute nitrides.

Yet one of the most critical parameters in MBE of GaAs-based materials is the ratio of group V and group III fluxes hitting the substrate surface, i.e. the As/group-III ratio or V/III ratio. The practical measure of this ratio is given by the beam equivalent pressure (BEP) defined as the pressure measured with *in-situ* ion gauge without corrections for different ionization efficiencies of the measured species. This affects the incorporation of impurities, generation of lattice defects, and indeed the dynamics of atomic incorporation at the growth front [15]. For growing high quality GaAs at growth temperatures of 580–600 °C, the V/III BEP ratios of 10–20 are often used. However, for efficient incorporation of N, the growth temperature is much lower than the optimum point corresponding to GaAs lattice, [10] leading to formation of several types of point defects [16]. In this case, the window for the V/III BEP ratios producing smooth surfaces gets smaller [17]. In general, the choice of the V/III BEP ratio has a strong influence on the properties of GaInNAs materials [7,10,18–20] as the As pressure influences the N neighboring configuration and has a strong effect on the photoluminescence emission intensity and the rapid thermal annealing behavior. Majority of studies have focused on revealing the influence of As flux on the structural and optical properties of GaInNAs quantum wells (QWs). For example, Jaschke *et al.* reported that when using relatively high N (~4%) and In compositions to reach emission at above 1500 nm, the optimal flux ratio for low temperature grown GaInNAs QWs had to be minimized close to the stoichiometric limit [18]. On the other hand, another report focused on maximizing the photoluminescence of QWs operating at 1300 nm, corresponding to a lower N content of about 1.5%, points to the use of an As/III BEP ratio as high as 12 [21]. While the published concerning the QWs is somewhat contradictory, it is indeed expected that the influence of the As/group-III ratio depends on other growth parameters, such as the growth temperature, or specific rapid thermal annealing conditions.

In this paper, we investigate the effects of the V/III BEP ratio on the properties of $GaIn_{0.1}N_{0.03}As$ bulk heterostructures with a bandgap of 1 eV, grown by MBE. These materials are essential building blocks for the development of monolithic high-efficiency multijunction solar cells with 4 or more junctions. In particular we focus on correlating the V/III BEP ratio to defect states formed during the epitaxy and to performance of the solar cell. The analysis is based on using capacitance spectroscopy, together with photoluminescence (PL) and electrical characteristics of the corresponding solar cells. We demonstrate high quality $GaIn_{0.1}N_{0.03}As$ solar cell, and discuss how the V/III BEP ratio links to solar cell performance and defect formation.

2. Material and methods

The experimental samples consisted of p–i–n structures grown on 2" p-type GaAs(100) substrates and are schematically depicted in Fig. 1. They were comprised of a p-GaAs buffer layer, p-type GaInP back surface field (BSF) layer, p-GaAs base, unintentionally doped lattice matched 1 eV band gap $GaIn_{0.1}N_{0.03}As$ i-region, n-GaAs emitter, n-AlInP window layer, and highly doped n-GaAs contact layer. The thickness of the $GaIn_{0.1}N_{0.03}As$ absorber layer was set to 1300 nm. During the growth of $GaIn_{0.1}N_{0.03}As$, the V/III BEP ratio was 6, 7, and 9 for samples S1, S2, and S3, respectively.

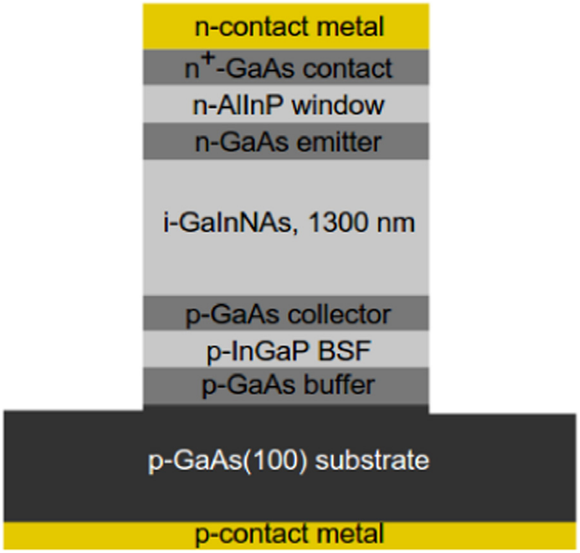

Fig. 1. Schematic representation of the sample structure used for electrical characterization. Mesa structures with diameter of 800 μm were etched through epitaxial layers. Ohmic contacts were fabricated by e-beam evaporation. Solar cells with top contact grid and antireflection coating were fabricated for LIV and EQE measurements.

More detailed epitaxial parameters have been reported elsewhere [7]. The V/III BEP ratio was varied by changing the As flux while all other fabrication parameters were kept constant. The N flux was not taken into account when BEP was calculated for group V. A BEP ratio of 6 was found to be close to the lower acceptable limit to ensure high crystal morphology and high optical properties. After the growth, mesa-type devices with top and bottom contacts were processed for capacitance–voltage (CV), dark current–voltage (IV) and deep level transient Fourier spectroscopy (DLTFS) [22,23] measurements. Solar cells with top grid and backside contacts were fabricated for light-biased current–voltage measurements (LIV) and external quantum efficiency measurements (EQE). To this end, the contact GaAs was selectively etched from the area between the grid fingers and a double-layer TiO_2/SiO_2 antireflection coating, optimized for $GaInP/GaAs/GaIn_{0.1}N_{0.03}As$ solar cell, was deposited on the cells by e-beam evaporation.

IV, CV, and DLTS measurements were conducted using a Bio Rad DL8000 deep level transient Fourier spectroscopy measurement system employing Fourier analysis of the capacitance transients. The frequency and the amplitude of the signal used for CV measurements were 1 MHz and 100 mV, respectively. Photoluminescence spectra were measured using an Accent RPM2000 PL mapper equipped with a 980 nm diode laser for excitation and an InGaAs detector array for signal collection. LIV measurements were performed with an Oriel solar simulator equipped with a 1000 W Xe-arc lamp and an AM1.5 G filter. The solar simulator was calibrated with a known GaInP/GaAs tandem calibration cell. The EQE measurements were performed using a setup consisting of a broadband light source, lock-in amplifier, a 750 nm long pass filter, a monochromator, and a NIST-traceable Ge detector.

3. Results and discussion

Fig. 2(a) shows the LIV characteristics of the solar cells processed from each sample wafer. Sample S1, grown with the lowest BEP ratio, shows clearly the best performance, whereas S3, grown with the highest BEP ratio, shows significant reduction in current and voltage compared to S1. Similar trend is observed in Fig. 2 (b) which shows the EQE data at wavelengths ranging from

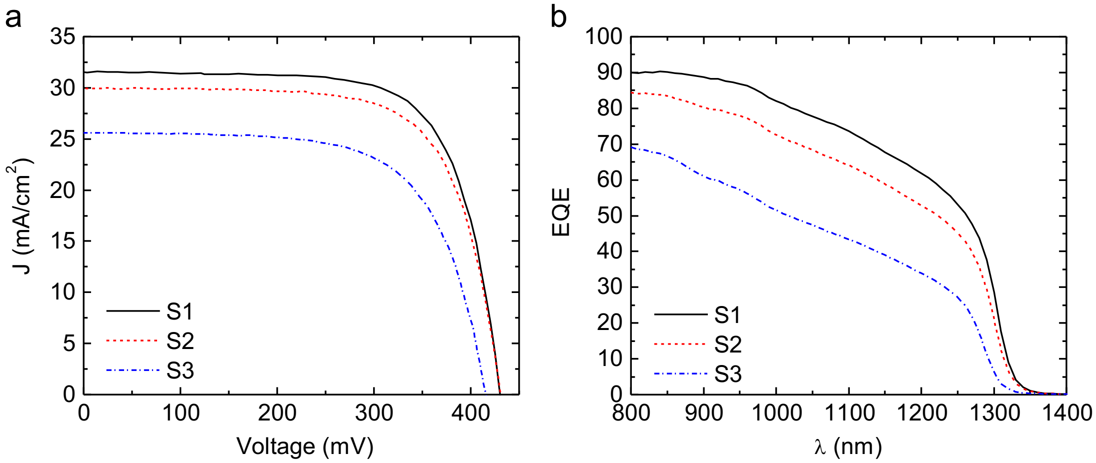

Fig. 2. (a) Current–voltage characteristics, and (b) EQE and the reflection of the investigated samples. Short circuit current and EQE increases with the decreasing V/III BEP ratio.

800 nm to 1400 nm. The highest EQE was measured from S1; reaching 90% close to the band edge of GaAs, whereas S3 shows only 63–68% EQE at the same wavelength range. Dark saturation current densities (J_S) were found to correlate with the LIV and EQE measurements, showing increase with the V/III BEP ratio. The results show that a relatively small change in the V/III BEP ratio, from 9 to 6, has a drastic influence on GaInNAs solar cell operation.

Table 1 summarizes the short circuit current densities (J_{SC}) for AM0, AM1.5D, and AM1.5 G illumination, [24] as calculated using EQE data presented in Fig. 2(b). The illumination is assumed to take place through a 870 nm low pass (LP) filter that resembles the effect of top-cells in multijunction solar cell architectures. Although the thickness of the intrinsic region is only 1.3 µm, S1 could produce a high current, fulfilling current matching condition for integration with state-of-the-art GaInP/GaAs tandem solar cell [25].

To investigate the reasons leading to remarkably improved solar cell characteristics for lower V/III ratios, we analyzed the background doping using CV measurements [26]. Although the dilute nitride layers (i-regions) are not intentionally doped, they always have a non-zero background doping caused by intrinsic or extrinsic defects. The background doping was determined to be p-type, based on the separate Hall samples as well as EQE data. We note that the p-type background doping is beneficial when using p-type substrates because: (i) the depletion region forms on the top part of the junction where light enters the material and (ii) the minority carriers are electrons, which have a longer diffusion length compared to holes. CV measurement results and the corresponding background doping profiles are shown in Fig. 3(a) and (b), respectively. The background doping was found to increase with the V/III ratio, attaining values of $2.2 \times 10^{16}\,\text{cm}^{-3}$, $4.6 \times 10^{16}\,\text{cm}^{-3}$, and $8.3 \times 10^{16}\,\text{cm}^{-3}$ for samples S1, S2, and S3, respectively. Samples S2 and S3 have higher leakage currents than S1 and thus they could not be measured down to -20.4 V, which is the maximum reverse voltage obtainable in the measurement setup.

DLTFS measurements were performed to link the observed changes in the background doping to deep levels in the GaInNAs layers. DLTFS spectra in Fig. 4 show three distinct majority carrier trap states, labeled as T1, T2, and T3. There might also be weaker deep level signals masked by T1–T3, which cannot be distinguished, especially on the high temperature side of T1 and on both sides of T3. Fig. 5 shows the Arrhenius evaluation of the DLTFS data. The extracted parameters i.e. thermal activation energies (E_A), capture cross sections (σ), and apparent trap densities (N_T) are presented in Table 2. Trap T1, occurring at the lowest temperature could not be evaluated for samples S2 and S3 due to lower peak temperature compared to S1 and freeze-out of the background-doping-related carriers at low temperatures. At very low temperatures the carrier concentration is reduced leading to extension of the depletion region through the GaInNAs layer to the highly p-doped GaAs base layer and thus the DLTFS signal, related to the GaInNAs layer, could not be measured.

Table 1
J_{SC} for samples S1–S3 assuming illumination through a 870 LP filter, based on the reference solar spectra for AM0, AM1.5D and AM1.5 G and EQE data shown in Fig. 2 (b). The target J_{SC} refers to current matching condition in state-of-the-art GaInP/GaAs multijunction solar cell.

Sample	J_{SC} AM0 (mA/cm^2)	J_{SC} AM1.5G (mA/cm^2)	J_{SC} AM1.5D (mA/cm^2)
S1	17.9	14.5	13.7
S2	15.7	12.7	12.0
S3	10.9	8.8	8.3
Target	17.8	14.5	13.8

PL intensity was also measured to give additional information on the defect density and overall material quality. Fig. 6 summarizes the measured data showing J_{SC}, open circuit voltage (V_{OC}), J_S, N_S, PL signal, PL spectra full width at half maximum (FWHM), T2 density (N_{T2}), and T3 density (N_{T3}) as a function of the V/III BEP ratio. Interestingly, there is a linear dependency between the V/III BEP ratio and J_{SC}, J_S, N_S, PL signal, N_{T2}, and N_{T3}. J_{SC} and PL signals were found to decrease linearly while J_S, N_S, N_{T2}, and N_{T3} increase linearly with the V/III BEP ratio. V_{OC} and the FWHM values did not show linear dependency on the V/III BEP ratio. However, the highest V_{OC} and the narrowest PL peak were recorded from S1, grown with the lowest BEP ratio.

The measurements show that decreasing the V/III BEP ratio increases the solar cell efficiency and decreases the N_S. The results are in line with drift-diffusion simulations run on GaInNAs single junction solar cells which show that lower p-type doping in GaInNAs should lead to improved EQE and LIV characteristics. More precisely, the decrease in the background doping results in wider depletion region, which increases the probability that light is absorbed in or in the vicinity of the volume having electric field inside the p–n junction and this helps in carrier collection. We expect that this is the main reason for the observed improvements in LIV and EQE data. In a recently published study by Langer *et al.*, it was reported that decreasing the V/III BEP ratio from 9.5 to 7.6, resulted in increased J_{SC} and IQE (measured at open circuit condition) but lower V_{OC}, FF, and increased dark saturation current density [27]. This is contrary to what was observed here, namely that lowering the V/III BEP ratio down to 6 improves all the measured material and solar cell parameters. In addition to the

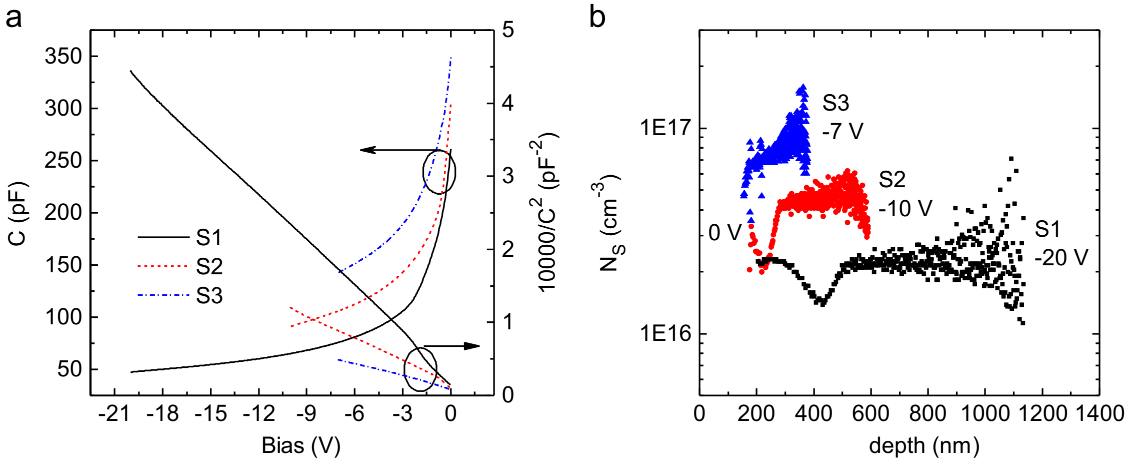

Fig. 3. (a) Capacitance-voltage characteristics with Mott-Schottky plots [27] of the CV data and (b) calculated background doping profiles.

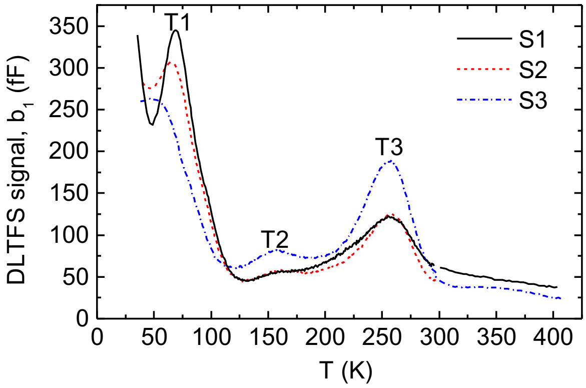

Fig. 4. Majority carrier (holes) DLTFS spectra. Three different peaks, labeled as T1, T2, and T3 are visible. Measurement parameters were: reverse bias $U_R = -3$ V, pulse voltage $U_P = -1$ V, period width $T_W = 20$ ms, and pulse time $t_P = 100$ ms.

Table 2
N_T, E_A, and σ for T1, T2, and T3 determined by Arrhenius evaluation of DLTFS data.

Trap	N_T (cm^{-3})	E_A (meV)	σ (cm^2)
T1	S1: 2.7×10^{14} S2: not eval. S3: not eval.	100–110	2.0×10^{-15}
T2	S1: 3.1×10^{13} S2: 4.9×10^{13} S3: 9.3×10^{13}	250–360	not eval.
T3	S1: 6.4×10^{13} S2: 1.1×10^{14} S3: 2.1×10^{14}	450–485	$1.1–3.2\times10^{-15}$

improvement observed in the solar cell performance and background doping, the defect densities and defect-sensitive J_S decrease and the PL intensity increase with the decreasing V/III BEP ratio.

The unintentional background doping in the present samples as well as in GaInNAs material general originates from defects. Gallium vacancies (V_{Ga}) associated with N, resulting in N-V_{Ga} complexes are assumed to act as acceptors in dilute nitride materials. Such N-V_{Ga} complexes also have lower formation energy compared to V_{Ga} alone. The presence of hydrogen further lowers the formation energy resulting in H–N–V_{Ga} complex, which, together with carbon doping, has been the cause for high background doping in MOCVD grown GaInNAs [28]. It was reported that V_{Ga} are the dominant acceptors in low-temperature MBE grown GaAs [16,29] and that the density of V_{Ga} increases with the V/III BEP ratio [30]. This goes in a line with the result that the formation energy of V_{Ga} in GaAs decreases when As pressure is increased and furthermore V_{Ga} density increases when growth temperature is lowered [31]. Compensating intrinsic donor type defects can also be formed in GaAs-based materials. For example, Ga antisite (Ga_{As}) is considered to be a double donor in GaAs [32,33] and could act as a compensating defect. However, the intrinsic defects observed in GaAs alone cannot explain the relatively high p-type background doping observed in GaInNAs because the background doping is dependent on the N concentration. Therefore, based on the previous studies, and the fact that background doping increases linearly with the V/III BEP ratio, we can assume that V_{Ga} are present and they and their complexes with N could explain, at least partly, the observed p-type background doping in S1–S3. Furthermore, EQE data in Fig. 2(b) shows that the absorption edge of S3 moves to higher energy (shorter wavelength), which indicates that the higher As pressure starts to limit N incorporation due to competition between group V element. This behavior goes in line with earlier reports on QW samples [18,34,35].

When the apparent trap densities and the background doping levels in GaInNAs are compared, a link between the trap densities and the background doping is found. Fig. 7 shows the change in the trap densities of T2 and T3 compared (ΔN_T) versus the change in the background doping density (ΔN_S). The normalized densities of T2 and T3 increase linearly and almost in identical fashion with p-type background doping, with the slope close to one. This could indicate, that the observed defects are related to the background doping, and that T2 and T3 have something in common. One possible interpretation could be that they are related to the same defect or defect complex, which furthermore could be behind the background doping by causing also shallow acceptor levels.

Trap levels, lying deep in the middle of the band gap, often act as efficient recombination centers, which becomes evident from the data shown in Fig. 6. The V/III BEP ratio influences directly the densities of T2 and T3, as well as J_S which is sensitive to non-radiative recombination. Several studies have revealed deep levels in MOCVD or MBE grown GaInNAs materials with thermal activation energies close to 0.1 eV, 0.2 eV, 0.4 eV, and 0.5 eV [9,36–40]. Part of these published levels has their trap signatures closely similar to those observed in the present study and could well be related to similar defects. Deep levels lying close to the middle of

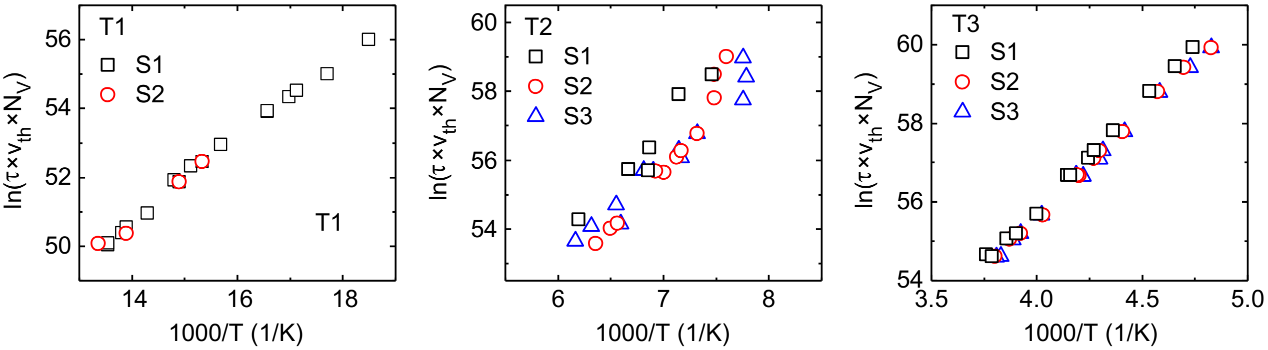

Fig. 5. Arrhenius evaluation for trap states T1, T2, and T3.

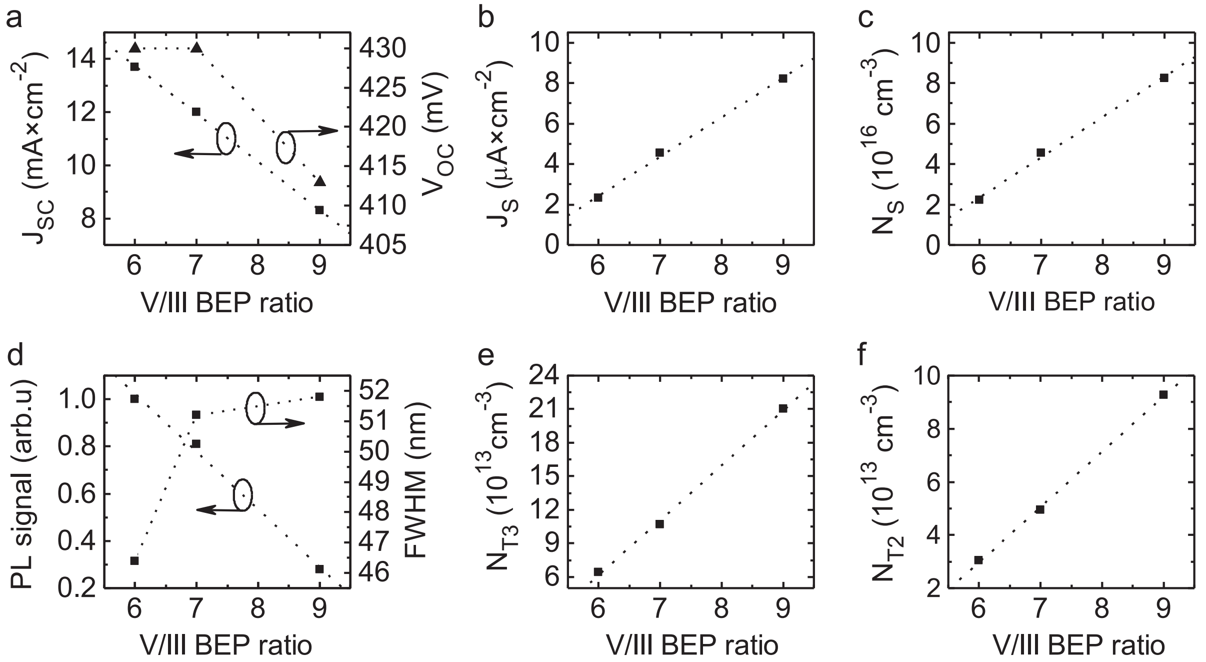

Fig. 6. (a) VOC and J_{SC}, calculated from the EQE data by assuming 870 nm LP filter and standard AM1.5D spectrum, (b) J_S, (c) N_S, (d) PL signal and FWHM, (e) N_{T3}, and (f) N_{T2} as a function of the V/III BEP ratio.

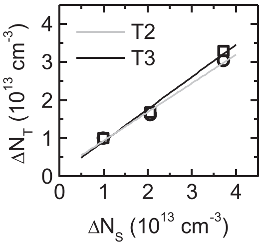

Fig. 7. Change in the trap density as a function of change in the background doping. The slopes are close to one and almost identical for T2 and T3.

the band gap are often claimed to be responsible for the nonradiative recombination. Furthermore, acceptor levels assigned to N-hydrogen-related deep acceptors with activation energy of ~0.11 eV have been observed in chemical-beam-epitaxy-grown GaNAs [41]. Thermal ionization of this particular level was considered to be responsible for the steep increase in the junction capacitance at low temperatures as well as ionized acceptor concentration. The behavior of this defect matches well with that of T1. Another link between this study and Ref. [41] is that a deep hole trap at $E_A = 0.51$ eV was claimed to be responsible in part for the nonradiative recombination in the depletion region.

One typical feature on dilute nitrides is the broad DLTFS peak signals. Broadening of DLTS peaks originates from non-exponential capacitance transients which arise from several possible origins. For example, material disordering effects that broaden the density of states of the defect level [42] as well as Gaussian broadening of the level, or several closely spaced discrete thermal activation energies of the point defect owing to different configurations of the nearest or second nearest neighbor atoms [38,43,44]. Non-exponential transients and peak broadening effects are also observed in extended defects and dislocations [45,46] and sometimes due to overlapping of closely space individual deep level peak signals. Due to broad peak signals, thermal activation energies and capture cross sections, determined from the Arrhenius evaluation can thus be expected to be “average” values for each defect type.

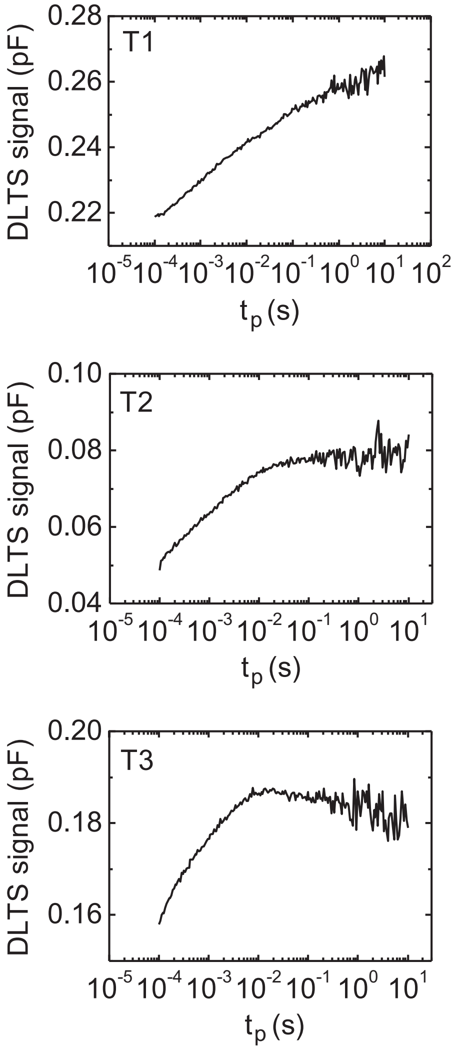

Fig. 8. Isothermal measurements recorded from each of the deep levels in S3. The filling pulse duration is varied from 1 ms to 10 s.

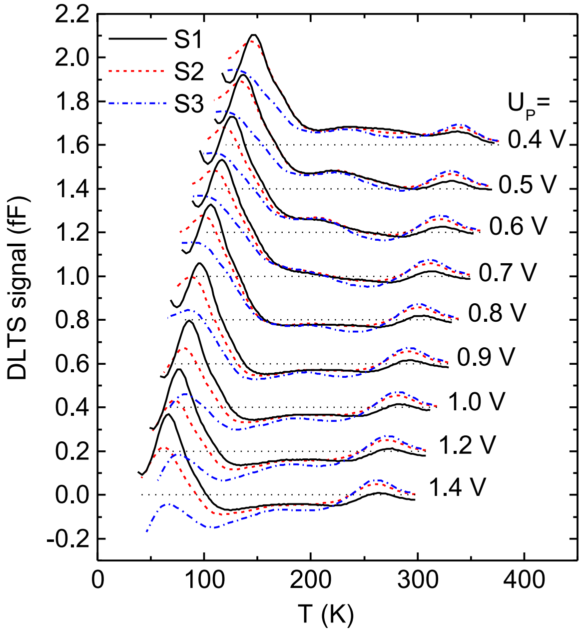

Fig. 9. DLTFS spectra with positive U_P, ranging from 0.4 V to 1.4 V. The offset of 0.2 fF and 10 K is added for clarity. Dashed lines show the zero level for each curve. Other measurement parameters were: $U_R = -1$ V, $T_W = 20$ ms, and $t_P = 10$ ms.

One method to characterize whether the DLTFS signal is caused by point defects or extended defects is to measure the amplitude of the DLTFS signal versus t_P. Fig. 8 shows the DLTFS signals (b_1 coefficient of the Fourier series) recorded from S3 for traps T1, T2, and T3 plotted in semi-logarithmic scale against t_P. The DLTFS signal is saturating for T2 and T3 already when $t_P < 100$ ms, which is a typical behavior of point defects [47]. For T1, the DLTFS signal increases almost linearly up to $t_P = 10$ s, which was the longest filling pulse duration used. Such a logarithmic dependence of the DLTS signal and non-saturating nature of the signal on the filling pulse duration is typically considered as a signature of extended defects or dislocation related defects [48]. However, the positions of T1–T3 do not shift when t_P is varied from 1 ms to 1 s (not shown here). This behavior indicates that the defects are concerned with localized states rather than band-like states [49]. Therefore, according to the three criteria given in ref. [49], T1 would be identified as an extended or dislocation related defect which involves localized states.

The peak position of T1 moves towards lower temperatures when moving from S1 to S3. Since the electric field increases together with background doping density, it is possible that the position of T1 depends on the electric field inside the p–n junction. The possible electric field dependence of the hole emission rate from T1 was studied by varying the reverse bias voltage to adjust the electric field strength in the p–n junction. No shift in the peak position to the lower temperature was observed, which suggests that the activation energy of T1 is not sensitive to electric field. Apparently, the thermal activation energy of the T1 trap depends on the V/III BEP ratio.

It is also possible to obtain information about minority carrier traps by using forward bias pulses in DLTFS. In this case, minority carriers (electrons in p-type material) are injected to GaInNAs and are trapped at minority carrier traps. The minority carrier traps are in this case seen as negative peaks in the DLTFS spectrum. Fig. 9 shows the DLTFS spectra recorded from S1–S3 when varying the pulse voltage used to inject minority carriers. Results show that S3 has the largest negative signal which indicates that higher V/III BEP ratio induces the highest number of minority carrier traps as well. Unfortunately, due to overlapping majority and minority carrier trap signals, the exact evaluation of minority carrier trap parameters and concentrations could not be obtained here.

4. Conclusions

In summary, we have investigated the influence of the V/III BEP ratio on electrical and optical properties of $GaIn_{0.1}N_{0.03}As$ p–i–n solar cells. The intrinsic background doping of the MBE-grown $GaIn_{0.1}N_{0.03}As$ layer was found to be p-type and strongly dependent on the V/III BEP ratio. Linear dependency was found between the V/III BEP ratio in the range of 6–9 and material and device parameters, i.e. J_{SC}, J_S, N_S, N_{T2}, N_{T3}, and PL intensity. The lowest V/III BEP ratio of 6 produced the highest J_{SC}, V_{OC} and PL signal, and lowest J_S, N_S, N_{T3}, N_{T2}, and PL FWHM. The corresponding EQE was 90%, slightly below the band gap of GaAs. The smallest V/III BEP ratio also corresponded to the highest V_{OC} and smallest PL peak FWHM.

The DLTFS measurements revealed three distinct hole levels. The thermal activation energies of deep hole levels T1, T2, and T3 were found to be 0.1 eV, 0.25–0.36 eV, and 0.45–0.485 eV, respectively, and they are comparable with earlier published studies on MOCVD and MBE grown GaInNAs. T1 showed clear extended-defect-like characteristics in DLTS whereas T2 and T3 are deemed to originate from point defects. The concentration of T2 and T3 changes in identical fashion when V/III BEP ratio was adjusted indicating a possible link between the two. No electric field effect was observed for activation energies of T1–T3. Minority carrier electron traps were also detected in S1–S3, when forward bias injection pulses were used, but their trap parameters could not be evaluated.

Overall, the data from the LIV characteristics together with the results from the CV, IV, DLTFS, and PL measurements showed that the V/III BEP ratio has a remarkable influence on defect formation in GaInNAs solar cells, and that the device performance improves significantly when the growth conditions are kept close to the stoichiometric limit. For the low III/V BEP ratio, the current generated by 1 eV band gap $GaIn_{0.1}N_{0.03}As$ p–i–n solar cell, estimated from the EQE data considering illumination through a 870 nm HP filter, matches the current generation of state-of-the-art GaInP/GaAs tandem solar cell, despite the use of relatively thin (1.3 μm) intrinsic $GaIn_{0.1}N_{0.03}As$ region.

Acknowledgments

This work is supported by the Finnish Funding Agency for Technology and Innovation (TEKES) projects “Solar III–V” (#40120/09) and “NextSolar” (#40239/12). Ville Polojärvi gratefully acknowledges National Doctoral Program in Nanoscience (NGS-NANO), Emil Aaltonen Foundation, KAUTE-Foundation, and Walter Ahlström Foundation for the financial support.

References

[1] M.A. Green, K. Emery, Y. Hishikawa, W. Warta, E.D. Dunlop, Solar cell efficiency tables (Version 45), Prog. Photovolt. Res. Appl. 23 (2015) 1–9.

[2] A. Luque, Will we exceed 50% efficiency in photovoltaics? J. Appl. Phys. 110 (2011) 031301.

[3] D. Friedman, J. Geisz, S.R. Kurtz, J. Olson, 1-eV solar cells with GaInNAs active layer, J. Cryst. Growth 195 (1998) 409–415.

[4] J. Geisz, D. Friedman, J. Olson, S.R. Kurtz, B. Keyes, Photocurrent of 1 eV GaInNAs lattice-matched to GaAs, J. Cryst. Growth 195 (1998) 401–408.

[5] J. Neugebauer, Walle Van de, G. Chris, Electronic structure and phase stability of GaAs $1-x$ N x alloys, Phys. Rev. B 51 (1995) 10568.

[6] D. Schlenker, T. Miyamoto, Z. Pan, F. Koyama, K. Iga, Miscibility gap calculation for Ga $1-x$ In x N y As $1-y$ including strain effects, J. Cryst. Growth 196 (1999) 97-70.

[7] A. Aho, V. Polojärvi, V. Korpijärvi, J. Salmi, A. Tukiainen, P. Laukkanen, M. Guina, Composition dependent growth dynamics in molecular beam epitaxy of GaInNAs solar cells, Solar Energy Mater. Solar Cells 124 (2014) 150–158.

[8] K. Volz, D. Lackner, I. Nemeth, B. Kunert, W. Stolz, C. Baur, F. Dimroth, A. Bett, Optimization of annealing conditions of (GaIn)(NAs) for solar cell applications, J. Cryst. Growth 310 (2008) 2222–2228.

[9] D.B. Jackrel, S.R. Bank, H.B. Yuen, M.A. Wistey, J.S. Harris Jr, A.J. Ptak, S. W. Johnston, D.J. Friedman, S.R. Kurtz, Dilute nitride GaInNAs and GaInNAsSb solar cells by molecular beam epitaxy, J. Appl. Phys. 101 (2007) 114916.

[10] A. Aho, V. Korpijärvi, A. Tukiainen, J. Puustinen, M. Guina, Incorporation model of N into GaInNAs alloys grown by radio-frequency plasma-assisted molecular beam epitaxy, J. Appl. Phys. 116 (2014) 213101.

[11] J. Allen, V. Sabnis, M. Wiemer, H. Yuen, 44%-efficiency triple-junction solar cells, In: proceedings of the 9th International Conference on Concentrator Photovoltaic Systems, Miyazaki, Japan, April 2013.

[12] D. Derkacs, R. Jones-Albertus, F. Suarez, O. Fidaner, Lattice-matched multi-junction solar cells employing a 1 eV GaInNAsSb bottom cell, J. Photon. Energy 2 (2012) 021805.

[13] S.R. Kurtz, A. Allerman, E. Jones, J. Gee, J. Banas, B. Hammons, InGaAsN solar cells with 1.0 eV band gap, lattice matched to GaAs, Appl. Phys. Lett. 74 (1999) 729–731.

[14] M.A. Wistey, S.R. Bank, H.B. Yuen, H. Bae, J.S. Harris, Nitrogen plasma optimization for high-quality dilute nitrides, J. Cryst. Growth 278 (2005) 229–233.

[15] E.C. Larkins, J.S. Harris Jr., in: R.F. Farrow (Ed.), Molecular Beam Epitaxy: Applications to Key Materials, Noyes Publications, Park Ridge, New Jersey, U.S. A, 1995, pp. 114–245.

[16] X. Liu, A. Prasad, J. Nishio, E. Weber, Z. Liliental-Weber, W. Walukiewicz, Native point defects in low-temperature-grown GaAs, Appl. Phys. Lett. 67 (1995) 279–281.

[17] M. Lagadas, Z. Hatzopoulos, K. Tsagaraki, M. Calamiotou, C. Lioutas, A. Christou, The effect of arsenic overpressure on the structural properties GaAs grown at low temperature, J. Appl. Phys. 80 (1996) 4377–4382.

[18] G. Jaschke, R. Averbeck, L. Geelhaar, H. Riechert, Low threshold InGaAsN/GaAs lasers beyond 1500 nm, J. Cryst. Growth 278 (2005) 224–228.

[19] E. Pavelescu, T. Hakkarainen, V. Dhaka, N. Tkachenko, T. Jouhti, H. Lemmetyinen, M. Pessa, Influence of arsenic pressure on photoluminescence and structural properties of GaInNAs/GaAs quantum wells grown by molecular beam epitaxy, J. Cryst. Growth 281 (2005) 249–252.

[20] A. Aho, A. Tukiainen, V. Polojärvi, J. Salmi, M. Guina, MBE growth of high current dilute III–VN single and triple junction solar cells, In: proceedings of the 27th European Photovoltaic Solar Energy Conference, Frankfurt, Germany, September 2012, pp. 290–292.

[21] R. Kudrawiec, V. Korpijärvi, P. Poloczek, J. Misiewicz, P. Laukkanen, J. Pakarinen, M. Dumitrescu, M. Guina, M. Pessa, The influence of As/III pressure ratio on nitrogen nearest-neighbor environments in as-grown GaInNAs quantum wells, Appl. Phys. Lett. 95 (2009) 261909.

[22] S. Weiss, R. Kassing, Deep Level Transient Fourier Spectroscopy (DLTFS)—A technique for the analysis of deep level properties, Solid-State Electron. 31 (1988) 1733–1742.

[23] D.V. Lang, Deep-level transient spectroscopy: a new method to characterize traps in semiconductors, J. Appl. Phys. 45 (1974) 3023–3032.

[24] G. ASTM, 173–03: Standard tables for reference solar spectral irradiances: direct normal and hemispherical on 37° tilted surface, West Conshohoken, ASTM International, PA (2003) http://dx.doi.org/10.1520/G0173-03R12.

[25] A. Aho, A. Tukiainen, V. Polojärvi, M. Guina, Performance assessment of multijunction solar cells incorporating GaInNAsSb, Nanoscale Res. Lett. 9 (2014) 61.

[26] P. Blood, J.W. Orton, The Electrical Characterization of Semiconductors: Majority Carriers and Electron States, Academic Press, London (1992), p. 220–264.

[27] F. Langer, S. Perl, S. Höfling, M. Kamp, p-to n-type conductivity transition in 1.0 eV GaInNAs solar cells controlled by the V/III ratio, Appl. Phys. Lett. 106 (2015) 063905.

[28] A. Janotti, S. Wei, S. Zhang, S. Kurtz, C. Van de Walle, Interactions between nitrogen, hydrogen, and gallium vacancies in GaAs $1-x$ N x alloys, Phys. Rev. B 67 (2003) 161201.

[29] J. Gebauer, R. Krause-Rehberg, S. Eichler, M. Luysberg, H. Sohn, E. Weber, Ga vacancies in low-temperature-grown GaAs identified by slow positrons, Appl. Phys. Lett. 71 (1997) 638–640.

[30] J. Gebauer, F. Borner, R. Krause-Rehberg, P. Specht, E. Weber, Vacancies in low-temperature-grown GaAs: Observations by positron annihilation, Semicond. Insul. Mater. 1998 Proc. Conf. 10th (1998) 118–121.

[31] D. Murdick, X. Zhou, H. Wadley, Low-temperature atomic assembly of stoichiometric gallium arsenide from equiatomic vapor, J. Cryst. Growth 286 (2006) 197–204.

[32] Z. Wang, L. Ledebo, H. Grimmeiss, Electronic properties of native deep-level defects in liquid-phase epitaxial GaAs, J. Phys. C: Solid State Phys. 17 (1984) 259.

[33] P. Krispin, S. Spruytte, J. Harris, K. Ploog, Origin and annealing of deep-level defects in p-type GaAs/Ga (As, N)/GaAs heterostructures grown by molecular beam epitaxy, J. Appl. Phys. 89 (2001) 6294–6301.

[34] V. Odnoblyudov, A.Y. Egorov, A. Kovsh, A. Zhukov, N. Maleev, E. Semenova, V. Ustinov, Thermodynamic analysis of the MBE growth of GaInAsN, Semicond. Sci. Technol. 16 (2001) 831.

[35] A.Y. Egorov, D. Bernklau, B. Borchert, S. Illek, D. Livshits, A. Rucki, M. Schuster, A. Kaschner, A. Hoffmann, G. Dumitras, Growth of high quality InGaAsN heterostructures and their laser application, J. Cryst. Growth 227 (2001) 545–552.

[36] R. Kaplar, D. Kwon, S. Ringel, A. Allerman, S.R. Kurtz, E. Jones, R. Sieg, Deep levels in p-and n-type InGaAsN for high-efficiency multi-junction III–V solar cells, Solar Energy Mater. Solar Cells 69 (2001) 85–91.

[37] D. Kwon, R. Kaplar, S. Ringel, A. Allerman, S.R. Kurtz, E. Jones, Deep levels in p-type InGaAsN lattice matched to GaAs, Appl. Phys. Lett. 74 (1999) 2830–2832.

[38] R. Kaplar, S. Ringel, S.R. Kurtz, J. Klem, A. Allerman, Deep-level defects in InGaAsN grown by molecular-beam epitaxy, Appl. Phys. Lett. 80 (2002) 4777–4779.

[39] F. Abulfotuh, A. Balcioglu, D. Friedman, J. Geisz, S. Kurtz, Investigation of deep levels in GaInNAs, AIP Conf. Proc. 462 (1999) 492–498.

[40] S. Johnston, R. Ahrenkiel, A. Ptak, D. Friedman, S. Kurtz, Defect Trapping in InGaAsN Measured by Deep-Level Transient Spectroscopy, No. NREL/CP-520-33557, National Renewable Energy Laboratory (NREL), Golden, Colorado, U.S. A, 2003.

[41] B. Bouzazi, N. Kojima, Y. Ohshita, M. Yamaguchi, Capacitance–voltage and current–voltage characteristics for the study of high background doping and conduction mechanisms in GaAsN grown by chemical beam epitaxy, J. Alloys Compd. 552 (2013) 469–474.

[42] A. Teate, N. Halder, Disorder-induced band-tailing effects on deep levels in semiconductors, J. Appl. Phys. 70 (1991) 1455–1460.

[43] J. Yoshino, M. Tachikawa, N. Matsuda, M. Mizuta, H. Kukimoto, Alloy fluctuation in mixed compound semiconductors as studied by deep level transient spectroscopy, Jpn. J. Appl. Phys. 23 (1984) L29.

[44] T. Takanohashi, Alloy fluctuation effects on the carrier emission from the Fe acceptor doped in liquid-phase-epitaxy-grown In0.49Ga0.51P, J. Appl. Phys. 65 (1989) 5222–5224.

[45] V. Polojärvi, A. Schramm, A. Aho, A. Tukiainen, M. Guina, Removal of strain relaxation induced defects by flushing of InAs quantum dots, J. Phys. D: Appl. Phys. 45 (2012) 365107.

[46] V. Polojärvi, A. Schramm, A. Aho, A. Tukiainen, M. Pessa, Dislocation-induced electron and hole levels in InAs quantum-dot Schottky diodes, Physica E 42 (2010) 2610–2613.

[47] T. Figielski, Electron emission from extended defects: DLTS signal in case of dislocation traps, Phys. Status Solidi A 121 (1990) 187–193.

[48] W. Schröter, J. Kronewitz, U. Gnauert, F. Riedel, M. Seibt, Bandlike and localized states at extended defects in silicon, Phys. Rev. B 52 (1995) 13726.

[49] L. Gelczuk, M. Dabrowska-Szata, G. Józwiak, Distinguishing and identifying point and extended defects in DLTS measurements, Mater. Sci. -Pol 23 (2005) 625–641.

Tampereen teknillinen yliopisto
PL 527
33101 Tampere

Tampere University of Technology
P.O.B. 527
FI-33101 Tampere, Finland

ISBN 978-952-15-3735-6
ISSN 1459-2045